

Atmospheric Turbulence and Surface Energy Exchange in Urban Environments

Results from the Basel Urban Boundary Layer Experiment (BUBBLE)

Inauguraldissertation
zur
Erlangung der Würde eines Doktors der Philosophie
vorgelegt der
Philosophisch-Naturwissenschaftlichen Fakultät
der Universität Basel

von

Andreas Christen
aus Basel (BS) und Affoltern i. E. (BE)

Basel, 2005

Genehmigt von der Philosophisch-Naturwissenschaftlichen Fakultät auf Antrag von Prof. Dr. Eberhard Parlow, Basel und PD Dr. Mathias W. Rotach, Zürich.

Basel, den 5. April 2005

Prof. Dr. Hans-Jakob Wirz
Dekan

Acknowledgements

First, I would like to thank Prof. Dr. Eberhard Parlow who gave me the opportunity to work in his motivating team. He supported me generously in all activities and let me participate in a number of interesting research projects. Dr. Mathias Rotach's excellent conceptual and practical management was essential for the success of the present experiment, but also the collaboration in details was always a pleasure. The fruitful discussions from early stages of planning up to the final data analysis enriched my scientific experience. Both supervisors gave me the valuable possibility to join several conferences and workshops.

I would like to express my special gratitude to Dr. Roland Vogt. He motivated me to work in the field of atmospheric turbulence a long time ago in the MAP Riviera project, and since then he continuously passed on his fascination and enthusiasm for experimental micrometeorology. Without his rich knowledge in micrometeorological measurement techniques and his practical field experience, this work would have never been possible in the present form. He not only managed the design and construction of the two urban towers, he also brought in many valuable instrumental aspects ensuring data quality and a number of important scientific suggestions during data analysis.

I would like to further thank the lively team of scientists working at the Institute of Meteorology, Climatology and Remote Sensing at the University of Basel for their support, assistance and contributions to the present work: Dr. Christian Feigenwinter for his support in the CO₂ measurements and providing programs for spectral analysis, Irene Lehner for the flux correction programming, Mathias Müller for infecting me with the 'mad scientist disease' and Dr. Eva van Gorsel for her innovative contributions to scientific discussions. Günter Bing and Josette Pfefferli-Stocky provided an excellent computer and administrative support, respectively.

I am indebted to a large number of people who did a great job contributing to the challenging set-up and maintenance of the towers and instruments,

namely Sven Bethke, Matthias Christen, Jan Eitel, Corinne Frey, Dr. Florian Imbery, Paul Müller, Sascha Pfändler, Karl Schroff, Gergely Rigo and Rainer Weissshaidinger.

The experimental contributions and discussions, but also the careful intercomparison of the postprocessing procedures with Prof. Dr. Mathias Roth and Dr. Achanta Satyanarayana (National University of Singapore) are highly appreciated. Dr. Ekaterina Batchvarova and her team (National Institute of Hydrology and Meteorology, Sofia, Bulgaria) substantially supported the activities at the suburban site and later welcomed me with hospitality during a research stay in Sofia in the framework of an institute partnership embedded in BUBBLE. The collaborations with Dr. Sven-Erik Gryning (Risø, Roskilde, Denmark), Prof. Dr. Tim Oke (University of British Columbia, Vancouver, Canada) and Dr. Jennifer Salmond (University of Birmingham, U.K.) were enriching and allowed me to gain insight into interesting research fields. Further, Prof. Dr. Christian Bernhofer (Technical University of Dresden, Germany) provided the valuable data-set from the parking lot site. Dr. Norbert Kalthoff (FZ Karlsruhe, Germany), Prof. Dr. Sue Grimmond (Indiana University) and Prof. Dr. Andrea Pitacco (University of Padova) contributed with additional instrumentation.

I would like to thank all house owners and open-minded inhabitants in the vicinity of the towers, who were very cooperative during the set-up and operation of the uncommon towers. The acceptance by Druckerei Peter Hochuli, Allschwil and Viollier AG, Basel, as well as Südwestfunk for using their radio tower as measurement platform are greatly acknowledged.

The experimental setup would have never been possible without the full support of the authorities of the city of Basel (Baudepartement and IWB). Markus Trautwein generously carried out traffic load measurements. The digital building model surveyed and programmed by the Grundbuch- und Vermessungsamt was an excellent source for morphometrical data. Dr. Hans-Rudolf Moser and Dr. Markus

Camenzind (Lufthygieneamt beider Basel) provided data from their extensive air quality network and analyzed the profiles of passive samplers.

The Swiss Federal Office for Education and Science provided funding of this study (Grant C00.0068). The involvement of the Bulgarian project partners was partly supported through an Institute Partnership financed by the Swiss National Science Foundation (Grant 7IP 065650.01). Part of the analysis linked with the tracer experiment was supported by the Swiss Federal Institute of Technology (Grant TH 35/02-1).

However, greatest thanks go to Tanja Gschwind. Her lovely support always encouraged me. And, she also did a great job in carefully reviewing the manuscript.

Basel, March 2005

Abstract

The present experimental study addresses turbulence and exchange processes in the urban roughness sublayer, namely the region from street canyon floor up to 2.5 times the mean building height. Measurements with ultrasonic anemometer-thermometers from three urban full-scale towers provided new insights into vertical profiles of mean flow, Reynolds stress, turbulent kinetic energy (TKE), dissipation rate, as well as exchange processes of heat, and partially water vapor and CO₂. With the help of ensemble profiles, which are a surrogate for a real horizontal average, results are discussed in the frame of an ‘urban family portrait’.

For the majority of realizations, the plane mixing layer analogy matches processes in the urban roughness sublayer much better than the classical boundary layer theory. The observed patterns suggest a conceptual division of the urban roughness sublayer into three parts, namely the *canyon layer*, the *roof layer*, and an *above-roof layer*.

In the *canyon layer*, local mechanical and thermal turbulence production are of minor importance. Turbulence is dominated by large coherent structures, it is very intermittent and highly uncorrelated. The majority of TKE is imported by turbulent and pressure transport from the roof layer. The well known street canyon vortex is only found on average and only for selected configurations. Upwind roof shape was determined as an important factor affecting its dynamics.

In the *roof layer*, profiles are characterized by strongest gradients and exchange is more efficient. Here, local shear production is a strong source of TKE. The skimming flow over the street canyons creates an inflected mean wind profile, from which instabilities evolve. Notable amounts of TKE and temperature variance are exported from the roof layer by sweeps into the upper street canyon and by ejections into the above-roof layer. As a consequence, dissipation rate is lower than locally produced turbulence and neutral limits of velocity variances are slightly lower than predicted with classical (local) approaches.

In the *above-roof layer*, the mean wind profile approximates the well known logarithmic form valid in the inertial sublayer. And, integral statistics approach surface layer values. Turbulent transport processes of momentum and heat are dominated by ejections. While shear production is the main source of TKE in the roof layer below, here both, buoyancy and shear production are important.

Finally, a network of spatially distributed energy balance measurements allowed a quantitative estimation of the urban energy balance modification. For this purpose, the surface energy balance was simultaneously measured over different land uses (urban, suburban, rural).

The impact of a lower urban albedo is roughly counterbalanced by a stronger long-wave emission, resulting in a nearly equivalent net radiation over urban and rural surfaces. Urban surfaces are characterized by a strong storage term and a high Bowen ratio. At night, turbulent flux densities remain upward directed in dense urban environments. This is explained by a strong nocturnal release of stored heat. As a consequence, the urban inertial sublayer and the roughness sublayer are thermally unstable most of the time.

Zusammenfassung

Die vorliegende Arbeit analysiert Turbulenz und Austauschprozesse in der urbanen Rauigkeitsschicht, welche von Strassenhöhe bis auf die 2.5-fache Gebäudehöhe beprobt wurde. An drei Masten wurden extensive Messungen mit Ultraschallanemometer-Thermometern durchgeführt, welche neuartige Einsichten in die vertikale Struktur der mittleren Strömung, des turbulenten Impulsflusses, der turbulenten kinetischen Energie (TKE) und der Dissipationsrate ermöglichten. Weiter wurden Austauschprozesse von Wärme, Wasserdampf und CO₂ analysiert. Mit Hilfe geeigneter Verfahren konnten räumliche Mittel angenähert werden und die Resultate im Rahmen eines ‘urbanen Familienportäts’ diskutiert werden.

In den meisten Situationen erlaubt die *plane mixing layer* Analogie eine weit angemessenere Beschreibung der Situation als die Theorie einer klassischen Grenzschicht. Die beobachteten Charakteristika liefen auf eine konzeptionelle Dreiteilung der urbanen Rauigkeitsschicht hinaus, und zwar in Strassenschlucht (*canyon layer*), Dachhöhe (*roof layer*) und eine durch Strukturen nicht mehr blockierte Schicht über den höchsten Dächern (*above-roof layer*).

In der Strassenschlucht sind lokale mechanische und thermische Produktion nur von untergeordneter Bedeutung. Die Turbulenz ist stark intermittent, höchst unkorreliert und dominiert von grossen kohärenten Strukturen. Der Grossteil an TKE wird von der Dachhöhe durch turbulenten Transport und Drucktransport importiert. Der bekannte Wirbel in der Strassenschlucht wird nur als mittlerer Zustand erfasst. Die Dachgeometrie der Gebäude beeinflusst massgebend seine Ausprägung.

Auf der mittleren Dachhöhe sind die Profile durch starke Gradienten charakterisiert. Der Austausch ist effizienter. In diesem Bereich ist mechanische Turbulenzproduktion die Hauptquelle für TKE. Die abscherende Strömung über den Strassenschluchten resultiert in einem mittleren Windprofil mit Wendepunkt, welcher weiter Instabilitäten initi-

iert. Ein bedeutender Anteil der lokal produzierten TKE und auch der Temperaturvarianz wird exportiert. Dies geschieht in Form von ‘Sweeps’, welche in die Strassenschlucht hineindringen, aber auch durch ‘Ejections’, welche Varianz in höhere Luftschichten transportieren. Auf Dachhöhe ist folglich die Dissipationsrate geringer als die lokal produzierte Turbulenz und auch die neutralen Grenzwerte der normierten Geschwindigkeitskomponenten sind tiefer als mit der klassischen (lokalen) Skalierung vorhergesagt.

In den Schichten über den höchsten Dächern gleicht sich das mittlere Windprofil der logarithmischen Form der Inertialschicht an. Die integralen Statistiken erreichen die vorhergesagten Grenzwerte. Turbulente Austauschprozesse von Impuls und Wärme sind charakterisiert durch ‘Ejections’. Während auf Dachhöhe die Produktion fast ausschliesslich mechanisch dominiert ist, gewinnt weiter oben auch thermische Produktion von TKE zunehmend an Bedeutung.

Durch ein Messnetz von Energiebilanzstationen wurde die Veränderung der städtischen Energiebilanz auch quantitativ erfasst. Die Energiebilanz verschiedener Oberflächen (urban, suburban, rural) wurde dazu über einen Monat simultan beprobt.

Der Einfluss einer bedeutend tieferen Albedo im Stadtzentrum wird durch die stärkere langwellige Emission der städtischen Oberfläche ausgeglichen, was in einer im Mittel etwa gleich grossen Strahlungsbilanz in der Stadt und im Umland resultiert. Städte sind geprägt von einem weitaus bedeutenderen Speicherwärmestrom und einem hohen Bowen-Verhältnis. In den dicht bebauten Gebieten beliben nachts die turbulenten Wärmeströme nach oben gerichtet. Dies wird durch die effizientere Speicherung und Freisetzung von Energie in den Strukturen der Stadt erreicht. Die bodennahe städtische Atmosphäre ist daher rund um die Uhr vorwiegend instabil geschichtet.

Contents

List of Figures	xi
List of Tables	xvii
List of Symbols	xxi
List of Abbreviations	xxv
1 Introduction	1
2 Theory	5
2.1 Fundamental concepts	5
2.1.1 Layer structure of the atmospheric boundary layer	5
2.1.2 Horizontal scales and resolution	6
2.2 Statistical description of turbulence	9
2.2.1 Continuum assumption	9
2.2.2 Reynolds decomposition	9
2.2.3 Integral statistics	9
2.2.4 Probability density functions	10
2.2.5 Quadrant analysis	10
2.2.6 Characteristic length and time scales	12
2.2.7 Spectral analysis	13
2.3 Analytical description and budget concepts	15
2.3.1 Turbulent flow equations	15
2.3.2 Turbulence closure	16
2.3.3 Surface boundary conditions	17

2.4	Simplifications and scalings	18
2.4.1	Monin-Obukhov similarity theory	18
2.4.2	Plane mixing layer analogy	19
3	Measurements	23
3.1	Observational sites	23
3.1.1	Basel-Sperrstrasse (U1)	25
3.1.2	Basel-Spalenring (U2)	27
3.1.3	Allschwil (S1)	29
3.1.4	Basel-Messe (U3)	30
3.1.5	Grenzach (R1)	30
3.1.6	Village-Neuf (R2)	32
3.1.7	Lange Erlen (R3)	32
3.2	Instruments, calibrations and corrections	34
3.2.1	Ultrasonic anemometer-thermometers	34
3.2.2	Open path gas analyzers	37
3.2.3	Corrections of turbulent flux densities	39
3.2.4	Radiation instruments	40
3.2.5	Cup anemometers	41
3.2.6	Temperature / humidity sensors	42
3.3	Data processing	43
3.3.1	Sonic block averaging	43
3.3.2	Sonic coordinate rotations	43
3.3.3	Horizontal averaging	44
4	Results and Discussion	47
4.1	Mean flow	47
4.1.1	Flow patterns in the street canyon	47
4.1.2	Vertical wind profile	52

4.1.3	Determination of z_0 and z_d	57
4.1.4	Summary	61
4.2	Momentum exchange	62
4.2.1	Definitions and restrictions	62
4.2.2	Vertical profile of Reynolds stress	62
4.2.3	Parameterization of Reynolds stress	67
4.2.4	Quadrant analysis of Reynolds stress	69
4.2.5	Estimation of dispersive stress	77
4.2.6	Summary	79
4.3	Turbulent kinetic energy	80
4.3.1	Length and time scales	80
4.3.2	Turbulent kinetic energy budget	81
4.3.3	Velocity variances	88
4.3.4	Eigenvalue analysis	90
4.3.5	Summary	93
4.4	Exchange processes of heat and mass	95
4.4.1	Turbulent exchange of heat	95
4.4.2	Turbulent exchange of water vapor	102
4.4.3	Turbulent exchange of CO_2	105
4.4.4	Summary	106
4.5	Surface energy balance	108
4.5.1	Definitions and concepts	108
4.5.2	Schedule of observations	108
4.5.3	Short-wave flux densities	109
4.5.4	Long-wave flux densities	111
4.5.5	Net radiation	112
4.5.6	Latent heat flux densities	113
4.5.7	Sensible heat flux densities	118

4.5.8	Storage heat flux densities	120
4.5.9	Anthropogenic heat flux densities	122
4.5.10	Urban energy balance modification	122
4.5.11	Summary	123
5	Conclusions	125
5.1	Methodology	125
5.2	Synthesis	125
5.2.1	Vertical structure of the urban roughness sublayer	125
5.2.2	Exchange processes	128
5.3	Implications	128
5.4	Outlook and future research	130

List of Figures

2.1	Concept of sublayers in the daytime convective ABL.	5
2.2	Illustration of urban scales and related surface heterogeneity in the city of Basel.	7
2.3	Sample joint probability functions illustrating the quadrant numbering convention used in this work.	10
2.4	Conceptual spatial autocorrelation function and corresponding integral length scale.	13
2.5	Conceptual spectra of a velocity component illustrating energy containing range, inertial sub-range and dissipation subrange.	14
2.6	Sketches of a turbulent boundary layer and a turbulent plane mixing layer.	19
3.1	Photo of the street canyon at Basel-Sperrstrasse (U1) with profile tower.	23
3.2	Map of all sites operated during the IOP in June / July 2002.	24
3.3	Schematic view of the tower at Basel-Sperrstrasse (U1) with sonic levels, cup anemometer levels and psychrometer levels.	25
3.4	Photo of the tower at Basel-Sperrstrasse (U1) viewed from inside the street canyon	26
3.5	Map of the station surrounding at Basel-Sperrstrasse (U1).	26
3.6	Photo of the avenue canyon at Basel-Spalenring (U2) with profile tower and canyon measurements.	27
3.7	Schematic view of the tower at Basel-Spalenring (U2) with sonic levels, cup anemometer levels and psychrometer levels	28
3.8	Schematic view of the tower at Allschwil (S1) with sonic levels	29
3.9	Photo of the hydraulic profile tower at Allschwil (S1).	29
3.10	Aerial orthophoto of the site Allschwil (S1)	30
3.11	Aerial photo of site Basel-Messe (U3).	30
3.12	Photo of the rural reference site Grenzach (R1).	32
3.13	Photo of the rural reference site at Village-Neuf (R2).	32
3.14	Photo of the long-term surface energy balance site Lange Erlen (R3).	33

3.15	Front view of a METEK USA-1 instrument attached to the rotation and tilting device in the wind tunnel.	34
3.16	Sample data from the wind tunnel for instrument METEK USA-1 200104018 at 4 ms^{-1}	35
3.17	Photo of the sonic field intercomparison setup at Aesch-Neuhof.	37
3.18	Average time lag for different wind directions between LICOR 7500 analyzer and sonic at U1 level F.	38
3.19	Individual impact of the WPL-correction on mass flux densities of CO_2 at U1 level F.	39
3.20	Impact of the f_k -correction to measurements of L_\downarrow	40
3.21	Absolute and relative impact of the overspeeding correction on the topmost cup anemometer at U1.	41
3.22	Illustration of the horizontal averaging procedure, with data from the sonic profile at U1. . . .	45
4.1	Channeling of flow into the street canyon at U1.	48
4.2	Inclination of mean wind as a function of ambient wind direction at U1.	48
4.3	Ensemble street canyon cross-section of measured wind vectors at U1 for flow situations in a sector perpendicular to the street canyon.	49
4.4	Average rotational frequency of the street canyon vortex Ω_c at U1 for flow perpendicular to the canyon.	49
4.5	Average street canyon vorticity index (CVI) at U1 as a function of ambient wind direction at tower top.	50
4.6	Ensemble street canyon cross-section at U1 for the specific flow situation with flow from 130° – 140°	50
4.7	Sample three-minute time period illustrating instantaneous values of wind velocity, instantaneous CVI and rotational frequency.	51
4.8	Neutral wind profiles of horizontal longitudinal wind velocity, local horizontal wind velocity and mean horizontal wind speed at U1, U2 and S1.	53
4.9	3d visualization of the horizontal local wind velocity $\bar{u}_l(z)$, and corresponding horizontal wind direction in the street canyon at U1 for selected cases.	54
4.10	Profiles of the average wind speed as a function of ambient wind direction at U1.	55
4.11	Wind profile classification with number of inflection points.	55
4.12	Height of the strongest inflection point z_e in the mean wind profile against wind direction of the ambient flow.	56
4.13	Relative frequency for wind profile types at U1 as a function of ambient wind direction and wind velocity.	57

4.14	Averaged profiles of mean horizontal wind velocity and mean horizontal wind speed normalized by corresponding values at canopy top for different stabilities at U1.	58
4.15	Zeroplane displacement and roughness length determined separately for different wind directions of the ambient flow at U1.	58
4.16	Vertical profiles of $\langle u_*(z)/u_*(\text{top}) \rangle$, $\langle u_*(z)/\bar{u}(z) \rangle$, $\langle \overline{u'_l w'} / u_*^2(\text{top}) \rangle$, $\langle \overline{v'_l w'} / u_*^2(\text{top}) \rangle$, $\langle r_{u_l w} \rangle$ and $\langle K_M / k z' u_*(z) \rangle$ at all three profile towers.	63
4.17	Histograms of the height of u_*^{max} at the two urban profile towers.	64
4.18	Vertical profiles of morphometric properties of the surface in a 250 m circle around the tower U1.	65
4.19	Neutral correlation coefficient $r_{u_l w}$ in dependence on ambient wind direction at U1.	66
4.20	Stability dependence of r_{uw} at the towers U1, U2 and S1 in comparison to the rural surface layer at R1.	67
4.21	Profiles of local $u_*(z)$ normalized by wind velocity $\bar{u}(z)$ in dependence on ambient wind direction at U1.	68
4.22	Neutral $\langle u_*(z)/\bar{u}_l(z) \rangle$ against non-dimensional height $(z - z_d)/z_0$	68
4.23	Parameterization of the vertical profile of $u_*(z)$ in comparison to the measured profiles at the three profile towers.	69
4.24	Measured neutral vertical wind profile $\langle \bar{u}/\bar{u}(\text{top}) \rangle$ at U1 compared to the parameterized profile.	69
4.25	Normalized joint probability density functions of $\overline{u'_l w'}$ at U1 for different local stabilities.	70
4.26	Vertical profiles of quadrant measures at U1, U2 and S1 in comparison to results reported from other experimental campaigns.	71
4.27	Conceptual influence from higher order mixed moments on the shape of JPDFs.	72
4.28	Profiles of triple correlations $\overline{u'_i u'_j u'_k}$ at all three towers for neutral conditions.	73
4.29	Stability dependence of quadrant measures ΔS_0 , Ex , H' and ϑ' for $\overline{u' w'}$ at U1.	74
4.30	Dependence of ΔS_0 and third order moments at $z/z_h = 2.17$ on stability.	75
4.31	Cumulant expansion method (CEM) applied to estimate ΔS_0 at U1.	75
4.32	Non-gaussian stress fractions $NGS(\hat{u}, \hat{w})$ in the normalized joint probability density functions of \hat{u}_l and \hat{w}	76
4.33	Dispersive quadrant analysis for $\overline{u''}/\bar{u}_0$ against $\overline{w''}/\bar{w}_0$ at the five lower levels at U1.	78
4.34	Scale analysis of the different terms the horizontally averaged equation of motion normalized by z_h/u_0^2	78
4.35	Length scale $L_{TKE}(z)$ deduced from peak frequency of TKE-spectra, normalized peak frequency of TKE-spectra and individual length scales $L_{u_i}(z)$ for neutral runs at U1.	80

4.36	Vertical profiles of the shear production term at U1, U2 and S1.	82
4.37	Profiles of the scaled shear production term at U1 for different ambient wind directions.	83
4.38	Vertical profiles of buoyancy production for convective runs at U1, U2 and S1.	84
4.39	Vertical profiles of dissipation rate of TKE at U1, U2 and S1.	84
4.40	Locally scaled dissipation rate ($\phi_\epsilon = kz'\epsilon(z)/u_*^3(z)$, class median) against local stability determined by z'/L	85
4.41	Longitudinal velocity spectra with the inertial subrange slope indicated and ratio S_w/S_u for all runs with neutral stability at U1.	85
4.42	Vertical profiles of turbulent transport of TKE at U1, U2 and S1.	86
4.43	Normalized TKE-budget for different stabilities at U1.	87
4.44	Ratio between turbulent kinetic energy (TKE) and mean kinetic energy (MKE) for neutral runs at U1, U2 and S1.	88
4.45	Profiles of the neutral limits of locally scaled velocity variances $\sigma_{ul}(z)/u_*(z)$ (a), $\sigma_{vl}(z)/u_*(z)$ (b) and $\sigma_w(z)/u_*(z)$ (c) at U1, U2 and S1.	89
4.46	Locally scaled $\sigma_{ul}(z)/u_*(z)$ against ambient wind direction at U1.	89
4.47	Locally scaled velocity variances $\sigma_w(z)/u_*(z)$ at the above roof levels against local stabilities at U1 for unstable runs	90
4.48	Locally scaled velocity variances $\sigma_{ul}(z)/u_*(z)$, $\sigma_{vl}(z)/u_*(z)$ and $\sigma_w(z)/u_*(z)$ against local stability at U1.	91
4.49	Orientation of the eigenvectors \mathbf{g}_i of the velocity correlation tensor \mathbf{M}_{ij} in the cartesian space.	92
4.50	Average ratio of the eigenvalues $e_1 : e_2 : e_3$ at U1 drawn into the ‘eigenvalue triangle’, and associated shape of the velocity variance components.	93
4.51	Vertical profiles of scaled neutral eigenvalues $e_i/\overline{u_i'^2}$ of the velocity correlation tensor \mathbf{M}_{ij} at the three profile towers U1, U2 and S1.	93
4.52	Horizontally averaged vertical profiles of $\overline{w'\theta'}$ normalized by its value at tower top at all three towers for convective situations.	95
4.53	Vertical profiles of $\overline{w'\theta'}$ normalized by their value at tower top at U1 for different wind directions and all situations.	96
4.54	Average diurnal variation of $\overline{w'\theta'}(z)$ within and above the street canyon at U1.	96
4.55	Histogram of locally scaled stability classes at different heights at U1, separately calculated for daytime and nocturnal situations.	97
4.56	Vertical profiles of $\langle\sigma_\theta(z)/\sigma_\theta(top)\rangle\langle\sigma_\theta(top)\rangle/\langle\sigma_\theta(2z_h)\rangle$, $\langle r_{w\theta}\rangle(z)$, $\langle\overline{\theta^3}/\sigma_\theta^3\rangle(z)$, $\langle\overline{w'^2\theta'}/(\sigma_w^2\sigma_\theta)\rangle(z)$, $\langle\overline{u'\theta'^2}/(\sigma_u\sigma_\theta^2)\rangle(z)$ and $\langle\overline{w'\theta'^2}/(\sigma_w\sigma_\theta^2)\rangle(z)$ at all three profile towers.	98

4.57	Local scaled temperature variances $\sigma_\theta(z)/\theta_*(z)$ at the above roof levels against local stability at U1 for unstable runs.	99
4.58	Vertical profiles of quadrant measures at U1, U2 and S1.	100
4.59	Normalized JPDFs and NGFs of $\overline{w'\theta'}$ for unstable conditions at U1.	101
4.60	Stability dependence of quadrant measures ΔS_0 , Ex , H' and ϑ' for $\overline{w'\theta'}$ at U1.	102
4.61	One-point integral length scales of heat, water vapor and CO ₂ under unstable conditions from tower top at U1.	102
4.62	Band median values of all cospectra of $\overline{w'\theta'}$, $\overline{w'\rho'_v}$ and $\overline{w'\rho'_c}$ from tower top and canyon top at U1.	103
4.63	Average diurnal course of $r_{w\theta}$, $r_{w\rho_v}$ and $r_{\theta\rho_v}$ at U1, U2, S1 and R1 during the summertime IOP.	104
4.64	Normalized JPDFs of the vertical flux of H ₂ O and CO ₂ for neutral, unstable and convective conditions at U1.	105
4.65	Diurnal courses of third order moments $\overline{w'\theta'^2}/(\sigma_w\sigma_\theta^2)$, $\overline{w'\rho_v'^2}/(\sigma_w\sigma_{\rho_v}^2)$, and $\overline{w'\rho_c'^2}/(\sigma_w\sigma_{\rho_c}^2)$ at tower top and canyon top (U1).	105
4.66	Average diurnal courses of CO ₂ -flux densities and traffic load at U1.	106
4.67	Locally scaled standard deviations $\sigma_s(z)/s_*(z)$ of heat, water vapor and CO ₂ during unstable conditions from tower top at U1.	106
4.68	Relative amount of the short-wave input radiation into different height layers of the urban canopy at U1 as a function of sun elevation.	109
4.69	Angular variation of the average measured albedo for an urban (U1), the suburban (S1) and a rural surface (R1, grassland).	110
4.70	Net radiation and albedo during a clear winter day with snow cover.	111
4.71	Daily variation and annual variation of the radiation balance components during the full year period.	112
4.72	Urban-rural differences in air temperature and absolute humidity.	113
4.73	The daytime Q_E/Q^* ratio and the daytime Bowen ratio β as a function of the vegetation aspect ratio.	113
4.74	Ensemble daytime variation of the energy balance partitioning at the different sites for the IOP.	115
4.75	Ensemble diurnal course of energy balance at 3 urban, 1 suburban and 2 rural sites during the IOP.	116
4.76	Isofluxdiagrams of annual and daily variation of Q^* , Q_H , Q_E and the residual ΔQ_S	117
4.77	Average daily totals of the energy balance components in the city center for each month.	117

4.78 Annual variation of precipitation and k -factor and annual variation of daytime Bowen ratio β over a rural and an urban surface for the period 1997–2002. 118

4.79 Near surface stability histogram for nighttime during the summertime IOP. 119

4.80 Joint probability density function between u_* and $\overline{w'\theta'}$ simultaneously measured at the topmost measurements at U1, U2, S1 and R1. 119

4.81 Relationship between storage heat flux and complete aspect ratio for different times of the day and average nocturnal sensible heat flux in function of complete aspect ratio. 121

5.1 Concept of generalized and horizontally averaged profiles through the roughness sublayer derived from the present study. 126

List of Tables

2.1	Semi-empirical constants a_i , b_i , c_i and f_i in the (locally-scaled) Monin-Obukhov similarity theory.	19
3.1	Directory of all sites operated during the IOP.	24
3.2	Turbulence instrumentation at Basel-Sperrstrasse (U1).	25
3.3	Integral three-dimensional morphometric parameters of the city surface for a circle of 250 m around the three profile towers.	27
3.4	Turbulence instrumentation at Basel-Spalenring (U2).	28
3.5	Turbulence instrumentation at Allschwil (S1).	29
3.6	Surface characteristics of the profile towers and surface energy balance sites.	31
3.7	Settings of the different sonics involved in BUBBLE.	35
3.8	Summary of calibrations and field intercomparisons of all sonics involved in BUBBLE.	36
3.9	Summarized results from the three-day sonic field intercomparison at Aesch-Neuhof.	37
3.10	CSI KH20 Krypton hygrometers involved in BUBBLE.	37
3.11	LICOR 7500 open path analyzers operated at U1.	38
3.12	Average impact of the lag-correction on flux densities of CO ₂ and H ₂ O at U1.	38
3.13	Average impact of different flux corrections applied to Q_H and Q_E	39
3.14	Kipp & Zonen CNR 1 net radiometer involved in BUBBLE, and f_k correction factors determined from the field calibration data.	40
3.15	Eppley PIR Pyrgeometers involved in BUBBLE.	40
3.16	Average impact of the overspeeding correction on cup anemometer data at U1.	41
3.17	Psychrometers used in temperature-humidity profile measurements during BUBBLE.	42
3.18	Separation of kinetic energy for a component i (E_i) into a mean kinetic energy \bar{E}_i , a part removed by the detrending \tilde{E}_i , and the resulting turbulent part E'_i	43
4.1	Vectical profiles of mean concentrations of NO ₂ and CO ₂ through the street canyon at U1.	47

4.2	Stability dependent linear regressions of Ω_c against \bar{u}_0	49
4.3	Absolute frequency for wind profile types detected in the range $0 < z < 2z_h$	56
4.4	Stability classification in the present study according the stability parameter ζ measured at tower top.	57
4.5	Spatial average z_0 and z_d determined with the logarithmic fit using local friction velocity.	59
4.6	Zeroplan displacement determined by the temperature variance method.	59
4.7	Spatial average of z_d determined from peak frequencies of u , v , w and θ - power spectra.	60
4.8	Ratio between zeroplan displacement z_d and mean building height z_h calculated with different morphometric approaches.	60
4.9	Frequency for each of the measurement levels at U1, U2 and S1 to measure highest $u_*(z)$ in the profile.	62
4.10	Relative difference between u_* calculated with locally rotated $\overline{u'_l w'}$ only and with taking lateral contribution into account.	66
4.11	Estimation of the dispersive stress at U1 for neutral conditions.	78
4.12	Summary of measured and calculated characteristics affecting momentum exchange at the urban towers, separately for the canyon layer, the roof layer, and the above-roof layer towards the inertial sublayer.	79
4.13	Neutral limits of normalized maximum peak frequency $n_{\max} = f_{\max} z' / \bar{u}$	81
4.14	Characteristics of the buoyant production term at U1.	83
4.15	Average properties of the inertial subrange of longitudinal velocity spectra relevant for the calculation of ϵ	84
4.16	Turbulent transport (Tt) of TKE and estimation of the dispersive transport (Td) of TKE for neutral conditions at U1.	86
4.17	Neutral limits a_i (Eq. 2.79) for locally scaled $\sigma_{ul}/u_*(z)$, $\sigma_{vl}/u_*(z)$ and $\sigma_w/u_*(z)$	90
4.18	Eigenvalues e_i of the velocity correlation tensor \mathbf{M}_{ij} at U1, normalized by twice the TKE.	92
4.19	Peak frequency $f_{\max} = (n_{\max} z') / \bar{u}(z)$ of cospectra determined from the peak of the median normalized spectra over all runs with given stability.	103
4.20	Horizontally averaged median of quadrant analysis measures for turbulent fluxes of momentum, heat, water vapor and carbon dioxide at two levels at U1, in comparison to surface layer values from R1.	104
4.21	Summary of characteristics affecting heat and mass exchange at the three urban towers, separately for the canyon layer, the roof layer, and the above-roof layer towards the inertial sublayer and for convective situations.	107
4.22	Yearly totals of the radiation balance components for the full-year period.	109

4.23	Average daily totals of all radiation fluxes for the summertime IOP period.	110
4.24	Average energy balance components of the daytime and nocturnal hours during the IOP.	114
4.25	Average daytime partitioning of the energy balance for the full year period.	118
4.26	Coefficients of the objective hysteresis model for the summertime IOP period.	120
4.27	Estimated urban energy balance modification for the summertime IOP period.	122

List of Symbols

a, b	Any variable, $a, b = \{u, v, w, \theta, p, \rho_v, \rho_c\}$	Var.
A_a	Semi empirical function in surface layer scaling for the variance of a	
A_c	Complete surface density per unit volume	$\text{m}^2 \text{m}^{-3}$
A_h	Horizontal surface density per unit volume	$\text{m}^2 \text{m}^{-3}$
A_v	Vertical surface density per unit volume	$\text{m}^2 \text{m}^{-3}$
\mathbf{C}_{ab}	Covariance tensor	Var.
C_D	Drag coefficient	
c_p	Specific heat at constant pressure for moist air	$\text{J kg}^{-1} \text{K}^{-1}$
E	Phase change rate	$\text{kg m}^{-3} \text{s}^{-1}$
\mathbf{e}_i	Cartesian base vectors	m s^{-1}
e_i	Eigenvalues of \mathbf{M}_{ab}	
Ex	Exuberance	
f	Normalized frequency	
g	Acceleration due to gravity	m s^{-2}
$G(\hat{a}, \hat{b})$	Gaussian joint probability density function	
\mathbf{g}_i	Eigenvectors of \mathbf{M}_{ab}	
H'	Hyperbolic hole size above which half of the flux occurs	
I_i	Turbulence intensity of velocity component $i = \{u, v, w\}$	
k	von Karman number	
K_{\downarrow}	Incoming short-wave radiation flux density at the surface	W m^{-2}
K_{\uparrow}	Outgoing short-wave radiation flux density at the surface	W m^{-2}
K^*	Net short-wave radiation flux density (in vertical direction to the surface)	W m^{-2}
Ku_a	Kurtosis of variable a	
K_X	Turbulent transfer coefficient (Eddy diffusivity) for property $X = \{M, H, Q, C\}$	Var.
L	Obukhov length	m
\mathcal{L}	Characteristic length scale of the surface	m
L_{\downarrow}	Incoming long-wave radiation flux density at the surface	W m^{-2}
L_{\uparrow}	Outgoing long-wave radiation flux density at the surface	W m^{-2}
L^*	Net long-wave radiation flux density (in vertical direction to the surface)	W m^{-2}
L_{ab}	One-point integral length scale	m
$L_{ab}^{\cdot\cdot}$	Two-point integral length scale	m
L_s	Shear length scale	m
L_v	Latent heat of vaporization	J kg^{-1}
M	Mean 3d scalar wind speed	m s^{-1}
m	Mean scalar horizontal wind speed	m s^{-1}
\mathbf{M}_{ij}	Velocity correlation tensor $i = \{u, v, w\}$	$\text{m}^2 \text{s}^{-2}$
$M_{ij}(ab)$	Joint moments of a and b	Var.
n	Natural frequency	s^{-1}
p	Pressure	Pa
$P(\hat{a}, \hat{b})$	Joint probability density function of a and b	
Q^*	Net all-wave radiation flux density (in vertical direction to the surface)	W m^{-2}
Q_i^*	Net all-wave radiation flux density in i -th Cartesian direction	W m^{-2}
Q_E	Latent heat flux density (in vertical direction to the surface)	W m^{-2}

Q_F	Anthropogenic heat flux density	W m^{-2}
Q_H	Sensible heat flux density (in vertical direction to the surface)	W m^{-2}
\mathbf{r}	Distance vector between two points	m
r_{ab}	Correlation coefficient between two variables a and b	Var.
\mathbf{R}_{ab}	Correlation tensor	Var.
s	Any scalar, $s = \{\theta, \rho_v, \rho_c\}$	Var.
S_i	Flux or stress fraction of quadrant i	
Sk_a	Skewness of variable a	
St	Strouhal number	
$S_{u_i}(n)$	Spectral density of velocity components $u_i = \{u, v, w\}$	$\text{m}^2 \text{s}^{-1}$
T	Number of time steps in a discrete time series	
t	Time	s
T_a	Averaging time	s
\mathcal{T}_{ab}	Integral time scale of a and b	s
U	3d vector wind velocity	m s^{-1}
\mathbf{u}	Wind vector	m s^{-1}
u	Longitudinal wind velocity component	m s^{-1}
$u_*(\text{IS})$	Friction velocity in the inertial sublayer	m s^{-1}
u_*	Scaling velocity, square of local vertical Reynolds stress	m s^{-1}
u_0	Wind velocity component perpendicular to the street canyon at $z/z_h = 2$	m s^{-1}
u_c	Characteristic convective velocity	m s^{-1}
u_i	Wind component in i -th Cartesian direction, $u_i = \{u, v, w\}$	m s^{-1}
u_l	Local horizontal wind velocity $u_l = (u^2 + v^2)^{0.5}$	m s^{-1}
u_s	Characteristic velocity difference	m s^{-1}
v	Lateral wind component	m s^{-1}
V_b	Building volume density	$\text{m}^3 \text{m}^{-3}$
w	Vertical wind component	m s^{-1}
\mathbf{x}	Position vector	m
x	Distance in longitudinal wind direction	m
x_b	Characteristic building breadth	m
x_c	Canyon width	m
x_d	Characteristic spacing of roughness elements	m
x_i	Distance in i -th Cartesian direction, $x_i = \{x, y, z\}$	m
y	Distance in lateral wind direction	m
y_c	Canyon length	m
z	Height above ground level	m
z'	Scaling length according to Eq. 4.28	m
z_*	Blending height, height of the roughness sublayer	m
z_0	Aerodynamic roughness length	m
z_d	Zeroplane displacement height	m
z_e	Height of the principal inflection point, 'effective' canopy height	m
z_f	Height of maximal local Reynolds stress	m
z_h	Mean obstacle / building height	m
z_i	Mixed layer height	m
α	Albedo	
α_k	Kolmogorov constant for longitudinal velocity	
β	Bowen ratio	
$\gamma_H(ab)$	Ratio of sweeps and ejections at holesize H	
δ	Characteristic flow width	m

δ_{ij}	Kronecker-delta (1 for $i = j$, 0 for $i \neq j$)	
ΔQ_S	Storage heat flux density of a surface	W m^{-2}
ΔQ_T	Energy flux density due to temperature change in an air column	W m^{-2}
ΔS_0	Difference between sweeps and ejections for hole size zero	
ϵ	Dissipation rate of turbulent kinetic energy	$\text{m}^2 \text{s}^{-3}$
ϵ_θ	Dissipation rate of temperature variance	$\text{K}^2 \text{s}^{-1}$
ε	Long-wave emissivity	
ζ	Stability	
θ	Virtual acoustic temperature	K
θ_*	Scaling temperature	K
θ_t	Potential thermodynamic temperature	K
ϑ_i	Time fraction of quadrant i	
ϑ'	Time fraction above the hyperbolic hole size H'	
$\boldsymbol{\kappa}$	Wavenumber vector	m^{-1}
κ	Wavenumber	m^{-1}
κ_i	i -th component of wavenumber vector $i = x, y, z$	m^{-1}
λ_C	Complete aspect ratio	$\text{m}^2 \text{m}^{-2}$
λ_F	Frontal aspect ratio	$\text{m}^2 \text{m}^{-2}$
λ_I	Plan area ratio of impervious non-building surfaces	$\text{m}^2 \text{m}^{-2}$
λ_K	Kolmogorov microscale	m
λ_P	Plan area ratio of buildings	$\text{m}^2 \text{m}^{-2}$
λ_T	Taylor microscale	m
λ_V	Plan area ratio of vegetated surfaces	$\text{m}^2 \text{m}^{-2}$
Λ_x	Mean longitudinal separation of coherent structures	m
ν	kinematic molecular viscosity	$\text{m}^2 \text{s}^{-1}$
ξ	vertical angle of attack	$^\circ$
ρ	Density of moist air	kg m^{-3}
ρ_c	Density of CO_2	kg m^{-3}
ρ_v	Absolute humidity (density of water vapour)	kg m^{-3}
σ_a	Standard deviation of a	Var.
σ_B	Stefan-Boltzmann constant	$\text{W m}^{-2} \text{K}^{-4}$
τ	Shear stress	$\text{kg m}^{-1} \text{s}^{-2}$
τ	Time lag	s
$\phi_i(\zeta)$	Semi-empirical diabatic function for property i in surface layer scaling	
ψ_s	Sky view factor	
ψ_{s0}	Average sky view factor at ground level	
ω	Horizontal wind direction	$^\circ$
Ω_c	Rotational frequency of a canyon vortex	s^{-1}
a	Scalar	
\mathbf{a}	Vector	
\mathbf{A}	Tensor of order 2	
\bar{a}	Temporal average	
$[a]$	Conditional average	
$\langle a \rangle$	Spatial average over a horizontal slice	
a'	Turbulent departure from the temporal average	
a''	Mean flow departure from the spatial-temporal average (dispersive term)	
\hat{a}	Fluctuating part a' normalized by standard deviation σ_a	

List of Abbreviations

ABL	Atmospheric boundary layer
AML	Aerosol mixed layer
ARL	Above-roof layer ($z > z_f$)
BUBBLE	Basel Urban Boundary Layer Experiment
CAL	Canyon layer ($z < z_d$)
CEM	Cumulant expansion method
CET	Central European Time (GMT+1)
CFD	Computational fluid dynamics
CSI	Campbell Scientific Instruments
CVI	Street canyon vorticity index
DKE	Dispersive kinetic energy
ETHZ	Eidgenössisch Technische Hochschule Zürich
FFT	Fast fourier transform
FOV	Field of view
GVA	Grundbuch- und Vermessungsamt Basel-Stadt
IOP	Intensive operation period (June 12 - July 12, 2002)
IS	Inertial sublayer
ISR	Inertial subrange
JPDF	Joint probability density function
LHA	Lufthygieneamt beider Basel, Liestal
LIDAR	Light detection and ranging
MKE	Mean kinetic energy
ML	Plane mixing layer
NGF	Non-Gaussian flux fractions
NGS	Non-Gaussian stress fractions
NGT	Non-Gaussian time fractions
NUS	National University of Singapore
NWP	Numerical weather prediction
PDF	Probability density function
RASS	Radio acoustic sounding system
RMS	Root mean square (error)
ROL	Roof layer ($z_d < z < z_f$)
SL	Surface layer
SODAR	Sound detecting and ranging
TKE	Turbulent kinetic energy
TVM	Temperature variance method (Rotach, 1994)
UBC	University of British Columbia, Vancouver
UCL	Urban canopy layer
UTZ	Urban terrain zone (Ellefsen, 1991)
UWO	University of Western Ontario, London
WPL	Webb-Pearman-Leuning Correction (Webb et al., 1980)

1 Introduction

Air pollution in urban areas is an environmental problem of major concern. Furthermore, knowledge of pollutant dispersion in cities is important for public security, e.g. in case of accidental releases. Both, the prediction of pollutant concentrations for planning, and emergency response, heavily rely on numerical modelling. However, the state of the art in most urban dispersion models is still to use turbulence and surface exchange parameterizations, which are designed for non-urban terrain, partially with slight urban adjustments, but without taking into account the effects of the extremely rough surfaces of cities (Hanna et al., 1993; Chang and Hanna, 2004).

Moreover, increasing computational power allows operational meso-scale meteorological models to be run at higher spatial resolution. Today, the smallest nesting domain of numerical weather prediction models has a typical horizontal resolution of 2 to 10 km, resulting in more grid points that will represent urban areas. Parameterizations that take into account urban surface characteristics and exchange processes are needed for these grid points. Most operational models ignore urban land use, or simply use modified values for a number of surface-characterizing variables without any modification due to the high roughness (Craig and Bornstein, 2002).

In an urban environment, most human activities take place within a shallow air volume reaching from street level up to roughly two times the average building height. Dispersion and energy exchange processes in this atmospheric layer, which is partially confined by buildings, are not well understood. This so called *roughness sublayer* does not allow the application of classical surface layer simplifications. For instance, the widely applied Monin-Obukhov similarity theory fails in the lower part of the roughness sublayer, and it is unknown, to what extent it is still appropriate. Further, material properties, three dimensional configuration, reduced water availability and human energy input strongly alter the urban energy balance partitioning at the surface-atmosphere interface. As a consequence, the ther-

modynamics of the whole urban boundary layer are modified.

State of current research

Up to the year 2000, experimental activities in the field of urban micrometeorology were relatively sparse. The early ‘St. Louis study’ (Clarke et al., 1982) was one of the first large efforts to address atmospheric turbulence in urban areas. Most subsequent urban field experiments focused on momentum transport and velocity variances in the roughness sublayer and were short-term case studies or activities limited to a single location (e.g. Rotach, 1993a; Feigenwinter et al., 1999; Louka et al., 2000). However, they revealed many important features, including the fact that the vertical profile of Reynolds stress in the roughness sublayer is not constant with height. Velocity variances have also been addressed in a number of early studies (Brook, 1972; Steyn, 1982; Högström et al., 1982). Most results are presented in a local scaling frame and suggested slightly modified parameters in the similarity relationships (Roth, 2000).

Parallel to the investigation of atmospheric turbulence, in the 1990s, a number of full-scale experimental studies have significantly increased the knowledge on energy exchange of urban surfaces (Arnfield, 2003). Most of the studies investigated the surface energy balance over suburban residential areas, because they cover the largest areas of today’s cities (e.g. Grimmond and Oke, 1995, 1999b). Due to methodological problems, only a few campaigns probed the dense and predominantly impervious city centers (Oke et al., 1999; Grimmond et al., 2004). There is little information on turbulent exchange characteristics of heat and water vapor (e.g. Roth and Oke, 1993a). Another field of growing interest is the urban CO₂ budget. Up to now, information on turbulent exchange of CO₂ over urban areas is very sparse (Grimmond et al., 2002; Moriwaki and Kanda, 2004; Vogt et al., 2005).

In the last five years, the urban roughness sublayer became a major focus of a number of collaborative field experiments. The increasing interest is mainly driven by the enhanced computational power of today's models and the lack of experimental knowledge and verification data. The political concern on air pollution, and finally the prevention of emergencies – or at least an adequate response – attributed a high priority to these topics. A number of international field campaigns were launched, which all address urban meteorology simultaneously at different spatial scales and apply manifold approaches: URBAN 2000 in Salt Lake City focused on pollutant dispersion processes at different scales in a city in complex terrain (Allwine et al., 2002). In Marseilles (France), the international ESCOMPTE/UBL project in summer 2001 was embedded in a larger scale effort to investigate the meteorological conditions leading to high ozone concentrations in the complex environment of the Mediterranean coast (Mestayer et al., 2005). The present work is part of the international BUBBLE - the Basel Urban Boundary Layer Experiment (2001-2002). BUBBLE is probably the most detailed European urban boundary layer experiment with a number of experimental activities in the city of Basel, Switzerland (Rotach et al., 2005). Recently, Joint 2003 in Oklahoma City started, which is a large U.S. project devoted to the dispersion of harmful substances in urban areas, including entrainment of pollutants into buildings (Allwine et al., 2004). DAPPLE is another effort in central London to address dispersion of pollutants at a street canyon intersection (Arnold et al., 2004).

Parallel to these experimental activities, there were many successful attempts to modify dispersion models for urban applications (Rotach, 2001; de Haan et al., 2001; Warner et al., 2004). Further, a number of sophisticated urban parameterizations for meso-scale models were developed (Masson, 2000; Martilli et al., 2002; Otte et al., 2004). Many approaches are not yet verified, and there is need for further improvements. It is an ongoing process to enhance the performance of these models, and to translate newest experimental results into appropriate turbulence and surface exchange parameterizations.

Experimental framework

The present thesis is embedded in BUBBLE, which was founded by the Swiss Ministry of Education and Science with the active contribution of 20 institutions from 10 different countries. It was directly associated with the European COST 715 action, devoted to 'Meteorology applied to urban air pollution' (Fisher et al., 2002, 2005). The general philosophy of BUBBLE was to involve simultaneously different scales and methods: numerical modelling, remote sensing, a large field measurement campaign and a wind tunnel investigation have been combined to gain a more detailed and complete picture of the urban boundary layer and to contribute to the understanding of exchange and dispersion processes in urban areas.

The present thesis covers the BUBBLE near surface measurements, addressing atmospheric turbulence in the urban roughness sublayer as well as its impact on diffusion and momentum, mass and energy exchange. In contrast to nearly all previous field studies, the spatial domain of interest combines both, above roof measurements, and simultaneous measurements in the urban street canyons. This was done with the help of three micrometeorological profile towers, reaching from street level up to approximately two times the mean building height. Further, the experimental investigation of the urban surface energetics at seven different sites allowed to investigate the surface energy partitioning over different land-use (rural, suburban, urban) under the same synoptic forcing.

Objectives

The fluid mechanical processes explaining the exchange of air between canyon/backyard air masses and the ambient flow are of essential interest in all above applications. In recent years, intermittency and turbulent exchange in plant canopies have been successfully addressed with the help of the *plane mixing layer analogy* (Section 2.4.2). The vertical wind profile (Section 4.1), turbulent structures (Section 4.2) and the associated turbulence length scales (Section 4.3) are important indications to assess the applicability of the plane mixing layer analogy over urban surfaces. Coupled with this question is the search of adequate scaling parameters in the urban

roughness sublayer. It must be kept in mind that the permeability of plant canopies does not allow a direct analogy with the stiff urban surface, and that many urban specific flow patterns like street canyon vortices are not found in natural canopies.

Previous studies already resulted in valuable information on the vertical profile of *Reynolds stress*, but there are still a number of open questions. Strategies to upscale and generalize specific results are needed and the profiles have to be related to the urban morphology. For example, the reported height of maximum Reynolds stress is different in most wind tunnel studies and full scale studies. Further, Rotach (1991) reported a dominance of downward directed sweeps in the momentum transport whereas Feigenwinter (2000) found upward directed ejections more relevant. The present data set allows to resolve these inconsistencies. The analysis of *probability density functions* and higher order moments is an important issue in order to determine relevant exchange structures and intermittency (Section 4.2).

Dissipation rate of turbulent kinetic energy (TKE) is one of the key parameters in numerical models, but little is known about its vertical profile within the urban roughness sublayer. The question of the applicability of the inertial subrange method, i.e. the practical procedure to determine dissipation rate from spectra, has to be addressed. Additionally, the analysis of all terms of the TKE budget will lead to insight into processes that create, relocate and destroy turbulence (Section 4.3). The TKE budget builds the basis for the discussion of velocity variances and turbulent exchange processes.

The vertical profiles of *turbulent flux densities of heat and mass* and corresponding exchange mechanisms in the urban roughness sublayer are mostly unknown. The COST 715 action identifies "a need to understand the physical processes driving the turbulent exchange in the urban roughness sublayer and to parameterize the typical vertical profiles for variables of interest therein." (Rotach, 2005). Especially, the knowledge on vertical profiles, higher order moments, and length scales of heat and mass will help to further identify driving processes and should clarify if transfer of momentum, heat, water vapor and CO₂ are similar or to what extent dissimilarities are revealed (Section 4.4).

Not only the physical exchange processes are im-

portant, but simply the magnitude of meteorological variables needed in air quality models are of high practical need. Many input parameters such as the surface flux are not routinely measured. Hence, it is of interest to present parameterizations and relate the *urban energy balance partitioning* to simple surface properties. In a climatological frame, the urban radiation and energy balance modification is analyzed in its diurnal and annual variation (Section 4.5).

2 Theory

2.1 Fundamental concepts

2.1.1 Layer structure of the atmospheric boundary layer

Observations as well as theoretical considerations suggest that the atmospheric boundary layer can be separated into different vertical layers where exchange mechanisms and turbulence are dominated by different parameters. A number of scalings have been developed, each simplifying processes of a certain layer and scale. Some scalings are only applicable to particular stratifications (stabilities), while others cover all states of the atmosphere.

The *atmospheric boundary layer* (ABL) refers to the whole vertical domain directly above the Earth's surface in which surface forcing influences the thermodynamics and flow properties of the atmosphere on time scales less than a day (Garratt, 1993). The ABL depth is variable and typically between 100–3000 m deep.

The vertical structure of the ABL is shortly outlined in this section. In the present work, we focus on processes in the (urban) surface layer and especially on its roughness sublayer, which are therefore presented in more detail.

In analogy to wall boundary layers, the ABL can be separated into an *outer region* and an *inner region*. In the outer region, turbulence is assumed to be independent of surface roughness. The Coriolis force is important and friction forces are neglected. The outer region is separated, depending on stratification and driving processes, into a daytime, convective *mixed layer* and into the *nocturnal boundary layer*.

The mixed layer — The mixed layer develops during daytime and is characterized by strong convection. The height of the mixed layer, the bound-

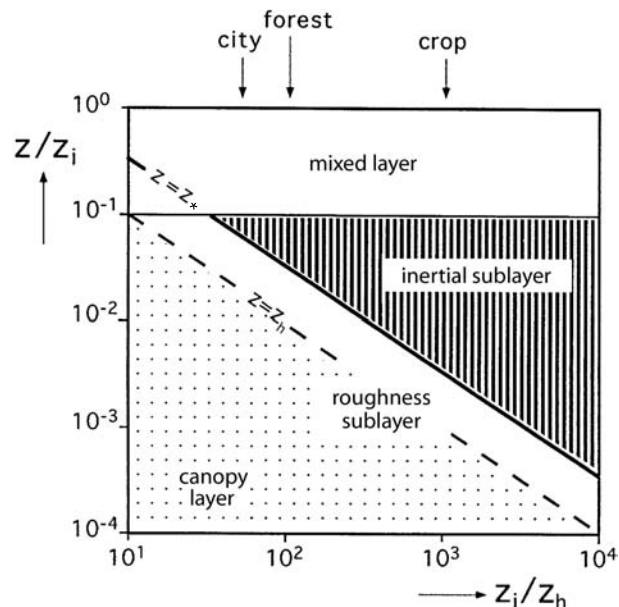


Figure 2.1: Concept of sublayers in the daytime convective ABL. z_h is the mean height of the roughness elements, z_* is the roughness sublayer height and z_i is the atmospheric boundary layer height. Slightly modified from Rotach (1999).

ary layer height z_i^* , is usually growing as the mixed ABL air entrains the free atmosphere driven by a continuous heating up of the surface. Mixed layer similarity theory applies with its scaling length z_i . Fluxes usually decrease with height.

The nocturnal boundary layer — The nocturnal boundary layer is the stable counterpart of the mixed layer, which typically forms at night. Turbulence and mixing often decay as radiative cooling of the surface generates the development of a shallow nocturnal boundary layer characterized by statically stable air with weak and intermittent turbulence. During periods with weak turbulence, the flow aloft is found to be decoupled from the surface. Over urban areas, an elevated inversion layer is often found several hundred meters above the surface, while the layer below stays in unstable stratification (cf. Section 4.5.7).

In boundary layer meteorology, the inner region is

* All mathematical symbols used in this thesis are defined in the list of symbols on page xxi.

called *surface layer*. Here, Coriolis force is neglected in favor of friction forces. The surface layer is the region where $z \ll z_i$ and usually covers the lowest 10% of the ABL. The surface layer above a rough surface can be further divided into an *inertial sublayer* and a *roughness sublayer* (Raupach et al., 1991). The inertial sublayer is the region where $z_0 \ll z \ll z_i$, but where the flow is not influenced by single roughness elements.

Inertial Sublayer — Within the inertial sublayer, shear stress is nearly constant with height, and hence, it is also called the *constant flux layer*. Monin–Obukhov similarity theory often applies and the principal scaling length is the height above ground z . Here, mean profiles of turbulence statistics obey the semi-logarithmic laws and their diabatic extensions (cf. Section 2.4.1).

Roughness Sublayer — The roughness sublayer (sometimes referred to as *interfacial layer*) is the lowest part of the surface layer beneath the inertial sublayer. It extends up to the blending height z_* where influences from single roughness elements vanish. The depth of the roughness sublayer is typically 1.5 to 4 times the mean obstacle height. With increasing height of the roughness elements, the roughness sublayer is of increasing practical interest. Above relatively smooth surfaces such as sand, ice or open water, the roughness sublayer may be neglected. The roughness sublayer depth is less than a meter above shallow crops, but it reaches up to tens of meters in urban areas or old-grown forests. As a consequence, the inertial sublayer extent is reduced, or may even vanish (Rotach, 1999). This is especially important in the nocturnal boundary layer when z_i is small (Fig. 2.1).

Within the roughness sublayer, local advection and horizontal turbulent transports are not negligible and time averaged turbulence statistics and flux densities are vertically and horizontally inhomogeneous. Moreover, the flow is not in local equilibrium, i.e. transport terms in the conservation equations (Section 2.3.1) are important.

In an urban area, we spend most of our lives within the roughness sublayer and also, the majority of emissions take place here. This underlines the im-

portance to understand, generalize and parameterize dispersion and turbulent exchange in the urban roughness sublayer. Many turbulence statistics and exchange processes in the urban roughness sublayer are not fully understood, due to its complex nature, and the inevitable experimental difficulties to retain a generalized view from single point measurements. Therefore, the urban roughness sublayer was in the focus of different field experiments in recent years — including the present one.

The lowest part of the roughness sublayer from ground up to the mean obstacle height z_h is referred to as *canopy layer* (Oke, 1987). It is partly confined by the presence of roughness elements such as buildings and vegetation. The mean flow is severely channelled and altered by the geometry of the roughness elements. The few data available suggest that the mean wind velocity profile in the canopy layer obeys an exponential decay law (Cionco, 1965; Macdonald, 2000). Turbulence is expected to be controlled by coherent structures at the same scale as the canopy height. Further, for vegetation canopies, a *basal layer* is suggested within the canopy layer, which is the layer closest to the ground (Villani et al., 2003). Due to the different geometry of an urban canopy, this term is not used in urban studies.

2.1.2 Horizontal scales and resolution

Most atmospheric processes are limited to a certain time- and length scale, which is reflected in the famous classification into macro-, meso- and microscale processes and the respective subgroups (Orlanski, 1975). The overlapping between the chosen scale of interest and the scale of any physical process determines whether the process may be neglected, parameterized (empirically or physically) or directly solved in a model. It is obvious that all scales are interrelated. Kinetic energy is passed down from larger scales to smaller scales and is finally dissipating to heat. On the other hand, small scale processes in their quantity initiate and evolve larger structures and patterns.

The classification into different scales is especially important for scale-dependent simplifications. The grid cell size of Eulerian models are limited to resolve only a certain level of detail, and have a lower

and upper resolution limit. Unresolved processes that are below the lower limit of the chosen scale are called *subscale processes*. In all applications concerning dispersion and transport processes in the atmospheric boundary layer, the unresolved (turbulent) processes are of essential importance. We try to parameterize the unresolved turbulent fluctuations by appropriate forcings at the resolved scale, which we have to identify first. Important subscale processes are tried to be solved under certain closure assumptions (parameterizations).

Unresolved processes that are above the upper limit of the chosen scale, e.g. larger than the whole domain of interest, are called *superscale processes*. They are implemented by variation of the boundary conditions (e.g. by model nesting). In turbulence research, superscale effects are often eliminated by spectral trend removal. Any remaining energy from larger scales that does not affect fluxes is referred to as inactive turbulence. Turbulence in any surface layer can be divided into active scales that transport momentum, heat and mass, and into inactive scales that are superimposed and do not affect the turbulent transport. Townsend's hypothesis states that these two kinds of turbulence do not interact, which allows us to conceptually separate them (Townsend, 1961; McNaughton and Brunet, 2002).

This view underlines that the terms homogeneity and stationarity are always scale dependent. Variables that are stationary at a certain time scale (e.g. wind velocity at the scale of hours) may be instationary in other scales (wind velocity at the scale of seconds or synoptic driven events at the scale of days). The same applies to homogeneity.

Britter and Hanna (2003) suggest four conceptual ranges of length scales in the urban context: regional (up to 100 or 200 km), city scale (up to 10 or 20 km), neighborhood scale (up to 1 or 2 km), and street canyon scale (less than 100 m). In fact, the atmospheric layer concept, the scale concept and also the typical duration of processes are all linked.

Street canyon scale — At street canyon scale, detailed flow and dispersion within street canyons and around single buildings or intersections are addressed. The nature of the urban roughness sublayer is a consequence of inhomogeneities at the street canyon scale. Practically, the street canyon



Figure 2.2: Illustration of urban scales and related surface heterogeneity in the city of Basel. Photos by courtesy of M. Roth, NUS Singapore, and R. Vogt, University of Basel.

scale is important in architecture (wind load), microscale dispersion and in air pollution applications. The flow at this scale can be directly modelled in CFD applications (e.g. large eddy simulations). When modelling at this scale, a detailed knowledge on the three-dimensional structure is needed, but many parameterizations are obsolete, because most processes are resolved with immense computational power. There are a number of wind tunnel studies, and some few field experiments focussing explicitly on processes on street canyon scale. Nearly all surface measurements are carried out at this scale, even if their representativeness is interpreted at larger scales.

Neighborhood scale — The neighborhood scale restores horizontal homogeneity of the surface at a larger scale by horizontal averaging over a homogeneous area of the city, large enough to filter out (repetitive) surface inhomogeneities at the street canyon scale (Fig. 2.2). The formation of an inertial sublayer is a consequence of the homogeneity at the neighborhood scale. The neighborhood scale is currently reached by experimental mesoscale numerical models, and sophisticated urban canopy parameterizations have been developed (e.g. Masson, 2000; Martilli et al., 2002; Otte et al., 2004). Fur-

ther, the neighborhood scale is the preferred level of detail where urban Lagrangian near-field dispersion models are run (e.g. Rotach, 2001; de Haan et al., 2001). The restored horizontal homogeneity allows many simplifications, but also needs important parameterizations of the underlying urban roughness and canopy sublayer. Finally, the neighborhood scale is the scale of choice for flux monitoring sites.

City scale and regional scale — These scales both focus on the modification of the whole boundary layer (mixed layer). This is of interest in NWP, since today's models already include many grid cells that are 100% urban, and especially urban areas need appropriate predictions due to the high number of human activities. On the other hand, urban areas modify the whole boundary layer, its stability, thermodynamic properties, and the mixed layer height. The modified urban surface exchange results in typical urban climate phenomena like the urban heat island. At this scale, many processes in the urban roughness sublayer and the canopy sublayer are not of central importance anymore. There are many attempts that simply alter the surface exchange parameterization of models to incorporate effects at the city scale (Taha, 1999a).

In the present work, we focus on the street canyon and neighborhood scales. Knowledge of processes at these scales is important to develop, test and support general or urban specific parameterizations, which are of high need in today's models.

2.2 Statistical description of turbulence

Single motions in a turbulent flow are chaotic and unpredictable. Luckily, they are seldom of importance, and any prediction focuses on resulting integral effects of turbulence on dispersion and exchange processes. A statistical view allows quantifying integral effects by already incorporating a huge number of single events. A statistical analysis of turbulence significantly reduces the amount of data and simultaneously retains basic information.

This chapter introduces statistical tools and concepts. The continuum assumption (Section 2.2.1) and the Reynolds decomposition (Section 2.2.2) provide both basics for a statistical description. The relevant statistic moments are defined in Section 2.2.3, and Sections 2.2.4 and 2.2.5 present sophisticated probabilistic approaches like probability density functions and quadrant analysis. Finally, integral time- and length scales as well as spectral analysis (Sections 2.2.6 and 2.2.7) allow to highlight turbulent motions and exchange processes from a different view. They allow a quantitative determination of the characteristic scales of processes.

2.2.1 Continuum assumption

The ratio between the free molecular path length to the characteristic length scale of turbulent motions is called *Knudsen-number* Kn (Brown, 1991). In the troposphere, $Kn \ll 1$ and typically is in the order $\approx 10^{-8}$ to 10^{-10} (Prölss, 2001). This allows us to treat the atmosphere as a continuum. Any variable can already be described as an integral state of a homogeneous fluid parcel without having the full knowledge of all single motions and states resolved down to the molecular level.

2.2.2 Reynolds decomposition

The *Reynolds decomposition* splits any instantaneous variable $a(\mathbf{x}, t)$ at a given location \mathbf{x} and time t into a resolved mean value (denoted by an overbar) and an unresolved fluctuating part (denoted by a prime),

$$a = \bar{a} + a'. \quad (2.1)$$

Commonly, the splitting is done in the time domain with \bar{a} , the temporal average over an averaging time T_a , which fulfills the assumption of (i) stationarity and (ii) the condition that T_a lies in the region of the spectral gap:

$$\bar{a} = \frac{1}{T_a} \int_{t=0}^{T_a} a(t) dt. \quad (2.2)$$

The concept of stationarity, which results in $\partial/\partial t = 0$, is seldom fulfilled, since superscale forcings (e.g. inactive turbulence, diurnal and synoptic effects) result in continuously changing boundary conditions. For the same reason, the presence of a spectral gap, which theoretically results from an energetic separation of the energy input at the synoptic scale and the energy produced at the turbulent scale (Stull, 1988), is in doubt. There are numerous procedures that try to remove trends in order to restore stationarity in real atmospheric data, which all have the disadvantage to break the rule of energy conservation.

2.2.3 Integral statistics

With Eq. 2.3 we can define higher order statistical moments where i is called their order (Schönwiese, 1992):

$$\overline{a^i} = \frac{1}{T_a} \int_{t=0}^{T_a} a^i(t) dt. \quad (2.3)$$

The second moment with $i = 2$ is the variance and its square root σ_a is the standard deviation:

$$\sigma_a = \sqrt{\overline{a'^2}}. \quad (2.4)$$

The higher order moments are usually non-dimensionalized and the nondimensional moments are called skewness

$$Sk_a = \frac{\overline{a'^3}}{\sigma_a^3} \quad (2.5)$$

and kurtosis

$$Ku_a = \frac{\overline{a'^4}}{\sigma_a^4} - 3. \quad (2.6)$$

In isotropic Gaussian turbulence, both, Sk_a and Ku_a are zero. The more general form of two-variable mixed moments for any variables a and b with $a \neq b$ is

$$\overline{a^i b^j} = \frac{1}{T_a} \int_{t=0}^{T_a} a^i(t) b^j(t) dt. \quad (2.7)$$

The most important case is the covariance with $i = 1$ and $j = 1$. Again, $i + j$ define the order of the moment. The correlation coefficient is the covariance scaled by the two standard deviations. According to the Schwarz's inequality, it is in the range between -1 and $+1$. If a and b are completely uncorrelated, r_{ab} is zero, and (minus) unity if they are perfectly (negatively) correlated.

$$r_{ab} = \frac{\overline{a'b'}}{\sigma_a \sigma_b}. \quad (2.8)$$

Using Reynolds decomposition, the total kinetic energy of the flow can be separated into mean kinetic energy and turbulent kinetic energy $0.5u_i'^2$ (TKE):

$$\frac{1}{2}u_i^2 = \frac{1}{2}\overline{u_i^2} + \frac{1}{2}u_i'^2. \quad (2.9)$$

We see that TKE is the sum of the diagonal components of the velocity covariance tensor \mathbf{M}_{ij} , and therefore is invariant to any arbitrary orientation of the coordinate axis.

$$\mathbf{M}_{ij} = \overline{u_i' u_j'} = \begin{pmatrix} \overline{u'u'} & \overline{u'v'} & \overline{u'w'} \\ \overline{u'v'} & \overline{v'v'} & \overline{v'w'} \\ \overline{u'w'} & \overline{v'w'} & \overline{w'w'} \end{pmatrix} \quad (2.10)$$

Analogous, higher order tensors can be defined, e.g. the third order velocity trippelcovariance tensor \mathbf{M}_{ijk} .

2.2.4 Probability density functions

We define $\hat{a}(a)$ as a measure of the fluctuating deviation from the mean of any parameter a (velocity component, pressure, heat or scalar) scaled by its corresponding standard deviation, i.e. $\hat{a}(t) = a'/\sigma_a$. The probability density function $P(\hat{a})$ is defined as the derivative of the cumulative distribution function $D(\hat{a})$ of \hat{a} in a stationary time series of length T_a , namely,

$$D(\hat{a}) = \lim_{T_a \rightarrow \infty} \frac{1}{T_a} \int_0^{T_a} I(t) dt = \int_{-\infty}^{\hat{a}} P(\hat{a}) d\hat{a} \quad (2.11)$$

where $I(t)$ is an indicator function,

$$I(t) = \begin{cases} 1 & \text{if } a'(t)/\sigma_a \leq \hat{a} \\ 0 & \text{if } a'(t)/\sigma_a > \hat{a} \end{cases} \quad (2.12)$$

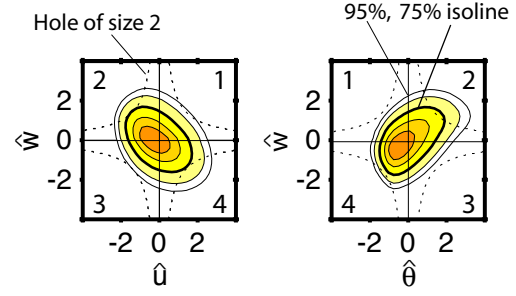


Figure 2.3: Sample joint probability functions $P(\hat{u}, \hat{w})$ and $P(\hat{w}, \hat{\theta})$ illustrating the graphical and the quadrant numbering convention used in this work. The isolines incorporate 95, 90, 75 (thick), 50 and 25% of all realizations.

The probability density function satisfies

$$\int_{-\infty}^{\infty} P(\hat{a}) d\hat{a} = 1. \quad (2.13)$$

In isotropic, uncorrelated Gaussian turbulence, the probability density function of \hat{a} is

$$G(\hat{a}) = \frac{1}{\sqrt{2\pi}} e^{(-\frac{1}{2}\hat{a}^2)}. \quad (2.14)$$

If \hat{a} and \hat{b} are two parameters (velocity components, enthalpy or scalars) that are scaled by their standard deviations, we can define a joint probability density function $P(\hat{a}, \hat{b})$, which again satisfies

$$\iint_{-\infty}^{\infty} P(\hat{a}, \hat{b}) d\hat{a} d\hat{b} = 1. \quad (2.15)$$

In the case of Gaussian turbulence, the joint probability density function of two parameters is

$$G(\hat{a}, \hat{b}) = \frac{1}{2\pi\sqrt{1-r_{ab}^2}} e^k \quad (2.16)$$

with

$$k = -\frac{\hat{a}^2 + 2r_{ab}\hat{a}\hat{b} + \hat{b}^2}{2(1-r_{ab}^2)} \quad (2.16)$$

where r_{ab} is the correlation coefficient, which has been already defined in Eq. 2.8, and can be also written as

$$r_{ab} = \overline{\hat{a}\hat{b}}. \quad (2.17)$$

2.2.5 Quadrant analysis

Definitions and Method — By applying quadrant analysis, we separate the joint probability density functions $P(\hat{a}, \hat{b})$ of two parameters a and b

into the four quadrants Q_i of the Cartesian plane with $i = \{1, 2, 3, 4\}$ (Wallace et al., 1972; Lu and Wilmarth, 1973; Antonia, 1981). For each of the quadrants, a time fraction ϑ_i can be calculated,

$$\vartheta_i = \int_{l_a}^{u_a} \int_{l_b}^{u_b} P(\hat{a}, \hat{b}) da db. \quad (2.18)$$

ϑ_i is the relative total duration of events in quadrant i . The lower (l_a, l_b) and upper (u_a, u_b) integration limits of the four quadrants are summarized in the following table.

		Quadrant Definition			
$a = u$	$b = w$	1	2	3	4
$a = t, \rho_v, \rho_c$	$b = w$	2	1	4	3
	l_a	0	$-\infty$	$-\infty$	0
	u_a	∞	0	0	∞
	l_b	0	0	$-\infty$	$-\infty$
	u_b	∞	∞	0	0

Note that the definition of quadrant numbering for momentum flux $\overline{w'w'}$ is different from the numbering of all other flux densities ($\overline{w'\theta'}$, $\overline{w'\rho'_v}$ or $\overline{w'\rho'_c}$). Usually, $\overline{w'w'}$ is directed towards the surface, while all other flux densities typically transport energy or mass away from the surface. In order to attribute the same physical processes to each quadrant, numbers are arranged in a way that assumes the mean vertical wind gradient to be opposite to the mean (unstable) vertical temperature gradient, humidity and CO₂-gradient*.

- $i = 1$: outward interactions
- $i = 2$: ejections or bursts
- $i = 3$: inward interactions
- $i = 4$: sweeps or gusts

From Eq. 2.15 and 2.18, we conclude that

$$\sum_{i=1}^4 \vartheta_i = 1. \quad (2.19)$$

Further, a flux (or stress) fraction S_i can be calculated with same definitions (Raupach, 1981):

$$S_i = \frac{1}{r_{ab}} \int_{l_a}^{u_a} \int_{l_b}^{u_b} \hat{a} \hat{b} P(\hat{a}, \hat{b}) da db. \quad (2.20)$$

* Some authors flip the orientation of the axis to account for the different signs of $\overline{w'w'}$ and the other flux densities (Katul et al., 1997). This is not necessary with the present definitions.

The flux fractions represents the contribution from this particular quadrant to the overall flux density. From Eq. 2.15 and 2.20, we see that

$$\sum_{i=1}^4 S_i = 1. \quad (2.21)$$

Quadrant Measures — Different quantities can be calculated from the flux (or stress) fractions. Important measures are the difference ΔS_0 between sweeps and ejections

$$\Delta S_0 = S_4 - S_2 \quad (2.22)$$

and their ratio

$$\gamma_0 = \frac{S_2}{S_4}. \quad (2.23)$$

If ΔS_0 is other than zero (or γ_0 not equal unity), this is an indication that moments of order 3 or higher are also non-zero. The joint probability density function $P(\hat{a}, \hat{b})$ is completely specified by an infinite set of joint moments M_{ij} (Nakagawa and Nezu, 1977):

$$M_{ij} = \overline{\hat{a}^i \hat{b}^j}. \quad (2.24)$$

Assuming that only third order moments explain ΔS_0 , Raupach (1981) showed that ΔS_0 can then be described by a third order cumulant expansion of the joint probability function $P(\hat{a}, \hat{b})$:

$$\Delta S_0 = \frac{r_{ab} + 1}{r_{ab} \sqrt{2\pi}} \left(\frac{2C_1}{(1 + r_{ab})^2} + \frac{C_2}{1 + r_{ab}} \right) \quad (2.25)$$

where

$$C_1 = (1 + r_{ab}) \left(\frac{M_{03} - M_{30}}{6} + \frac{M_{21} - M_{12}}{2} \right) \quad (2.26)$$

$$C_2 = - \left(\frac{(2 - r_{ab})(M_{03} - M_{30})}{6} + \frac{M_{21} - M_{12}}{2} \right). \quad (2.27)$$

A further measure in quadrant analysis is the exuberance introduced by Shaw et al. (1983), which describes the ratio of (unorganized) counter flux contributions to (organized) contributions in direction of the average flux:

$$Ex = \frac{S_1 + S_3}{S_2 + S_4}. \quad (2.28)$$

Holesize — By introducing an additional holesize function $O_H(\hat{a}, \hat{b})$ in 2.20, we exclude contributions from small and frequent structures in the near-isotropic range and focus on contributions of large and sparse structures, which is done by

$$S_{i,H} = \frac{1}{r_{ab}} \int_{l_a}^{u_a} \int_{l_b}^{u_b} \hat{a}\hat{b}P(\hat{a}, \hat{b})O_H(\hat{a}, \hat{b})dadb \quad (2.29)$$

with

$$O_H(\hat{a}, \hat{b}) = \begin{cases} 1 & \text{if } \hat{a}\hat{b} \geq |r_{ab}| \\ 0 & \text{otherwise} \end{cases} \quad (2.30)$$

The holesize function defines a hyperbolic hole. Values within this hole are excluded from analysis. By varying the holesize H , contributions from large and sparse structures in regions outside the hole can be investigated. Raupach et al. (1986) defined a holesize H' above which half of the flux density occurs, hence where

$$\sum_{i=1}^4 S_{i,H'} = \frac{1}{2}. \quad (2.31)$$

With the holesize H' , another set of parameters can be deduced, e.g. we can rewrite 2.22 and 2.23 and calculate the difference ΔS_0 between sweeps and ejections larger than H' :

$$\Delta S_{H'} = S_{4,H'} - S_{2,H'} \quad (2.32)$$

and their ratio

$$\gamma_{H'} = \frac{S_{2,H'}}{S_{4,H'}}. \quad (2.33)$$

And finally, the holesize function $O_H(\hat{a}, \hat{b})$ can be inserted into Equation 2.18

$$\vartheta_{i,H} = \int_{l_a}^{u_a} \int_{l_b}^{u_b} P(\hat{a}, \hat{b})O_H(\hat{a}, \hat{b})dadb \quad (2.34)$$

and applied to define ϑ' as the relative time fraction of events in which half of the flux density occurs,

$$\vartheta' = \sum_{i=1}^4 \vartheta_{i,H'}. \quad (2.35)$$

2.2.6 Characteristic length and time scales

Again, a and b represent any velocity components or scalars. We can define a general form of an Eulerian

covariance tensor that relates the value of a' at any point \mathbf{x} and any time t to the value of b' at location $\mathbf{x}^{(1)}$ in a distance $\mathbf{r} = \mathbf{x}^{(1)} - \mathbf{x}$ and a time $t^{(1)}$ that is shifted by the time-lag $\tau = t^{(1)} - t$ (Rotta, 1972):

$$\mathbf{C}_{ab}(\mathbf{x}, t, \mathbf{r}, \tau) = \overline{a'(\mathbf{x}, t)b'(\mathbf{x} + \mathbf{r}, t + \tau)}. \quad (2.36)$$

The special case with $\tau = 0$ and $\mathbf{r} = 0$ is the (co)variance, which has been already defined in Eq. 2.7. The corresponding normalized correlation tensor is given by

$$\mathbf{R}_{ab}(\mathbf{x}, t, \mathbf{r}, \tau) = \frac{\overline{a'(\mathbf{x}, t)b'(\mathbf{x} + \mathbf{r}, t + \tau)}}{\left(\overline{a'^2(\mathbf{x}, t)b'^2(\mathbf{x} + \mathbf{r}, t + \tau)}\right)^{1/2}}. \quad (2.37)$$

For both, $|\mathbf{r}| \rightarrow \infty$ or $|\tau| \rightarrow \infty$, a' and b' become statistically independent,

$$\lim_{|\mathbf{r}| \rightarrow \infty} \mathbf{R}_{ab}(\mathbf{x}, t, \mathbf{r}, \tau) = 0 \quad (2.38)$$

and

$$\lim_{|\tau| \rightarrow \infty} \mathbf{R}_{ab}(\mathbf{x}, t, \mathbf{r}, \tau) = 0. \quad (2.39)$$

A special case of 2.36 is the Eulerian autocovariance function $R_{aa}(\mathbf{x}, t, 0, \tau)$, where $a = b$, and $\mathbf{r} = 0$. This leads to the definition of the Eulerian *integral length scales* (or *outer length scales*, see Fig. 2.4)

$$L_{ab,k}^{\cdot\cdot}(\mathbf{x}, t) = \frac{1}{2\overline{a'(\mathbf{x}, t)b'(\mathbf{x}, t)}} \int_{-\infty}^{\infty} \mathbf{R}_{ab}(x, t, r_k, 0)dr_k \quad (2.40)$$

with k the k -th Cartesian direction, i.e. $k = \{x, y, z\}$. Similarly, the Eulerian *integral time scales* (or *outer time scales*) are

$$\mathcal{T}_{ab}(\mathbf{x}, t) = \frac{1}{2\overline{a'(\mathbf{x}, t)b'(\mathbf{x}, t)}} \int_{-\infty}^{\infty} \mathbf{R}_{ab}(x, t, 0, \tau)d\tau. \quad (2.41)$$

In practice, for a finite and stationary time series, \mathcal{T}_{ab} is calculated by numerically integrating up to the first zero-crossing.

Taylor's Hypothesis — With point measurements, we are only able to determine \mathbf{R}_{ab} for cases where $\mathbf{r} = 0$ and hence, $L_{ab,k}^{\cdot\cdot}$ can not be determined directly from measurements at a single point. The Taylor hypothesis surrogates spatial measurements

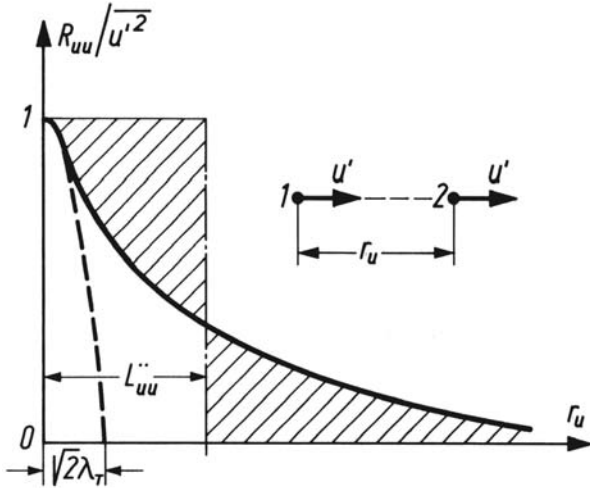


Figure 2.4: Conceptual spatial autocorrelation function and corresponding integral length scale $L_{uu,u}$. λ_T is the Taylor-microscale, which could be derived from the curvature of the autocovariance function at $t = 0$ if instrument resolution (very small path length) would allow its measurement. Modified from Rotta (1972).

by time series from one point. Under some circumstances, turbulence can be considered frozen, which implies that the total Lagrangian derivative da/dt of any variable a is zero. A continuous time series of measurements from a single point can be folded back into space by simply assuming advection as the only process that changes a in this Eulerian point of view (Stull, 1988), which can be expressed by

$$\frac{\partial a}{\partial t} \approx -\bar{u}_i \frac{\partial a}{\partial x_i}. \quad (2.42)$$

In the atmosphere, Taylor's Hypothesis is seldom fulfilled. It works well in the surface layer, but its application is problematic in canopies. If temporal variations in a moving frame of reference are strong and different wavenumbers are transported in different velocities, the Taylor hypothesis fails (Wyngaard and Clifford, 1977). But at certain scales, it is a valuable approximation. Taylor's hypothesis allows calculating integral length scales from integral time scales by

$$L_{ab}(\mathbf{x}, t) = \bar{u}_i T_{ab}(\mathbf{x}, t). \quad (2.43)$$

To distinguish between integral length scales that have been transformed using Taylor's hypothesis and length scales directly derived from spatial separated measurements, the first ones are called *one point length scales* and the latter ones are *two point length scales*. One-point length scales only provide information in the direction \mathbf{r}_u of the advecting wind

\bar{u} , while two-point length scales can be formed for each direction of \mathbf{r}_k in space. Following Raupach et al. (1996), the difference between one-point and two-point length scales is indicated by the number of dots in L_{ab} and $L_{ab,k}$, respectively.

2.2.7 Spectral analysis

Turbulence can be viewed as a superposition of many single eddies (coherent events of velocity, vorticity and scalar properties). The Fourier transformation provides the basic tool for the separation of eddies by scale. It allows to represent TKE of a continuous and stationary time series as the sum of an infinite number of sine and cosine terms:

$$\mathbf{S}_{ab}(\mathbf{x}, \kappa) = \frac{1}{(2\pi)^3} \iiint_{-\infty}^{\infty} \mathbf{C}_{ab}(\mathbf{x}, \mathbf{r}) e^{-i\kappa \mathbf{r}} d\mathbf{r}. \quad (2.44)$$

\mathbf{C}_{ab} is a special case of the covariance tensor of Eq. 2.36 of a stationary time series, where $a = b = \{u, v, w\}$ and $\tau = 0$. κ is the wavenumber vector, and \mathbf{S}_{ab} is the resulting two point spectrum tensor that is complex. Its real part is the amplitude of the cosine wave whereas the imaginary part describes the sine wave. The resulting spectra tell us how much a given frequency band contributes to the total TKE (or the variance of a single velocity component). In this phase space, the absolute physical reference — time or location — is lost. Instead of the timing of an eddy, statistical information on the energy of all eddies of similar size (duration) can be extracted from a spectrum.

The Fourier transformation can be similarly applied to scalars ($a = b = \{\theta, \rho_v, \rho_c\}$). If in Eq. 2.44 $a \neq b$ we retain cospectra. A detailed overview of the theoretical background of the Fourier transformation and its manifold applications in micrometeorology can be found in Stull (1988), Sorbjan (1989) or Kaimal and Finnigan (1994).

Using Taylor's Hypothesis (Eq. 2.42), we can convert wavenumbers k into frequency n by

$$k = \frac{2\pi n}{\bar{u}}. \quad (2.45)$$

When drawing spectra from one-point time series, natural frequency n — the independent variable — is typically plotted against frequency multiplied by

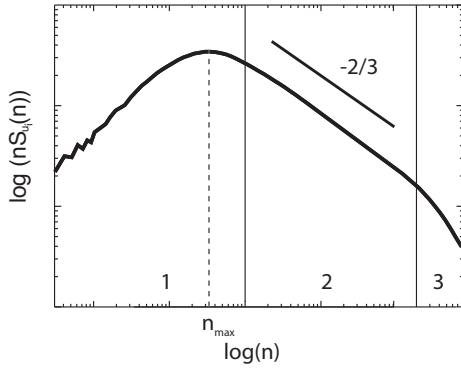


Figure 2.5: Conceptual spectra of a velocity component u_i illustrating (1) energy containing range, (2) inertial subrange and (3) dissipation subrange. n_{\max} is the peak frequency.

spectral energy $nS(n)$ (Fig. 2.5). The total spectral energy $S(n)$ integrated over all frequencies again is equal the (co)variance and twice the TKE in the case of the TKE spectra, hence we write

$$\overline{a'b'} = \int_n S_{ab}(n) dn. \quad (2.46)$$

Equation 2.46 is used to normalize spectral density by the variance, i.e. the y-axis is set to $nS(n)/\overline{u_i'^2}$.

Atmospheric velocity spectra (TKE, velocity components) can be divided into three subranges: the energy containing subrange (1), the inertial subrange (2), and the dissipation subrange (3) at the high-frequency end (Fig. 2.5).

Energy containing range — This is the range of large scale eddies, which contain most of the energy. At this scale, energy is converted from the mean flow into TKE. The forcing mechanisms that extract TKE from the mean flow are shear, buoyancy and potentially pressure perturbations (which may produce TKE in smaller ranges, see McBean and Elliott (1975)). The energy containing range is dominated by the integral length scale L_{aa}'' (Eq. 2.40). $\mathbf{E}_{ab}(\kappa)$ reaches its maximum at a wavenumber roughly corresponding to the Eulerian integral length scale L_{ab}'' .

Inertial subrange — This is the range of wavenumbers that are smaller than the smallest energy input ($\approx 10^1$ m) but larger than the Kolmogorov microscale λ_K ($\approx 10^{-3}$ m). In this range, TKE is neither produced nor dissipated. Eddies do not interact with the mean flow anymore, and turbulence at this scale is statistically uncorrelated to the mean

flow. It is isotropic and does not contribute to turbulent flux densities. Energy is passed down from larger scales to smaller ones, and according to Kolmogorov (1941), the spectral density decays with $n^{-5/3}$ (which results in the $-2/3$ slope in Fig. 2.5 where the y-axis is multiplied by n). $\mathbf{E}_{ij}(\kappa)$ is the three dimensional velocity spectrum as function of wavenumber κ , and a_u is the Kolmogorov-constant (0.52),

$$\mathbf{S}(\kappa) = \alpha_k \epsilon^{2/3} \kappa^{-5/3}. \quad (2.47)$$

Applying the Taylor hypothesis and solving Eq. 2.47 for spectral energy results in

$$nS_u(n) = (2\pi)^{-2/3} \alpha_k \epsilon^{2/3} n^{-5/3} u^{2/3}. \quad (2.48)$$

The 4/3-law of Kolmogorov (1941) relates the one-dimensional lateral and vertical velocity spectra in the inertial subrange to the one-dimensional longitudinal velocity spectra, where κ_1 is the component of the wavenumber vector in longitudinal direction. If local isotropy exists, he showed that

$$E_{33}(\kappa_1) = E_{22}(\kappa_1) = \frac{4}{3} E_{11}(\kappa_1). \quad (2.49)$$

Dissipation subrange — In the dissipation subrange, TKE is transformed by dissipation into heat. Dissipation of TKE starts roughly at wavenumbers that are smaller than the Kolmogorov microscale λ_K ,

$$\lambda_K = \left(\frac{\nu^3}{\epsilon} \right)^{1/4}. \quad (2.50)$$

ν is the kinematic molecular viscosity and ϵ the dissipation rate of TKE. With ultrasonic anemometers, this part of the spectra can not be measured directly, because the frequency response of these instruments is too slow and the measurement volume is too large. Indirectly, dissipation can be calculated from the inertial subrange slope (Eq. 2.48).

Spectral analysis became an important tool in atmospheric turbulence research. It allows the quantitative determination of the dominant scales of a process and relates them to the scale of the application (Section 2.1.2). Further, the characteristic scales determined from spectral analysis can be used to identify driving mechanisms and to develop meaningful scalings and simplifications.

2.3 Analytical description and budget concepts

The analytical approach predicts integral effects of a turbulent flow. This is performed with Reynolds decomposed conservation equations. The equations for mean flow and higher order moments are presented in Section 2.3.1. Unfortunately, the resulting set of equations have the big disadvantage that — up to now — no solution exists and simplifications and closure schemes are needed (Section 2.3.2). Finally, Section 2.3.3 focuses on the energy conservation at the surface-atmosphere interface.

2.3.1 Turbulent flow equations

Mean properties — With the Reynolds decomposition (Eq. 2.1) applied to the conservation equations of mass, momentum and heat, we get the Boussinesq equations for the mean motions in the turbulent atmosphere (see Panofsky and Dutton (1984), Stull (1988) or Kaimal and Finnigan (1994) for details). In the inner region, Coriolis forces are neglected, and we rewrite the Reynolds decomposed conservation of momentum as

$$\begin{aligned} \frac{\partial \bar{u}_i}{\partial t} + \bar{u}_j \frac{\partial \bar{u}_i}{\partial x_j} = \\ -\delta_{i3}g - \frac{1}{\bar{\rho}} \frac{\partial \bar{p}}{\partial x_i} + \frac{\nu \partial^2 \bar{u}_i}{\partial x_j^2} - \frac{\partial \overline{u'_i u'_j}}{\partial x_j}. \end{aligned} \quad (2.51)$$

The terms from left to right are: storage of mean momentum, advection of mean momentum, gravity acceleration in the vertical direction, pressure gradient forces, viscous stress on the mean motions and Reynolds stress. Note that i and j indicate summation according to Einstein's convention for the three Cartesian axis $i, j = \{1, 2, 3\}$.

The conservation equations of any scalar quantity $s = \{\theta, \rho_v, \rho_c\}$ is

$$\frac{\partial \bar{s}}{\partial t} + \bar{u}_j \frac{\partial \bar{s}}{\partial x_j} = \frac{\nu_s \partial^2 \bar{s}}{\partial x_j^2} + S_s - \frac{\partial \overline{u'_j s'}}{\partial x_j}. \quad (2.52)$$

The terms from left to right are: storage, advection, mean molecular diffusion, net source or sink term, and the divergence of turbulent flux densities. In the case of virtual temperature θ , the net source or sink

term S_θ can be written as

$$S_\theta = -\frac{1}{\bar{\rho} c_p} \frac{\partial \overline{Q'_j}}{\partial x_j} - \frac{L_v E}{\bar{\rho} c_p}. \quad (2.53)$$

where the first term represents the effects of radiation divergence, and the second term is the heat produced / destroyed by condensation / evapotranspiration with L_v , the latent heat of vaporization of water, c_p , the specific heat at constant pressure for moist air, and E , the phase change rate in J kg^{-1} due to evaporation.

Variances — The last terms in Eq. 2.51 and 2.52 contain both second order moments. In order to solve the equations, we have to predict these second order moments. In the next step, prognostic equations for variances are introduced, which are needed to understand prognostic equations of kinematic flux densities and turbulent kinetic energy later in this section. The prognostic equation for the velocity component variance $\overline{u'_i u'_i}$ is

$$\begin{aligned} \frac{\partial \overline{u'_i u'_i}}{\partial t} + \bar{u}_j \frac{\partial \overline{u'_i u'_i}}{\partial x_j} = \\ -2 \overline{u'_i u'_j} \frac{\partial \bar{u}_i}{\partial x_j} + 2 \delta_{i3} \frac{g}{\bar{\theta}} \overline{u'_i \theta'} \\ - \frac{\partial \overline{u'_j u'_i u'_i}}{\partial x_j} - \frac{2}{\bar{\rho}} \frac{\partial \overline{u'_i p'}}{\partial x_i} - 2\epsilon. \end{aligned} \quad (2.54)$$

The two terms on the left hand side are again local rate of change (storage) and advection of variance by the mean wind. The third term is the production of turbulence by wind shear. The fourth term describes production or destruction of variance by a buoyancy flux density. The fifth term describes turbulent transport of a turbulent fluctuation. This is done by larger scale eddies, which incorporate air masses with smaller scale turbulent motions. If we observe a turbulent transport, variances of the smaller eddies embedded in the larger ones are correlated with the transport direction of the large eddy. The sixth term is called pressure transport and describes the redistribution of variances by pressure perturbations. The last term ϵ is the viscous dissipation of variance.

We get the turbulent kinetic energy budget by summing three variance equations of type Eq. 2.54 and dividing the sum by two:

$$\frac{\partial \overline{u'_i u'_i} / 2}{\partial t} + \bar{u}_j \frac{\partial \overline{u'_i u'_i} / 2}{\partial x_j} =$$

$$\begin{aligned}
& \underbrace{-\overline{u'_i u'_j} \frac{\partial \overline{u_i}}{\partial x_j}}_{Ps} + \underbrace{\delta_{i3} \frac{g}{\theta} \overline{u'_i \theta'}}_{Pb} \\
& - \underbrace{\frac{\partial \overline{u'_i u'_j u'_j} / 2}{\partial x_j}}_{Tt} - \underbrace{\frac{\partial \overline{p' u'_j}}{\partial x_j}}_{Tp} - \epsilon. \quad (2.55)
\end{aligned}$$

In this work, the following nomenclature is used: Ps is the conversion of resolved scale kinetic energy into TKE by wind shear. The production (or destruction) of turbulence by buoyant effects is called Pb . The turbulent transport and pressure transport are referred to as Tt and Tp , respectively.

The prognostic equations for variances of scalar quantities $s = \{\theta, \rho_v, \rho_c\}$ are

$$\begin{aligned}
& \frac{\partial \overline{s' s'}}{\partial t} + \overline{u_j} \frac{\partial \overline{s' s'}}{\partial x_j} = \\
& -2\overline{u'_j s'} \frac{\partial \overline{s}}{\partial x_j} - \frac{\partial \overline{u'_j s' s'}}{\partial x_j} - 2\epsilon_s - \epsilon_R \quad (2.56)
\end{aligned}$$

with (from left to right) storage, advection, variance production of variance associated by perturbation of a mean scalar gradient, turbulent flux of the scalar variance, and molecular dissipation. ϵ_R is the radiation destruction term of heat. It is only important in the equation of $s = \theta$ and is zero for any other scalar.

Turbulent kinematic fluxes — By combining two equations of the type of Eq. 2.54, we retain the budget equations of momentum flux. We again neglect Coriolis effects, and additionally molecular diffusion is assumed to be negligible small (Stull, 1988), namely

$$\begin{aligned}
& \frac{\partial \overline{u'_i u'_k}}{\partial t} + \overline{u_j} \frac{\partial \overline{u'_i u'_k}}{\partial x_j} = \\
& -\overline{u'_i u'_j} \frac{\partial \overline{u_k}}{\partial x_j} - \overline{u'_k u'_j} \frac{\partial \overline{u_i}}{\partial x_j} - \frac{\partial \overline{u'_i u'_j u'_k}}{\partial x_j} \\
& + \frac{g}{\theta} \left(\delta_{k3} \overline{u'_i \theta'} + \delta_{i3} \overline{u'_k \theta'} \right) \\
& - \frac{1}{\bar{\rho}} \left[\frac{\partial \overline{u'_k p'}}{\partial x_i} + \frac{\partial \overline{u'_i p'}}{\partial x_k} - \overline{p'} \left(\frac{\partial \overline{u'_i}}{\partial x_k} + \frac{\partial \overline{u'_k}}{\partial x_i} \right) \right] \\
& - 2\epsilon_{u_i u_k} \quad (2.57)
\end{aligned}$$

The prognostic equations of any kinematic flux density of a scalar quantity $s = \{\theta, \rho_v, \rho_c\}$ are obtained by multiplying any set of Eq. 2.54 and 2.56,

$$\begin{aligned}
& \frac{\partial \overline{u'_i s'}}{\partial t} + \overline{u_j} \frac{\partial \overline{u'_i s'}}{\partial x_j} = \\
& -\overline{u'_j s'} \frac{\partial \overline{u_i}}{\partial x_j} - \overline{u'_i u'_j} \frac{\partial \overline{s}}{\partial x_j} - \frac{\partial \overline{u'_i u'_j s'}}{\partial x_j} \\
& + \delta_{i3} g \left(\frac{\overline{s' \theta'}}{\theta} \right) - \frac{1}{\bar{\rho}} \left[\frac{\partial \overline{s' p'}}{\partial x_i} - \frac{\overline{p' \partial s'}}{\partial x_i} \right] - 2\epsilon_{u_i s}. \quad (2.58)
\end{aligned}$$

2.3.2 Turbulence closure

Unfortunately, by introducing prognostic equations for the previously unknown second moments in Eq. 2.51 and 2.52, we get new third-order terms in Eq. 2.57 and 2.58, which we are still not able to predict. With each higher order set of equations, we have even more unknown terms than equations. This is called *closure problem*. Practically, the process of continuously introducing new prognostic equations for even higher moments has to be stopped at a certain level of detail. Any turbulence closure scheme considers only a finite set of equations and approximates the missing higher order moments in terms of known moments.

There are local and non-local closure schemes. Local closure schemes approximate any unknown parameter by known parameters at the same point in space. A common local scheme is the K-theory, which approximates turbulent transports with a transfer coefficient K , which is proportional to the local mean gradient. We can approximate the turbulent flux density of a scalar s by

$$\overline{u'_i s'} = -K_s \frac{\partial \overline{s}}{\partial x_i}. \quad (2.59)$$

A slightly modified approach is the mixing-length theory, which introduces a mixing length ℓ similar to the free molecular path length. An example for higher order is the well known TKE- ϵ closure (Stull, 1988; Versteeg and Malalasekera, 1995; Cebeci, 2004). These basic gradient-diffusion closures are not valid close to rough surfaces such as in the urban canopy layer — because their assumption that the length scale of the mixing process should be much smaller than the inhomogeneities in the mean

scalar or momentum gradient is not fulfilled anymore (Corrsin, 1974).

In nonlocal closure schemes, unknown parameters can be parameterized by known parameters at another point in space. An example is the turbulence transilient theory by Stull (1984). There is still lack of information that would be needed to fill in transilient matrices and consequently, this approach is not widely used. Another group of closures use probabilistic approaches with PDFs (Pope, 2000).

2.3.3 Surface boundary conditions

At the air-surface interface, many important energy exchange processes take place. The concept of the surface plane that has no volume implies that energy must be directly converted. Further any exchange at the surface can be treated one-dimensional in the normal direction of the surface and advection is not possible*.

Surface energy balance — The relevant energetic exchange processes at the surface are surface net all-wave radiation Q^* , sensible heat flux density at ground level Q_H , latent heat flux density at ground level Q_E , and heat diffusion into ground and buildings ΔQ_S (Oke, 1987). In the urban context, an additional term Q_F , called the anthropogenic heat flux density, includes all additional energy input produced by human activities such as the energy released by combustion of fuels and electric heat e.g. in industry, traffic, firing and air conditioning per surface area. Q_F must be either converted to radiation, sensible or latent heat, or be stored:

$$Q^* + Q_H + Q_E + \Delta Q_S + Q_F = 0 \quad (2.60)$$

with

$$Q_H = \bar{\rho} c_p (\overline{w' \theta'_T})_0. \quad (2.61)$$

and

$$Q_E = L_v (\overline{w' \rho'_v})_0 \quad (2.62)$$

Their ratio is called *Bowen ratio*

$$\beta = \frac{Q_H}{Q_E}. \quad (2.63)$$

* Practically, the surface energy balance can not be measured directly at the surface and it has to be derived from measurements in the inertial sublayer (cf. Section 4.5)

Here, a simple budget view is applied with the following sign convention: all positive terms transport energy towards the surface, while negative terms indicate an energy loss of the surface. Note that this is in contrast to the conventional sign convention in flux-gradient relationships. Here, upward directed turbulent flux densities are negative because they represent an energy loss of the surface. This has the advantage that all terms have a consistent sign convention, which defines whether a term is currently an energy gain (+) or loss (−) of the surface.

Surface radiation balance — The net all-wave radiation Q^* is the result of incoming and outgoing radiative fluxes at the surface. It is partitioned into solar short-wave (K) and terrestrial long-wave (L) components:

$$Q^* = K_{\downarrow} + K_{\uparrow} + L_{\downarrow} + L_{\uparrow}. \quad (2.64)$$

The arrows denote the directions of the radiation flux densities, and the same sign convention as above is applied: Components transporting energy to the surface are positive, those removing energy are negative. The equation is sometimes rewritten as

$$Q^* = (1 - \alpha) K_{\downarrow} + L_{\downarrow} - \varepsilon \sigma_B T_s^4 \quad (2.65)$$

where α is the albedo, defined as the absolute value of the ratio $\alpha = |K_{\uparrow}/K_{\downarrow}|$, ε the long-wave emissivity of the surface, and σ_B the Stefan-Boltzmann constant.

2.4 Simplifications and scalings

2.4.1 Monin-Obukhov similarity theory

Monin-Obukhov similarity theory (Monin and Obukhov, 1958) can be viewed as a type of zero-order closure for the special case of a turbulent boundary layer. It is framed in terms of local parameters only. It simplifies the processes in the inertial sublayer by assuming that turbulent flux densities of heat, mass, and momentum are almost constant with height (Section 2.1.1). Together with the assumption of homogeneity, and stationarity we can approximate

$$\frac{\overline{\partial u'_i s'}}{\partial x_i} \approx 0 \quad (2.66)$$

Local gradients and the magnitude of second order moments are then believed to be driven by only four key parameters, which are (1) surface shear stress τ , (2) surface kinematic heat flux density $\overline{w'\theta'}$, (3) effective height above ground z , and (4) the ratio g/θ , which accounts for the buoyancy. The coordinate system is aligned in a way that x points into direction of the mean wind \mathbf{u} , and hence, $\bar{v} = 0$, and $\bar{w} = 0$. This allows us to treat the problem one-dimensional.

Above rough surfaces, z is replaced by $z - z_d$, where z_d is the zeroplane displacement height. When individual roughness elements are packed close together, the tops of the elements begin to act like a displaced surface. z_d is introduced to account for this shift in order to retain the logarithmic form of the wind profile.

The chosen scaling variables are the friction velocity u_*

$$u_* = \left(\frac{\tau}{\bar{\rho}} \right)^{1/2} = (-\overline{u'w'})^{1/2} \quad (2.67)$$

and the temperature scale θ_*

$$\theta_* = \frac{-\overline{w'\theta'}}{u_*} \quad (2.68)$$

The Obukhov Length L (introduced by Obukhov in 1946) describes the ratio between mechanical produced turbulence and buoyancy produced turbulence, where k is the von Karman number.

$$L = \frac{\theta u_*^2}{k g \theta_*} \quad (2.69)$$

L is roughly constant through the inertial sublayer. Dimensional analysis returns the dimensionless group $(z - z_d)/L$. It is a measure of stability.

$$\zeta = \frac{z - z_d}{L} \quad (2.70)$$

By definition, in similarity theory, every other parameter nondimensionalized by an appropriate variable can now be explained as a universal function of ζ . For instance, the dimensionless wind shear is a function of ζ , namely

$$\frac{k(z - z_d)}{u_*} \frac{\partial \bar{u}}{\partial z} = \phi_m(\zeta). \quad (2.71)$$

Equation 2.71 is the differential form of the logarithmic wind profile under neutral stratification. The dimensionless temperature gradient is

$$\frac{k(z - z_d)}{\theta_*} \frac{\partial \bar{\theta}}{\partial z} = \phi_h(\zeta) \quad (2.72)$$

Under the above assumptions for the inertial sublayer, the equation for turbulent kinetic energy (2.55) can be simplified. The driving parameters that create turbulence are local shear production, which is proportional to $\overline{u'w'}$, and local buoyancy production which is described by $\overline{w'\theta'}$.

$$0 = -\overline{u'w'} \frac{\partial \bar{u}}{\partial z} + \frac{g}{\theta} \overline{w'\theta'} - \epsilon \quad (2.73)$$

dividing all terms by $k(z - z_d)/u_*^3$ results in the corresponding ϕ -functions, which are all a function of ζ ,

$$0 = \phi_m + \phi_b - \phi_\epsilon \quad (2.74)$$

with

$$\phi_b \equiv \zeta. \quad (2.75)$$

From measurements, the semi-empirical relationships are determined to be

$$\phi_m(\zeta) = \begin{cases} (1 - 16\zeta)^{-1/4} & \text{for } \zeta \leq 0 \\ (1 + 5\zeta) & \text{for } 0 \leq \zeta \end{cases} \quad (2.76)$$

$$\phi_h(\zeta) = \begin{cases} (1 - 16\zeta)^{-1/2} & \text{for } \zeta \leq 0 \\ (1 + 5\zeta) & \text{for } 0 \leq \zeta \end{cases} \quad (2.77)$$

and

$$\phi_\epsilon(\zeta) = \begin{cases} (1 - 0.5|\zeta|^{2/3})^{3/2} & \text{for } \zeta \leq 0 \\ (1 + 5\zeta) & \text{for } 0 \leq \zeta \end{cases} \quad (2.78)$$

Table 2.1: Semi-empirical constants a_i , b_i , c_i and f_i in the (locally-scaled) Monin-Obukhov similarity theory. Surface-layer values (SL) are compiled from Panofsky et al. (1977), Panofsky and Dutton (1984), de Bruin et al. (1993) and Wyngaard et al. (1971), urban values are taken from Roth (2000) who compiled urban measurements in heights $z/z_h > 2.5$.

		a_i	b_i	c_i	f_i
$i = u$	SL	2.2	3	1/3	
	urban	1.88	0.15	0.94	
$i = v$	SL	1.9	3	1/3	
	urban	1.52	3.34	0.31	
$i = w$	SL	1.25	3	1/3	1.8
	urban	1.15	2.09	0.33	
$i = \theta$	SL	-2.9	28.4	-1/3	0.95
	urban	-4.10	65.0	-0.33	

Integral statistics — If TKE production and destruction can be described as a function of ζ only, velocity variances and variances of scalars must also be a function of ζ . A general form of the semi-empirical relationships for variances was introduced by de Bruin et al. (1993), where $i = \{u, v, w, \theta, \rho_v, \rho_c, \dots\}$

$$A_i = \sigma_i / i_* \quad (2.79)$$

and i_* stands for u_* (Eq. 2.67) in the cases $i = \{u, v, w\}$ and

$$i_* = \frac{-\overline{w'i'}}{u_*} \quad (2.80)$$

for scalars ($i = \{\theta, q, c\}$). The relations are usually approximated with (Panofsky and Dutton, 1984):

$$A_i(\zeta) = \begin{cases} a_i(1 - b_i\zeta)^{c_i} & \text{for } \zeta \leq 0 \\ a_i & \text{for } 0 \leq \zeta \end{cases} \quad (2.81)$$

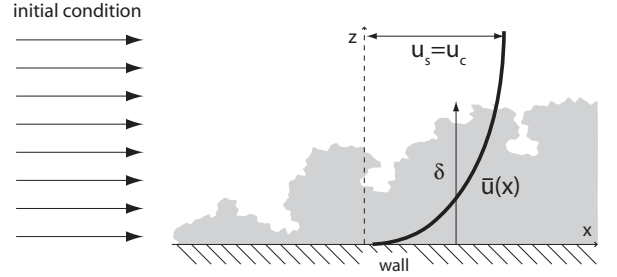
Relationship 2.81 suggests a constant $A_i(\zeta)$ for stable conditions. A special case is the free convection limit for $\zeta \rightarrow -\infty$ where $\overline{w'\theta'} \gg \overline{u'w'}$ and $A_i(\zeta)$ simplifies to (Wyngaard et al., 1971)

$$A_i(\zeta) = f_i(\pm\zeta)^{c_i} \quad (2.82)$$

Table 2.1 summarizes empirically determined values of the constants a_i , b_i , c_i and f_i in the surface layer over flat and homogeneous terrain (SL) and typical values in the urban inertial sublayer. The sign of ζ in Eq. 2.82 is equal the sign of c_i .

Monin-Obukhov similarity theory can neither be used to explain inactive turbulence nor effects of turbulent or pressure transport close to the surface. Its

(a) Boundary Layer



(b) Plane Mixing Layer

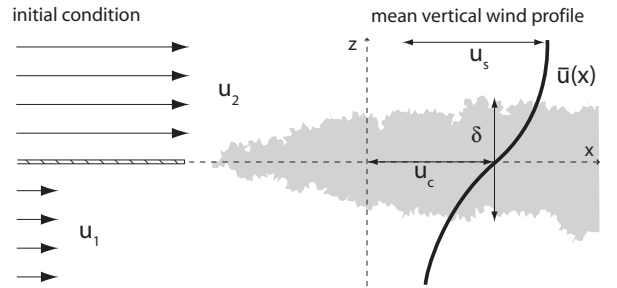


Figure 2.6: Sketches of (a) a turbulent boundary layer and (b) a turbulent plane mixing layer. Modified from Pope (2000).

applications are limited above urban surfaces to the inertial sublayer under homogeneous and stationary conditions. In the urban roughness sublayer, the assumption 2.66 does not hold.

2.4.2 Plane mixing layer analogy

Raupach et al. (1989) proposed that flows within and in the layer directly above plant canopies show analogies to the turbulent plane mixing layer. A turbulent plane mixing layer forms, when two uniform and nearly parallel flows of different free-stream velocities u_1 and u_2 are allowed to mix (Pope, 2000). In fluid mechanics, the turbulent plane mixing layer is initiated at a single point (origin), usually at the end of a thin splitter plate, which separates two flows (Fig. 2.6b).

The mean vertical flow profile and turbulence statistics in a neutral stratified turbulent plane mixing layer depend on the characteristic convective velocity

$$u_c = \frac{1}{2}(u_1 + u_2) \quad (2.83)$$

and the characteristic velocity difference

$$u_s = (u_2 - u_1) \quad (2.84)$$

The turbulent plane mixing layer is self-similar. The flow is not symmetric around the x-axis and it spreads preferentially into the low velocity stream.

Inflected velocity profile — A characteristic feature of the turbulent plane mixing layer is an inflected profile of the mean velocity. In plant canopies, this inflection point is typically found at canopy top z_h (Raupach and Thom, 1981; Kaimal and Finnigan, 1994; Finnigan, 2000).

A Kelvin Helmholtz instability is arising from the inflected velocity profile. It creates vortex streets, which further determine the vorticity thickness and length scales of the flow. The vortices are detected as quasi-periodic coherent structures at a fixed location in space. The characteristic turbulent vorticity thickness δ (Fig. 2.6b) is increasing with longitudinal distance to the origin, while simultaneously the maximum velocity gradient $\partial\bar{u}/\partial z$ is decreasing.

$$\delta = \frac{u_s}{\left.\frac{\partial\bar{u}}{\partial z}\right|_{max}} \quad (2.85)$$

In the mixing layer analogy of (plant) canopies, the turbulent plane mixing layer is repetitively initialized, and the flow is a superposition of many instabilities created at the roughness elements. The slower flow roughly corresponds to the average flow through the permeable canopy space where initial (external) acceleration forces are decelerated by the presence of obstacles. The flow above z_h corresponds to the faster u_2 with an unchanged external acceleration. In real canopies, there is a transition to a boundary layer flow above the canopy, which makes the estimation of the characteristic free-stream velocities, u_1 , u_2 , and the corresponding scaling velocities u_c (Eq. 2.83) and u_s (Eq. 2.84) very difficult. Within and at top of canopies, the mean Eulerian velocity $u(z_h)$ is a poor estimate of the convection velocity u_c , which is underlined by results from a wind tunnel study, where two-point length scales are not equal one-point length scales anymore in the canopy space (Shaw et al., 1995). Typically, the translation velocity of structures is faster than the mean wind velocity at given height. Finnigan (1979) empirically found that $u_c \approx 1.8u(z_h)$.

Scaling parameters — Raupach et al. (1996) introduced a characteristic shear length scale L_s ,

which is equal half the vortices thickness δ . It is easier to retrieve from real-world measurements. L_s is the ratio between the mean wind velocity at canopy top $\bar{u}(z_h)$ and the mean wind gradient at same height*.

$$\frac{\delta}{2} \approx L_s = \frac{\bar{u}(z_h)}{\left.\frac{\partial\bar{u}}{\partial z}\right|_{z=z_h}} \quad (2.86)$$

Raupach et al. (1996) observed that the canopy shear scale L_s is independent of wind velocity. L_s normalized by canopy height z_h is a function of canopy density only. They found L_s/z_h to be in the order of 0.1 for dense, 0.5 for moderate, and 1 for sparse canopies under neutral stratification.

Further, the Strouhal Number St represents a measure of the ratio of inertial forces due to the unsteadiness of the flow or local acceleration to the inertial forces due to changes in velocity from one point to another in the flow field. In the turbulent plane mixing layer, St is

$$St = \frac{\delta n_{max}}{u_c} \approx \frac{L_s}{\Lambda_x} \quad (2.87)$$

where n_{max} is the peak frequency of vortices in the vortex street, typically determined from fluctuations in w . Using the Taylor hypothesis we can write for the mean longitudinal separation of coherent structures

$$\Lambda_x = \frac{u_c}{n_{max}(z_h)}. \quad (2.88)$$

Replacing δ by $2L_s$ (Eq. 2.86) and using the approximation $\bar{u}(z_h) \approx 2u_c$ we get the term on the right hand side of Eq. 2.87. According to Raupach et al. (1996) the inverse of the Strouhal number St^{-1} for neutral conditions should result in ≈ 8.1 .

Applications — The mixing layer analogy has been successfully addressed to the flow in and over a number of wind tunnel and real-world plant canopies (e.g. Brunet et al., 1994; Raupach et al., 1996; Katul et al., 1998; Brunet and Irvine, 2002). The characteristic density, the non-permeability and stiffness of buildings that form an urban canopy compared to the flexible and highly fractal structures that are present in permeable plant canopies do not imply a direct applicability of the results from plant

* Eq. 2.86 assumes that the height of the inflection point z_e is equal the mean height of the canopy z_h , which can be on the other hand seen as a definition of the ‘effective canopy height’.

canopies to urban environments. However, Roth (2000) suggested that the strong similarities of profiles in and above urban canopies to flow over plant canopies indicate that many features observed in the urban roughness sublayer could be interpreted in the framework of a plane mixing layer analogy. Up to now, no study tested this approach.

3 Measurements

3.1 Observational sites

The experimental phase of BUBBLE started in summer 2001 and ended in summer 2002. Between June 10 and July 10, 2002, an intensive observation period (IOP) was carried out, which embedded many activities from international research groups. The overall framework and the experimental activities during BUBBLE are documented in Rotach et al. (2005).

The BUBBLE data set involves 30 experimental or permanent sites from the greater Basel area (Tab. 3.1). Basel is a mid-size town at the border of Switzerland, France and Germany. The region has a built-up area of approximately 130 km^2 (30 km^2 dense urban, 80 km^2 suburban and 20 km^2 industrial areas), and a population of approximately 400'000. The map in Fig. 3.2 shows the topography and setting of the experimental activities in city of Basel. Site labels are coded according to surface characteristics (U: urban, S: suburban, R: rural).

Profile Towers — The investigation of turbulence parameters and turbulent momentum, mass and heat-exchange within the urban roughness sublayer is of essential interest in this work. Highest relevant differences, and hence strongest gradients at least in a horizontally averaged view, are expected along the vertical axis in the roughness sublayer. Therefore, three experimental sites (U1, U2 and S1) were set up with towers supporting profiles of ultrasonic anemometers, cup anemometers and temperature / humidity sensors through the roughness sublayer, as well as radiation balance measurements well above the urban surface. The vertical profiles address the domain from street level up to approximately 2.5 times the mean building height z_h .

Energy Balance Network — During the IOP, the three profile tower sites were extended by a network of four additional experimental sites (U3, R1, R2 and R3). Three of them were equipped with eddy

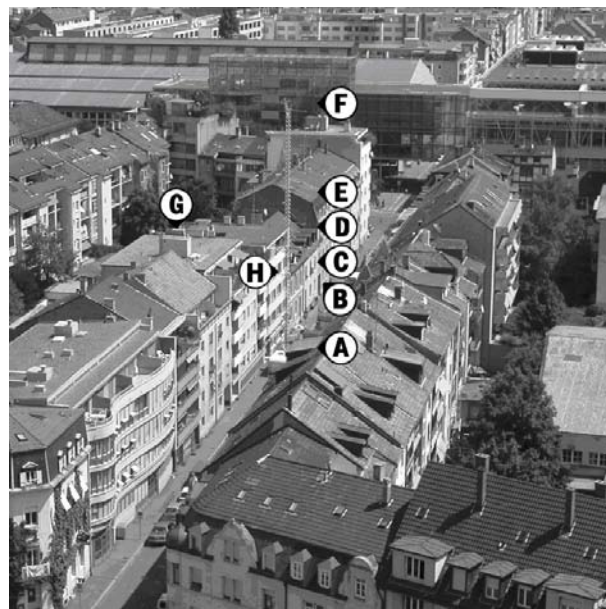


Figure 3.1: Photo of the street canyon at Basel-Sperrstrasse (U1) with profile tower. Ultrasonic anemometer levels are labelled by letters A to H. View in direction NE. Photo by courtesy of M. Roth, NUS.

correlation instrumentation at one level (U3, R1 and R2). These sites were installed in areas of different land use, mainly in the rural surrounding of the city (Fig. 3.2 and Tab. 3.6). Together with the profile towers, this network of total seven surface energy balance sites provides the basis for a detailed investigation of the urban modification of mean and turbulent properties, especially turbulent flux densities, under the same synoptic forcing.

Additional Observations — Further, a number of remote sensing systems (RASS, SODARs, wind profiler, tethered balloon) are indicated by squares on the map in Fig. 3.2) and are described in detail in van Gorsel (2005). The standard meteorological surface sites — small triangles on the map — were mainly permanent observations, operated by public and private institutions. The white area in the city center indicates the domain of SF_6 tracer release experiments during the IOP (Rotach et al., 2004).

In the present work, the three profile towers (U1, U2 and S1) and the additional energy balance sites (U3,

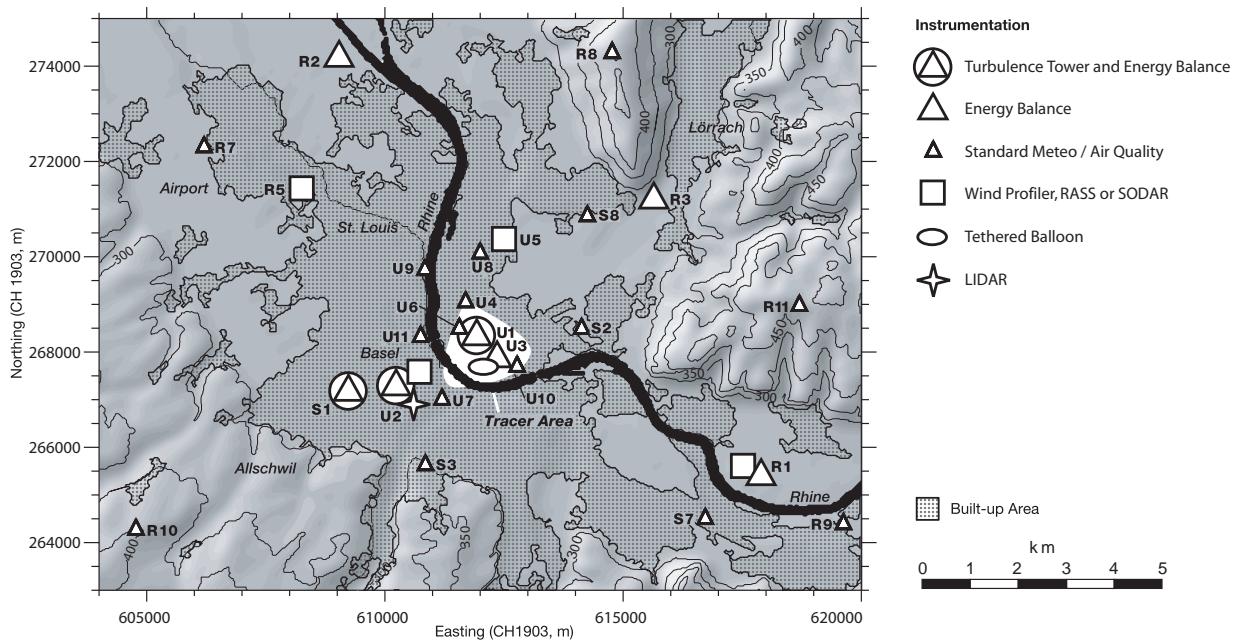


Figure 3.2: Map of all sites operated during the BUBBLE IOP in June / July 2002.

Table 3.1: Directory of all sites operated during the IOP. Sites marked by an asterisk are located outside the map in Fig. 3.2. An ‘E’ marks experimental sites.

Code	Name	Operated by	Easting	Northing	Height (m)
U1	E Basel-Sperrstrasse	U Basel, ETHZ, UBC, NUS, UWO	611890	268365	255
U2	E Basel-Spalenring	U Basel, MeteoSwiss, Obs. NE	610360	267140	278
U3	E Basel-Messe	TU Dresden, U Freiburg	612200	268070	255
U4	E Basel-Horbürg	U Basel, Risø	611695	269040	254
U5	E Basel-Kleinhüningen	Metek GmbH	612465	270475	265
U6	Basel-Feldbergstrasse	LHA b. Basel	611775	268500	255
U7	Basel-Leonhard	City Colleges	611200	267055	273
U8	Basel-Klybeck	Indust. Firepatrol Roche	612000	270125	255
U9	Basel-Novartis	Indust. Firepatrol Roche	610840	269775	257
U10	Basel-Roche	Indust. Firepatrol Roche	612775	267748	255
U11	Basel-St. Johann	LHA b. Basel	610750	268375	260
S1	E Allschwil	ETHZ, U Basel, Bulg. Met. Inst.	609250	267180	277
S2	Basel-Bäumlihof	City Colleges	614130	268540	289
S3	Basel-Binningen	MeteoSwiss, U Basel, LHA	610850	265620	316
S4*	Dornach	Kt. Solothurn	613080	258930	325
S5*	Liestal-Rheinstrasse	LHA b. Basel	621800	259950	320
S6*	Rheinfelden	UMEG	626360	268045	285
S7	Schweizerhalle	LHA b. Basel	616725	264550	270
S8	Weil am Rhein	UMEG	614250	270905	250
R1	E Grenzach	U Basel, ETHZ	617830	265130	265
R2	E Village Neuf	U Basel	608940	274240	240
R3	E Lange Erlen	U Basel	615835	271310	275
R4*	E Gempfen	U Basel	617640	257965	710
R5	E St. Louis	U Freiburg	608100	271500	250
R6*	Aesch-Schlatthof	LHA b. Basel	610375	258775	353
R7	Airport	Meteo France	606300	272750	256
R8	Oetlingen	U Basel	614770	274270	450
R9	Pratteln-Hardwasser	LHA b. Basel	619625	264500	272
R10	Schönenbuch	Inst. f. Pflanzenökologie	604775	264325	400
R11	St. Chrischonatum	MeteoSwiss, LHA b. Basel	618700	269025	493

Table 3.2: Turbulence instrumentation at Basel-Sperrstrasse (U1). Listed are ultrasonic anemometers and corresponding open path gas analyzers. The capital letters denote the labels on Fig 3.1

	z	z/z_h	Instrument type	Variables
A	3.6	0.25	Gill R2O ^a	u_i, θ
B	11.3	0.77	Gill R2O ^a	u_i, θ
C	14.7	1.01	Gill R2O, Licor 7500 ^b	u_i, θ ρ_v, ρ_c
D	17.9	1.23	Gill R2O	u_i, θ
E	22.4	1.53	Gill R2A	u_i, θ
F	31.7	2.17	Gill HS, CSI KH20, Licor 7500 ^c	u_i, θ ρ_v, ρ_c
G	11.5	0.78	CSI CSAT 3 ^d	u_i, θ
H	19.3	1.32	Young 81000 ^e	u_i, θ

^a From May 23 to July 15, 2002 these instruments were replaced by Metek USA-1 for logistic reasons.

^b operated June 24 to July 14, 2002 only.

^c operated June 15 to July 15, 2002 only.

^d operated July 3 to 14, 2002 only.

^e operated July 1 to 14, 2002 only.

R1, R2, R3) are of interest. These sites are documented in the subsequent sections.

3.1.1 Basel-Sperrstrasse (U1)

Site — The main urban experimental site U1 is located in a heavily built-up part in the city center (Fig. 3.1). The station surrounding is characterized by a typical European urban surface with residential row houses ($z_h = 14.6$ m), enclosing large inner courtyards. The backyards are either open (green spaces) or built-up by one-storey garages, parking lots and flat commercial-industrial buildings. The neighborhood has a high population density between 200 and 300 inhabitants ha^{-1} , a high plan aspect ratio of buildings $\lambda_P = 0.54$, and a small plan aspect ratio of vegetation $\lambda_V = 0.16$ (Tab. 3.6). The shape of the roofs is a mixture of approximately 50% flat and 50% pitched roofs. The roof and building materials are summarized in Tab. 3.6, the three-dimensional morphometric parameters are listed in Tab. 3.3. Figure 3.5 shows a map of the street canyon configuration.

Instrumentation — A triangular lattice tower was set up in October 2001 reaching up to 32 m ($2.2 z_h$).

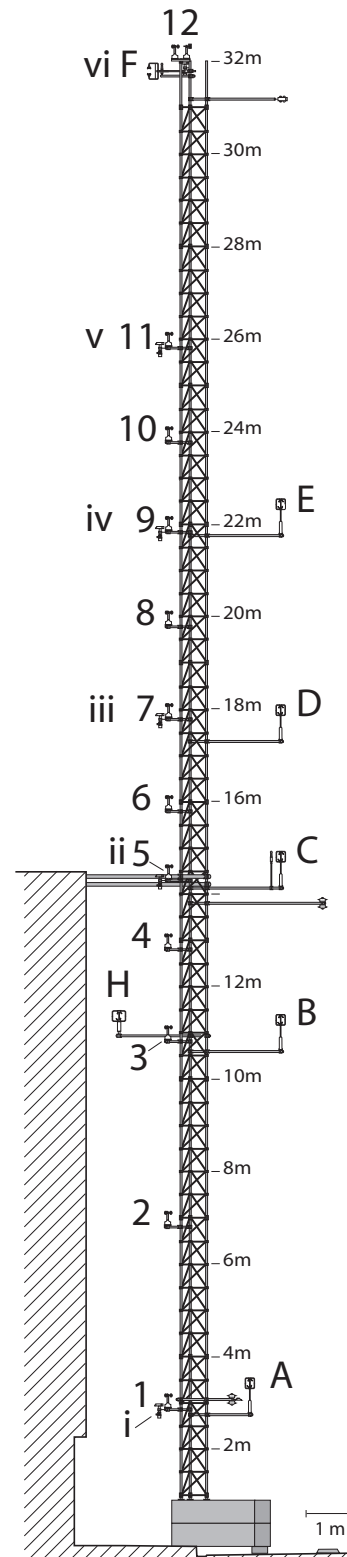


Figure 3.3: Schematic view of the tower at Basel-Sperrstrasse (U1) with sonic levels (A–H), cup anemometer levels (1–12) and psychrometer levels (i–vi). View into direction 40° (roughly along the canyon axis). The location of Sensor G on the nearby roof is not shown.

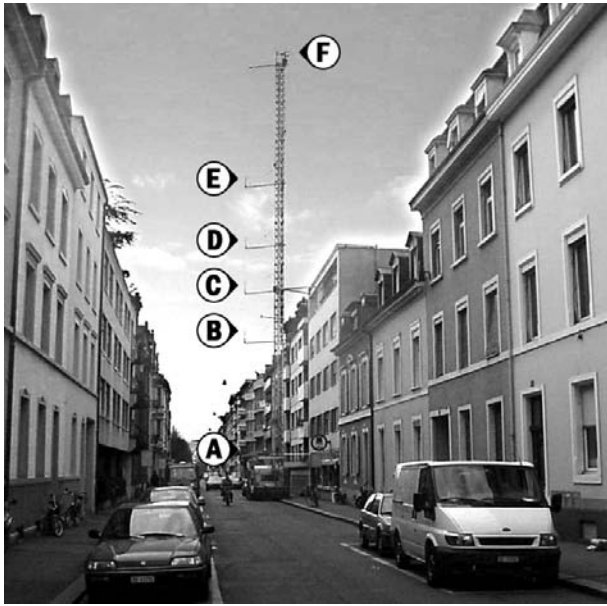


Figure 3.4: Photo of the tower at Basel-Sperrstrasse (U1) viewed from inside the street canyon in direction SSW. The instrumentation is shown in the long-term configuration.

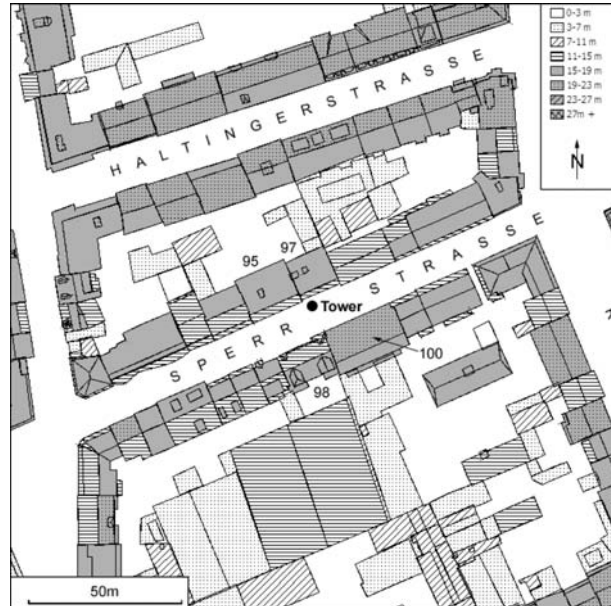


Figure 3.5: Map of the station surrounding at Basel-Sperrstrasse (U1), with the tower in the central section of the Sperrstrasse canyon. Map base data from GVA Basel-Stadt.

The tower was installed inside the 13 m wide street canyon of the ‘Sperrstrasse’, 3 m off the northern building wall (Fig. 3.3 and 3.4). Measurements were continuously carried out from November 1, 2001 to July 15, 2002, with intensified activities during the IOP. The tower supported a profile of six ultrasonic anemometer-thermometers (sonics, labels A–F, Tab. 3.2). The sonics were mounted on booms reaching into the center of the canyon, except the instrument at tower top which was aligned towards NNE to allow an optimal measurement in the predominant wind directions. The lower instruments measured inside the northern half of the street canyon ($x/x_c = 0.13$ with x : distance to canyon center, x_c : canyon width). The orientation of the canyon is along the axis 67° to 247° . During the IOP, two additional sonics were placed by the University of Birmingham, Great Britain and the National University of Singapore for a short period. One sonic (G) was operated at rooftop of an adjacent roof 3.5 m above local roof height and one 0.65 m off the northern wall. Additionally, these institutions run two scintillometers (Scintec SLS20, not used in the present work), one over the street canyon and one over the roof top of the northern building row. See Salmond et al. (2004) or Roth (2004) for details on the scintillometry experiment.

A total of twelve cup anemometers (Vaisala WAA15) were mounted at heights 3.2, 7.1, 11.1,

13.1, 14.6, 16.1, 18.1, 20.1, 22.1, 24.1, 26.1 and 33.0 m^* ($x/x_c = 0.28$). Six levels of actively ventilated psychrometers measured at 2.6, 13.9, 17.5, 21.5, 25.5 and 31.2 m. All four components of the radiation balance were recorded twice, inside the canyon at 3.2 m ($z/z_h = 0.22$, Kipp & Zonen CG2 and 2 x Kipp & Zonen CM 11), and at 31.5 m ($z/z_h = 2.16$, Kipp & Zonen CNR 1). Further, a number of sensors during the IOP focused on the investigation of thermal properties of the urban surface: a total of 11 infrared thermometers, 20 thermocouples and heat flux plates were placed to observe surfaces of different configurations and materials. The canyon was scanned with two thermal cameras and an experimental infrared dual channel radiometer. All measurements focusing on thermal properties were carried out by the University of British Columbia, Canada, the University of Western Ontario, Canada, and the Remote Sensing Group at the Institute of Meteorology, Climatology and Remote Sensing of the University of Basel. The analysis of these systems is not part of the present work, and therefore, these systems are not described in detail.

There were a number of activities to investigate carbon dioxide exchange at U1. For a limited period during the IOP, two Licor 7500 open path analyzers were installed at the site together with

* Heights always denote the height of the measurement volume.

Table 3.3: Integral three-dimensional morphometric parameters of the city surface derived from the 1m digital building model of the city of Basel for a circle of 250 m around the three profile towers.

		U1	U2	S1
Mean building height	z_h	14.6 m	12.5 m	7.5 m
Standard deviation of building height	σ_h	6.9 m	5.4 m	—
Standard deviation considering only buildings $> 0.5z_h$	σ_h	4.9 m	4.1 m	—
Frontal aspect ratio	λ_F	0.37	0.31	0.12
Complete aspect ratio	λ_C	1.92	1.75	1.31
Sky view factor at $z = 0$ m ^a	ψ_{S0}	0.36	0.51	0.62
Characteristic length (spectral) ^b	\mathcal{L}	63 m	44 m	42 m
Characteristic spacing ^c	x_d	24.5 m	23.5 m	16.5 m
Characteristic canyon width ^c	x_c	11.3 m	14.8 m	11.9 m
Characteristic canyon width to height ratio ^c	x_c/z_h	0.77	1.19	1.59
Local canyon width to height ratio	x_c/z_h	1	1.8	—
Characteristic building breadth ^c	x_b	13.2 m	8.7 m	4.6 m
Building breadth to height ratio ^c	x_b/z_h	0.91	0.70	0.61

^a ψ_{S0} is the average sky view factor at ground level averaged over all open spaces (i.e. streets, parks, backyards), which was calculated for each non-building-raster-element taking local horizon angles into account.

^b Spectral method: Characteristic length is the size where the FFT of the city surface has its maximal normalized spectral energy. It corresponds to the size of the blocks surrounded by streets.

^c Characteristic length scales were calculated under the assumption that the surface represents infinite long canyons. Then, the average ψ_{S0} in the canyon is related to the inverse of the canyon height to width ratio by $z_h/x_c = 0.5 \tan(\cos^{-1}(\psi_{S0}))$ (Oke, 1981) and $x_b = x_c \lambda_P / (1 - \lambda_P)$.

the National University of Singapore. The open path analyzers were coupled with sonics at $z/z_h = 1.01$ and 2.17 (Tab. 3.2). Additionally, from January to July 2002 profiles of mean $\text{CO}_2/\text{H}_2\text{O}$ -concentrations were sampled at 10 heights from street level up to the tower top with a closed path gas-multiplexer system (Licor 6262) that sucked sequentially air from 10 inlets at 0.1, 1.5, 3.1, 6.8, 10.8, 13.6, 17.2, 21.2, 25.2 and 31.0 m. The system is similar to the one described in Xu et al. (1999) and details of the current setup can be found in Vogt et al. (2005). Traffic in the canyon was registered by an automatic traffic counter (Tiefbauamt Basel-Stadt). Traffic load was determined to be 2000 vehicles per day, with a peak in the late afternoon (one-way street out of the city).

3.1.2 Basel-Spalenring (U2)

Site — The experimental site U2 is located in the western part of the city in an area of similar building structure, but a smaller plan aspect ratio of buildings and with more vegetation compared to U1 (Tab. 3.6). The site is located beside a tree-lined avenue (Spalenring) with a high traffic intensity (Fig. 3.6).

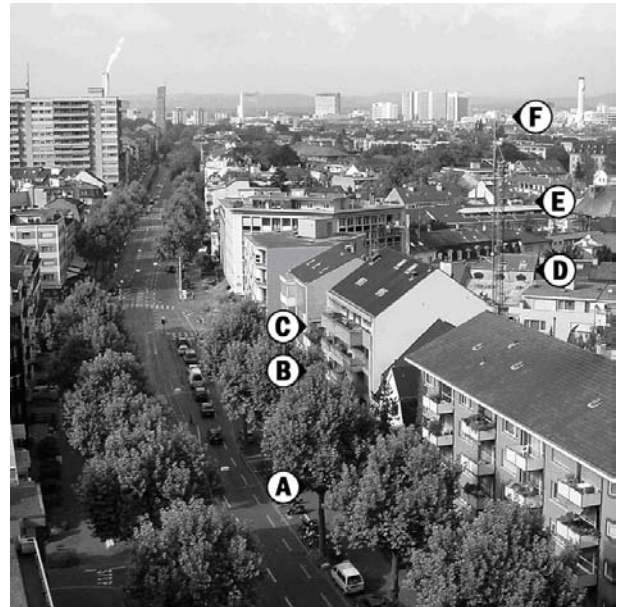


Figure 3.6: Photo of the avenue canyon at Basel-Spalenring (U2) with profile tower and canyon measurements. Ultrasonic anemometer levels are labelled with letters A to F. Photo taken in direction N.

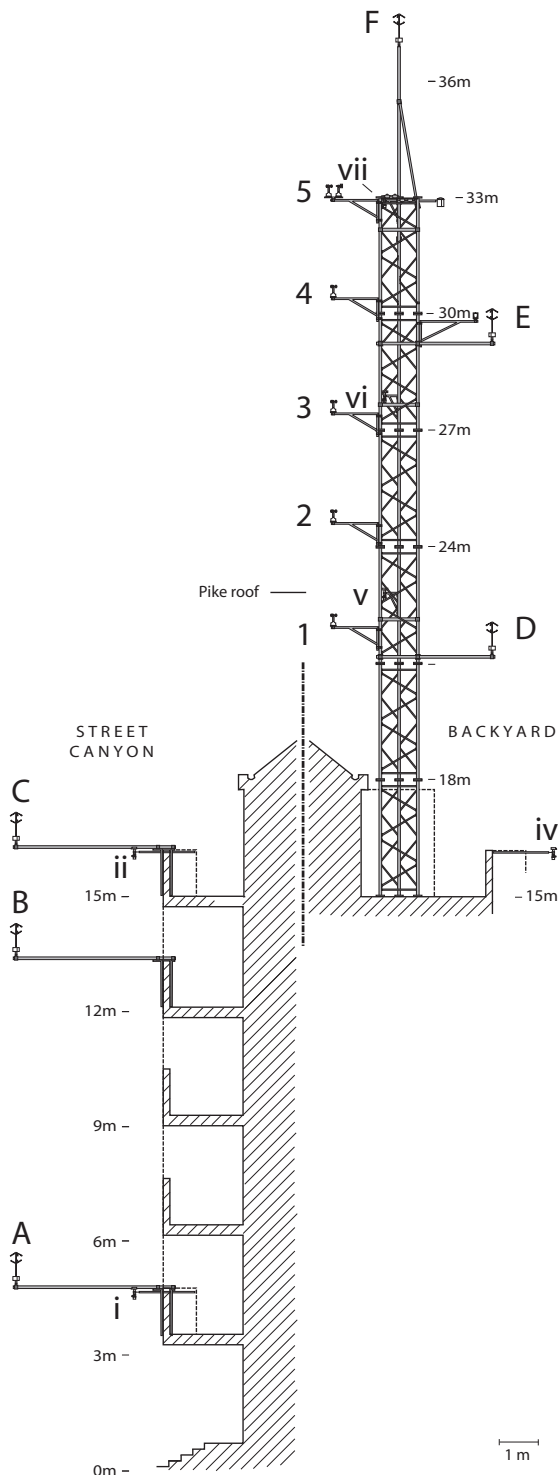


Figure 3.7: Schematic view of the tower at Basel-Spalenring (U2) with sonic levels (A–F), cup anemometer levels (1–5) and psychrometer levels (i–vii, iii in the backyard is not shown). View into direction 350° (along the canyon axis). Note that the horizontal distance between the canyon and the backyard side is not in scale (dash-dotted separation line).

Table 3.4: Turbulence instrumentation at Basel-Spalenring (U2). The capital letters denote the labels on Fig. 3.6.

	z	z/z_h	Instrument type	Variables
A	5.6	0.37	Metek USA-1 ^a	u_i, θ
B	13.9	0.92	Metek USA-1 ^a	u_i, θ
C	16.6	1.10	Metek USA-1 ^a	u_i, θ
D	21.8	1.44	Metek USA-1	u_i, θ
E	29.9	1.98	Metek USA-1 CSI KH20	u_i, θ ρ_v
F	37.6	2.49	Metek USA-1	u_i, θ

^a operated from September 1, 2001 to July 13, 2002

In this neighborhood, the average roof height z_h is 15.1 m, with a mixture of 70% pitched and 30% flat roofs. Building and roof materials are summarized in Tab. 3.6.

Instrumentation — Measurements are available since 1992 from a tower on the roof of the former building of the Institute of Meteorology, Climatology and Remote Sensing of the University of Basel. In the framework of BUBBLE, the instrumentation has been enhanced by a profile of six sonics, a wind profiler and a LIDAR. The sonic profile at U2 was a combination of measurements from the 18 m tower on top of the building and measurements from the building’s adjacent street canyon (Spalenring 145). The orientation of the canyon is along the axis 169° to 349° .

In contrast to the tower at U1, the profile was not probing the same vertical column: three sonics measured within the vegetated street canyon (A to C, Fig. 3.7). The instruments in the street canyon were mounted on 4 m booms reaching from the balconies into the street canyon (position $x/x_c = 0.34$, Fig. 3.7). The two upper sensors (B and C) were located in the vicinity of two tree tops (*Platanus sp.*, Fig. 3.6). The tower part (D to F) was shifted by 20 m towards East (backyard). The tower prolonged the setup up to 38 m above ground. Here, sonics were mounted on booms reaching 1.75 m away from the tower (D and E) in direction 50° , and one instrument was installed on an extension tube on top of the tower (F). At level E, a fast hygrometer was installed. The turbulence profile was continuously operated from September 1, 2001 to August 20, 2002. Prior to September 2001, one sonic was installed for long-term measurements at 34 m (Gill

Table 3.5: Turbulence instrumentation at Allschwil (S1). The capital letters denote the labels on Fig 3.9.

	z	z/z_h	Instrument type	Variables
A	8.3	1.11	CSI CSAT3	u_i, θ
B	12.1	1.61	Metek USA-1	u_i, θ
C	15.8	2.11	Metek USA-1 CSI KH20	u_i, θ ρ_v

Enhanced, August 1994 – June 2000, replaced by a Metek USA-1, June 2000 to August 2001). A total of 7 actively ventilated psychrometers were run at U2, two levels in the street canyon (i and ii), two levels in the backyard (iii and iv) and three levels at the tower (v to vii, Tab. 3.17). A profile of 5 cup anemometers (Vaisala WAA15) was available above roof level (1–5; 22.3, 24.9, 27.8, 30.9 and 32.4 m). Radiation instrumentation included a Kipp & Zonen CM 21 (short-wave downwelling), a Kipp & Zonen CM11 (short-wave upwelling), and two Eppley PIR (long-wave up- and downwelling), all operated at 33 m ($z/z_h = 2.19$).

Further, the site U2 hosted a 1290 MHz wind profiler, installed on the backyard side and run by MeteoSwiss (Ruffieux et al., 2002). A LIDAR constructed by the Observatoire de Neuchâtel allowed detecting the variation of atmospheric aerosol in the PBL and the troposphere. From the LIDAR signal, an aerosol mixed layer height (AML height) could be derived (Martucci et al., 2004). These remote sensing systems are not used in the present work.

3.1.3 Allschwil (S1)

Site — The suburban tower S1 was installed in a vegetated backyard within a uniform residential neighborhood. It completes the BUBBLE data set with information from a less dense built-up area (Fig. 3.10). The suburban area around the site Allschwil consists of old 2–3 storey, single and semi-detached houses constructed at the beginning of the 20th century. The tower is about 1 km westward of the urban site U1, and at least 1 km away from any rural area. In the backyards, there are many trees and scrubs. Surface characteristics are summarized in Tab. 3.6.

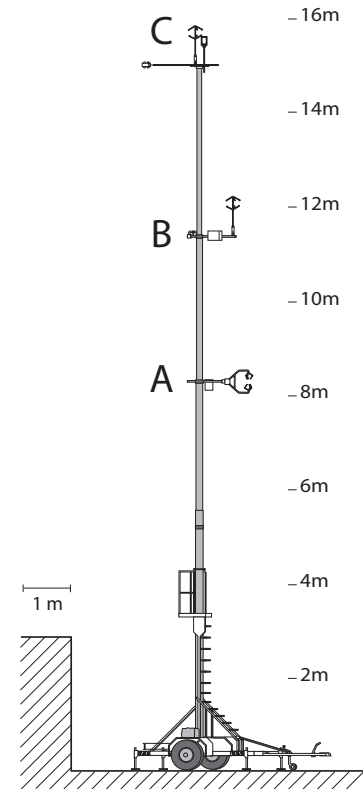


Figure 3.8: Schematic view of the tower at Allschwil (S1) with sonic levels (A–C). View into direction W.

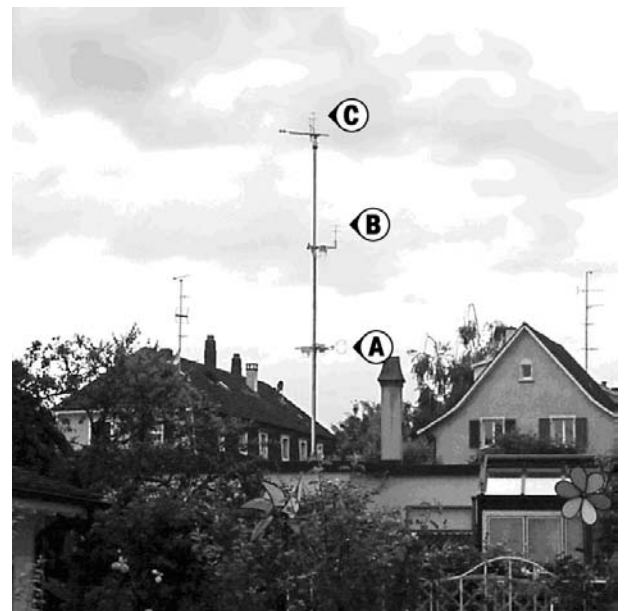


Figure 3.9: Photo of the hydraulic profile tower at Allschwil (S1) with the three ultrasonic anemometer levels labelled. Photo taken in direction W.



Figure 3.10: Aerial orthophoto of the site Allschwil (S1). The location of the tower is indicated by the white circle. The subset is aligned to North (top) and covers an area of 200 by 200 m around the site. Data source: Aerial photo copyright by the Swiss Fed. Office of Topography, Wabern, 213NE268-4097 / 213NE268-4094.

Instrumentation — The hydraulic tower was operated for 6 weeks from July 4 to July 12, 2002 (Fig. 3.8 and 3.9). It was set up in cooperation with the Institute for Atmospheric and Climate Science of the ETH Zürich and the National Bulgarian Meteorological and Hydrological Institute. It supported three sonics, and a fast hygrometer at tower top (Tab. 3.5). All four radiation components were measured at tower top (15.1 m) by a Kipp & Zonen CNR 1. An actively ventilated temperature and humidity sensor provided data from 11.5 m. There are no measurements available from below the mean building height z_h , which was determined to be roughly 7.5 m.

3.1.4 Basel-Messe (U3)

Site — The urban energy balance site U3 was placed near U1, on a large, 170 by 80 m roof in a recently developed downtown area characterized by big building blocks (Fig. 3.11). The roof is used as a parking lot, but was closed to public during the period of measurements. The site provides very local information from this 100% impervious surface. The site U3 was set up and run by the Institute of Hydrology and Meteorology of the Technical Uni-



Figure 3.11: Aerial photo of site Basel-Messe (U3) located on a large concrete roof. The marker 'A' indicates the location of the sonic and radiation instrumentation. Photo by courtesy of R. Vogt, University of Basel. View from NW.

versity of Dresden.

Instrumentation — A sonic anemometer and a fast hygrometer were operated 3.3 m above a concrete roof (CSI CSAT 3 and CSI Krypton KH20). Full radiation components over the concrete surface were measured by a Kipp & Zonen CNR 1. Storage heat flux was experimentally determined using heat flux plates, attached to the surface, and modified to represent surface materials. This site provides data only for a limited period during the IOP from June 24 to July 10, 2004.

3.1.5 Grenzach (R1)

Site — The rural surface energy balance station R1 is located 5 km East of the city inside the plain of the river Rhine. The land use is mainly agriculture (non-irrigated grassland and crops), with some building complexes (farm, dumping site) 200 m to the East, and the river Rhine 300 m to the South.

Instrumentation — A sonic was mounted on an existing 110 m radio tower at a height of 28 m (Metek USA-1). A fast hygrometer at same height (CSI Krypton KH20) provided information on hu-

Table 3.6: Surface characteristics of the profile towers and surface energy balance sites.

Code	U1	U2	U3	S1	R1	R2	R3
Name	Basel-Sperrstrasse	Basel-Spalenring	Basel-Messe	Allschwil	Grenzach	Village-Neuf	Lange-Erlen
Land use (UTZ)	Urban Residential 3-4 storey buildings (A1/A2)	Urban Residential / commercial 3-5 storey buildings (A1)	Urban Newly developed commercial city centre area (Dc1)	Suburban Residential single and row houses 2-3 storey (Dc3)	Rural Grassland	Rural Agriculture	Rural Grassland
Tower	32m tower within and above street canyon	18m tower on top of building	EC system 2m over par- king lot	16m tower in vegetated backyard	Instrumented radio tower	5 m mast	10 m mast
λ_P	0.54	0.37	1.00	0.28	0.02	0.00	0.01
λ_V	0.16	0.31	0.00	0.53	0.91	0.98	0.94
λ_I	0.30	0.32	0.00	0.19	0.07	0.02	0.05
Roof materials	45% tiles, 50% gravel, 5% corrugated iron	70% tiles, 30% gravel	100% concrete	95% tiles, 5% gravel			
Building materials	Plaster, concrete, brick	Plaster, concrete	Concrete, glass	Plaster, brick			

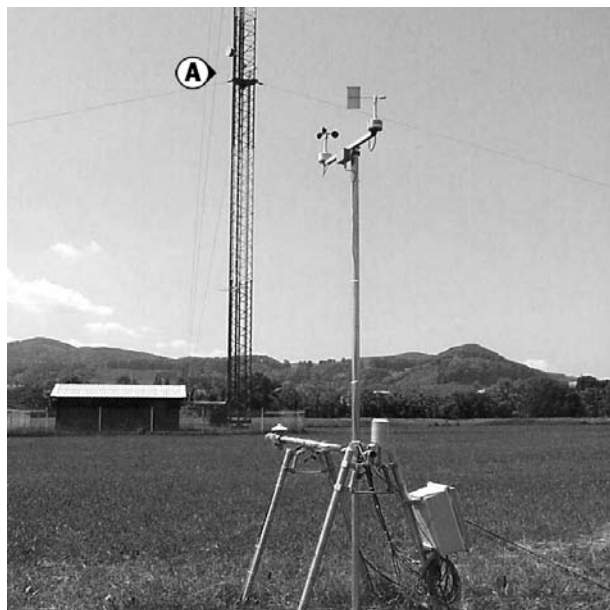


Figure 3.12: Photo of the rural reference site Grenzach (R1). Radiation components, soil temperatures and soil heat flux as well as standard meteorological parameters are measured over grassland at the small mast in the foreground. The marker 'A' indicates the location of the sonic and fast hygrometer at 28 m on the radio tower in the background.

midity fluctuations. Additionally, surface measurements were carried out 100 m north of the tower base over grassland, where all radiation components were monitored with two Eppley PIR and two Kipp & Zonen CM11 at 1.4 m (Fig. 3.12). Soil temperatures were available from -2 , -5 , -10 and -15 cm. Soil heat flux was monitored with three heat flux plates in a depth of -3 cm. One temperature / humidity sensor (Vaisala HMP 35A, 1.5 m) and a wind wave / wind direction sensor (Vaisala WAC15, 3.6 m) completed the setup. The turbulence and surface energy balance measurements were operated from April 24, 2002 until July 12, 2002. During the IOP, a Scintec FAS64 SODAR was operated approximately 200 m NW of the radio tower base (June 5 to July 12, 2002).

3.1.6 Village-Neuf (R2)

Site — This rural surface energy balance station is located 4 km North of the city in the Upper Rhine River Plain. The station was placed over flat and homogeneous non-irrigated agricultural land (bare soil).

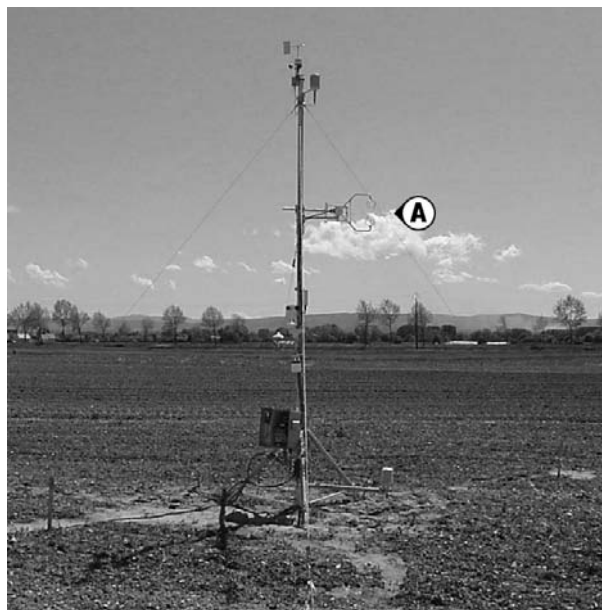


Figure 3.13: Photo of the rural reference site at Village-Neuf (R2) over the bare soil surface. The marker 'A' indicates the location of the sonic and fast hygrometer. View from N.

Instrumentation — Turbulence was monitored on a small 5 m mast (Fig. 3.13). One sonic (CSI CSAT 3, 3.3 m) and a co-located fast hygrometer at same height (CSI Krypton KH20) recorded turbulent fluctuations and fluxes. Temperature / humidity was monitored at three heights (0.5, 2 and 5 m). The measurement at 2 m was actively ventilated. Radiation components were sampled at 1.4 m by two Pyranometer Kipp & Zonen CM11 and a net radiometer (Schenk). Additionally during the IOP, all four components of the radiation balance have been measured by a Kipp & Zonen CNR 1 at same height (only the latter system is used in the present work). Soil temperature probes were placed in a profile of 4 depths (-2 , -5 , -10 , -15 cm) and three soil heat flux plates were buried into the bare soil (-3 cm). The station was set up for the IOP and operated from May 6, 2002 to July 12, 2002.

3.1.7 Lange Erlen (R3)

Site — The surface energy balance station R3 is located in the valley of the river Wiese to the NE of the city. In the vicinity of the tower (500 m radius), the topography is flat and the land-use is dominated by non-irrigated grassland. To the SE and NE, the site is surrounded by built-up areas. The larger scale topographic setting in the Wiese valley results in thermal wind systems (mainly nocturnal



Figure 3.14: Photo of the long-term surface energy balance site Lange Erlen (R3), viewed from NW.

cold air drainage from NE) and forced mesoscale channelling effects.

Instrumentation — A 10 m profile tower, originally set up in 1991 for a regional energy balance network (Parlow, 1996), has been operated continuously since that time by the University of Basel (Fig. 3.14). It provides data for the full observation period of BUBBLE. The tower hosts 4 levels of temperature / humidity measurements (one level actively ventilated at 2 m) and 4 levels of wind speed at 1, 2, 5 and 10 m. All four radiation components are measured at 2 m over grassland. Soil measurements include a profile of 4 soil temperatures (–2, –5, –10, –15 cm) and three soil heat flux plates (–4 cm).

3.2 Instruments, calibrations and corrections

3.2.1 Ultrasonic anemometer-thermometers

3d-ultrasonic anemometers (sonics) are widely applied in the field of atmospheric turbulence measurement. Their principle is based upon the exact determination of the transit time of ultrasonic sound pulses measured along three nonparallel paths. From forward and backward transit times, the 3d-wind vector \mathbf{u} and hence the components u , v and w can be reconstructed (Foken, 2003). Sonics additionally provide a measurement of acoustic temperature θ . The speed of sound depends on static pressure p , the air density ρ , and the Poisson ratio. With the ideal gas law, the acoustic temperature θ can be derived from these parameters. The acoustic temperature θ is strictly not equal the virtual temperature θ_v needed for the buoyancy flux density. Differences are small, and we assume $\theta \approx \theta_v$.

During BUBBLE, a total of 22 sonics were operated: 5 Gill R2 (4 omnidirectional / 1 asymmetric), 11 Metek USA-1, 4 CSI CSAT3, 1 Gill HS and 1 Young 81000. Sonics are the central instruments in this work, and with this variety of models, it is essential to know the reliability and problems of all the different models and individual instruments. The sonics were run with the settings summarized in Tab. 3.7.

Data sampling and processing — All sonics involved in BUBBLE provided digital data output. At U1, U2, S1 and R1 the serial output data from the sonics was continuously monitored and collected using industrial PCs (PIP 6-1, PIP 5 by MPL) equipped with a LabView-based software programmed by the author. The software streams data from up to 10 sonics directly and synchronous into 30 min files. During the experiment, a total of approx. 100'000 hours of raw were collected and archived. At R2 and U3, sonic data were processed on site by data loggers (CSI 21x at R2, CSI 23x at U3). At these sites, only 10 min averages and second order moments over 10 min were stored.

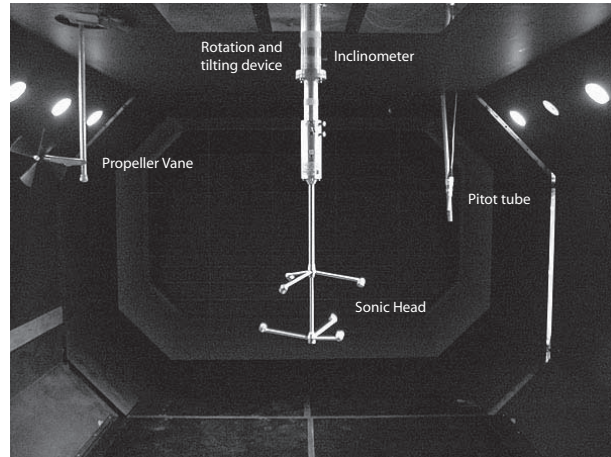


Figure 3.15: Front view of a METEK USA-1 instrument attached to the rotation and tilting device in the wind tunnel.

Flow distortion correction — Sonics neither have threshold nor overspeeding effects, so they can resolve atmospheric turbulence with high temporal resolution. However, flow distortion by the head itself, the spars, and the mounting of a sonic may attenuate (or speed up) wind (Wyngaard, 1988). Furthermore, if wind blows exactly along a path, a velocity loss in the wakes of the transducers is observed, which is known as *transducer shadow effect*. The transducer shadow effect was especially a problem with early sonic models when the transducers were arranged inside a horizontal plane (Grant and Watkins, 1989). Today, this effect has been reduced by designs with a path-inclination to the horizontal. All sonics in the present study have inclined paths. However, the problem reencounters in strong deformed flows, e.g. within a street canyon, where sonic heads are not necessary aligned into the streamlines of the flow.

Hence, to minimize errors of flow distortion and the transducer shadow effect, a matrix correction was applied to most sonics. For this purpose, 16 of the 23 sonics were checked and calibrated in the wind tunnel of the Institute of Fluid Dynamics at the ETH Zürich in two calibration campaigns (Apr. 2001 and Aug. 2002) and compared with data from a previous wind tunnel campaign in March 1999. The tunnel has a test section of 4 m length and is 3 by 2 m in diameter. In the tunnel, the instruments were mounted upside down attached to a rotation and tilting device (Fig. 3.15). The individual sonics were each exposed in 4 runs to different wind velocities (2, 4, 6 and 8 m s^{-1}). During the runs, instruments were continuously rotated around their vertical axis

Table 3.7: Settings of the different sonics involved in BUBBLE.

No.	Manufact.	Model	Operation mode	Sampling rate	
				Internal (Hz)	Output (Hz)
5	Gill	R2	Internal calibration off (Mode 2)	166.6	20.8
1	Gill	HS	Internal calibration off (uvw uncal)	100	20
4	CSI	CSAT 3	Internal calibration on	60	10/20 ^a
12	Metek	USA-1	Head correction on (HC=1)	40/20 ^b	20
1	Young	81000	Internal calibration on	160	20

^a Instruments at U3 and R2 were operated with 10 Hz output rate and data were collected with a datalogger.

^b Instruments at U2 (29.9 m) and R1 (28.0 m) were operated with 20 Hz, all others with 40 Hz internal sampling rate.

at eleven tilt positions between -25 and $+25^\circ$. One rotation at one tilt position lasted five minutes, so a single instrument was in the tunnel during 4 hours. Additionally, a reference propeller vane (Meteolabor ONZ), temperature and humidity were continuously sampled. The alignment was checked by a digital inclinometer. The sonic raw data and all additional sensors were collected at 20 Hz on a computer with a software written by the author for this calibration. The wind vectors recorded by the sonics were compared to the wind velocity in the tunnel. Differences were analyzed as a function of wind velocity, azimuth, and instrument tilt.

From the wind tunnel data, instrument individual correction matrices \mathbf{A}_{ij} and \mathbf{B}_i were calculated with a horizontal azimuth resolution of $\omega = 4$ degrees. The correction was performed according methods described in Vogt (1995) and Vogt et al. (1997), namely

$$u_i(\text{corr.}) = \mathbf{A}_{ij}(\omega)u_j + \mathbf{B}_i(\omega). \quad (3.1)$$

Figure 3.16 shows an example of wind tunnel data. The upper plot visualizes the difference between the sonic measurement and tunnel velocity as a function of horizontal azimuth and tilt (angle of attack). Significant flow distortion errors are visible associated with the geometry of the three transducer pairs of the Metek USA-1, where the dark regions indicate a lower wind velocity measurement. The lower plot illustrates the vanishing differences with the matrix-correction applied. Note that this illustration is statistically not independent because the run shown in Fig. 3.16 was one of four involved in the calculation of the linear matrix.

The matrix-correction was applied during post-processing for all instruments during BUBBLE where raw data was available, and the corresponding

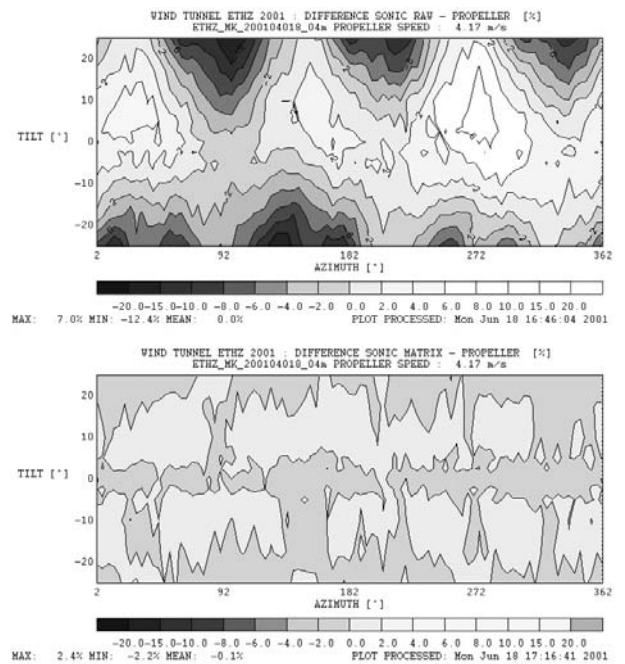


Figure 3.16: Sample data from the wind tunnel for instrument METEK USA-1 200104018 at 4 ms^{-1} .

instrument was calibrated at least once in the tunnel before or after the experiment. Table 3.8 summarizes the applied calibrations. The column "Calibr:" refers to the postprocessing, where "Matrix" indicates that the 2d-matrix obtained from the wind tunnel was applied, and "Manuf." is the (instrument-individual) correction for Gill R2 provided by the manufacturer (Gill Instruments, 1992). "None" indicates that no further flow distortion correction was applied to the sonic during postprocessing.

The wind tunnel investigations, as well as earlier studies (Christen et al., 2000, 2001) indicate that different classes of instrument performance can be formed: CSI CSAT3 and Gill HS show highest agreement, followed by USA-1 and Gill R2. The

Table 3.8: Summary of calibrations and field intercomparisons of all sonics involved in BUBBLE. "ETH99", "ETH01", "ETH02" denote calibrations of the sensors in the wind tunnel in the corresponding years. "Sv99" refers to a field intercomparison in an experiment prior to BUBBLE at San Vittore, Map Riviera 1999 (Christen et al., 2000), "Ae01" denotes instruments involved in a field intercomparison in the frame of BUBBLE at Aesch-Neuhof, South of Basel in August 2001 (see text).

Site	Level	Model	No.	Calibr.	Wind tunnel	Field Intercomparison
U1	A	Gill R2O	0208	Manuf.	—	Sv99
		Metek USA-1	200104017	Matrix	ETH01	—
	B	Gill R2O	0107	Manuf.	—	—
		Metek USA-1	200104018	Matrix	ETH01	—
	C	Gill R2O	0160	Matrix	ETH99	Sv99
	D	Gill R2O	0212	Matrix	ETH99	Sv99
	E	Gill R2A	0043	Matrix	ETH99	Sv99
	F	Gill HS	000046	Matrix	ETH99, ETH01	Sv99
G	CSI CSAT3	0545	None	—	—	
H	Young 81000	00545	None	—	—	
U2	A	Metek USA-1	200104016	Matrix	ETH01	Ae01
	B	Metek USA-1	200104015	Matrix	ETH01	Ae01
	C	Metek USA-1	200104014	Matrix	ETH01	Ae01
	D	Metek USA-1	200104012	Matrix	ETH01	Ae01
	E	Metek USA-1	9903006	Matrix	ETH01	Ae01, Sv99
	F	Metek USA-1	200104013	Matrix	ETH01	Ae01
U3	A	CSI CSAT3	0530	None	—	—
S1	A	CSI CSAT3	0199	Matrix	ETH99	Sv99, Ae01
	B	Metek USA-1	200103001	Matrix	ETH02	—
	C	Metek USA-1	200204003	Matrix	ETH02	—
R1	A	Metek USA-1	200204004	Matrix	ETH02	—
R2	A	CSI CSAT3	0118	None	ETH99	Sv99

METEK USA-1 instruments can be substantially improved in most cases by applying a matrix calibration.

Generally, an angle of attack less than 10° from the horizontal plane (tilt) leads to more precise wind velocity values than higher tilts, where systematic errors are increasing due to flow distortion. Strong angles of attack — as encountered in the street canyons — are not covered by the calibration. The above technique is limited to an angle of attack between $\pm 25^\circ$. In a recent wind tunnel campaign, Vogt and Feigenwinter (2004) measured all possible angles of attack with different sensors. They concluded that the above matrix-calibration procedure does not enhance data from regions above or below $\pm 25^\circ$, but on the other hand, data from this region are not further falsified. They showed that larger uncertainties are associated with data from high angles of attack with all instruments.

Field intercomparison — Nevertheless, a wind tunnel can not reproduce all possible wakes and waves in the flow around an instrument (Grelle and Lindroth, 1994). The wind tunnel is creating a quasi-laminar flow, and is not able to simulate real atmospheric conditions. In order to test instruments under atmospheric conditions, six Metek USA-1 (later installed at U2) have been compared with a reference instrument (CSI CSAT3 199) between August 20 and 22, 2001. All instruments were installed 1.90 m above ground on an open grassland site (Aesch, Neuhof, 259000/611300, 310 m, Fig. 3.17) and were compared under wind velocities up to 4 m s^{-1} . The results are encouraging and support the enhancement of Metek USA-1 data by applying an instrument individual matrix (Tab. 3.9). Especially, the agreement of the second order moments with the high-end reference instrument is substantially increased by the matrix.



Figure 3.17: Photo of the sonic field intercomparison setup at Aesch-Neuhof. August 21, 2001.

Error sources — All instruments have been corrected for crosswind either internally by the sensor electronics or in the postprocessing (Schotanus et al., 1983). This crosswind correction is of minor impact on $\overline{w'\theta'}$ with less than 1% at all sites. The transit time measured by sonics can be further seriously altered by liquid water or snow on transducers. A liquid water film or ice on the transducers changes significantly the speed of sound (Laubach and Teichmann, 1996). Since none of the instruments involved in BUBBLE have been heated, data from periods of heavy rain and snow is excluded from analysis.

3.2.2 Open path gas analyzers

CSI KH20 — At all energy balance sites with eddy correlation instrumentation, a CSI KH20 Krypton hygrometer was operated (Tab. 3.10). The principle of this fast open-path hygrometer is to measure extinction of H₂O at the ultraviolet wavelength of 123.6 nm and at a secondary band at 116.5 nm. Practically, the extinction is directly related to the water vapour density ρ_v in the measurement volume (CSI, 1995) by

$$\rho_v = \frac{\log(V_0) - \log(V)}{x_p k_w} \quad (3.2)$$

where x_p is the path length, and V is the measured voltage at the photodetector. Two calibration ranges were applied, a low range for $\overline{\rho_v} < 9 \text{ g m}^{-3}$, and a high range for conditions with $\overline{\rho_v} > 9 \text{ g m}^{-3}$. For

Table 3.9: Summarized results from the three-day sonic field intercomparison at Aesch-Neuhof. The CSI CSAT3 reference instrument was compared to 6 Metek USA-1. The difference between the Metek USA-1 and the reference instrument Δ is listed in terms of the slope of a linear regression (USA-1 = a CSAT3, with $\Delta = (a - 1)$ in %). The average of the square of the Pearson correlation coefficients, once with Matrix calibration applied to the USA-1 and once without are indicated by r^2 .

Parameter	without Matrix		with Matrix	
	Δ	r^2	Δ	r^2
\bar{m}	+1.2%	0.99	-0.8%	0.99
σ_u	+3.8%	0.99	+1.5%	0.99
σ_w	-8.2%	0.98	+3.5%	0.98
σ_θ	-6.5%	0.98	— ^a	—
u_*	+11.2%	0.75	+2.5%	0.73
$\overline{w'\theta'}$	-16.9%	0.97	-6.8%	0.97

^a Matrix calibration does not affect acoustic temperature measurement.

Table 3.10: CSI KH20 Krypton hygrometers involved in BUBBLE. Calibrations and average effects of O₂-correction on $\overline{w'\rho'_v}$ for the period June 10 to July 10, 2002 and situations with $|L_v \overline{w'\rho'_v}| > 20 \text{ W m}^{-2}$. "Separ." is the sensor separation between the KH20 and the sonic measurement volume.

Site	L.	No.	Calibr.	Separ.	O ₂ -Corr.
U1	F	1448	Dec-98	0.5 m	+20.8%
U2	E	1094	May-01	0.5 m	+11.5%
U3	A	1123	Feb-96	0.2 m	+5.0%
S1	C	1461	Oct-01	0.3 m	+7.7%
R1	A	1096	Dec-01 ^a	0.5 m	+1.5%
R2	A	1199	Oct-01	0.2 m	+2.4%

^a Internal calibration by Indiana University, Bloomington IN, USA. All other calibrations were performed by the manufacturer.

each instrument and both ranges, the output signal in absence of any gas V_0 , and the extinction coefficient for H₂O k_w are determined in a calibration procedure by the manufacturer.

Unfortunately, the wavelengths are not only sensitive to H₂O, but also slightly to O₂. Tanner and Greene (1989) suggested that the output of the hygrometer can be corrected by multiplying ρ_v by a correction factor, which accounts for the absorption by O₂, namely

$$\rho_{v \text{ corr.}} = \frac{C_O m_O}{c_p m_a} \frac{k_O}{k_w} \frac{L_v \beta}{T} \rho_{v \text{ uncorr.}} \quad (3.3)$$

C_O is the atmospheric concentration of oxygen, m_O and m_a are the molecular weights of O₂ and dry air,

Table 3.11: LICOR 7500 open path analyzers operated at U1.

L.	No.	Calibr.	Separ.	Axis
F	75H-0332	19-Apr-02	0.40 m ^a	165°
			0.26 m ^b	165°
C	75H-0254	11-Oct-01	0.24 m	7°

a before July 5 2002 09:30 CET

b after July 5 2002 09:30 CET

respectively. k_O is the extinction coefficient for O₂ for which a global value of 0.45 m³ g⁻¹ m⁻¹ was used (Tanner et al., 1993). The impact of the O₂-correction is most pronounced at the urban sites, where it increases the magnitude of $\overline{w'\rho'_v}$ between 5% and 20%, compared to the smaller influence at the rural sites (around 2%). The large urban correction term is a consequence of the extremely high Bowen ratios β measured over the urban surfaces (cf. Section 4.5.6).

Licor 7500 — The Licor 7500 is an infrared open path gas-analyzer designed to measure fluctuations of CO₂ and H₂O at 150 Hz, with a path length of 12.5 cm and a 1 cm diameter optical beam. It measures quasi-simultaneously at 4.26 μm (CO₂), 2.59 μm (H₂O), and at two non-absorbing wavelengths (3.95 μm and 2.40 μm). During BUBBLE, two Licor 7500 were operated at U1 (Section 3.1.1).

After the field phase of BUBBLE, a timing error of the analyzer was published by the manufacturer (Licor, 2003). The error affects the time delay (lag) between the measurement and the digital and analog outputs of the analyzer in the firmware version used during BUBBLE. This time delay error results in an underestimation of the flux density, since the wind measurement and the concentration measurements, which were supposed to be simultaneously during BUBBLE, are not simultaneously taken in reality. They suggested that "customers who have collected raw time-series data may be able to minimize this timing error by performing a time-shift to the gas density data relative to the vertical wind data."

The correlation function $\mathbf{R}_{wt}(\tau)$ between vertical wind w and concentrations of CO₂ or H₂O was calculated as a function of the time lag τ for all data. For each half-hourly run, the measured time lag τ_m was determined by maximizing $\mathbf{R}_{wt}(\tau)$. Due to the physical sensor separation, the measured lag τ_m

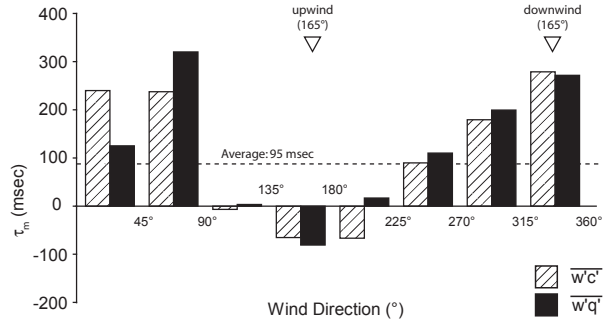


Figure 3.18: Average time lag τ_m for different wind directions between LICOR 7500 analyzer and sonic at U1 level F (June 15 to July 5, 2002). The labels up- and downwind indicate the axis of the separation which was $x_d = 0.40$ m.

Table 3.12: Average impact of the lag-correction on flux densities of CO₂ and H₂O at U1 for situations with $|w'\rho'_c| > 2 \mu\text{mol m}^{-2} \text{s}^{-1}$, and $|w'\rho'_v| > 0.01 \text{ mmol m}^{-2} \text{s}^{-1}$. Time periods: 14.7 m: June 25 – July 13, 2002; 31.7 m: July 5 – July 15, 2002. "glob." indicates that the covariance was calculated with a global lag τ_e determined as the average a_0 with the regression method. "indiv." denotes a covariance that was calculated with individual lags τ_m for each run separately.

Level	C	F
$\overline{w'\rho'_c} \text{ indiv.} / \overline{w'\rho'_c} \text{ old}$	+1.44%	+0.86%
$\overline{w'\rho'_c} \text{ glob.} / \overline{w'\rho'_c} \text{ old}$	+0.37%	+0.71%
$\overline{w'\rho'_v} \text{ indiv.} / \overline{w'\rho'_v} \text{ old}$	+1.28%	+0.85%
$\overline{w'\rho'_v} \text{ glob.} / \overline{w'\rho'_v} \text{ old}$	-0.46%	+0.30%

shows a strong relation to wind direction and wind velocity. The influence of the sensor separation, i.e. the time needed for an air parcel to travel from the sonic to the analyzer, is dominating over the effect of the electronic lag τ_e , making it difficult to separate these two effects. We assume the Taylor hypothesis to be valid over the distance of the sensor separation and write $\tau_m = \tau_e + x_d/u_d$, where x_d is the sensor separation and u_d the wind component along the axis sonic - analyzer. Practically, two methods were applied to separate the electronic lag τ_e from the effects of the sensor separation.

Equalization Method: Here, for each level, data are classified into 8 wind direction classes. An average lag was determined for each class separately (Fig. 3.18). Then, the electronic lag τ_e is equal the equalized weighted average of all 8 wind direction averages, because the sensor separation effect will be counterbalanced by opposite wind directions as illustrated in Fig. 3.18. This method does not take into account wind velocity, and assumes the same

Table 3.13: Average impact of different flux corrections applied to Q_H and Q_E . Statistics are calculated for situations with $|Q_H|$ or $|Q_E| > 20 \text{ W m}^{-2}$

Site	Level	Q_H	Q_E	Q_E
		Humidity Corr.	WPL Corr.	Sensor Separation
U1	F	-2.2%	+26.7%	+1.7%
U2	E	-2.7%	+17.8%	+2.1%
U3	A	-0.9%	+8.4%	+8.5%
S1	C	-5.4%	+11.5%	+2.2%
R1	A	-14.2%	+3.5%	+1.7%
R2	A	-13.6%	+5.2%	+6.7%

velocity histogram in each wind direction class. For CO_2 , it results in a τ_e of 100 msec (Level F) and 410 msec (Level C).

Regression-Method: Since sensor separation x_d and the position of instruments are exactly known, the travelling time (x_d/u_a) for an air parcel between the sonic and the closest point of its trajectory to the analyzer can be calculated from the sonic data. By applying a linear regression between travelling time and total lag τ_m , the offset a_0 of the linear regression $\tau_m = a_1(x_d/u_d) + a_0$ (i.e. for a travelling time of 0 sec) returns directly the electronic lag τ_e whereas a_1 should be around 1. For CO_2 , the regression mode results in a τ_e of 110 msec (Level F) and 400 msec (Level C).

Table 3.12 shows that effects of the corrections on vertical flux densities of CO_2 and H_2O are very small and in average below 2%. The corrections are higher with the instrument mounted closer to the surface because of the higher peak frequency of the co-spectra. This agrees with results from other experiments (Christen, 2003). For further calculations, the global values of τ_e from the regression method were applied.

3.2.3 Corrections of turbulent flux densities

Humidity correction for Q_H — The direct determination of Q_H by a sonic (Eq. 2.61) is influenced by humidity in the measurement volume. The measured speed of sound from the sonic is converted into acoustic temperature θ , which is not equal the thermodynamic temperature θ_T . Schotanus et al. (1983) introduced a humidity correction to convert the mea-

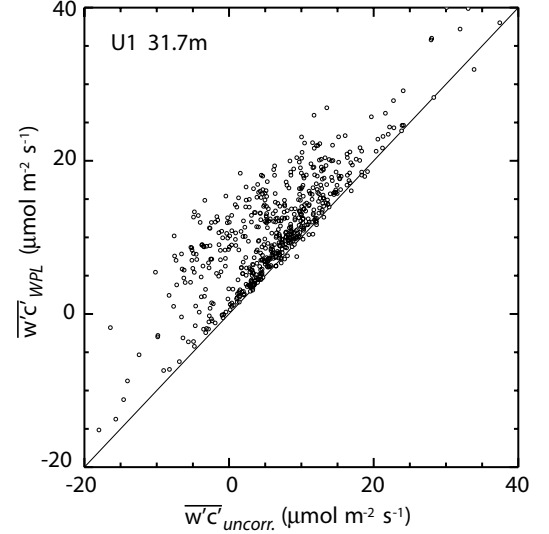


Figure 3.19: Individual impact of the WPL-correction on mass flux densities of CO_2 at U1 level F.

sured $\overline{w'\theta'}$ into $\overline{w'\theta'_T}$, using simultaneous measurements of $\overline{w'\rho'_v}$:

$$\overline{w'\theta'_T} = \overline{w'\theta'} - 0.51\overline{w'\rho'_v}. \quad (3.4)$$

This conversion was applied to the levels, where a simultaneous humidity flux density is available for the energy balance investigations. By applying the conversion, the resulting magnitude of Q_H is reduced only slightly at the urban sites, but more pronounced at the rural sites (Tab. 3.13). The higher impact at the rural sites is because of their higher evapotranspiration.

WPL-Correction — A non-zero turbulent flux density of sensible heat results in continuous changes in air density correlated with vertical wind. If we measure a non-zero $\overline{w'\theta'_v}$, this implies a small vertical wind component, which is too small to be measured by the eddy correlation system. Webb et al. (1980) suggested a correction for this small vertical wind component

$$\overline{w'\rho'_{\text{scorr.}}} = \left(1 + \frac{m_a \overline{\rho_s}}{m_s \overline{\rho_a}}\right) \left(\overline{w'\rho'_{\text{uncorr.}}} + \frac{\overline{\rho_s}}{\overline{\rho}} \frac{Q_H}{c_p T}\right) \quad (3.5)$$

where ρ_s is the concentration of any trace-gas, m_s its molecular weight and ρ_a is the density of dry air. This so called WPL-correction was applied to both mass flux densities, $\overline{w'\rho'_v}$ and $\overline{w'\rho'_c}$. The correction results in a significant higher relative impact to the

small urban values of Q_E compared to rural sites, where generally $Q_E > Q_H$ (Tab. 3.13). The impact on the mass flux density of CO_2 is stronger, and may even result in a change of the direction, as shown in Fig. 3.19.

Sensor separation — Furthermore, a spectral correction was calculated taking into account sensor separation according to Moore (1986). The correction is based on classical surface layer spectra. Therefore, it is only applied to the top most measurements over the urban surfaces, and only for Q_E in the study of the surface energy balance. The impact on Q_E is strongest when sensor separation is large and measurement height is low (Tab. 3.13).

3.2.4 Radiation instruments

A detailed description of radiation instruments operated during BUBBLE, the field intercomparisons and calibrations, and the resulting effects can be found in a technical report by Christen and Vogt (2005).

Kipp & Zonen CNR 1 — The Kipp & Zonen CNR 1 operated at the energy balance sites were intercompared side-by-side during a field intercomparison in July 2002 in Southern Italy, just after the BUBBLE experiment ended. There, four of the five CNR 1 used in this work were compared to a high-end Kipp & Zonen CM21 (Pyranometer) and an Eppley PIR (Pyrgometer), which were both recently calibrated by the World Radiation Centre (WRC) in Davos, Switzerland. The calibration factors derived from this week long intercomparison confirmed that shortwave downward radiation K_\downarrow measured with a CNR 1 is generally underestimated by 2%. The underestimation can be attributed to instrumental problems, since it was observed systematically and significantly with all four instruments involved.

Longwave downward radiation L_\downarrow measured by CNR 1 instruments show a small, systematic dependence on K_\downarrow (pers. comm. R. Vogt). Hence, an additional factor f_k is introduced to correct this shortwave sensitivity of the long-wave sensor

$$L_\downarrow^{corr} = L_\downarrow^{uncorr} + f_k K_\downarrow. \quad (3.6)$$

Table 3.14: Kipp & Zonen CNR 1 net radiometer involved in BUBBLE, and f_k correction factors determined from the field calibration data.

Site	z	No.	Calib.	f_k
U1	31.5 m	980098	Jul-02	-0.018
U3	3.3 m	980126	Jul-02	-0.021
S1	15.1 m	010285	Jul-02	-0.018
R2	1.4 m	020419	Jul-02	-0.023
R3	2 m	980080	—	-0.019 ^a

^a Average value of above instruments used

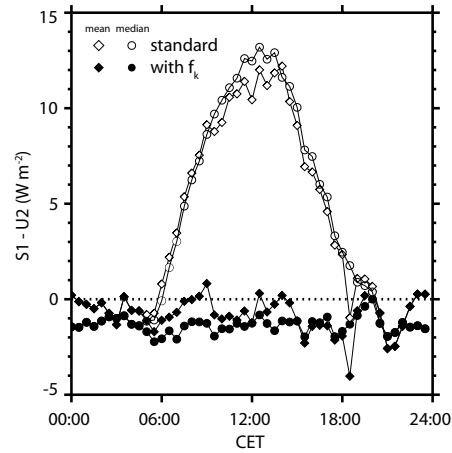


Figure 3.20: Impact of the f_k -correction to measurements of L_\downarrow during BUBBLE with sample data from Sites S1 and U2 for the period June 4 to July 13 2002.

f_k was determined for each instrument individually and is in the order of -0.02 (Tab. 3.14). Figure 3.20 illustrates the successful f_k correction with independent measurements taken during BUBBLE. The average diurnal course of the difference in L_\downarrow between two sites (S1 and U2) is drawn. The sites are supposed to have the same L_\downarrow in average, despite their spatial separation of 1 km. At S1, values were measured with a CNR1 and at U2 with an Eppley PIR pyrgometer. The manufacturer calibration is drawn with open (white) symbols whereas the values corrected with the f_k factors are shown with filled symbols.

Table 3.15: Eppley PIR Pyrgometers involved in BUBBLE.

Site	z	No.	WRC Calib.	Field Interc.
U2	L_\downarrow	33 m	30323F3	Jun-98
	L_\uparrow	33 m	28961F3	Mar-97
R1	L_\downarrow	1.4 m	31207F3	May-98
	L_\uparrow	1.4 m	28962F3	Jan-02

Table 3.16: Average Impact of the overspeeding correction on cup anemometer data at U1. Sonic values have been linearly interpolated between levels, due to the vertical shift between cups and sonics.

z	m_{raw}	$m_{\text{corr.}}$	$(m_{\text{sonic}} - m_{\text{cup}})$
m	m_{sonic}	m_{sonic}	$/m_{\text{sonic}}^a$
	m s^{-1}	m s^{-1}	%
32.40	0.16	0.02	1.5
26.10	0.05	-0.12	-5.9
24.10	0.02	-0.17	-9.1
22.10	-0.11	-0.33	-18.5
20.10	0.09	-0.13	-7.5
18.10	-0.09	-0.35	-22.5
16.10	0.02	-0.26	-16.9
14.60	-0.10	-0.45	-30.1
13.10	-0.34	-0.75	-52.0
11.10	0.07	-0.21	-16.4
7.10	-0.08	-0.34	-25.4
3.20	-0.47	-0.77	-61.8

^a Situations with $m_{\text{sonic}} > 1\text{ms}^{-1}$

Eppley PIR Pyrgeometer — The upward-looking instruments were modified with three dome thermistors separated by 120° and were corrected according to Philipona et al. (1995). The downward-looking instruments have only 1 dome thermistor. The instruments were all calibrated at the WRC and were intercompared after BUBBLE in two different field campaigns in 2002 and 2003 (Tab. 3.15).

Dewfall — Periods with dew on the sensors - a phenomenon mainly observed at the rural sites - were detected using the differences between dew point and case temperature and masked out by visual inspection. The resulting missing data were linearly interpolated for gaps shorter than 2 h. Gaps with a longer duration are homogenized with a box-car type of linear regression with data from other sites of similar land use.

3.2.5 Cup anemometers

Over 20 Vaisala WAA15 cup anemometers have been operated at the sites of interest in this work. The WAA15 is an opto-electronic cup anemometer which creates 14 pulses per revolution.

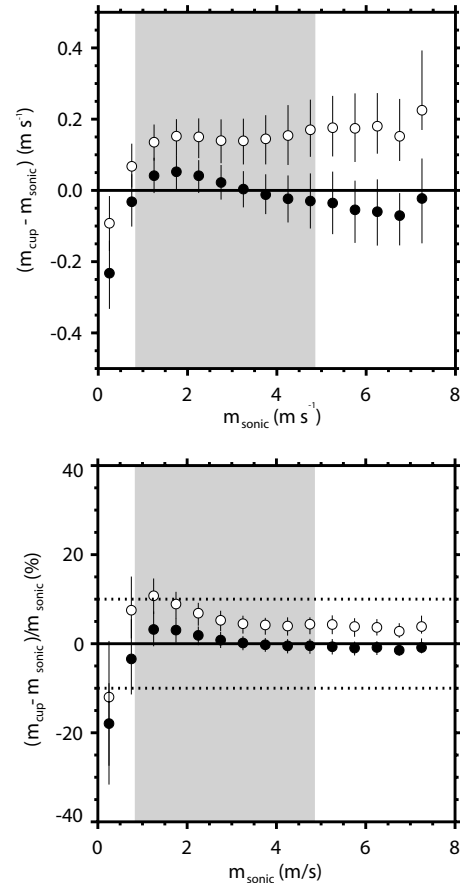


Figure 3.21: Absolute (top) and relative (bottom) impact of the overspeeding correction on the topmost cup anemometer at U1 (33 m). Uncorrected data are drawn with open circles, overspeed corrected data with black circles. The grey shaded area indicate the range where 90% of all data are.

Overspeeding — Cup anemometers have a non-linear response to fluctuating winds. They respond faster to increasing wind speeds than to a decrease of same magnitude, an effect of their inertia. This leads to a general overestimation of the determined wind speed, especially if turbulence intensities are high, which is expected close to an urban surface. Overspeeding is important if time scales T_x of the energy containing eddies, and the response time of the cup anemometer (expressed by the distance constant ℓ_0) overlap. This is addressed in the correction method described in Busch and Kristensen (1976), where Δm is the overspeeding, and m is the measured mean (scalar) wind speed, both in m s^{-1} :

$$m_{\text{corr.}} = m(1 + I_s^2(1 + L_x/\ell_0)^{-1} + cI_w^2). \quad (3.7)$$

The WAA15 has a ℓ_0 of 1.5 m (Vaisala, 1991). L_x was retrieved from the sonic velocity spectra at corresponding height, and c was set to 1. I_s and I_w are the horizontal and vertical turbulence intensities,

Table 3.17: Psychrometers used in temperature-humidity profile measurements during BUBBLE.

Site	Level	z	No.	Calibration
U1	i	2.6 m	FK13	02-Jun-01
	ii	13.9 m	FK15	02-Jun-01
	iii	17.5 m	FK24	28-May-01
	iv	21.5 m	FK25	30-May-01
	v	25.5 m	FK26	28-May-01
	vi	31.2 m	FK30 ^a	30-May-01
U2	i	5.0 m	FK04	13-May-01
	ii	15.8 m	FK05	13-May-01
	iii	3.0 m	FK08	13-May-01
	iv	15.8 m	FK06	13-May-01
	v	22.9 m	FK21	28-May-01
	vi	27.8 m	FK14	13-May-01
	vii	32.9 m	FK19	28-May-01

^a Only temperature measured

which were derived from the simultaneously operated sonics and linearly interpolated between two measurement levels.

Figure 3.21 illustrates the overspeed correction applied to the most ideal measurement at tower top at U1. Here, the correction reduces the error-source associated with overspeeding. However with decreasing height, wind speed measurements from the cup anemometers are significantly overcorrected compared to the corresponding sonic wind speed, especially under low wind conditions. At most levels, uncorrected values match better sonic values (Tab. 3.16). This may be attributed to model failure due to the high turbulence intensities, but also to the fact that sonics and cups were horizontally separated at the tower. The separation becomes important in the street canyon, where cup anemometers were operated close to the wall. Further, all cup-anemometers are affected by a mechanical threshold problems, which lower the measured wind speed under low wind conditions as encountered in the street canyon. Due to all these problems, whenever possible, sonic measurements were considered the more reliable source for wind speed data in the present work.

3.2.6 Temperature / humidity sensors

At the two urban profile towers U1 and U2, actively ventilated psychrometers were operated (Tab. 3.17). The instruments constructed by the Institute of Meteorology, Climatology and Remote Sensing use Pt100 thermistors. All instruments were calibrated in the range -15° to $+40^{\circ}$ in the laboratory prior to the BUBBLE field experiments. Instrumental design and the calibration procedure are described in Vogt and Reber (1992).

3.3 Data processing

3.3.1 Sonic block averaging

Statistical moments are calculated and stored for blocks over 10 min. Neither a linear detrending nor another low-frequency filter was applied, in order to conserve energy and to allow an appropriate upscaling of higher-order moments to longer averaging periods. For instance, six consecutive 10-min covariances $\overline{a'b^{10}}(t)$ can then be upscaled to an hourly flux covariance $\overline{a'b^{60}}$ by

$$\overline{a'b^{60}} = \frac{1}{6} \sum_{t=1}^6 \overline{a'b^{10}}(t) + \frac{1}{6} \sum_{t=1}^6 (\overline{a^{10}}(t) - \overline{a^{60}}) (\overline{b^{10}}(t) - \overline{b^{60}}) \quad (3.8)$$

where $\overline{a^{60}}$ and $\overline{b^{60}}$ are the averages over 60 minutes.

Further, any detrending would not ensure that at all tower levels the same amount of energy is removed (or re-attributed to the mean flow). This would not only violate energy conservation but also inhibit the possibility to calculate vertical flux density divergences in the prognostic equations of higher order moments introduced in Section 2.3.1.

It is shown later (Section 4.4), that the average co-spectra of the relevant vertical flux densities significantly drop off in the low-frequency range (over 5 to 10 minutes), so that omitting any low-frequency filtering does not influence vertical flux densities in average. However, it may affect horizontal wind components and any higher order moments with horizontal components involved. To test the impact of omitting a linear detrending, the total kinetic energy per unit mass of all three wind components $E = 0.5\overline{u_i^2}$ is split into a mean part \overline{E} , a part which would classically be removed by the detrending \tilde{E} , and the remaining turbulent part E' :

$$E = \overline{E} + \tilde{E} + E'. \quad (3.9)$$

Table 3.18 illustrates the relative partitioning of the kinetic energy according to Eq. 3.9 with data from the tower at U1 for all three components separately. Detrending over 60 minutes does only marginally affect the variance $\overline{w'^2}$. Spectral energy of w is low in the low-frequency band affected by the detrending.

But in the horizontal wind components u and v , the energy removed by a linear detrending may be up to twice the remaining turbulent kinetic energy in the street canyon.

Table 3.18: Separation of kinetic energy for a component i (E_i per unit mass in J) into a mean kinetic energy \overline{E}_i , a part removed by the detrending \tilde{E}_i , and the resulting turbulent part E'_i .

z/z_h	Absolute	Relative		
	E_3	\overline{E}_3	\tilde{E}_3	E'_3
2.17	0.30	1.3%	0.6%	98.0%
1.53	0.28	1.6%	0.6%	97.8%
1.23	0.26	1.5%	0.6%	97.9%
1.01	0.25	2.8%	0.8%	96.5%
0.75	0.22	13.5%	1.7%	84.8%
0.23	0.14	20.1%	1.5%	78.4%
z/z_h	$E_{1,2}$	$\overline{E}_{1,2}$	$\tilde{E}_{1,2}$	$E'_{1,2}$
2.17	7.49	73.9%	3.5%	22.6%
1.53	4.52	62.0%	5.9%	32.1%
1.23	2.99	54.7%	8.4%	36.9%
1.01	1.62	41.6%	16.2%	42.2%
0.75	1.36	27.7%	49.6%	22.7%
0.23	1.40	31.6%	48.0%	20.4%

3.3.2 Sonic coordinate rotations

In most micrometeorological studies, the coordinate systems of sonics with the base vectors \mathbf{e}_i are rotated in a way that \mathbf{e}_1 is aligned collinear to the mean wind vector \mathbf{u} , and \mathbf{e}_3 is then believed to be normal to the surface. This rotation is called *double rotation* and was first introduced by Tanner and Thurtell (1969). Typically, the rotation is performed for each run and each height level independently. The resulting frame of reference is very popular in experimental micrometeorology because it allows many simplifications as \overline{v} and \overline{w} both become zero, and the terms $\overline{u'v'}$ and $\overline{v'w'}$ usually vanish. The rotation assumes small vertical wind components to be an effect of sensor misalignment only.

For the present study, this procedure is highly questioned, because (i) the individual rotation of the coordinate system at each level of a tower does not ensure anymore that vertical wind gradients and vertical flux density divergences are referring to the same coordinate direction in space, and (ii) two rotations are not sufficient to ensure that the coordinate system is independent of the original orientation of the

sonic. The directions of the resulting \mathbf{e}_2 and \mathbf{e}_3 base vectors are not defined by the double rotation (Finnigan, 2000). These concerns are not of practical importance, as long as the flow is mainly parallel to the surface and the sonic is originally aligned with \mathbf{e}_3 approximately normal to the surface, an assumption which is fulfilled in most ‘classical’ applications. To have a correct definition of the frame of reference, McMillen (1988) introduced a third rotation in which the $v' - w'$ tensor is diagonalized. In practice, the third rotation often results in even more unphysical orientations and it is therefore rarely applied. Recently, Wilczak et al. (2001) introduced a planar fit technique, which reduces the run-to-run variability, but must again be applied to each level separately and secondly assumes a horizontally homogeneous non-curved mean flow with planar and parallel streamlines.

Since the flow in the urban roughness sublayer is highly three dimensional, all above rotation techniques are not suitable and the simplifications are often not fulfilled. There is no physical reason for \bar{w} to be zero at all points in the roughness sublayer. Especially around obstacles, a mean up- or downwind is the normal case. Any rotation would falsify results especially within the street canyon in a dramatic manner. The terms $\overline{u'v'}$ and $\overline{v'w'}$ do not necessarily vanish in this highly deformed flow field.

During BUBBLE, instruments were assumed to be correctly aligned in the vertical (7 instruments were checked with continuously recording inclinometers). Only a single rotation around the \mathbf{e}_3 -axis into mean wind at tower top was applied for all levels simultaneously. In this semi-fixed frame of reference, \mathbf{e}_3 is always oriented strictly vertical to the surface. \mathbf{e}_1 is aligned into the horizontal mean wind at tower top, and \mathbf{e}_2 is the resulting lateral component. This coordinate system allows the calculation of vertical gradients and flux densities as needed for example in the conservation equations (Section 2.3.1). With this procedure, all three base vectors \mathbf{e}_i are parallel at all levels. But neither \bar{w} nor \bar{v} are mandatorily zero. This further questions the interpretation of flux densities. If w is other than zero, any vertical flux density of mass, momentum or heat does split up into an advective mean flux density (which would be otherwise zero) and a turbulent flux density:

$$Q = \bar{w} \bar{s} + \overline{w' s'}. \quad (3.10)$$

Again, s denotes any scalar. In order to reduce the

complexity back to one dimension (the vertical) and to eliminate the problem of mean flux densities in the vertical, we introduce the concept of horizontal spatial averages.

3.3.3 Horizontal averaging

The horizontal spatial average $\langle a(t) \rangle$ of any variable a within an indefinite slice at height z and time t is defined by

$$\langle a(t, z) \rangle = \frac{1}{\mathcal{L}_{x1,2}} \iint_{x_{1,2}-\mathcal{L}_{x1,2}/2}^{x_{1,2}+\mathcal{L}_{x1,2}/2} I(x, y, z) a(x, y, z, t) dx dy \quad (3.11)$$

where $I(x, y, z)$ is an indicator function according to Miguel et al. (2001), which is 1 if the point (x, y, z) lies within airspace and 0 otherwise (building, vegetation). The horizontal domain \mathcal{L}_x and \mathcal{L}_y of the averaging volume must be both larger than the characteristic scale of the surface inhomogeneities \mathcal{L} (cf. Tab. 3.3). In the case of an urban surface, this corresponds to the characteristic length scale of repetitive building-blocks.

This horizontally averaged view allows further implications. If the flow is horizontally homogeneous at scales larger than \mathcal{L}_x then $\langle \partial \bar{a} / \partial x_j \rangle = 0$ and $\langle \partial \overline{a' u'_j} / \partial x_j \rangle = 0$ for any i and $j = \{1, 2\}$, and for parameters a which are constant at the air-building interface. If a is constant at the interface, a commutation of the horizontal averaging operator and the horizontal spatial differentiation operator is allowed, i.e. $\langle \partial \bar{a} / \partial x_i \rangle = \partial \langle \bar{a} \rangle / \partial x_i$ for $i = \{1, 2\}$ (Raupach and Shaw, 1982). This becomes important when applying the horizontal averaging operator to the conservation equations. All wind components fulfill this condition, but especially pressure p and strictly speaking concentrations ρ_s and temperature θ are not mandatory constant at the interface and hence, do not allow this simplification.

Averaging procedure — Directly measuring spatial averages in full scale is nearly impossible. It would require huge arrays of simultaneously measuring instruments. As already suggested by Rotach (1993a, 1995) for urban surfaces, spatial horizontal averages can be approximated from a large en-

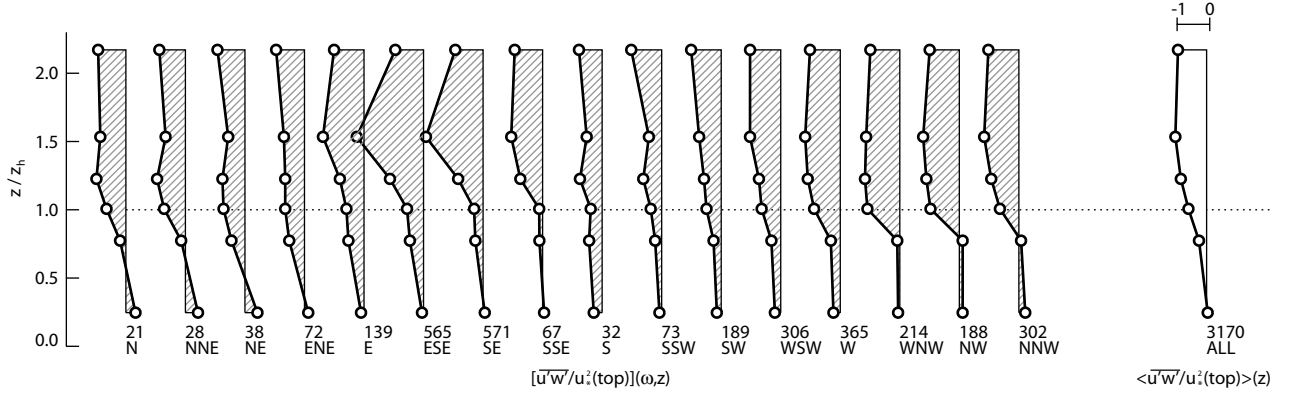


Figure 3.22: Illustration of the horizontal averaging procedure, with data from the sonic profile at U1. Details see text. The numbers below the profiles indicate the number of hourly data blocks involved.

semble of measured profiles under different conditions, which reflect different flow geometries. The real horizontal average, deduced from simultaneous measurements at different locations under a particular ambient flow may converge with the ensemble average of many realizations measured at one location with varying ambient flow. The huge data set collected during BUBBLE, allows a systematical procedure to retrieve horizontally averaged vertical profiles from different wind directions of approaching flow. In the present work, the following procedure is applied to turbulence tower data at U1, U2 and S1:

1. Any term or parameter of interest $\bar{a}(z, t)$ is scaled by an appropriate local or global scaling parameter $a_*(z, t)$ or $a_*(t)$, respectively. This eliminates effects of different boundary conditions (e.g. different wind velocity). If appropriate, only cases within a certain stability range $\zeta(t)$ measured at tower top are included in further analysis. The instruments at tower top are assumed to measure within the inertial sublayer and hence to deliver an appropriate information on overall stability.
2. The scaled profiles of $\bar{a}/a_*(t, z)$ are then classified into N equally spaced wind direction classes ω based upon wind direction at tower top.
3. For each of the wind direction classes ω , a conditional average $[\bar{a}/a_*](\omega, z)$ is calculated from the full time series of T averaged blocks. The conditional average is denoted by square brackets and describes the average value at given

height with wind from given direction ω ,

$$[\bar{a}/a_*](\omega, z) = \frac{1}{T\bar{J}} \sum_{t=1}^T (\bar{a}/a_*)(t, z) J(t) \quad (3.12)$$

where $J(t)$ is an indicator function that is 1 if at the corresponding time step t , wind blows from the wind direction sector ω and 0 otherwise. \bar{J} is the temporal average of $J(t)$ over the whole data set and denotes the frequency of wind from given sector.

4. Now, the equally weighted average over all $[\bar{a}/a_*](\omega, z)$ at a given height z is taken as a surrogate of a horizontal average and is denoted by angle brackets:

$$\langle \bar{a}/a_* \rangle(z) = \frac{1}{N} \sum_{\omega=1}^N [\bar{a}/a_*](\omega, z). \quad (3.13)$$

All terms in angle brackets in the present work are evaluated with the above procedure, with a resolution of $N = 16$ wind direction classes. Figure 3.22 illustrates an example of the above procedure. The covariance $\overline{u'w'}(t, z)$ has been normalized by $u_*^2(t)$ at tower top for each time step. Based on this, the 16 conditional averages $[\overline{u'w'}/u_*^2](\omega, z)$ drawn in the figure have been calculated separately for each wind direction class. The horizontally averaged profile $\langle \overline{u'w'}/u_*^2 \rangle(z)$ — illustrated on the right side of Fig. 3.22 — was calculated by equally weighting the 16 single profiles of $[\overline{u'w'}/u_*^2](\omega, z)$.

Dispersive Terms — Extending the concept Reynolds decomposition (Section 2.2.2), any vari-

able $a(\mathbf{x}, t)$ at any point and any time can be separated into a spatial-temporal mean part, a temporal mean deviation from the spatial-temporal mean (dispersive part) and a turbulent part (Raupach and Shaw, 1982),

$$\bar{a}(\mathbf{x}, t) = \langle \bar{a} \rangle + \bar{a}''(\mathbf{x}) \quad (3.14)$$

and hence

$$a(\mathbf{x}, t) = \langle \bar{a} \rangle + \bar{a}''(\mathbf{x}) + a'(\mathbf{x}, t). \quad (3.15)$$

From 3.14 and 3.15 it follows

$$\langle \bar{a}'' \rangle = 0. \quad (3.16)$$

Note that the product of two dispersive terms $\langle \bar{a}'' \bar{b}'' \rangle$ (called a *dispersive flux density*) does not have to be mandatory zero. The problem encountered in Eq. 3.10, due to the fact that \bar{w} may be other than zero, can now be rewritten using dispersive terms as

$$Q = \langle \bar{w} \rangle \langle \bar{s} \rangle + \langle \bar{w}'' \bar{s}'' \rangle + \overline{w' s'}. \quad (3.17)$$

With the assumption that $\langle \bar{w} \rangle = 0$ due to mass continuity on a larger scale, the first term on the right hand side of Eq. 3.10 vanishes. Any remaining local mean vertical flux density is now interpreted as a dispersive contribution, which is only of any importance if the horizontally averaged dispersive flux density $\langle \bar{w}'' \bar{s}'' \rangle$ is non-zero.

4 Results and Discussion

4.1 Mean flow

In this chapter, the mean flow within and above an urban canopy is addressed in different levels of detail: First in Section 4.1.1, the three dimensional flow in the urban street canyon is analyzed. Then, in Section 4.1.2, we construct the mean vertical wind profile in a horizontally averaged view (which corresponds to the neighborhood scale). Finally, in Section 4.1.3, the specific features of the wind profile in the roughness sublayer are neglected, and the flow in the inertial sublayer above is simply described by an appropriate set of z_d and z_0 . Results in this chapter are rather descriptive. We will analyze the driving processes more deeply in the subsequent chapters addressing momentum and turbulent kinetic energy. Further, we mainly focus on results from site U1. Here, conditions are close to ideal, and with a profile of six instruments in the same vertical column, this site provides the most comprehensive data set.

4.1.1 Flow patterns in the street canyon

The flow within urban street canyons is of particular interest in air pollution. Table 4.1 lists average concentrations of CO₂ and NO₂ for a period of two weeks at different heights at U1. Highest concentrations for both pollutants are observed at street canyon floor where they are emitted by motor vehicles. Gradients are strong at street canyon floor, but continuously decrease with height in the street canyon. Above z_h , again, stronger vertical gradients are measured for both trace gases. The reason for this pattern is found in the exchange mechanisms: The whole street canyon shelters and traps pollutants. This results in higher local gradients at roof top than in the upper street canyon part, a phenomena well known from wind tunnel experiments and numerical street canyon models (Vardoulakis et al., 2003). The key parameters that determine flow within any street canyon are the canyon width to height ratio x_c/z_h and canyon length to height ratio y_c/z_h . x_c is the local street canyon width, and

Table 4.1: Vertical profiles of mean concentrations of NO₂ and CO₂ through the street canyon at U1. Values in brackets denote the average gradients to the next lower level. Data source: NO₂ was monitored with passive sampler tubes (analyzed by the Lufthygieneamt beider Basel), CO₂ data was averaged from the gas-multiplexer profile. Averaging period is June 14 to July 28, 2002.

z/z_h	NO ₂		CO ₂	
	$\mu\text{g m}^{-3}$	$\mu\text{g m}^{-4}$	ppm	ppm m ⁻¹
1.45	28.6	(-0.66)	392.2	(-0.31)
1.03	32.7	(-0.45)	394.1	(-0.19)
0.74	34.6	(-0.55)	394.9	(-0.10)
0.47	36.8	(-0.84)	395.3	(-0.27)
0.21	39.9	(-4.94)	396.3	(-1.75)
0.10	47.8		399.1	

y_c is the length of the street canyon between two adjacent intersections (Hunter et al., 1992). For ambient wind perpendicular to the street canyon axis and wind velocities $> 1.5 \text{ m s}^{-1}$, Oke (1988) distinguishes three flow regimes with decreasing x_c/z_h : (i) *isolated roughness flow*, (ii) *wake interference flow* and (iii) *skimming flow*. Isolated roughness flow is found in sparsely built-up areas. Here, the disturbed flow of a first roughness element can readjust to the surface before it encounters the next element. With closer spacing, there is insufficient space for a readjustment. In skimming flow, which is found in narrow canyons ($x_c/z_h < 1.5$), the bulk of the overlying flow skims over the cavity. The skimming flow regime is most critical in air pollution management, since it is least efficient in removing pollutants. Further, Kastner-Klein and Plate (1999) concluded in their wind tunnel study that roof shape is another important factor determining flow in canyons.

In contrast to numerical models and wind tunnel experiments, there is no control of the geometry in a real-world street canyon, hence the profile measurements at U1 and U2 provide only point measurements from a specific configuration. At U1, the configuration is close to an ideal street canyon with $x_c/z_h = 1.0$ and $y_c/z_h = 11$. The position of the tower is exactly in the center between two intersections (refer to map in Fig. 3.5). The configuration in the avenue at U2 is more complicated, not only be-

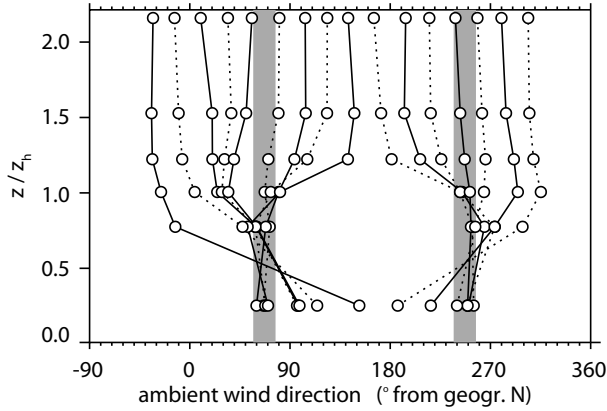


Figure 4.1: Channeling of flow into the street canyon at U1. Data source: Sonics A to F, 10 min averages classified into 16 different wind direction classes, November 1, 2001 to July 15, 2002, $n=1600$ h. Only data with wind velocity at $2.2z_h > 1 \text{ m s}^{-1}$ are included.

cause of the separation of the street canyon and the tower profile, but also because of interactions between trees and the flow. Here, $x_c/z_h \approx 1.8$ and $y_c/z_h = 6$ with an asymmetric T-intersection to the South. No information is available from the open backyard at S1 where no instruments were operated below z_h .

It is not possible to reconstruct the full three dimensional flow from a limited number of measurement locations in the street canyon. Nevertheless, average properties can be interpreted by analyzing the large number of realizations with different wind velocity, wind direction and thermal stratification of the ambient flow.

Channeling — It is no surprise that flow channelling increases continuously with decreasing height into the street canyon. This is illustrated for U1 in Fig. 4.1 where the average local horizontal wind direction from the 6 levels is drawn. The figure shows 16 realizations classified by ambient wind direction measured at $2.2z_h$. Following down a line, one can see how wind from a starting direction at tower top is deflected and forced into the street canyon axis. Below mean building height, the majority of all cases show wind directions channelled either into direction 67 or 247° , which corresponds to the axis of the street canyon indicated by the grey bars in the figure. An asymmetry in the channelling effect is observed because instruments were mounted closer to one building wall (cf. Fig. 3.3), and roof shapes are different at both sides of

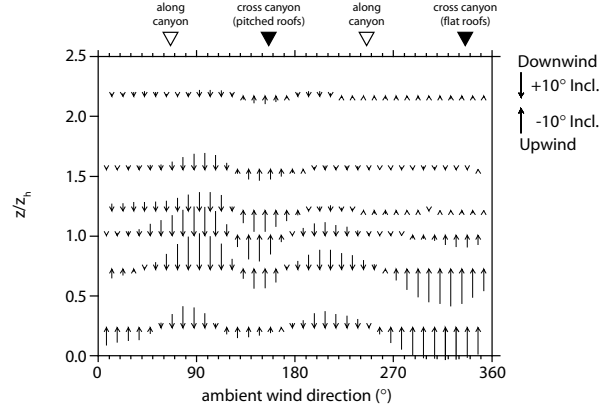


Figure 4.2: Inclination ξ of mean wind as a function of ambient wind direction at U1. Data source: Sonics A to F, 10 min averages classified into 10° classes, November 1, 2001 to July 15, 2002, all stabilities, $n=1600$ h.

the street canyon. Flow from NW passes flat-roofs (buildings 95 and 97, cf. Fig. 3.5) whereas from SE, pitched roofs are overflowed (buildings 98 and 100). channelling is also observed in the wide street canyon at U2, but the corresponding flow patterns are more complex.

Vertical motions — Fig. 4.2 illustrates the inclination of mean wind ξ as a function of ambient wind direction. ξ describes the vertical angle of attack of the mean wind vector as defined by

$$\xi = -\arctan\left(\frac{\bar{w}}{\sqrt{\bar{u}^2 + \bar{v}^2}}\right). \quad (4.1)$$

First, it can be seen that flow at the topmost level is nearly horizontal. With decreasing height, a non-negligible vertical wind is observed. Along-canyon flow results in small vertical motions. Stronger upwinds are measured when the tower is located in the leeward wall (flow over flat roofs from NNW). Downwinds are found in the majority of cases when instruments measure closer to the windward wall (oblique flow over the pitched roofs from E and SSW). ξ does not describe the expected well behaved sine-curve. There is a region between 130 and 150° that shows unexpected upwinds instead of downwinds, despite the fact that the tower measured closer to the windward wall in this configuration. We will discuss this phenomena later in this section, but will first address the simpler situation with flow from NNW.

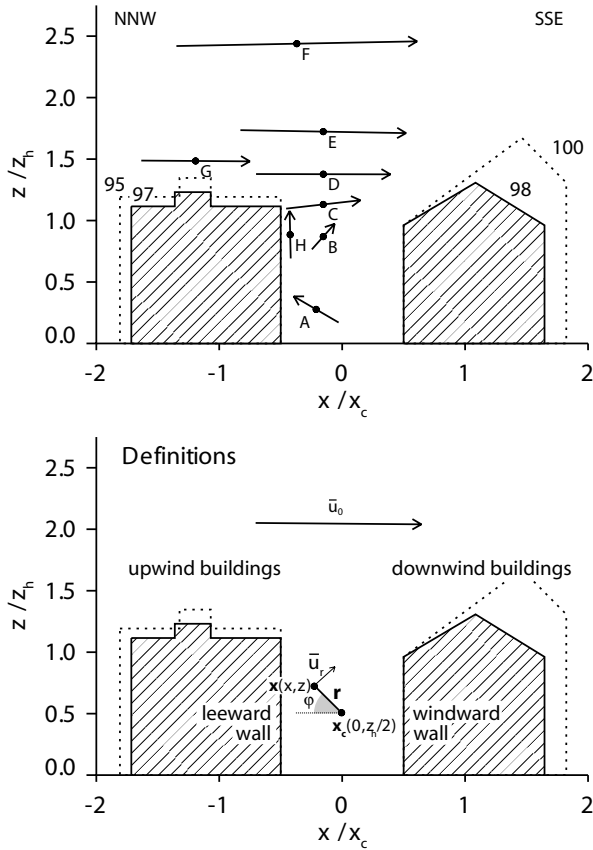


Figure 4.3: Ensemble street canyon cross-section of measured wind vectors at U1 for flow situations in a sector perpendicular to the street canyon (flow from 315 – 360°). Numbers denote corresponding buildings labelled on the map in Fig. 3.5. Data source: Sonics A to H, 10 min averages, June 15 to July 15, 2002, all stabilities, $n=250$ h.

Vortex — Wind tunnel results show that high pollution in street canyons are typically associated with low wind velocities and/or situations with an ambient wind perpendicular to the street canyon axis (Kastner-Klein et al., 2001). Flow situations perpendicular to a street canyon with $x_c/z_h \approx 1$ and $y_c/z_h > 8$ result in a primary vortex (Sini et al., 1996). Figure 4.3 (top) shows average wind components in the street canyon at U1 for situations with flow perpendicular to the street canyon (flow from NNW). The arrows indicate the mean vector wind components in the xz -plane normalized by wind velocity at tower top. The labels A to G refer to the instrument locations in this xz -plane, with x as the lateral axis in the street canyon (point of origin in the street canyon center) and z as the vertical axis. In the example of Fig. 4.3, the observed wind direction at street level is opposite to the direction above the roofs, and a primary vortex in the street canyon can easily be interpreted from the measurements.

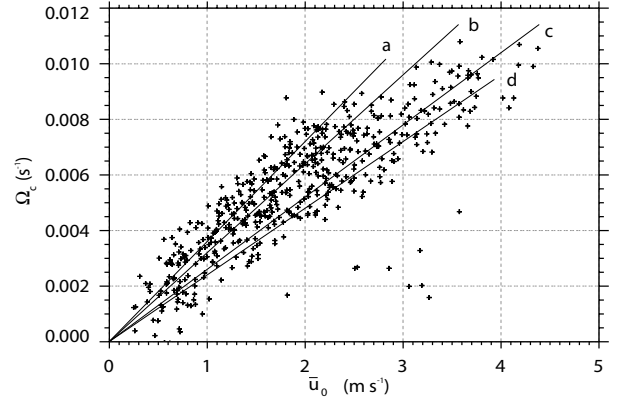


Figure 4.4: Average rotational frequency of the street canyon vortex Ω_c at U1 against wind component \bar{u}_0 perpendicular to the street canyon at tower top (flow 315 – 360°). Data source: Sonics A to C, hourly averages, November 1 to July 15, 2002, all stabilities.

Table 4.2: Stability dependent linear regressions of Ω_c against \bar{u}_0 for flow situations drawn in Fig. 4.4. The letters denote corresponding regression lines.

	Ω / \bar{u}_0	r^2	Stability	n
a	0.0036 m^{-1}	0.67	$-10 < \zeta \leq -1$	67
b	0.0032 m^{-1}	0.69	$-1 < \zeta \leq -0.4$	132
c	0.0026 m^{-1}	0.70	$-0.4 < \zeta \leq -0.1$	178
d	0.0024 m^{-1}	0.45	$-0.1 < \zeta \leq 0$	38

This approach simplifies the problem by reducing the flow field to two dimensions, and the third y -component (which is small in this case) is not shown. This is justified by the length y_c of the street canyon and the position of the tower. If the street canyon would be shorter, or if the tower would have been installed closer to an intersection, we would be in a region of edge vortices caused by the building corners (Hoydysh and Dabberdt, 1988). These edge vortices have a vertical axis that result in non-negligible along-canyon y -components, even if the flow is exactly perpendicular to the street canyon. With increasing distance to the intersection, the edge vortices transform into a primary vortex with a horizontal axis (Baik and Kim, 2004). At the tower location, we are far enough from the vertical edge vortices and uniquely a vortex with a horizontal axis is observed. Nevertheless, the non-uniform roof geometry (different building heights and shapes) may cause deflections of the primary vortex.

From each of the four instruments operated in the street canyon (A, B, C and H), a local vortex rotational frequency Ω can be calculated in this xz -

plane. Given $\mathbf{r} = \mathbf{x} - \mathbf{x}_c$, the vector between the location $\mathbf{x}(x, z)$ of the instrument and the street canyon centerline at $\mathbf{x}_c(0, z_h/2)$, and r its length (Fig. 4.3, bottom), we write

$$\Omega = \frac{\bar{u}_r}{2\pi r}. \quad (4.2)$$

\bar{u}_r is the measured average wind velocity component in the rotational direction of a circular vortex at the instrument location $\mathbf{x}(x, z)$, namely

$$\bar{u}_r = I(z) (\cos(\varphi)\bar{u} - \sin(\varphi)\bar{w}) \quad (4.3)$$

where $I(z)$ determines the sign to account for the direction of the vortex rotation. $I(z)$ is equal 1 for $z > z_h/2$, and -1 otherwise. \bar{u} and \bar{w} are the lateral and vertical wind components at $\mathbf{x}(x, z)$ in the fixed street canyon system. φ is the inclination angle between r and the horizontal plane (Fig. 4.3, bottom):

$$\varphi = \arctan\left(\frac{z - z_h/2}{y}\right). \quad (4.4)$$

This approach includes many simplifications. The axis of the vortex is assumed to be in the street canyon center. Numerical and physical scale studies show that the axis of the vortices are typically asymmetric and slightly shifted to the downwind-building (Baik and Kim, 1999; Baik et al., 2000). Further, flow close to walls and especially in the corners of the street canyon is described completely unrealistic, since no roughness and blocking effects are considered.

Visualization experiments in a water channel show that the average flow field (but not the instantaneous motions) resembles a solid body rotation (Caton et al., 2003). If we have a solid body rotation, an average rotational vortex frequency Ω_c can be calculated. Ω_c determines the time of an air parcel to complete a full circuit in the vortex. It is approximated by averaging the individual Ω from the four instruments at different positions within the street canyon. Ω_c is drawn against reference velocity \bar{u}_0 in Fig. 4.4. Typically, the reference velocity \bar{u}_0 is measured upwind in a wind tunnel before the flow encounters the roughness elements. In a real city, its determination is problematic. Hence, we define the reference \bar{u}_0 as the wind vector component perpendicular to the canyon axis at $z/z_h = 2$. For flow from $315 - 360^\circ$, the average ratio Ω_c/\bar{u}_0 was found to be fairly constant. Table 4.2 illustrates that

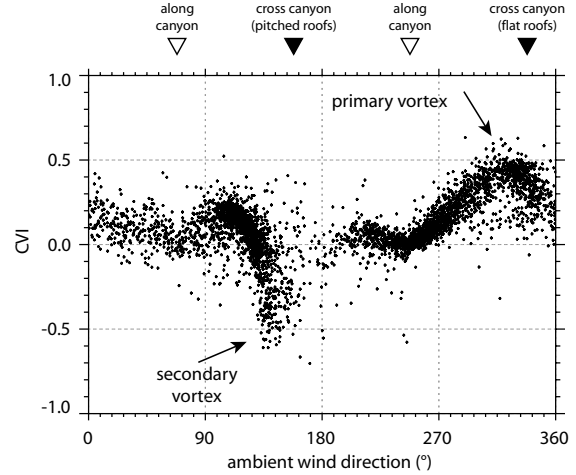


Figure 4.5: Average street canyon vorticity index (CVI) at U1 according Eq. 4.4 as a function of ambient wind direction at tower top. Data source similar to Fig. 4.4.

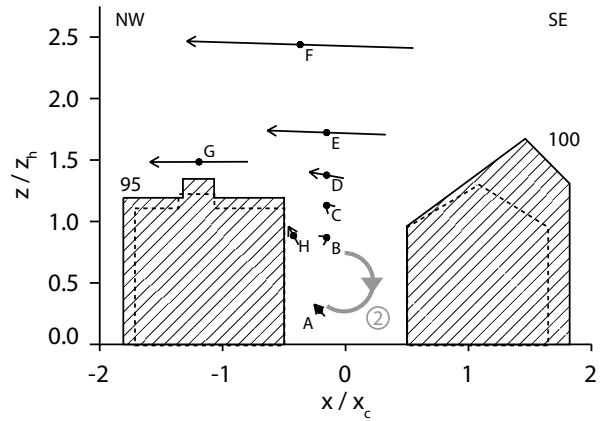


Figure 4.6: Ensemble street canyon cross-section at U1 for the specific flow situation in a sector with 75° inclination to the street canyon. Data source: similar to Fig. 4.3 for flow from $130 - 140^\circ$, $n=143$ h).

the value of Ω_c/\bar{u}_0 is related to stability. With increasing stability*, the ratio becomes lower, which is mainly attributed to the shape of the wind profile above the roofs and hence affects \bar{u}_0 . There is a slight tendency for Ω_c/\bar{u}_0 to be smaller towards higher wind velocities, which is an indication that the vortex becomes more decoupled from the ambient flow.

For each measurement level and time step, a canyon vorticity index (CVI) was calculated by relating the component \bar{u}_r to the mean 3d wind velocity \bar{U} . The CVI is a measure how similar the measured three

* If not indicated, stability is always calculated at the topmost tower level by $\zeta = (z - z_d)/L$, which is assumed to represent conditions in the overlying inertial sublayer.

dimensional wind direction (not the velocity) compares to the above simplified model of a primary vortex with a horizontal axis:

$$\text{CVI} = \frac{\bar{u}_0 \bar{u}_r}{|\bar{u}_0| \bar{U}}. \quad (4.5)$$

The first term accounts for the sign, according to the direction of the ambient flow. A positive sign indicates that in the upper street canyon, air flows in the direction of the ambient wind and flows in the opposite direction at street level. A negative sign indicates a counter-rotating vortex. Since \bar{U} is always greater or equal \bar{u}_r , the CVI is between -1 and $+1$. The closer the absolute value is to 1, the more the flow field resembles a perfect, symmetric primary vortex. Numbers around zero indicate that the mean flow at the point is completely different from the vortex-model.

Figure 4.5 illustrates the average CVI at U1 (from levels A, B and C) for different ambient wind directions. As expected, CVI is close to zero with flow along the street canyon axis. Flow perpendicular to the street canyon over the flat roofs from NW show a CVI which is up to $+0.5$. This corresponds to the text-book case of the primary vortex illustrated in Fig. 4.3 (top). In situations where the wind blows from SE ($120 - 150^\circ$), the air first overflows the high pitched roof of building 100, which reaches up to $1.7 z_h$. These conditions result in a CVI that is strongly negative, indicating similarity to a counter-rotating vortex in the street canyon. Here, we have a ‘step-down’ situation. Air flows from the high pitched roof with 75° inclination to the street canyon axis over the cavity and then over the lower flat roofs in the NW. Figure 4.4 illustrates the wind vectors in a cross-section for this specific flow situation. The building heights have been readjusted to represent the cross-section with 75° to the street canyon, because building heights vary along the street canyon. The observed wind direction at street level (A) is parallel to the ambient wind whereas in the upper canyon (B), wind blows slightly in the opposite direction. The grey circle in the lower street canyon is an interpretation of a secondary weak counter-rotating vortex. The observed wind velocity in the street canyon (normalized by \bar{u}_0) is low compared to the situation in Fig. 4.3 (top) with flow over the flat roof. This fits well to observations reported from wind tunnels where secondary vortices are typically weak (Kovar-Panskus et al., 2002). In the upper street canyon, no well defined primary vortex can be

found. Upwinds and channelling along the canyon dominate.

The present observations have similarities with results presented by Longley et al. (2004). They investigated the flow field in a street canyon in Manchester, U.K. with different wall heights at the two sides. They concluded that if air flows first over the building row with the lower wall (‘step-up’ situation), this results in a clear primary vortex, as observed in the present dataset. But if air flows first over the higher row (‘step-down’), they interpreted an elevated vortex from the measurements, and only upwinds were measured in the street canyon. There was little evidence for a secondary counter-rotating vortex.

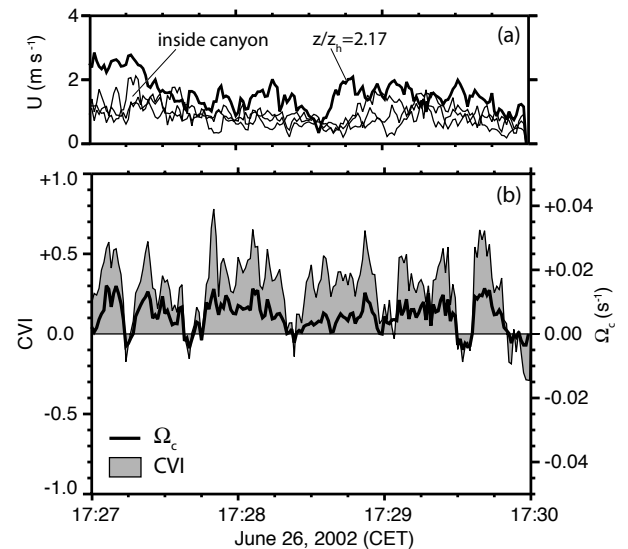


Figure 4.7: Sample three-minute time period illustrating (a) instantaneous values of wind velocity at tower top (thick line) and within the street canyon (3 thin lines from levels A, B, C) and (b) instantaneous CVI and rotational frequency Ω_c . Data source: Sonics A to C and F, 1 s averages.

Intermittency — The vortex can be found only in the average wind field. Looking at high-frequency instantaneous data, the vortex is highly intermittent. It builds up and decays continuously. Figure 4.7b illustrates a three-minute time series of average vortex rotational frequency Ω_c and the CVI with an ambient wind direction from the flat roof perpendicular to the street canyon (333°). In the time-series, 30 to 40 second blocks of high CVI can be found, associated with higher Ω_c . Quasi-periodic events of shorter duration destroy the vortex and let Ω_c drop down, or even change the sign of the rotation. This

can not be attributed to the ambient flow, because wind velocity \bar{U} neither at tower top nor in the street canyon does show the same pattern (Fig. 4.7a). Instationarities have their typical peak frequency in the order of 30 to 60 s (all data with ambient wind from NNW), and no dependence on peak frequency from the wind velocity aloft can be seen. This supports that instationarities are determined through Kelvin-Helmholtz instabilities arising from the shear at roof top and not from larger organized structures in the flow aloft. Instationarities and intermittency of the vortex is also reported from wind tunnel studies addressing flow in cavities (Rambert et al., 2000) and from real-world measurements (Louka et al., 2000; Nielsen, 2000).

4.1.2 Vertical wind profile

Definitions — In many applications, the specific flow pattern in the street canyon are not of central interest. Instead, a horizontally averaged wind profile is preferred in the urban roughness sublayer. We can address the mean wind profile in the roughness sublayer with different parameters. In the present study, the following definitions are applied:

- The *longitudinal wind velocity* (or just *wind velocity*) \bar{u} is the average vector wind component pointing in the direction of the mean horizontal wind at tower top. It is assumed that the measurement at tower top reflects the ambient wind direction in the inertial sublayer. The individual \bar{u} -component at lower measurement levels all point to the same direction in space, enabling the calculation of gradients. Therefore, \bar{u} can be negative, for example within a vortex where the local wind direction is opposite to the wind at tower top.
- The horizontal *local wind velocity* \bar{u}_l is defined as $\bar{u}_l = (\bar{u}^2 + \bar{v}^2)^{1/2}$. It is always positive, and is equal the length of the horizontal projection of the average wind vector at given height.
- \bar{m} is the scalar horizontal *wind speed* and is close to the speed measured by a cup anemometer. \bar{m} is important in questions addressing wind load and wind comfort in canyons. It is always positive and $\bar{m} \geq \bar{u}_l \geq \bar{u}$. Note that \bar{m} is incompatible with the Reynolds

decomposition in the present Cartesian frame. It already includes energy, which is attributed to turbulent motions.

- \bar{U} is the *3d wind velocity*. It is always positive, and corresponds to the length of the local average wind vector. $\bar{U} = (\bar{u}^2 + \bar{v}^2 + \bar{w}^2)^{1/2}$
- Analogous, \bar{M} is the mean *3d wind speed*.

The horizontally averaged profile — Figures 4.8a to c illustrate that the different definitions lead to significant differences in the average vertical wind profile. When addressing dispersion and advection in the urban roughness sublayer, a horizontally averaged view is preferred. In a horizontally averaged view, only the profile of the topmost definition, the longitudinal wind velocity $\langle \bar{u} \rangle(z)$, is of interest. $\langle \bar{u} \rangle(z)$ describes the average longitudinal advection velocity. $\langle \bar{w} \rangle = 0$ and — assuming an isotropic urban configuration — also $\langle \bar{v} \rangle = 0$. This results in $\langle \bar{U} \rangle(z) = \langle \bar{u} \rangle(z)$. All exchange processes associated with a local, non-zero \bar{w} or \bar{v} are addressed as dispersive motions, i.e. $\bar{w} = \bar{w}''$ and $\bar{v} = \bar{v}''$ respectively. In the horizontally averaged view, they affect exchange of mass, momentum or energy only if corresponding dispersive covariances are non-zero (cf. Section 3.3.3). Hence, we try to conceptually separate the average profile of horizontal wind $\langle \bar{u} \rangle(z)$ from the local three dimensional wind vectors $\bar{U}(z)$.

The profiles in Fig. 4.8a show the longitudinal wind velocity $\langle \bar{u}(z) \rangle$ normalized by its value at tower top. Profiles from the three towers are compared. To allow a comparison between sites, profiles are further normalized to coincide at $z/z_h = 2$. The profiles are averaged using the procedure described in Section 3.3.3. They include selected data with neutral stability and $\bar{u}(\text{top}) > 1.0 \text{ m s}^{-1}$.

The average profile of $\langle \bar{u}(z) \rangle$ can be conceptually divided into three layers: At the bottom there is the *canyon layer*, where channelling and partially vortices result in high variability between data from different ambient wind directions, as indicated by the error bars. However, the horizontally averaged profiles from the two sites with measurements in the street canyon are surprising similar. In the middle of the street canyon, gradients are rather low, and they increase in the upper street canyon. Except, in the very lowest part ($z < 0.2z_h$), the street canyon

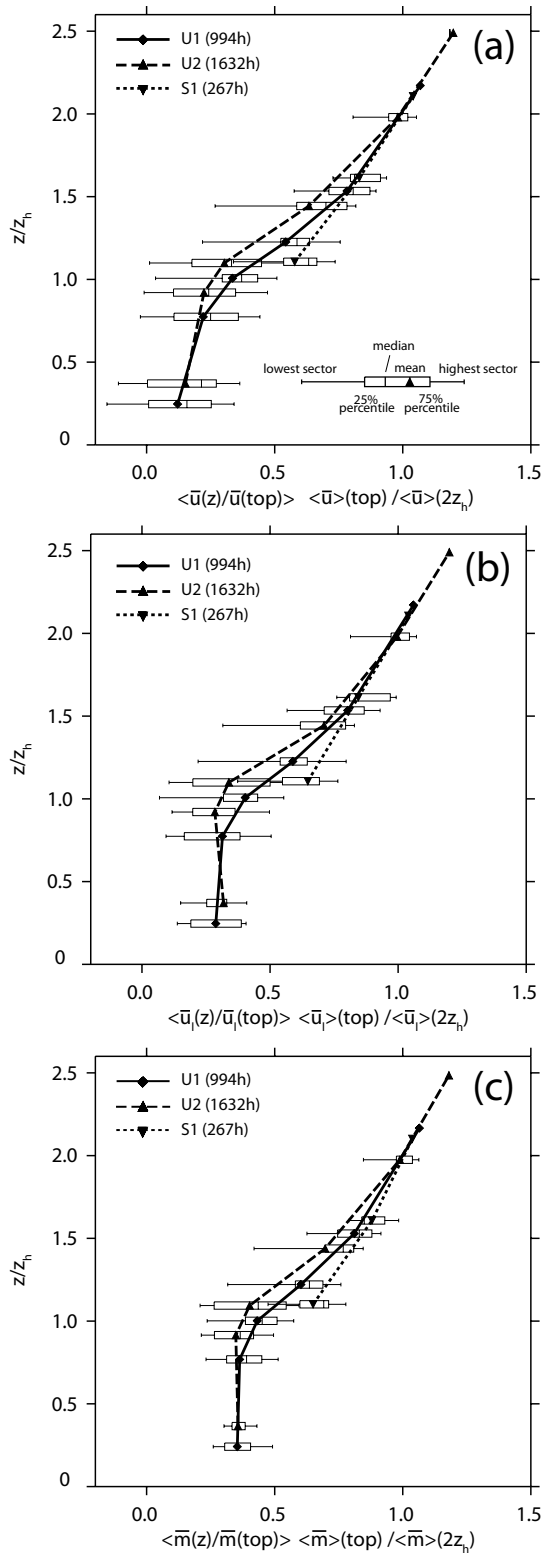


Figure 4.8: Neutral wind profiles of (a) horizontal longitudinal wind velocity $\langle \bar{u}/\bar{u}(2z_h) \rangle$, (b) local horizontal wind velocity $\langle \bar{u}_l/\bar{u}(2z_h) \rangle$ and (c) mean horizontal wind speed $\langle \bar{m}/\bar{m}(2z_h) \rangle$ at U1, U2 and S1. Data source: Sonics, hourly averages, full measurement period (differs between sites), neutral stability at tower top.

part of the profile resembles the exponential function suggested by Cionco (1965) for canopies. The *roof layer* around roof top is characterized by highest gradients due to the skimming flow over the street canyon. Similarly to profiles measured over and within plant canopies (Finnigan, 2000), an upper* inflection point is found around canopy top. The inflection point is of central interest, because it creates an instability, which further dominates turbulent exchange in this part of the roughness sublayer. In the open backyard at S1, the gradient just above roof level is less pronounced. Here, a wake interference flow is expected due to the lower building density. Finally, the *above-roof layer* is expected to approximate the well known logarithmic wind profile of the inertial sublayer.

Figure 4.8c shows the vertical profile of \bar{m} . Analogously, \bar{m} is normalized by its value at tower top and the average profiles are normalized to coincide at $z/z_h = 2$. Only data with wind $\bar{m}(2z_h) > 1.0 \text{ m s}^{-1}$ are considered. Differences between $\langle \bar{u} \rangle$ and $\langle \bar{m} \rangle$ are significant in the street canyon where lateral and vertical deviations from the wind direction at tower top are frequent. In the street canyon, the vertical profile of $\langle \bar{m} \rangle$ is nearly constant with height ($\langle \bar{m} \rangle_{\text{canyon}} \approx 0.35 \bar{m}(2z_h)$ for neutral conditions). Further, the scatter for $\langle \bar{m} \rangle$ is smaller in the street canyon, compared to $\langle \bar{u} \rangle$.

Variability — When analyzing single profiles, a variety of local features are revealed that evolve under specific conditions. These features include additional elevated inflection points, reversal of the flow direction in the street canyon, or local deflections. They are lost by the above averaging procedure.

Figure 4.9 shows six selected 3d views of the street canyon at U1. Each panel shows the average profile from the indicated wind direction and n refers to the number of observations (60 min blocks). Black dots represent the exact values at measurement heights. In between a cubic spline interpolation was performed.

Profiles with cross-canyon flow (a and b) show stronger gradients towards rooftop, and the vortex with flow from NNW results in the counter directed

* Considering the lower boundary $\bar{u} = 0$ at $z = 0$, there is a weak first inflection point in Fig. 4.8a where curvature changes from negative to positive in the lower street canyon.

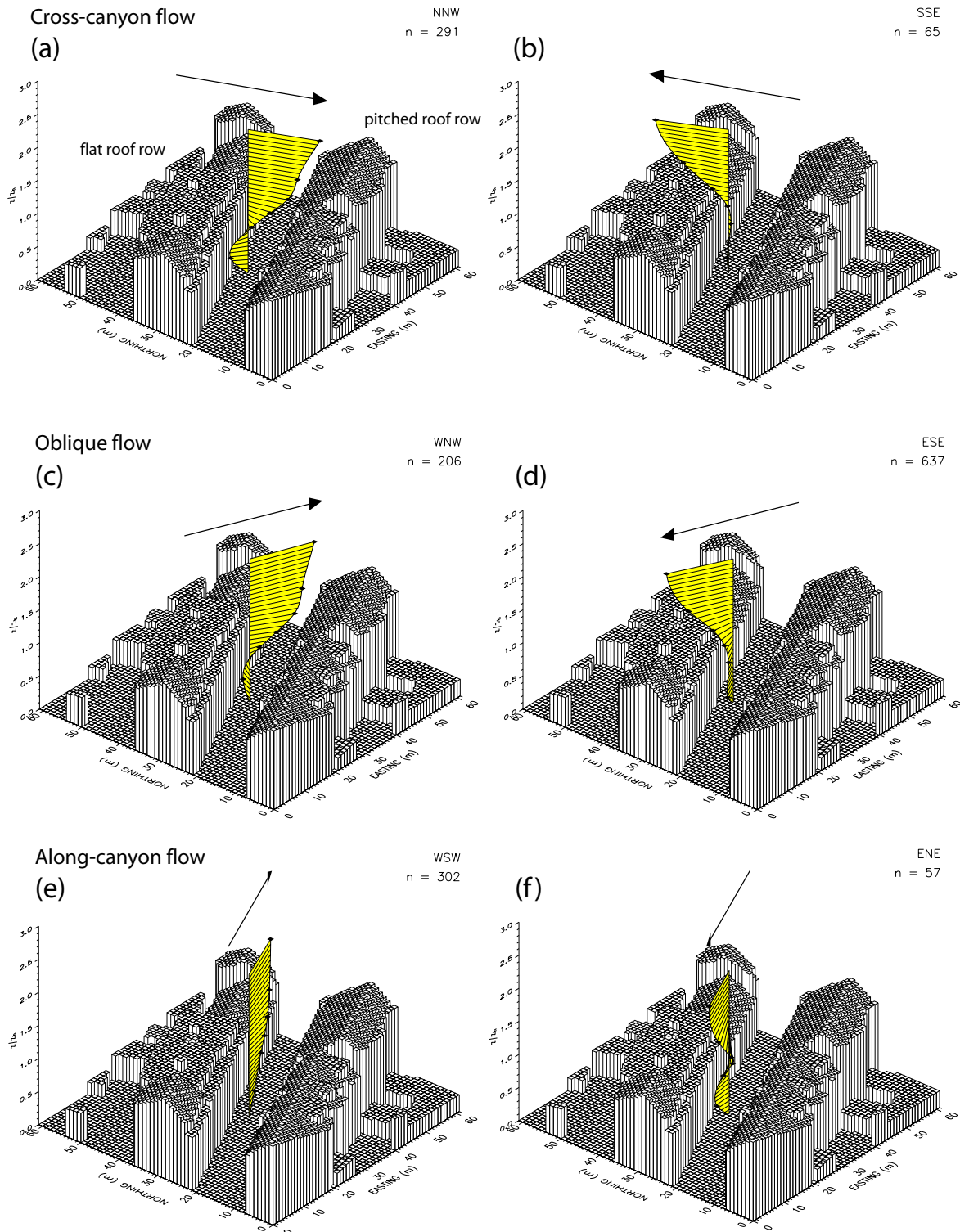


Figure 4.9: 3d visualization of the horizontal local wind velocity $\bar{u}_l(z) = (\bar{u}(z)^2 + \bar{v}(z)^2)^{1/2}$, and corresponding horizontal wind direction in the street canyon at UI for selected cases. Data source: Sonics level A to F, hourly averages, November 1, 2001 to July 15, 2002, all stabilities.

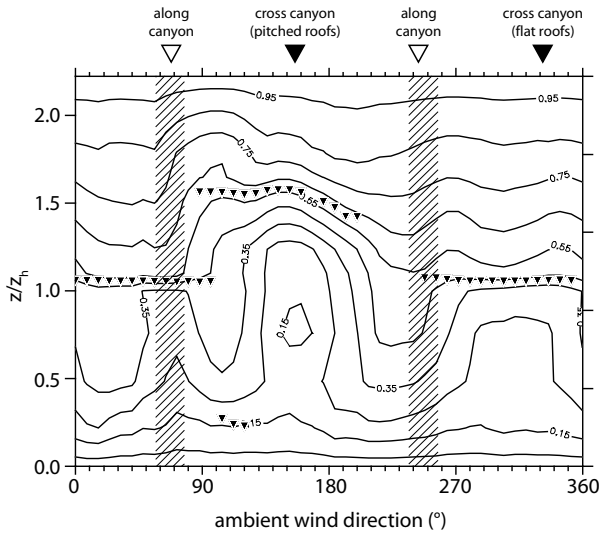


Figure 4.10: Profiles of the average scalar wind speed $\bar{m}/\bar{m}(top)$ as a function of ambient wind direction at U1. Iso-lines denote heights of similar scaled wind speed $\bar{m}/\bar{m}(top)$. The dashed areas indicate the street canyon axis. Important inflection points are marked by triangles. Data source: 12 cup anemometers, 10 min averages, November 1, 2001 to July 15, 2002, all stabilities.

flow in the street canyon. The figure illustrates the fundamental differences between flow over flat roofs and flow over pitched roofs, as already discussed in the previous section. Generally, flow over pitched roofs results in much lower wind velocities in the street canyon than flow over flat roofs. Wind tunnel results support this observation and show that vortices do not develop in canyons with pitched-roof buildings (Kastner-Klein et al., 2004). As a consequence, vertical exchange is significantly reduced during these conditions. A similar pattern can be observed for ambient wind oblique to the street canyon. Here, the situation where wind first blows over the flat roofs (c) can be interpreted as a helix-shaped vortex with an along-canyon component. Oblique flow over the pitched roofs mainly results in along-canyon channelling. The weak counter rotating secondary vortex observed for a specific sector can not be found in Fig. 4.9. The cases (e) and (f) with along-canyon flow are characterized by a nearly linear wind profile. The profile in panel (f) shows a distinct deflection into the street canyon at the third and fourth level, attributed to a very local phenomena: The next downwind building (95) is slightly higher but at measurement location, we are already above the adjacent roof (97). Further upwind, buildings of the adjacent row are even lower. With this narrowing configuration, the flow is forced to con-

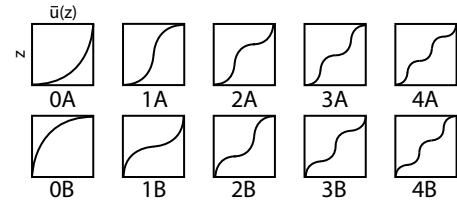


Figure 4.11: Wind profile classification with number of inflection points.

verge into the street canyon.

Figure 4.10 addresses again the same topic, but with data from the cup anemometer profile. The cup anemometer profile with its 12 levels provides an enhanced vertical resolution and highlights a region closer to the walls. Above z_h , the normalized profiles $\bar{m}/\bar{m}(top)$ show no difference between flow over the flat roof and flow in an along-canyon configuration, and the corresponding isolines are nearly parallel. Different patterns are associated with flow over the pitched roof row. Here, the inflection point is elevated and gradients are stronger. Horizontal wind speed in the middle and upper street canyon is significantly higher with along-canyon flow compared to the two cross-canyon situations. These differences vanish at pedestrian levels where \bar{m} is nearly constant with ambient wind direction.

Classification — Due to the high number of individual profiles, an automated classification was performed. The classification sorts profiles of $\bar{u}(z)$ and $\bar{m}(z)$ according to their number of inflection points and their sequence in the curvature. Figure 4.11 illustrates the notation with the number denoting the number of inflection points and the letters indicating, if the first section from ground to the first inflection point has a negative (A) or a positive (B) curvature $\partial^2 \bar{u} / \partial z^2$.

In practice, the measured profiles of $\bar{u}(z)$ and $\bar{m}(z)$ (aggregated over 10 min) were vertically interpolated by a parametric cubic spline interpolation. As a lower boundary condition, wind velocity at ground level $z = 0$ was set to zero. The upper boundary was described by minimizing tension. From the interpolation, the gradient and the curvature were calculated. Further, the number, height and sequence of inflection points were detected. The strength of inflection points is not considered. Conditions with a nearly linear wind increase with height are associ-

Table 4.3: Absolute frequency for wind profile types detected in the range $0 < z < 2z_h$. Data source: Sonics A to F (U1 and U2), 10 min averages, November 1, 2001 to July 15 2002, all stabilities.

	U1		U2	
	$n = 28635$		$n = 24298$	
	$\bar{m}(z)$	$\bar{u}(z)$	$\bar{m}(z)$	$\bar{u}(z)$
0A	0.0%	0.0%	0.0%	0.0%
1A	0.7%	0.4%	0.6%	0.2%
2A	53.3%	46.0%	16.6%	10.9%
3A	17.7%	6.2%	44.6%	24.7%
4A	27.9%	17.6%	38.2%	17.8%
0B	0.0%	0.0%	0.0%	0.0%
1B	0.0%	0.0%	0.0%	0.0%
2B	0.0%	8.4%	0.0%	2.4%
3B	0.0%	13.0%	0.0%	25.5%
4B	0.0%	4.7%	0.0%	12.7%
Others	0.4%	3.7%	0.0%	6.0%

ated with higher error-sensitivity, and small changes in the curvature may trigger artifact inflections in the interpolated profile.

For the shape of \bar{u} and \bar{m} , Tab. 4.3 separately lists the frequency of the different profile types. At U1, the most frequent type is 2A, followed by 4A. Type 2A profiles reflect the shape of the mean wind profile $\langle \bar{u} \rangle(z)$ with two inflection points (Fig. 4.8a). Type 2A profiles are similarly to the ones observed in most plant canopies. 4A are staggered wind profiles with two steps, both typically above z_h . Figure 4.13 (left) illustrates the profile classification as a function of ambient wind direction for U1. It illustrates that for the majority of flow directions, 2A is the predominant profile type. 4A-profiles are mainly observed in along-canyon flow where wind is nearly linear with height. Here, the first step corresponds to the street canyon profile, the second step is found at the canyon top, and the last one at the height of the highest pitched roofs.

For \bar{m} , no profiles of the type ‘B’ exist (Tab. 4.3). All profiles first start with a stronger gradient, which then is continuously decreasing with height in the lowest section below the first inflection point. Profiles of type ‘B’ are observed for \bar{u} , which is due to the fact that the street canyon vortex may result in a negative \bar{u} at the first measurement height. Figure 4.13 illustrates that profiles of type ‘B’ are mainly associated with flow over the flat roof from NNW where the primary vortex develops. At U2, ‘B’-

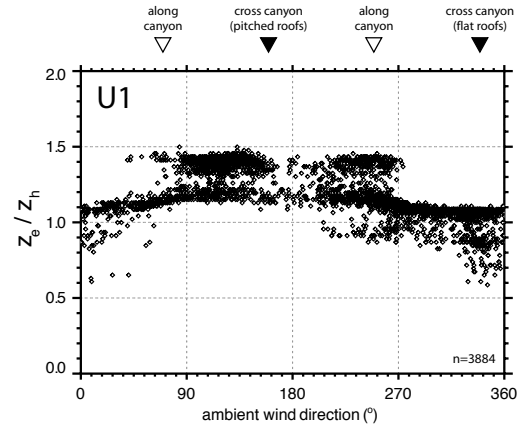


Figure 4.12: Height of the strongest inflection point in the mean wind profile z_e relative to mean building height z_h at U1 against wind direction of the ambient flow. Data source: Sonics A to F, hourly averages, November 1, 2001 to July 15 2002, all stabilities.

profiles are more frequent with cross-canyon flow from both over the pitched roof and from the backyard (not shown). These observations underline the importance of recirculations in the canopy layer.

At U1, types 1A, 3A, 0B, 2B and 4B are less frequent ($< 20\%$). They have an increasing wind gradient at the topmost section. Since the wind gradient is supposed to decrease with height in the inertial sublayer, there must be another inflection point above the topmost measurement, which is not covered by the vertical extent of the tower. In contrast, these profiles are more frequent at U2 (40%), and are mainly associated with overflow over the pitched roof which separates the profile. The roof extends up to $1.5z_h$, and it is likely that the flow at tower top is still influenced by the roof geometry.

Figure 4.13 (right) illustrates that with increasing wind velocity, profiles with simpler geometry evolve.

Height of inflection points — We define z_e^* as the height of the inflection point with the strongest local wind gradient $\partial \bar{u} / \partial z$. z_e was detected in the range $0.5z_h < z_e < 2z_h$. Figure 4.12 illustrates the height of z_e for all data available at U1. The highest frequency is found between 1 and $1.2z_h$. z_e is slightly higher with wind from the pitched

* ‘e’ stands for ‘effective building height’. The observed dissimilarity between z_h and z_e may be an indication that many low buildings do not influence the flow, since typically over roughness elements of uniform height, $z_e = z_h$ (see Section 4.2.2)

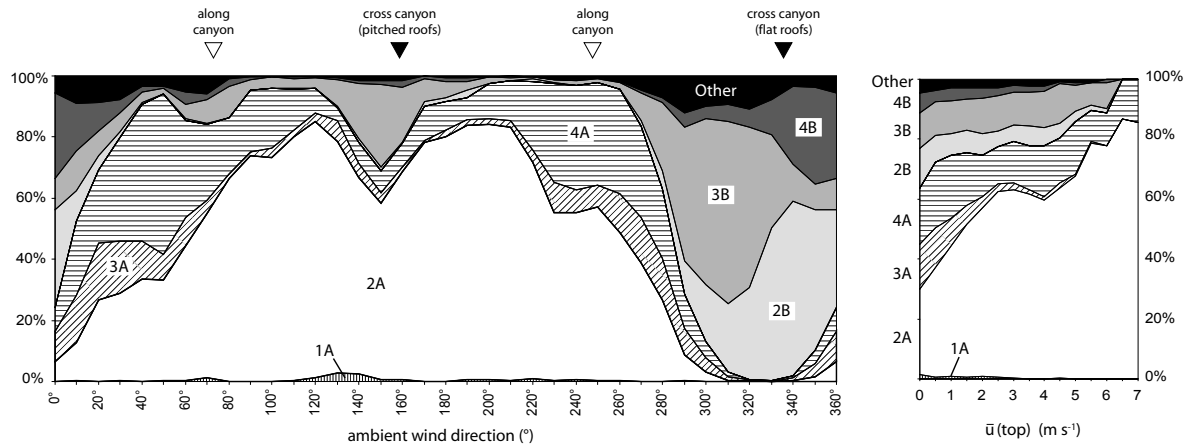


Figure 4.13: Relative frequency for wind profile types at U1 as a function of ambient wind direction (left) and wind velocity (right). Data source: Sonics A to F, hourly averages, November 1, 2001 to July 15, 2002, all stabilities.

Table 4.4: Stability classification in the present study according to the stability parameter ζ measured at tower top.

Class	Range
Convective	$-10 < \zeta \leq -0.5$
Unstable	$-0.5 < \zeta \leq -0.1$
Neutral	$-0.1 < \zeta \leq +0.1$
Stable	$+0.1 < \zeta \leq +10$

roof row. Here, another elevated group of inflection points is observed at roughly $1.4z_h$. These regions are characterized with two co-existing bands of z_e . Note that this corresponds exactly to the flow directions with highest frequency of staggered 4A-profiles (Fig. 4.13).

Stability influence — Figure 4.14 shows mean wind profiles $\langle \bar{u}(z)/\bar{u}(top) \rangle$ at U1 for different overlying stabilities measured at tower top. The stability classification used in the present work is summarized in Tab. 4.4. First of all, normalized gradients are strongest during neutral runs and decrease further with increasing instability. Stable runs do not show strongest gradients as expected. Stable stratification is measured at tower top, while simultaneously street canyon air masses are slightly unstable. Within the street canyon as well, profiles are strongest under neutral conditions and decrease with destabilization. Again, during seldom observed stable runs, gradients in the street canyon are smallest or even negative, which is due to a complete decoupling of the street canyon air masses during these low wind situations.

4.1.3 Determination of z_0 and z_d

If the roughness sublayer is not explicitly simulated in a model, i.e. if the lowest model level is higher than the roughness sublayer height, the urban surface is typically addressed by an appropriate set of zeroplane displacement z_d and roughness length z_0 . There is a number of approaches to determine z_0 and z_d from profiles of wind velocity and/or turbulence measurements (Grimmond et al., 1998). These methods typically need input data from instruments operated in the inertial sublayer and do not work correctly within the roughness sublayer. However, with increasing height, we are leaving the neighborhood scale internal boundary layer, because urban surfaces are rarely homogeneous over large areas. The question “how high is low enough?” expresses this dilemma. To investigate this problem, a method taking into account a variable Reynolds stress with height, the temperature variance method (Rotach, 1994) and a new spectral method are evaluated. Results are compared to simple rule-of-thumb expressions and empirical relationships between z_d , z_0 and surface morphometry.

Logarithmic fit with local u_* — At least three sonics were operated above mean building height z_h at all turbulence towers, U1, U2 and S1. These measurement levels at heights z_j provide all local mean vector wind velocity $\bar{u}(z_j)$ and local $u_*(z_j)$ (for the definition cf. Section 4.2.1). 30 min block averages of $\bar{u}(z_j)$ and $u_*(z_j)$ were calculated from runs that have (i) neutral stability, (ii) a continuously increas-

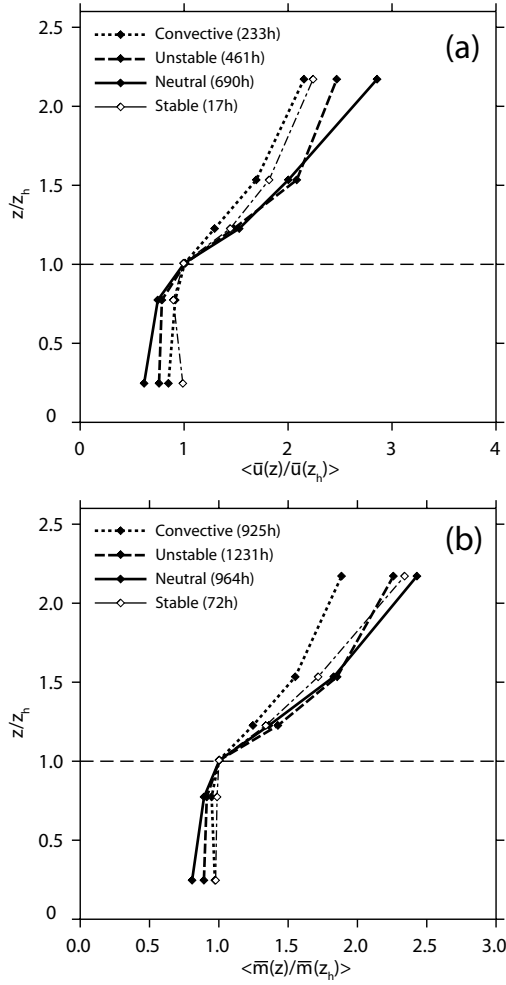


Figure 4.14: Averaged profiles of (a) mean horizontal wind velocity and (b) mean horizontal wind speed normalized by corresponding values at canopy top for different stabilities at U1. Data source: Sonics A to F, hourly median values. Only values with $\bar{u}(z_h)$ or $\bar{m}(z_h) > 0.5 \text{ m s}^{-1}$ are considered.

ing wind velocity with height, and (iii) a mean wind velocity \bar{u} at the topmost level $> 1.5 \text{ m s}^{-1}$.

The integration constant r from the logarithmic wind profile equation was evaluated for each measurement height z_j by varying the parameter d between 0 and $1.5 z_h$. The logarithmic wind profile is extrapolated down with an explicitly local $u_*(z_j)$ from each measurement level separately:

$$r(z_j, d) = (z_j - d) \exp\left(-\frac{k\bar{u}(z_j)}{u_*(z_j)}\right). \quad (4.6)$$

The variability of r determined from the three measurement heights for given d is calculated by

$$E(d) = \left(\frac{1}{N} \sum_{j=1}^N (r(z_j, d) - \{r\}(d))^2 \right)^{\frac{1}{2}} \quad (4.7)$$

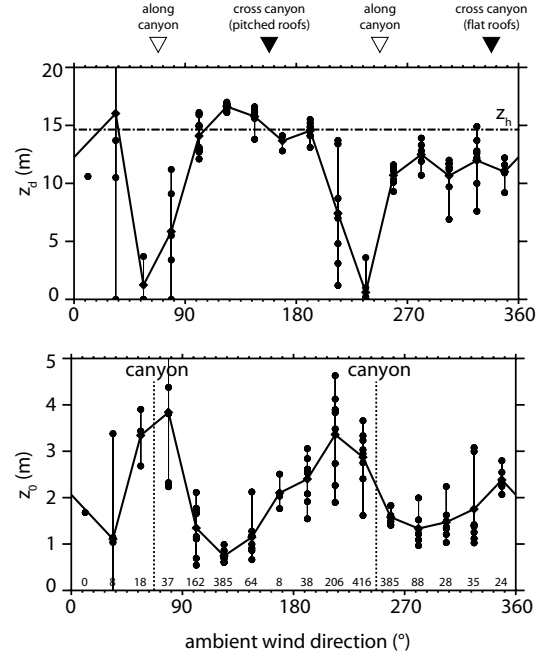


Figure 4.15: Zeroplane displacement (top) and roughness length (bottom) determined separately for different wind directions of the ambient flow at U1. Values were determined with a local u_* -fit. Symbols indicate monthly values and the thick line indicates the average value over the full year. Data source: Sonics D to F, hourly values, November 2001 to July 2002, neutral stability only. The number of runs is indicated in the lower plot separately for the different wind direction classes.

where $\{r\}$ is the average r of all measurement heights for given d ,

$$\{r\}(d) = \sum_{j=1}^N r(z_j, d). \quad (4.8)$$

The function $E(d)$ in Equation 4.7 is minimized to $E|^{min}$ by varying d . d and $\{r\}$ at its minimum are taken as the overall zeroplane displacement z_d and roughness length z_0 . The value of $E|^{min}$ is a measure of how appropriate the logarithmic law describes the profile with given z_d and z_0 .

This procedure was applied separately for 16 equally spaced wind direction sectors. The separation of the data into different wind direction classes allows the identification of surface inhomogeneities. For each wind direction sector, an individual z_d and z_0 was calculated by minimizing Equation 4.7.

Figure 4.15 illustrates the variability of z_0 and z_d for different wind directions at site U1. If we observe a cross-canyon flow, z_d is between 0.8 and $0.9 z_h$, and z_0 typically between 1 and 2.5 m . Along-canyon flows result in a very low z_d (1 – 3 m above street

Table 4.5: Spatial average z_0 and z_d determined with the logarithmic fit using local friction velocity. Data source: Sonics E to F (U1, $n=1920$ h), E to F (U2, $n=4777$ h) and A to C (S1, $n=386$ h), hourly values, full operation periods, neutral stability and $\bar{u}(\text{top}) > 1.5 \text{ m s}^{-1}$ only.

Site	$\langle z_0 \rangle$	$\langle z_0 \rangle / z_h$	$\langle z_d \rangle$	$\langle z_d \rangle / z_h$
U1	2.05m	0.14	10.8m	0.74
U2	1.41m	0.09	14.0m	0.93
S1	2.04m	0.27	1.3m	0.17

level) and a remarkably higher roughness length z_0 . Here, the logarithmic profile extends down into the street canyon and the friction at the walls additionally increases z_0 .

These sector-individual z_0 and z_d are then equally weighted averaged to a global $\langle z_0 \rangle$ and $\langle z_d \rangle$, which are a surrogate for the spatial average. The procedure results in realistic and sound estimates of $\langle z_0 \rangle$ and $\langle z_d \rangle$, which correspond to the range reported in literature and from calculations with morphometric methods.

Gempeler (1995) calculated z_0 and z_d for the site U2 with only one level of u_* at $z/z_h = 2.25$ and the profile of cup anemometers. His average values are $z_d = 14.7$ m and $z_0 = 1.78$ for the direction range 0 to 180°, and $z_d = 19.2$ m and $z_0 = 0.34$ for western flow direction over the roof (180 to 360°), where the first pair agrees with values obtained with the above method.

Temperature variance method (TVM) — The TVM uses the empiric relationship of the dimensionless temperature variance (Eq. 2.81) to solve for z_d , if $\sigma_\theta(z)/\theta_*(z)$ is measured (Rotach, 1994). Practically, the error between measured $\sigma_\theta(z)/\theta_*(z)$ and the prediction according Eq. 2.81 is minimized by varying z_d in Eq. 2.81. The method only works if the urban surface is thermally homogeneous and z_d is the same for momentum and temperature exchange.

The TVM method has been applied to all above roof levels at the profile towers. Results were calculated once with classical surface layer values, and once with the urban modified values proposed by Roth (2000) (Tab. 2.1). Values of z_d from the topmost levels are summarized in Tab. 4.6. Unfortunately, the determined values are highly unrealistic, and in

Table 4.6: Zeroplan displacement determined by the temperature variance method. Data source: Sonics F (U1), F (U2) and C (S1), hourly averages, June 10 to July 10, 2002, unstable cases only.

Site	z/z_h	$\langle z_d/z_h \rangle_{SL}$	$\langle z_d/z_h \rangle_{urban}$	n
U1	2.17	2.06	1.98	575
U2	2.49	2.22	2.09	560
S1	2.11	1.89	1.41	433

the majority of cases $z_d(\text{TVM}) > z_h$. Also, the introduction of the urban values does not significantly decrease z_d .

There are several explanations for this failure. First, the thermal roughness of the present urban surfaces may be higher than the roughness of momentum. Secondly, low-frequency contributions produced in larger scales (inactive turbulence) may enhance σ_θ , which do not scale with surface exchange. The long averaging period over 60 min and the fact that no detrending was applied may support the overestimation. The most important reason for the failure of the TVM is the fact that temperature variance is vertically relocated, i.e. the import by turbulent transport $w'\theta'^2$ at this height is stronger than in the surface layer. Excess temperature variance from lower regions affects the sensors at tower top. Hence, temperature variance can not be described by local production of variance. Interestingly, and this supports the latter explanation, the TVM results in significant better estimates closer to z_h where temperature variance is exported (see Section 4.4.1). At U1, the estimates of $z_d(\text{TVM})$ are 0.87, 0.91 and 1.31 times z_h for $z/z_h = 1.01, 1.23$ and 1.53 (urban values).

Feigenwinter (2000) reported from a measurement tower located 400 m to the south-east of U1 in 1995/96 that the TVM applied to levels closer to z_h provided realistic estimates of z_d . But his topmost measurement at $z/z_h = 3.2$ resulted in similar unrealistic values for z_d . Grimmond et al. (1998) found the TVM only useful at one of four sites investigated. Hence, we seek for a more suitable alternative, which is neither affected by inactive turbulence nor by vertically relocated temperature variance.

Spectral method — Spectral analysis of the wind velocity components provides an independent approach to determine z_d . The spectral method introduced and tested here uses the fact that peak fre-

Table 4.7: Spatial average of z_d determined from peak frequencies of u , v , w and θ - power spectra. Data source: Sonics F (U1), F (U2) and C (S1), hourly averages, June 10 to July 10, 2002, neutral cases only.

Site	U1	U2	S1
n	821	2123	302
$\langle z_d(n_{\max}(u)) \rangle$	13.3 m	15.3 m	6.3 m
$\langle z_d(n_{\max}(v)) \rangle$	12.0 m	15.2 m	5.0 m
$\langle z_d(n_{\max}(w)) \rangle$	11.8 m	13.0 m	3.5 m
$\langle z_d(n_{\max}(u)) \rangle / z_h$	0.91	1.01	0.84
$\langle z_d(n_{\max}(v)) \rangle / z_h$	0.82	1.01	0.67
$\langle z_d(n_{\max}(w)) \rangle / z_h$	0.81	0.86	0.47

quencies of neutral power spectra $n_{\max}(u)$, $n_{\max}(v)$ and $n_{\max}(w)$ scale only with height above zero-plane displacement. This height dependent shape of spectra is known from surface layer scaling, but has also been observed above a number of plant canopies, provided that the measurement location is far enough above the surface i.e. in the inertial sublayer. The neutral limits of normalized peak frequencies seem to be fairly constant in the inertial sublayer above all types of surfaces, with values of $n_{\max}(u) = 0.08$, $n_{\max}(v) = 0.22$ and $n_{\max}(w) = 0.55$ (Kaimal and Finnigan, 1994).

n_{\max} is defined as the natural peak frequency f_{\max} scaled by a scaling length $(z - z_d)$ and mean wind velocity \bar{u} . This is used to solve for z_d from the measured peak frequencies f_{\max} of a large ensemble of neutral power spectra by

$$z_d = z - \frac{n_{\max} \bar{u}}{f_{\max}}. \quad (4.9)$$

Peak frequencies f_{\max} were determined with a polynomial fit through spectra, namely

$$f_{\max} = \exp\left(-\frac{c_1}{2c_2}\right) \quad (4.10)$$

with

$$\log(fS(f)) = c_2 \log f^2 + c_1 \log f + c_0. \quad (4.11)$$

Estimations of z_d by the spectral method are encouraging, and values are summarized in Tab. 4.7 for the topmost measurement levels and separately for the spectra of u , v and w . The spectra of w result in most realistic estimates, which is supported by the fact that fluctuations in w are uniquely determined by near-field surface processes, and u and v incorporate — like θ — inactive turbulence from far field

Table 4.8: Ratio between zeroplane displacement z_d and mean building height z_h calculated with different morphometric approaches.

	U1	U2	S1
Kutzbach (1961)	0.84	0.75	0.69
Counihan (1971)	0.73	0.48	0.36
(Raupach, 1994)	0.62	0.59	0.45
Macdonald et al. (1998)	0.79	0.63	0.53
Kastner-Klein and Rotach (2004)	0.92	0.81	0.71
Jackson (1981)	0.90	0.78	0.70

processes. This explains the higher z_d values determined from spectra of u and v compared to w . Close to the roofs, the method fails. Here, length scales of turbulent fluctuations are no longer depending on height above z_d (cf. Section 4.3.1).

Morphometric methods — If z_d would be unknown from measurements, it could be estimated using morphometric parameters of the urban surface. For an increasing number of cities, authorities provide digital 3d building data sets, which are a powerful tool for the analysis of urban surface forms. Such high resolution models can provide detailed measures of three dimensional parameters. Many empirical relations are described in literature to relate morphometric parameters to aerodynamic properties of the urban surface. A comprehensive overview of methods is presented in Grimmond and Oke (1999a).

For the present calculations, morphometric input data were deduced from a high resolution digital building model with 1 m raster size and for a circle of 250 m around the sites (cf. Tab. 3.3). Table 4.8 presents calculated values of z_d for three urban surfaces. The method of Jackson (1981) determines z_d from a combination of measured profiles of Reynolds stress and morphometric parameters. The given values are calculated from neutral runs according the formulation in Kastner-Klein and Rotach (2004).

Many empiric relationships between morphometry and flow are the result of extensive wind tunnel studies. In most wind tunnel studies, regular arrays of obstacles are investigated and related to the measures of building breadth x_b and canyon width x_c . For the urban surface, these measures are not avail-

able, and are replaced by *characteristic length measures*. The characteristic measures were calculated using geometric methods. For U1 and U2, the assumption that the surface represents infinitely long canyons gives the most realistic assumption. These values and the corresponding formulas are summarized in Tab. 3.3.

4.1.4 Summary

- The mean wind profile is conceptually divided into three regions: At bottom there is the *canyon layer*, where channelling and partially vortices result in high variability between data from different ambient wind directions. The street canyon wind profile shows similarities to an exponential profile. The *roof layer* around roof top is characterized by strongest gradients, and an inflection point is found in the region $1 < z/z_h < 1.4$. Finally, the *above-roof layer* approximates the logarithmic wind profile of the inertial sublayer.
- The various definitions of mean wind, namely $\langle \bar{u} \rangle(z)$, $\langle \bar{u}_l \rangle(z)$ and $\langle \bar{m} \rangle(z)$, result in distinctly different profiles, especially within the street canyon. For applications in dispersion modelling, it is highly recommended to use $\langle \bar{u} \rangle$, since only this vector component in its global frame of reference allows a correct calculation of a (horizontally) averaged longitudinal advection within a given height layer.
- It is no surprise that the individual wind profiles are strongly determined by the direction of the ambient wind relative to the street canyon: flow channelling increases continuously with decreasing height. Flow perpendicular to the street canyon is characterized by strong gradients at rooftop whereas the profile in along-canyon flow is nearly linear with height.
- Roof shape is an important factor determining flow in canyons. Flow over flat roofs results in a clear primary vortex in the street canyon and is characterized by higher wind speed at street level. Flow over pitched roofs results in low wind speed in the street canyon and no clear vortex develops.
- The observed vortex at U1 is intermittent, and only found in the average wind field. The high-

frequency flow is uncorrelated with processes above roofs, indicating that intermittency is mainly driven by Kelvin-Helmholtz instabilities.

- For the dense urban surfaces, z_d is higher compared to flexible plant canopies where the rule-of-thumb is typically $2/3z_h$. The higher urban values of z_d can be attributed to the stiffness of the urban surface, which prevents the mean flow to penetrate deep into canyons. At U1 and U2, z_d is in the order of 0.8 to $0.9z_h$. For the suburban surface, $z_d = 0.6z_h$ is suggested, but a high variability is found between different methods.
- The less dense suburban surface at S1 ($\lambda_P = 0.28$) shows a higher roughness length of $z_0 = 0.3z_h$ compared to the two dense urban surfaces ($\lambda_P = 0.54$ at U1 and 0.37 at U2) with a z_0 in the order of $0.1z_h$.

4.2 Momentum exchange

In this chapter, momentum transfer in the urban roughness sublayer is addressed. After introductory definitions (Section 4.2.1), the vertical profile of turbulent momentum transport and its parameterization is discussed in Section 4.2.2 and 4.2.3, respectively. Further, in Section 4.2.4, structures contributing to turbulent momentum transfer are analyzed with the help of quadrant analysis. Finally, in Section 4.2.5, the magnitude of the dispersive stress is estimated.

4.2.1 Definitions and restrictions

A main characteristic of the urban roughness sublayer is a profile of turbulent momentum transport, which is not constant with height (Rotach, 1999). To account for this, the notation $u_*(z)$ denotes explicitly height-dependent local values in the present study. A global *friction velocity* is only valid within the inertial sublayer and is denoted $u_*(IS)$.

Further, local wind direction at any height can differ from the direction at tower top. Therefore, the classical surface-layer calculation of u_* (Eq. 2.67) is extended by taking into account local lateral contributions from $\overline{v'w'}$:

$$u_*(z) = \left(\overline{u'w'^2}(z) + \overline{v'w'^2}(z) \right)^{1/4}. \quad (4.12)$$

The two covariances $\overline{u'w'}$ and $\overline{v'w'}$ incorporate the total turbulent transport of horizontal momentum. Unfortunately, in the street canyon, values of $\overline{u'w'}$ and $\overline{v'w'}$ are not only affected by vertical transport of horizontal momentum, but also contaminated by local horizontal transport of vertical momentum in direction towards the walls. There is no possibility to separate these effects without having lateral and longitudinal gradients simultaneously measured. Hence, the local three dimensional turbulent momentum transport is not covered by the one-dimensional parameter $u_*(z)$.

However, in the horizontally averaged view, positive and negative horizontal turbulent transport is assumed to counterbalance.

Table 4.9: Frequency f for each of the measurement levels at U1, U2 and S1 to measure highest $u_*(z)$ in the profile. Data source: All sonics, full operation periods, all stabilities.

U1		U2		S1	
$n=3752h$		$n=4416h$		$n=595h$	
z/z_h	$f(\%)$	z/z_h	$f(\%)$	z/z_h	$f(\%)$
2.17	19.3	2.49	23.1	2.11	51.3
1.53	61.5	1.98	9.8	1.61	36.8
1.23	11.9	1.44	58.6		
1.01	4.4	1.10	5.4	1.11	11.9
0.77	1.1	0.92	2.9		
0.25	1.7	0.37	0.3		

4.2.2 Vertical profile of Reynolds stress

At U1 and U2, the vertical profile of u_* (Fig. 4.16a) is characterized by a maximum well above z_h and by a strong reduction with height below. This agrees qualitatively with previous urban full-scale studies (Rotach, 1991; Oikawa and Meng, 1995; Feigenwinter et al., 1999). Also at S1, $u_*(z)$ decreases with height, but the limited vertical resolution does not allow an identification of a clear maximum. The upper two levels indicate a nearly constant Reynolds stress with height.

Rotach (2001) suggests that the height of maximum $u_*(z)$ may be used as a definition for the roughness sublayer height over urban areas. Further, its value referred to as u_*^{max} , can be regarded the basis for a velocity scale for the whole roughness sublayer. Its magnitude is interpreted as the result of the total drag the surface exerts on the ambient flow.

Height of maximum u_* — In the present work, the height of maximum $u_*(z)$ is denoted z_f and is not mandatorily equal to the blending height z_* (which may be different for momentum exchange, scalars, and flux densities of mass and heat). The blending height z_* is defined as the height where influences from single roughness elements vanish, and hence for a parameter a , the height where $\langle \bar{a} \rangle = \bar{a}$. Wind tunnel results from the modelled city surface around U1 show that horizontal inhomogeneities are measurable up to a height of $3.5z_h$ (Feddersen et al., 2004). The blending height z_* is rather a gradual transition and difficult to define whereas z_f can be easily determined from the profiles.

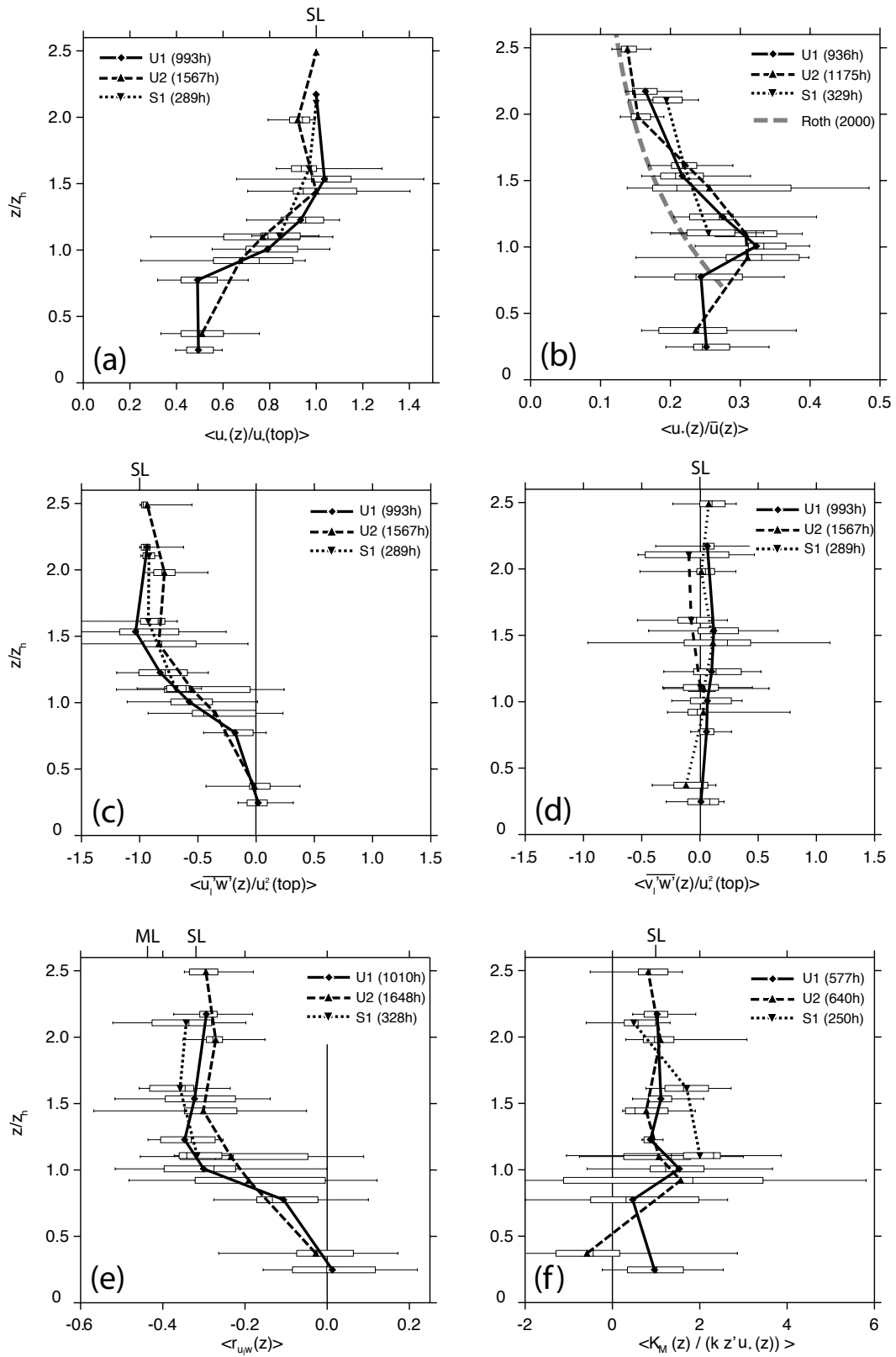


Figure 4.16: Vertical profiles of (a) $\langle u_*(z)/u_*(\text{top}) \rangle$, (b) $\langle u_*(z)/\bar{u}(z) \rangle$, (c) $\langle \overline{u'_1 w'} / u_*^2(\text{top}) \rangle$, (d) $\langle \overline{v'_1 w'} / u_*^2(\text{top}) \rangle$, (e) $\langle r_{uw} \rangle$ and (f) $\langle K_M / k z' u_*(z) \rangle$ at all three profile towers. SL and ML denote the surface layer and the mixing layer values, respectively. Error bars in this and subsequent figures are defined in Fig. 4.8. Data source: All sonics, hourly averages, full operation periods, neutral stability only.

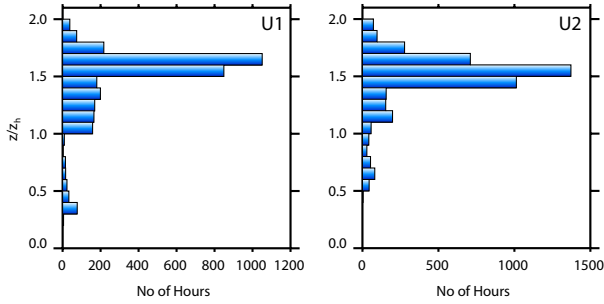


Figure 4.17: Histograms of the height of u_*^{max} at the two urban profile towers. Data source: Sonics A to F at U1 and U2, hourly averages, November 1, 2001 to July 15, 2002, all stabilities and all wind directions.

Table 4.9 lists the relative frequency of u_*^{max} to be measured at the different tower levels. If highest $u_*(z)$ is found at tower top, there is evidence for an elevated u_*^{max} that is above tower top, and not captured by the present setup. If $u_*(z)$ decreases from the fifth to the topmost measurement level, there is no second maximum assumed above the highest tower level. In that case, the maximal $u_*(z)$ in the profile corresponds to u_*^{max} . Highest frequency for u_*^{max} is measured at U1 at $z/z_h = 1.53$, and at U2 at $z/z_h = 1.44$. There are nearly no runs where u_*^{max} is found at z_h or even in the street canyon. At S1, the majority of runs show highest u_*^{max} at tower top. There is a remarkable number of profiles with u_*^{max} at the middle level ($z/z_h = 1.61$). These situations are associated with wind from sector N to E. Flow from this direction overflows an adjacent building row with pitched roofs reaching up to roughly same height (see Fig. 3.10).

To determine z_f with enhanced vertical resolution, a parametric cubic spline interpolation was performed through all individual profiles of $u_*(z)$ at U1 and U2. The interpolation is similar to the procedure described for mean wind in Section 4.1.2. The actual height of z_f was calculated as the height where the interpolated $u_*(z)$ shows its maximum, and hence is somewhat influenced by the vertical resolution of the instruments and the parameters of the interpolation. Runs where maximal $u_*(z)$ was determined above $z/z_h = 2$ were removed from analysis. This affected approximately 20% of all data. Figure 4.17 illustrates the histogram for z_f in the range 0 to $2z_h$. Data include all wind directions, all wind velocities and all stabilities at both urban towers. Highest frequency for u_*^{max} is found at $z/z_h = 1.6$ at U1 and at $z/z_h = 1.5$ at U2. The height is sur-

prisingly constant for different flow directions. The value $z_f = 1.55z_h$ is taken for all three profile towers, all stabilities and all wind directions in the subsequent analysis. There are local features that alter this height. For example, wind over the flat roof at U1 results in a small number of profiles that show their u_*^{max} at roughly $1.1z_h$. z_f is neither sensitive to wind velocity nor to ambient stability.

Above z_f , most profiles are characterized by a slight reduction of $u_*(z)$ to the topmost measurement level. This decrease is in the order of 10 to 15% at U1 and U2, but not found at S1. The magnitude of $\partial u_*/\partial z$ is significantly lower above z_f compared to gradients below. Hence, the region above z_f can be approximated by a constant $u_*(z)$ with height. This is an indication for the transition to the inertial sublayer, as suggested by Rotach (2001) and Kastner-Klein and Rotach (2004)

Relations to morphometry — The roughness sublayer below the highest roughness elements corresponds to a less permeable layer where momentum is absorbed by form and viscous drag. In contrast to plant canopies, the characteristic pattern of permeable and non-permeable regions is dominated by larger structures in the order of the characteristic length scale \mathcal{L} (Tab. 3.3) in the urban canopy. \mathcal{L} corresponds roughly to the size of repetitive building-blocks. The plane mixing layer analogy is therefore not suitable per se.

With stationary and horizontal homogeneous conditions on the neighborhood scale, and with a negligible horizontal pressure gradient, the simplified horizontally averaged equation of motion (Eq. 2.51) results in (Raupach and Shaw, 1982):

$$\frac{\partial \langle \overline{u'w'} \rangle}{\partial z} + \frac{\partial \langle \overline{u''w''} \rangle}{\partial z} = -\frac{1}{\rho} \langle \frac{\partial \overline{p''}}{\partial x} \rangle + f_v. \quad (4.13)$$

Hence, the observed negative $\partial \langle \overline{u'w'} \rangle / \partial z$ can be attributed to either a positive *dispersive stress divergence* (second term), canopy drag due to the non-hydrostatic pressure field around obstacles (*form drag*, third term) or the effect of *viscous drag* (f_v). Rotach (1991) concluded that for an urban street canyon, f_v can be neglected. The third term is relevant in a layer that incorporates building volumes. Typically, windward walls of buildings show a positive, leeward walls a negative $\overline{p''}$, and hence,

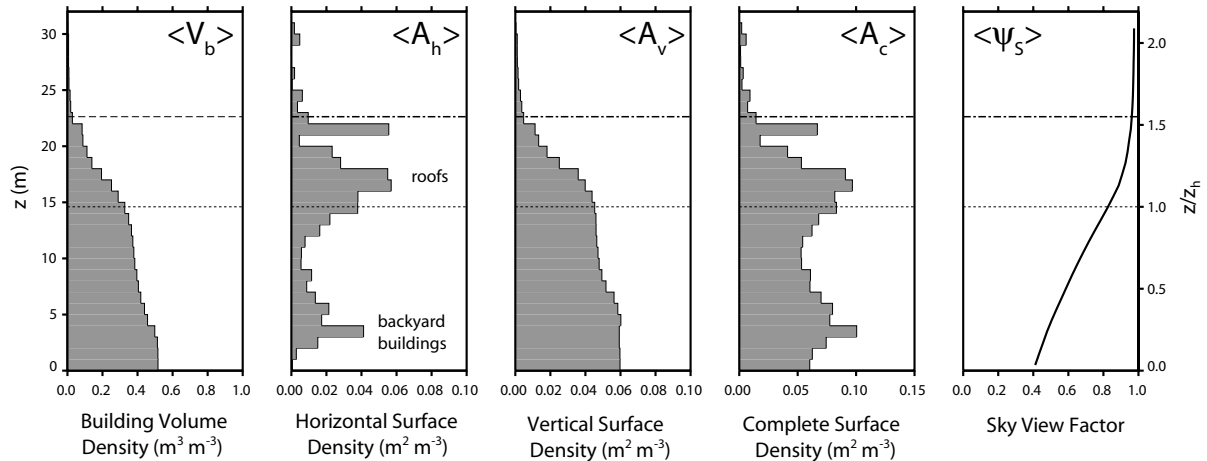


Figure 4.18: Vertical profiles of morphometric properties of the surface in a 250 m circle around the tower U1. The average sky-view factor $\psi_s(z)$ was calculated for all open spaces at given height z taking local horizon angles into account. The dash-dotted line denotes the height of u_*^{max} . The dotted line indicates the average buildings height z_h . Data source: High-resolution digital building model, 1 by 1 m horizontal resolution, provided by GVA Basel-Stadt.

$\langle \partial \bar{p}'' / \partial x \rangle$ is positive. Note that \bar{p}'' is not constant at the air-building interface. As a consequence, the commutation of the horizontal averaging operator and the horizontal spatial differentiation operator is not allowed (see Section 3.3.3). The influence of the dispersive stress divergence $\partial \langle \bar{u}'' \bar{w}'' \rangle / \partial z$ will be addressed later in Section 4.2.5.

Wind tunnel experiments with obstacles of uniform height show their u_*^{max} directly at z_h (Macdonald, 2000; Cheng and Castro, 2002). Analogous, in many plant canopies with uniform height, a decrease in $u_*(z)$ is only found below z_h (Kaimal and Finnigan, 1994). Why do we find an elevated u_*^{max} over urban surfaces?

The term $\langle \partial \bar{p}'' / \partial x \rangle$ in Eq. 4.13 can be only non-zero, if there are solid roughness elements present at a given height layer z . Hence, an important aspect is the definition of z_h . In urban areas, the mean building height z_h is calculated as the plan-area-weighted average roof height of the surface fraction occupied by individual buildings, regardless of whether roofs are high-rise or even below z_d . In contrast, in canopies with a nearly uniform height, such as many forests, z_h is equal or close to the height of the highest obstacles. In most calculations, for example understorey scrubs and young trees in a forest are not incorporated. In contrast, in an urban canopy, single storey buildings in backyards (commercial buildings, garages) lower the average z_h , but aerodynamically, they are not important. Martilli et al. (2002) demonstrated in numerical experiments with non-

uniform roof heights that u_*^{max} will occur above z_h , and that the exact height depends on the standard deviation of the building height distribution. Britter and Hanna (2003) suggest that the height of u_*^{max} corresponds to the height of the highest obstacles extending into the urban roughness layer.

Figure 4.18 shows vertical profiles of morphometric properties of the surface at site U1. There are numerous building obstacles present above the average z_h . These obstacles result in a non-zero form drag term, and as a compensation, $\partial \langle \bar{u}' \bar{w}' \rangle / \partial z$ becomes negative in these height layers. At the present sites, these initial roughness elements are mainly formed by the higher pitched roofs. Further, exposed roofs form an initial point for the development of local shear layers. The height of the prominent obstacles can be interpreted analogously to the location of the splitter plate in the classical wind tunnel plane mixing layer, where low (canyon) and a high-speed flow are initially separated, and instabilities evolve behind.

In an urban canopy with non-uniform building height, the above definitions of z_h allows form drag to start well above z_h whereas in a canopy with uniform height, it can be only non-zero below z_h . In extreme cases, the above definition of z_h in urban environments would even justify that $z_d > z_h$.

Contributions from $\overline{v'w'}$ to u_* — If the local coordinate system is rotated by a single rotation around the z -axis into local horizontal mean wind veloc-

Table 4.10: Relative difference between u_* calculated with locally rotated $\overline{u_l'w'}$ only (u_*^{lon}) and with taking lateral contribution into account (Eq. 4.12, u_*^{both}), expressed as $\Delta = (\langle u_*^{both} \rangle - \langle u_*^{lon} \rangle) / \langle u_*^{both} \rangle$. Data source: All sonics, full operation periods, neutral stability.

U1		U2		S1	
$n=3733h$		$n=5249h$		$n=679h$	
z/z_h	$\Delta(\%)$	z/z_h	$\Delta(\%)$	z/z_h	$\Delta(\%)$
2.17	4.1	2.49	5.4	2.11	5.5
1.53	6.1	1.98	7.0	1.61	3.2
1.23	6.3	1.44	15.7		
1.01	8.6	1.10	7.8	1.11	6.5
0.77	12.0	0.92	11.6		
0.25	26.0	0.37	24.7		

ity at given height, we retrieve $\overline{u_l'w'}$ and $\overline{v_l'w'}$ (Fig. 4.16c and d). In single profiles, we often do not find $\overline{v_l'w'}$ to be zero, as it is supposed in the surface layer. The magnitude of $|\overline{v_l'w'}|$ compared to $|\overline{u_l'w'}|$ is small at tower top. At $z/z_h = 1$, the contribution to u_* is typically in the order of 10%, and at street level — where overall $u_*(z)$ are small — in the order of 25% (Tab. 4.10). These non-zero values are either caused by a rotation of the wind direction with height as an effect of flow-channelling into the street canyon (re-visit Fig. 4.1) or by contamination from lateral flux densities of vertical momentum.

The sign of v_l' and hence $\overline{v_l'w'}(z)$ does not reveal the direction of the associated Reynolds stress. In Eq. 4.12, we implicitly assume momentum to be transported towards the surface. The profile of mean horizontal wind velocity justifies this, and there is no change of sign in $\partial\langle\bar{u}\rangle/\partial z(z)$. Hence, in a horizontally averaged view, momentum has to be transported downwards in the whole vertical profile.

In the horizontally averaged view, negative and positive $\overline{v_l'w'}$ counterbalance each other, assuming that right-handed and left-handed rotations with height are of the same frequency. Indeed, the horizontally averaged profile of $\langle\overline{v_l'w'}\rangle$ in Fig. 4.16d is close to zero, and only $\langle\overline{u_l'w'}\rangle$ is relevant. The incorporation of $\overline{v_l'w'}$ in the calculation of $u_*(z)$ according to Eq. 4.12 does not nullify these contributions. Due to the square, any non-zero $\overline{v_l'w'}$ is assumed to enhance the Reynolds stress in direction towards the surface. Strictly spoken, u_* must be seen as the upper limit of the turbulent transport of horizontal momentum,

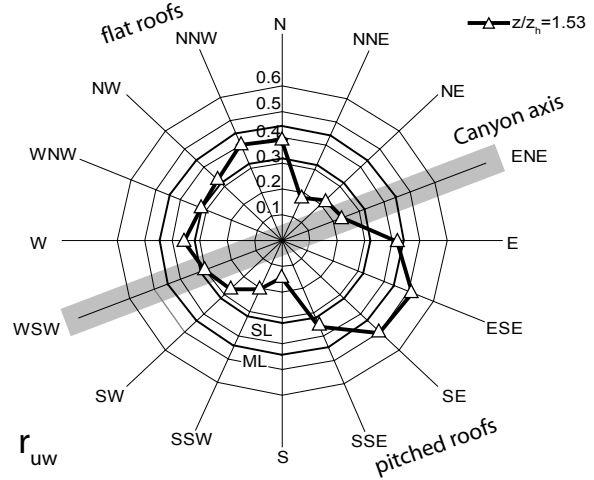


Figure 4.19: Neutral correlation coefficient r_{u_1w} in dependence on ambient wind direction at $z/z_h = 1.53$ at U1. SL and ML denote the surface layer and the mixing layer values, respectively. Data source: Sonic E, hourly average values, November 1, 2001 to July 15, 2002, neutral stability only, $n=1010$ h.

and

$$\left(\langle\overline{u_l'w'}\rangle^2 + \langle\overline{v_l'w'}\rangle^2\right)^{0.25} \leq \left(\langle\overline{u_l'w'^2} + \overline{v_l'w'^2}\rangle\right)^{0.25}. \quad (4.14)$$

Efficiency — The correlation coefficient (Eq. 2.8) is a measure of the efficiency of turbulent exchange. At street level, u_l and w are completely uncorrelated (Fig. 4.16e). With increasing height in the street canyon, $\langle r_{u_1w} \rangle$ becomes relevant and its maximum is typically found at $1.25z_h$ (U1) and at $1.45z_h$ (U2). The horizontally averaged profile is nearly constant with height above z_h and close to the surface layer prediction of -0.32 in the upper levels.

Individual profiles from different wind directions reveal a consistent pattern, illustrated for U1 in Fig. 4.19. The figure shows r_{u_1w} at an above-roof level ($z/z_h = 1.53$) at U1. Small r_{u_1w} are found for along-canyon flow. With this flow configuration, the magnitude of r_{u_1w} is around -0.25 at all heights above z_h . This indicates a low efficiency, which is even below the surface layer prediction. The pattern is different for cross-canyon flow. Here, strong correlations up to -0.5 are measured, exceeding even proposed plane mixing layer values. In the individual profiles, the highest magnitude of r_{u_1w} ($r_{u_1w}^{max}$) is found in profiles with flow over the pitched roofs at $z/z_h = 1.5$ (-0.52) and at $z_h = 1.0$ (-0.41) for flow over the flat roofs. At street level, r_{u_1w} is slightly positive for situations with a vortex (not

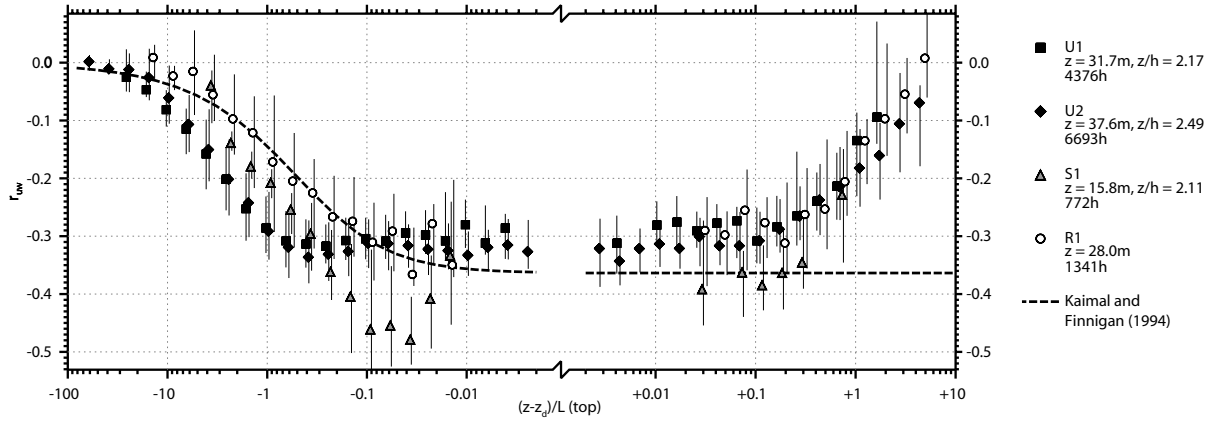


Figure 4.20: Stability dependence of r_{uw} at the towers U1, U2 and S1 in comparison to the rural surface layer at R1. Data source: Sonics F (U1), F (U2), C (S1) and A (R1), full operation periods.

shown). Here, higher longitudinal fluctuations are correlated with an upwind. At S1, several regions of higher $r_{u'w'}^{max}$ (on average, up to -0.55) are associated with upwind flow over exposed pitched roofs in this neighborhood.

In plant canopies, $r_{u'w'}^{max}$ is typically found directly or even below z_h (Raupach et al., 1996; Kruijt et al., 2000; van Gorsel et al., 2003). The urban roughness sublayer shows an elevated $r_{u'w'}^{max}$, which is found distinctly above z_h , around z_f . This may be regarded again an effect of the definition of z_h .

Figure 4.20 illustrates the stability dependence of r_{uw} for the topmost measurements at U1, U2, S1 and R1. The magnitude of $\overline{u'w'}$ decreases with decreasing stability, while simultaneously σ_u and σ_w are enhanced by buoyancy. In the surface layer, r_{uw} can be predicted by the empirical functions for the standard deviations, A_u and A_w (Eq. 2.81) by

$$r_{uw}(\zeta) = (A_u(\zeta)A_w(\zeta))^{-1}. \quad (4.15)$$

In unstable conditions, applying the SL-values for A_u and A_w (dashed line) leads to a good agreement with rural values at R1. At the urban sites however, r_{uw} is above the prediction in neutral conditions, and lower (stronger correlation) during unstable runs. This cannot be an effect of the scaling height. A reduction of the local stability by a factor 0.1 would be needed to bring the curves to an overlap. The difference is attributed to non-local transport of velocity variance, which vertically relocate $\overline{u'^2}$ and/or $\overline{w'^2}$. To seek for possible explanations, we need to look at higher order moments of type $\overline{u_i'^2 u_j'}$ for $i, j = \{1, 3\}$ (see Sections 4.2.4 and 4.3.3).

4.2.3 Parameterization of Reynolds stress

Drag coefficient — Many practical applications simply use the drag coefficient $C_D = (u_*/\bar{u})^2$, which is inherently related to the wind profile. Figure 4.16b shows profiles of the square root of C_D , $\langle u_*(z)/\bar{u}_l(z) \rangle$ for all three profile towers. Highest values are found at both urban stations between $z/z_h = 0.8$ and 1.0 , and are up to 0.33 on the horizontal average in this region. From the integration of the neutral logarithmic wind profile (Eq. 2.71), we rewrite

$$C_D^{1/2} = u_*(z)/\bar{u}(z) = \frac{k}{\ln((z - z_d)/z_0)}. \quad (4.16)$$

This relation is expressed in Fig. 4.22. Note that values in this graph are not independent, since both, z_d and z_0 , are already based on the neutral wind profile itself. In all above roof measurements, $C_D^{1/2}$ follows the prediction, but is larger than the calculated line. Close to the roofs, values drop off. In the roughness sublayer, local $u_*(z)$ is larger than values in the inertial sublayer, which corresponds to the region of u_*^{max} . With decreasing height towards roofs, u_* decays and $u_*(z)/\bar{u}(z)$ becomes smaller.

Based on a review of different urban data sets, Roth (2000) suggests an empirical fit of the form

$$u_*(z)/\bar{u}(z) = c_0 + c_1 \exp(c_2(z/z_h)) \quad (4.17)$$

where $c_0 = 0.094$, $c_1 = 0.353$ and $c_2 = 0.094$. This fit is drawn in Fig. 4.16b. Values of $\langle u_*(z)/\bar{u}_l(z) \rangle$ from the two urban towers U1 and U2 are higher than values reported from previous studies (Rotach, 1995; Feigenwinter et al., 1999), and hence, the

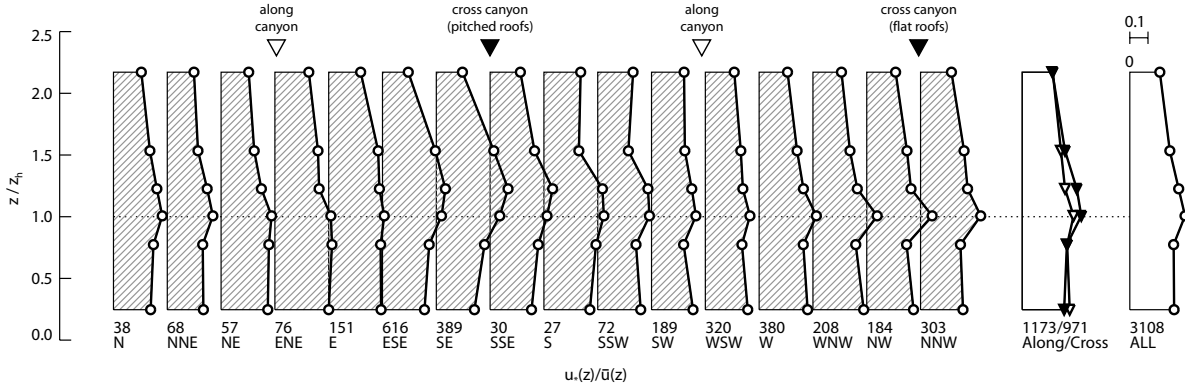


Figure 4.21: Profiles of local $u_*(z)$ normalized by mean wind velocity $\bar{u}(z)$ in dependence on ambient wind direction at U1. Numbers above wind directions indicate the number of hourly runs included in the average profile. Data source: Sonics A to F, hourly averages, November 1 to July 15, 2002, all stabilities, $u(z)$ at all levels $< 0.5 \text{ m s}^{-1}$.

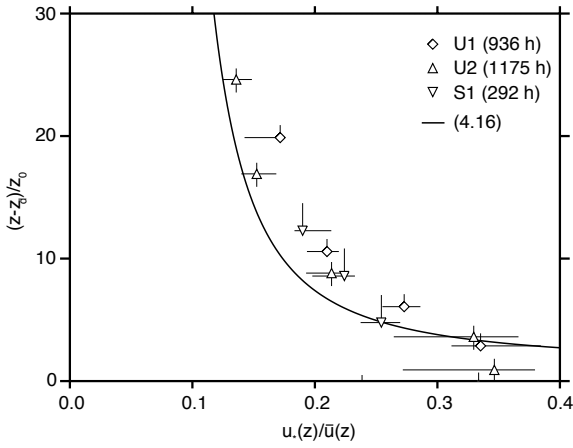


Figure 4.22: Neutral $\langle u_*(z)/\bar{u}_l(z) \rangle$ against non-dimensional height $(z - z_d)/z_0$. z_0 values are taken from Tab. 4.5, and z_d are determined from the peak frequency of vertical velocity spectra (Tab. 4.7). The horizontal error bars denote the 25 and 75% percentiles, the vertical bars indicate the range associated with the estimation of z_d and include the determination from the wind profile (Tab. 4.5), the spectral method, and a global z_d of $0.8z_h$. Data source: Sonics C to F (U1), B to F (U2) and A to C (S1), hourly averages, full operation periods, neutral stabilities.

empirical fit from Roth (2000) underestimates the present values in the roughness sublayer. Data at the three towers are more adequately described with a modified $c_2 \approx 0.6$.

The above relationships assume a local equilibrium between $\langle u'w' \rangle$ and $\langle \partial \bar{u} / \partial z \rangle$, as observed over smooth surfaces. The neutral wind profile implies that the turbulent transfer coefficient for momentum $K_m = -\bar{u}'w' / (\partial \bar{u} / \partial z)$ is equal $ku_*(z)z'^{\dagger}$. The normalized profiles of K_m in Fig. 4.16f show that if

\dagger z' is a scaling length which is equal $z - z_d$ above the roofs. For the definition in the canopy see Eq. 4.28.

we introduce a local $u_*(z)$, K_m is higher than predicted towards the canopy in neutral conditions, and is associated with higher scatter between different wind directions.

The ratio $u_*(z)/\bar{u}_l(z)$ strongly depends on ambient wind direction relatively to the street canyon (Fig. 4.21). High drag is caused by configurations with skimming flow over the cavities. Between z_h and z_f , an ambient flow perpendicular to the street canyon increases $u_*(z)/\bar{u}_l(z)$ compared to flow along the street canyon. Flow over the pitched roof row results in a maximum $u_*(z)/\bar{u}_l(z)$ at $1.23z_h$, while flow over the flat roofs show maximum $u_*(z)/\bar{u}_l(z)$ directly at z_h .

At tower top, the ratios $u_*(z)/\bar{u}_l(z)$ are between 0.15 and 0.2 at the different sites and nearly independent of wind direction. Individual roughness elements and the street canyon orientation do not influence momentum exchange anymore, and we can interpret the response as an integral effect of the underlying urban surface. This is another independent indication for the transition to the inertial sublayer.

Height-dependent $u_*(z)$ -profile — To account for the observed height dependence of local Reynolds stress, Rotach (2001) proposed an empirical parametrization for the vertical profile of $u_*(z)$ in the roughness sublayer, namely

$$\left(\frac{u_*(z)}{u_*^{max}} \right)^b = \sin \left(\frac{\pi}{2} \frac{(z - z_d)}{(z_f - z_d)} \right)^a \quad \text{for } z_d < z < z_f \quad (4.18)$$

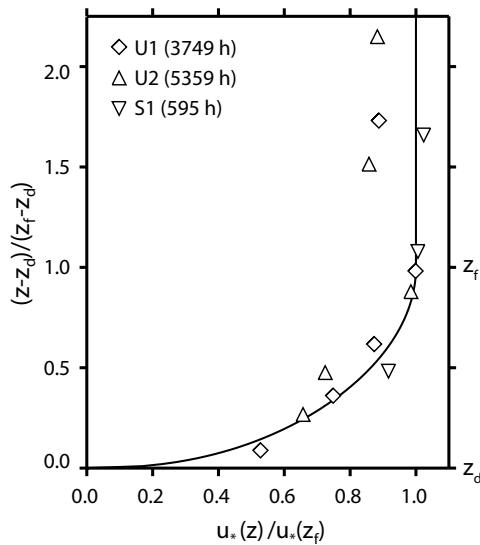


Figure 4.23: Parameterization of the vertical profile of $u_*(z)$ according to Eq. 4.18 and Eq. 4.19 in comparison to the measured profiles at the three profile towers. At all three towers, the rule-of-thumb z_d of 0.7 and $z_f = 1.55z_h$ are used. Data source: Sonics B to F at U1 and U2, A to C at S1, hourly averages, full operation periods, all stabilities and all wind directions.

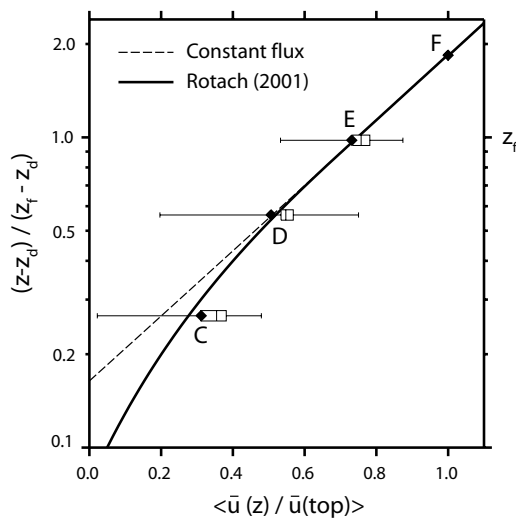


Figure 4.24: Measured neutral vertical wind profile $\langle \bar{u} / \bar{u}(\text{top}) \rangle$ at U1, compared to the wind profile constructed using the parameterization according to Eq. 4.18 and Eq. 4.19, and measured $u_*(\text{IS})$ at tower top (solid line) and the classical ‘constant flux’ profile with a constant $u_*(\text{IS})$ through the whole roughness sublayer (dashed line). Error bars are similar to Fig. 4.8. Data source: Sonics C to F at U1, hourly averages, November 1, 2001 to July 15, 2002, neutral stability, z_d from the spectral method (Tab. 4.7, $0.81z_h$).

and

$$u_*(z) = u_*^{max} \quad \text{for } z > z_f \quad (4.19)$$

where a and b are empirical constants, which are 1.28 and 3.0 respectively. Figure 4.23 shows the parameterized profile according to Equations 4.18 and 4.19 in comparison to measured data from U1, U2, and S1. The parameterization fits well the observed data below and around z_f .

Below z_f , the decreasing $u_*(z)$ with height modifies the wind profile, and lowers the gradient $\partial \bar{u} / \partial z$. Figure 4.24 shows the measured vertical wind profile close to the roofs in comparison to the parameterized wind profile (solid line). At level C ($z/z_h = 1.01$), the parameterization results in significantly better estimations compared to the assumption of a constant $u_*(\text{IS})$ through the whole roughness sublayer (dashed line). However, the wind profile is still underestimated.

In the context of BUBBLE, the above parameterization has been independently evaluated to estimate the shape of the urban wind profile. With the help of this parameterization, a procedure was successfully tested to estimate a reference wind velocity from wind velocity measurements at any other height (Christen and Rotach, 2004; Rotach and Christen, 2005).

4.2.4 Quadrant analysis of Reynolds stress

Joint probability density functions — Joint probability density functions (JPDFs) were calculated with a resolution of 32 by 32 bins for the scaled turbulent velocity deviations $\hat{u}_i = u'_i / \sigma_{u_i}$ in the range -4 to $+4$ times the standard deviation. Events with \hat{u}_i greater than 4 are excluded from JPDFs. This cuts off extremely large contributions, but on the other hand, reduces the error-sensitivity in situations with small turbulence intensity. All JPDFs have been calculated with one local rotation around the z -axis into longitudinal mean wind at given height, as indicated by the subscript l in the components \hat{u}_l and \hat{v}_l . The panel in Fig. 4.25 illustrates horizontally averaged JPDFs from the tower at U1. Quadrant measures were deduced directly from the JPDFs. To facilitate the interpretation, Fig. 4.27 summarizes some conceptual JPDFs and relates them to higher order moments.

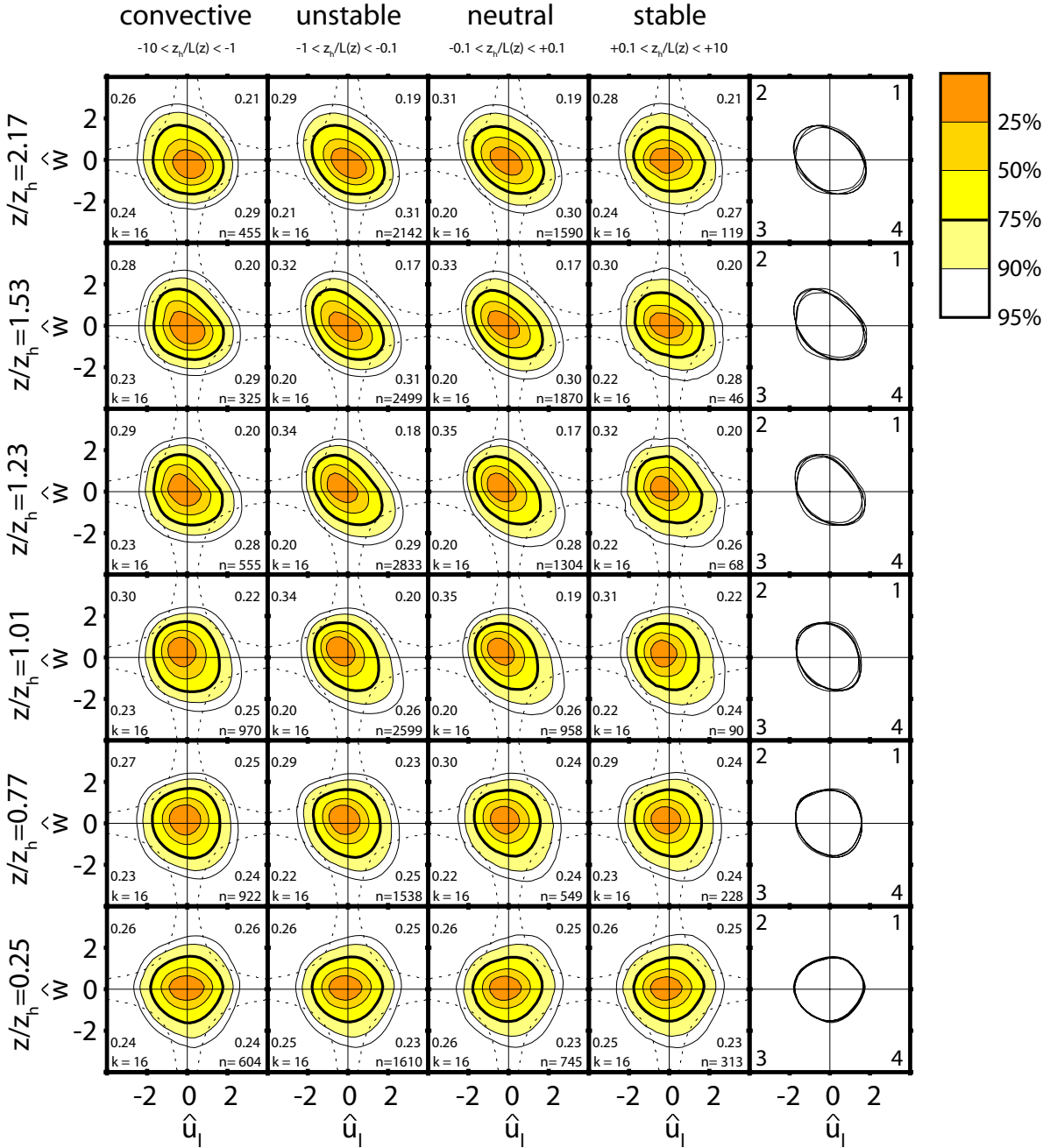


Figure 4.25: Normalized JPDFs of $\overline{u_l'w_l'}$ at U1 for different local stabilities. The rightmost column shows the difference in the 75% isoline between the different local stabilities and denotes the quadrant numbering. Note that u_l is rotated into horizontal mean wind direction at the corresponding tower level. The numbers labelling the individual quadrants denotes the average time fractions. n is the number of hourly runs included in the average, k is the number of the 16 wind direction classes included in the horizontal average.

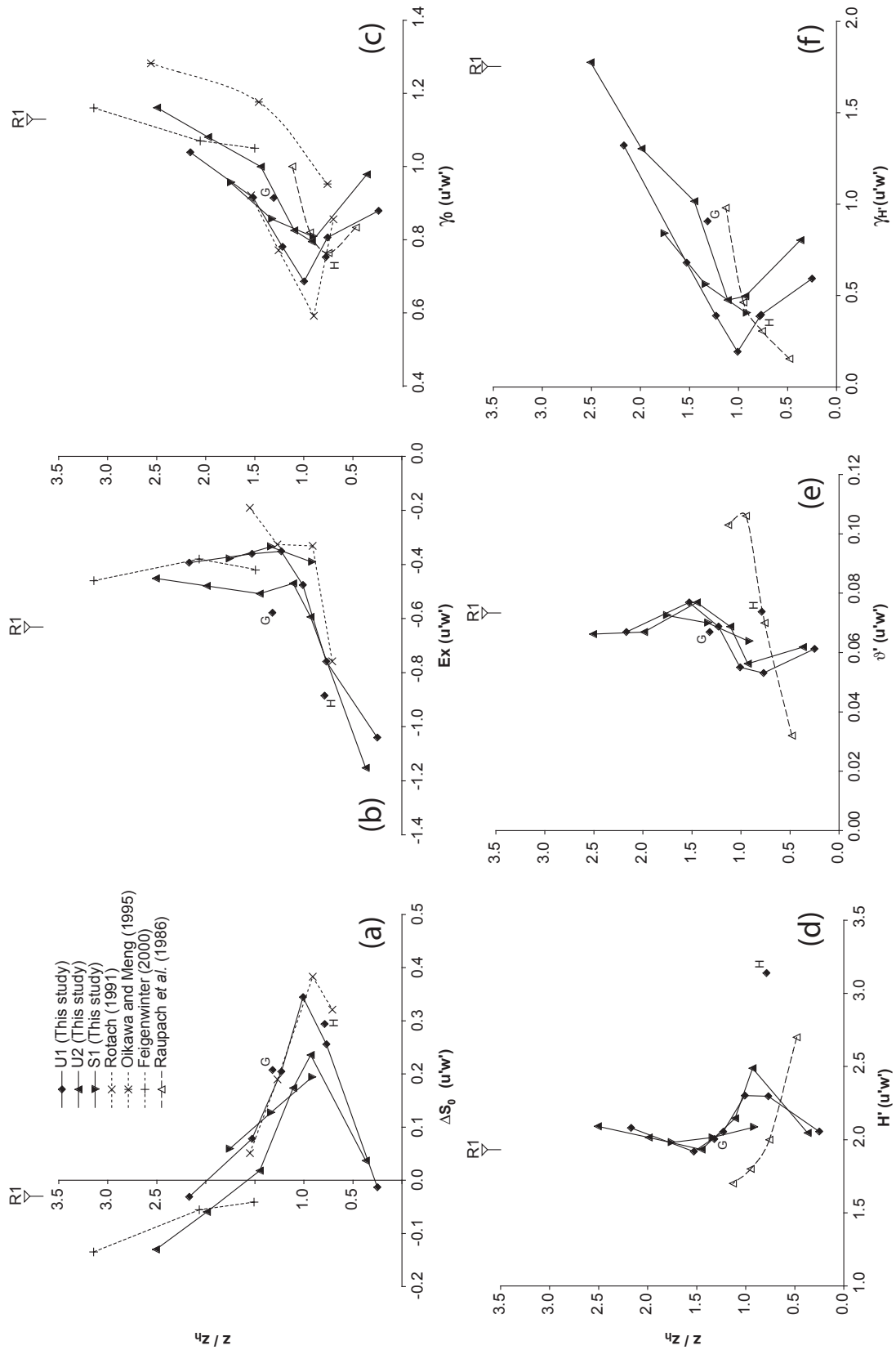


Figure 4.26: Vertical profiles of quadrant measures at U1, U2 and S1 in comparison to results reported from other experimental campaigns in real cities and from a wind tunnel experiment. Data source: Median profiles including all stratifications from June 10 to July 10, 2002. G and H refer to the additional sonics at roof top and at the canyon wall at U1.

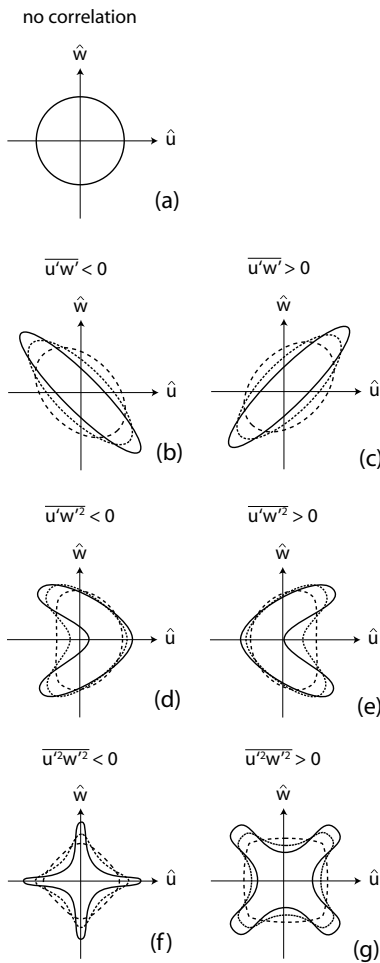


Figure 4.27: Conceptual influence from higher order mixed moments on the shape of JPDFs. In reality, a superposition of the different types is found.

At *street level*, u and w are uncorrelated. The JPDFs are characterized by a nearly rotational symmetric shape (Fig. 4.25) and ΔS_0 is close to zero (Fig. 4.26). All quadrants have roughly same time fractions, an indication that higher order moments are nearly negligible. There is evidence for a small positive $\overline{u^3}$, since JPDFs are slightly skewed towards higher \hat{u} . Further, with increasing \hat{u} , \hat{w} shows stronger excursions. The JPDFs resemble a very weak form of Fig. 4.27e, which indicates a slightly positive $\overline{u'w'^2}$.

Further up, in the *upper canyon*, a ‘quadratic shape’ is observed, but simultaneously, r_{uw} is low. A ‘quadratic shape’ is an indication that fourth order moments can be of importance. The quadratic shape is characterized by negligible $\overline{u'w'}$, negligible (or counteracting) third order moments, but a positive fourth order moment $\overline{u'^2w'^2}$ (Type (g) in Fig. 4.27).

Around *roof level*, JPDFs are well correlated, indicating that r_{uw} becomes significant. In the whole layer between z_d and z_f , a significant dominance of sweeps over ejections is found at all three towers. This results in a strongly positive ΔS_0 (Fig. 4.26a). Highest dominance of sweeps are measured directly at z_h . With increasing height above z_h , the influence of sweeps is reduced. This compares well to the urban full scale experiment from Rotach (1991).

Above z_f , in the transition to the inertial sublayer, ejections are of increasing importance. On average, ejections start to slightly dominate over sweeps. ΔS_0 becomes negative (Fig. 4.26a). The dominance of ejections is even more pronounced higher up, as earlier measurements 400 m to the South-East of U1 from Feigenwinter (2000) suggest. The BUBBLE wind tunnel experiments from the surface around U1 support an increasing dominance of ejections in the inertial sublayer (Feddersen et al., 2004). In the present data set, the crossover from negative to positive ΔS_0 is at roughly z_f on average. This indicates a transition to the inertial sublayer. In the roughness sublayer, sweeps dominate (Raupach, 1981) whereas the inertial sublayer is characterized by a dominance of ejections. For comparison, the rural surface layer value from R1 ($z = 28$ m) is indicated by the arrow symbol above the plots in Fig. 4.26. The ratio γ_0 is another way to look at the relative importance of ejections and sweeps and reveals the same pattern with a change from < 1 below to > 1 above z_f (Fig. 4.26c).

Exuberance — The exuberance Ex (Fig. 4.26b) is related to the correlation coefficient r_{uw} . An Ex close to zero show a high efficiency, while values towards -1 indicate a less efficient momentum exchange. Similar to r_{uw} , Ex is rather constant above z_h with a value around -0.4 . There is a tendency for a reduction with increasing height, approaching the rural value of R1. An exuberance < -1 is only found at street level. Here, turbulence is dominated by small scale motions, and the very weak Reynolds stress is slightly directed upwards on average.

Intensity and intermittency of events — The holesize H' and the corresponding time fraction ϑ' address the intensity (size) and intermittency of structures dominating momentum exchange (cf. Eq.

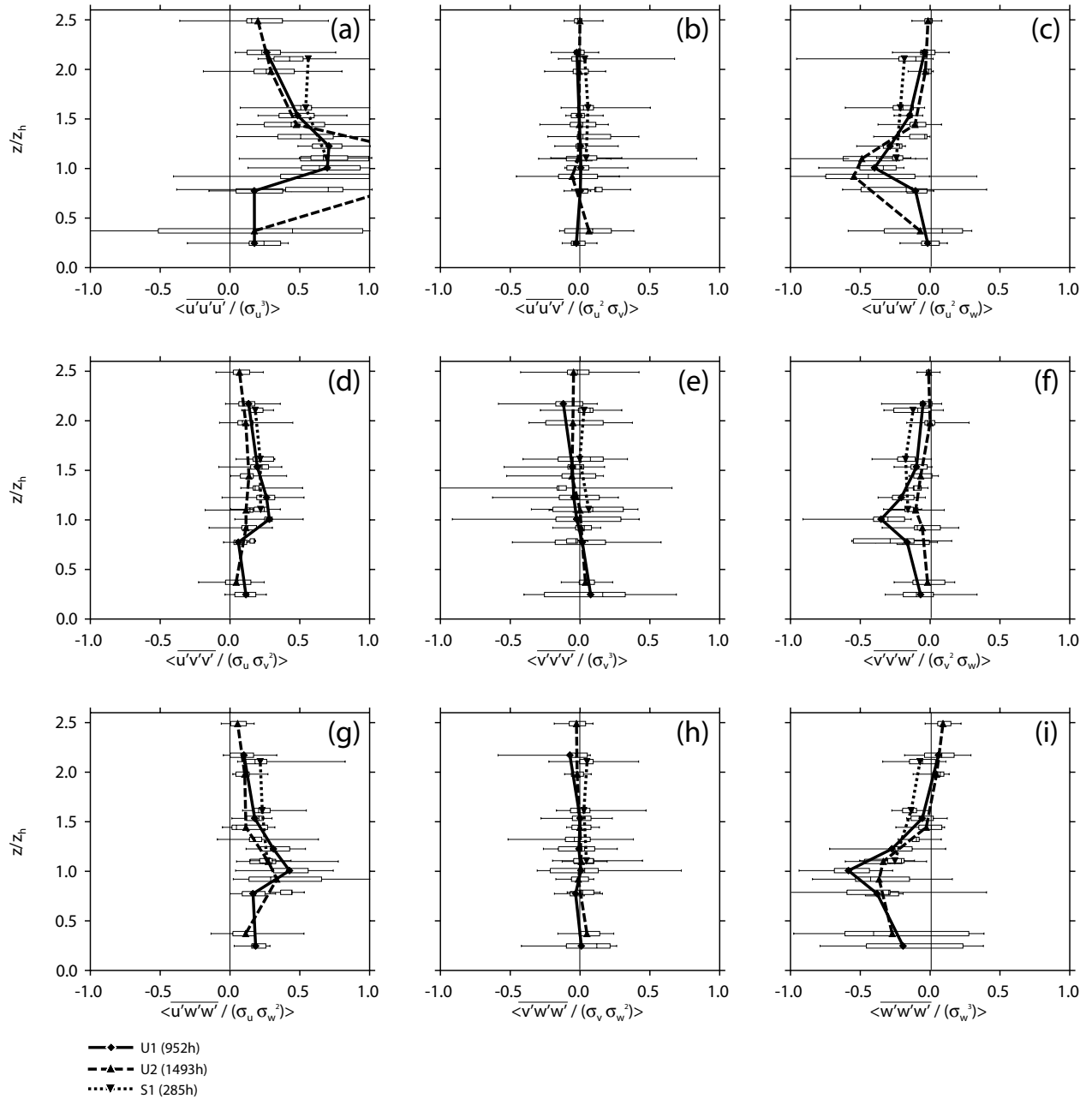


Figure 4.28: Profiles of triple correlations $\overline{u'_i u'_j u'_k}$ at all three towers. Error bars are defined in Fig. 4.8. Data source: All sonics, hourly averages, full operation periods, neutral stability only.

2.31 and 2.35). If holesize H' is low, small scale turbulence determines the exchange. With increasing H' , larger and non-local processes contribute to the exchange. In Gaussian turbulence, H' is 1.7 and $\vartheta' \approx 0.1$.

In the vertical profile, holesize H' is lowest at z_f (Fig. 4.26d). This can be interpreted as an indication of an initial shear layer where instabilities evolve. Here, momentum exchange is efficient and locally determined. Time fractions ϑ' are largest and perturbations that contribute to $\overline{u'w'}$ are common (Fig. 4.26e). With increasing distance to z_f , local (small) structures that contribute to the momentum exchange become less frequent and H' is larger. The flow is more intermittent, both above and below z_f , as indicated by a decreasing ϑ' in both directions. At street level, flow is again less intermittent and small scale dominated.

In Fig. 4.26d to f, additionally data from a wind tunnel study with uniform height (Raupach et al., 1986) are drawn. Curves from the wind tunnel study show similar trends, but (i) differences are more dominant, and (ii) generally curves are shifted towards lower heights. The first difference can be explained by the averaging procedure. Differences in H' and ϑ' are much more prominent in individual profiles and for different stabilities separately. The averaging procedure over all stabilities and wind directions blurs these trends. The lower height of the wind tunnel curves can be again related to the definition of z_h .

Modification by buoyancy effects — The effect of a non-zero buoyancy flux density on quadrant measures is analyzed in terms of stability at the topmost measurement level. Effects are summarized in Fig. 4.29 for U1. The crossover from negative to positive ΔS_0 strongly depends on stability. In convective situations, the crossover is at $z/z_h = 1.5$. It is higher during unstable runs ($z/z_h = 1.9$) and above the tower in neutral runs (approximated at $z/z_h = 2.5$). Figure 4.30 draws ΔS_0 from the topmost measurement level at U1 against stability. With destabilization, momentum transfer turns from sweep based exchange in near-neutral conditions to strongly ejection based transfer. Buoyancy creates mainly small scale ejections. The destabilization lowers $\overline{w'^3}$. In free convection, $\overline{w'^3}$ is — as expected — close to zero. On the other hand, buoyancy en-

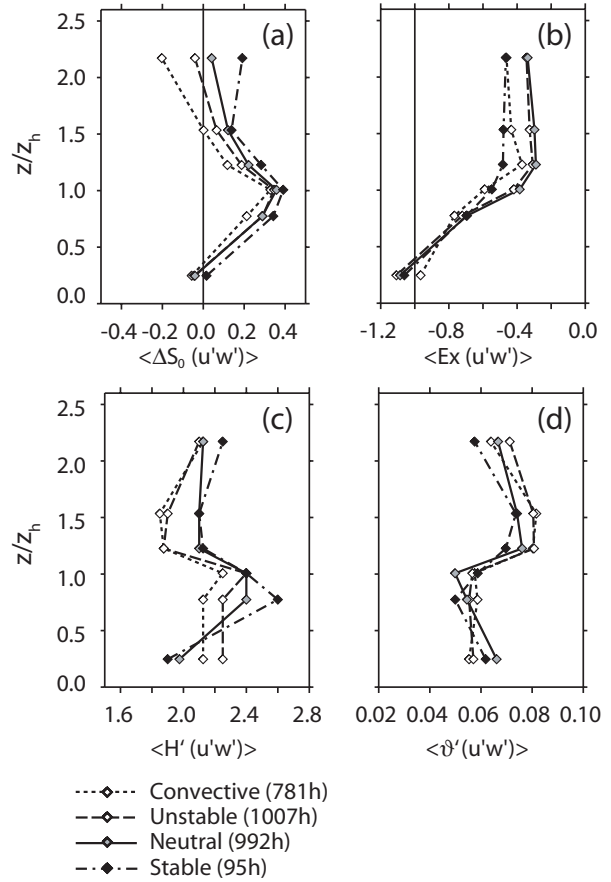


Figure 4.29: Stability dependence of quadrant measures (a) ΔS_0 , (b) Ex , (c) H' and (d) ϑ' for $\overline{u'w'}$ at U1. Data source: Sonics A to F, hourly values, November 1, 2001 to July 15, 2002, median profiles. Stability determined at tower top.

hances $\overline{w'^3}$. The figure further underlines that effects of $\overline{u'^2 w'}$ and $\overline{u' w'^2}$ are of opposite sign.

Earlier in this chapter, the strong stability dependence of r_{uw} was addressed. Hence, it is no surprise that the related Ex is driven by stability. At above roof levels, Ex ranges from neutral values around -0.35 to -0.5 during convective runs (Fig. 4.29b).

Non-Gaussian contributions — Since the asymmetry in the ejection-sweep character is related to higher order moments, it is of interest to separate these higher order effects from an ideal Gaussian turbulence. In Gaussian turbulence, ΔS_0 is zero, γ_0 is 1 and the JPDFs can be completely described by the Gaussian function $G(\hat{u}, \hat{w})$, which is determined by r_{uw} only (cf. Eq. 2.16).

Non-Gaussian time and stress fractions $NGT(\hat{u}, \hat{w})$ and $NGS(\hat{u}, \hat{w})$ are introduced. $NGT(\hat{u}, \hat{w})$ are cal-

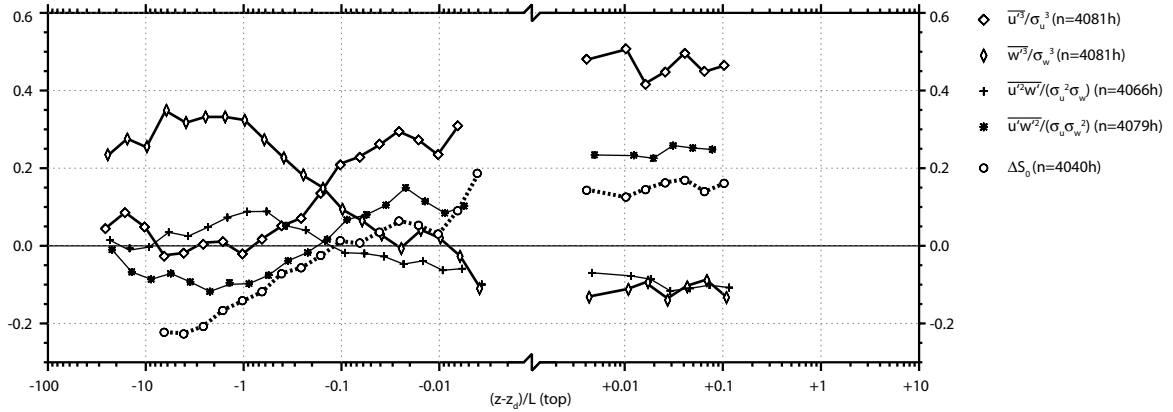


Figure 4.30: Dependence of ΔS_0 and third order moments at $z/z_h = 2.17$ on stability. Data source: Sonic F, hourly averages, November 1 to July 15, 2002

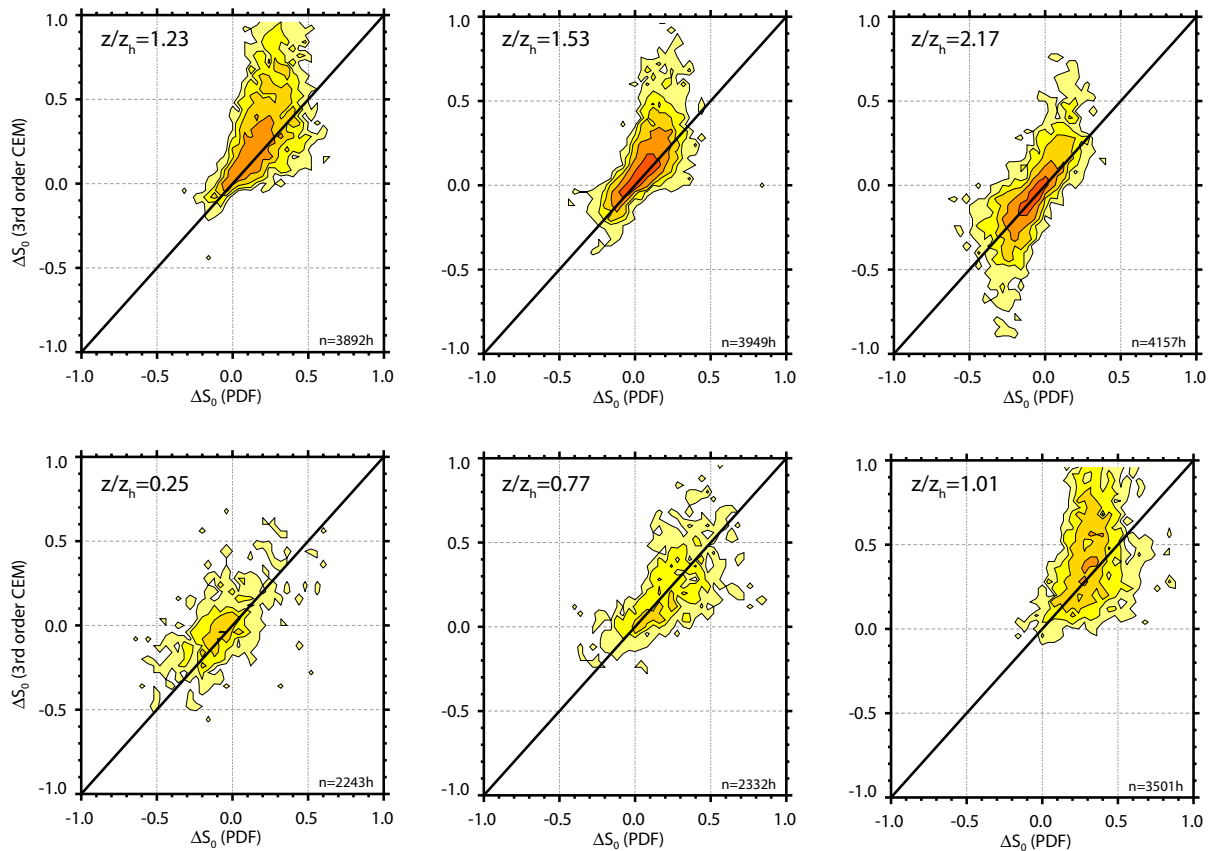


Figure 4.31: Cumulant expansion method (CEM) applied to estimate ΔS_0 at U1. Areas show joint probability density between ΔS_0 determined from the data (PDF) and ΔS_0 determined with a third order CEM. Data source: Sonics, hourly averages, November 1, 2001 to July 15, 2002, all stabilities.

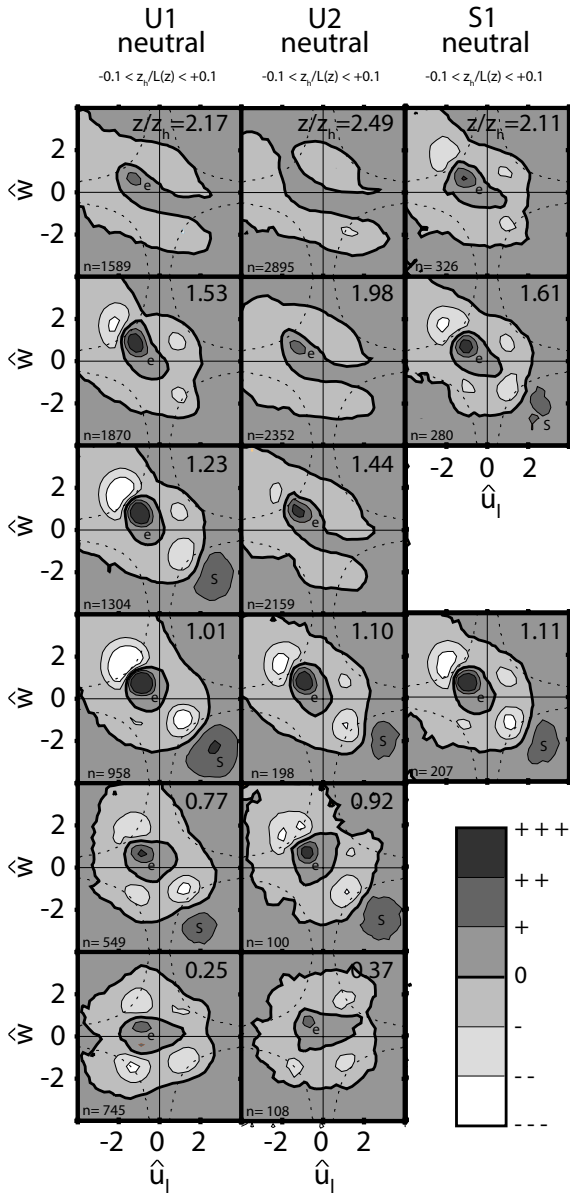


Figure 4.32: Non-gaussian stress fractions $NGS(\hat{u}, \hat{w})$ in the normalized JPDFs of \hat{u}_l and \hat{w} . Shown are neutral cases (local stability $z_h/L(z)$) from the three profile towers. The processing is similar to Fig. 4.25

culated as the difference between the actual JPDF $P(\hat{u}, \hat{w})$ and the Gaussian model $G(\hat{u}, \hat{w})$ (Eq. 2.16) at given r_{uw} :

$$NGT(\hat{u}, \hat{w}) = P(\hat{u}, \hat{w}) - G(\hat{u}, \hat{w}). \quad (4.20)$$

The non-Gaussian time fractions satisfy

$$\int_{-\infty}^{+\infty} \int_{-\infty}^{+\infty} NGT(\hat{u}, \hat{w}) du dw = 0. \quad (4.21)$$

Positive regions in $NGT(\hat{u}, \hat{w})$ have an enhanced temporal frequency due to higher order moments. Negative regions are less represented in the current JPDFs compared to a Gaussian distribution. The non-Gaussian stress fraction NGS is calculated by

$$NGS(\hat{u}, \hat{w}) = |\hat{u}\hat{w}|NGT(\hat{u}, \hat{w}). \quad (4.22)$$

Positive regions in the NGS indicate an enhanced magnitude* of the stress contribution from the given quadrant to the overall Reynolds stress. Negative regions lower the contribution in the current JPDF compared to a Gaussian distribution with same r_{uw} . Note that both measures address the internal distribution. There is no relation to the magnitude of $\overline{u'w'}$ anymore.

Figure 4.32 shows $NGS(\hat{u}, \hat{w})$ for all three towers and all levels. Around roof level and in the upper street canyon, there are significant non-gaussian contributions from large-scale (far-field) sweeps (positive contributions in the lower right corners). On the other hand, ejections are found closer to the origin in the 2nd quadrant. Ejections are shifted towards small scale (near-field) processes. This mainly reflects the positively skewed u and a negatively skewed w under neutral conditions (Fig. 4.28a and i). With increasing height above z_h , non-Gaussian sweeps become less relevant, but ejections are roughly constant with height. Mainly the decreasing magnitude of non-Gaussian sweeps explain the decrease of ΔS_0 with height.

With increasing buoyancy, more small scale ejections are produced whereas the contribution from far field sweeps is not altered. This has been previously expressed by the decreasing height of the crossover from negative to positive ΔS_0 with increasing stability. A new aspect of this shift is the size of the

* The magnitude of $\hat{u}\hat{w}$ is taken to simplify the graphical interpretation. The missing information on the direction of the Reynolds stress can be deduced from the corresponding quadrant.

structures involved. The size of structures contributing to momentum change is smaller with destabilization. With the relative shift from large-scale sweeps to small-scale ejections, H' becomes smaller (Fig. 4.29c).

In all above roof measurements, a slight dominance of inward interactions over outward interactions is found. As a consequence, higher non-Gaussian time fractions are found in quadrant 3. The positively skewed distribution of u lowers the time fractions of \hat{u} in quadrants 2 and 3 compared to 1 and 4. In the upper street canyon, the opposite situation is encountered. Here, a dominance of time fractions of outward interactions over inward interactions is observed (Fig. 4.25).

It is obvious that at least third order moments are necessary to describe all above patterns — especially close to the roofs. But are third-order moments sufficiently or do we need to evaluate fourth or even higher order moments?

Cumulant expansion method — The cumulant expansion method (CEM) relates analytically the departure of the JPDFs from the Gaussian distribution to higher order moments. The third-order CEM in Eq. 2.25 to 2.27) reproduces ΔS_0 with second and third order moments only. Figure 4.31 plots the measured ΔS_0 against predicted ΔS_0 by the third order CEM for all stabilities. Any difference between these two ΔS_0 values are an indication for the existence of non-zero moments of order ≥ 4 .

Within the street canyon, the CEM reproduces well ΔS_0 in most cases. At z_h and above roof level, there is a strong overestimation of ΔS_0 by the CEM. This suggests that moments of higher order work against the asymmetry between sweeps and ejections. Differences are decreasing with height above the canopy. At the tower top level, a systematical underestimation of ΔS_0 by the third order CEM is found in unstable situations (lower left corner in Fig. 4.31).

Above z_f and in the street canyon, differences are not crucial. An implementation of third order moments in a model is adequate to reproduce the key processes in turbulent momentum exchange. At canopy top however ($z/z_h = 1.01$ and 1.23), higher order moments (≥ 4) are important for a correct de-

scription of momentum transfer.

4.2.5 Estimation of dispersive stress

In this section, the magnitude of the dispersive stress divergence term in Eq. 4.13 is estimated. This is important to decide whether the decrease of Reynolds stress with height can be attributed to a dispersive stress divergence or to form drag.

Wind tunnel results suggest that dispersive stress is insignificant above and in the upper part of canopies (Raupach et al., 1986; Cheng and Castro, 2002). LES simulations however demonstrated that dispersive stress may be relevant in the upper part of the urban canopy layer (Kanda et al., 2004).

Recently, physical scale model studies investigated the dispersive stress in the bottom layers of model canopies. It was found that they can have the same magnitude as Reynolds stress (Böhm et al., 2000). Poggi et al. (2004b) concluded that dispersive stress is only important in sparse canopies. Dispersive stress directly measured in the trunk space of a plant canopy showed that it is statistically reliable in the order of $\approx 15\%$ of Reynolds stress (Christen and Vogt, 2004a).

Directly measuring dispersive stress divergence in an urban full scale experiment is nearly impossible and would require huge arrays of simultaneously measuring instruments at different locations. There is no possibility to directly determine the dispersive stress divergence with the present setup.

The precedent analysis of momentum exchange in the urban roughness sublayer may be interpreted in a way that the inertial sublayer starts at $z/z_h = 2$. Hence, we can write $\langle \bar{u}_0 \rangle = \bar{u}_0$ for all realizations of the approaching flow. Based on this assumption, we approximate the dispersive covariance $\langle \bar{u}'' \bar{w}'' \rangle$ with the help of the constructed horizontally averaged profile of $\langle \bar{u}/\bar{u}_0 \rangle$, which was calculated by applying the procedure described in Section 3.3.3:

$$\langle \bar{u}/\bar{u}_0 \rangle(z) = \langle \bar{u} \rangle(z)/\bar{u}_0 \quad (4.23)$$

and hence

$$\bar{u}'' = \bar{u} - \langle \bar{u} \rangle = \bar{u} - \bar{u}_0 \langle \bar{u}/\bar{u}_0 \rangle(z). \quad (4.24)$$

Further, assuming for neutral conditions $\overline{w'\rho'} = 0$ and $\overline{w''\rho''} = 0$, mass continuity leads to $\langle \bar{w} \rangle = 0$,

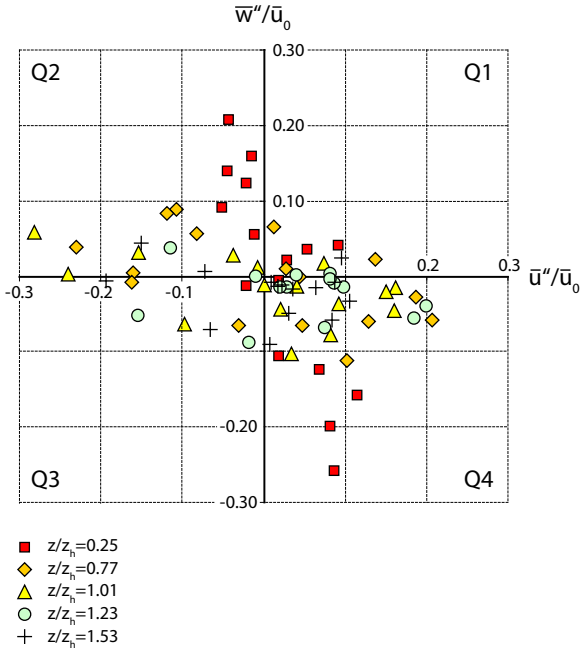


Figure 4.33: Dispersive quadrant analysis for \bar{u}''/\bar{u}_0 against \bar{w}''/\bar{u}_0 at the five lower levels at U1. Symbols denote the 16 individual wind sectors. Data source: Sonics A to F, hourly averages, November 1, 2001 to July 15, 2002, neutral stability only, $n = 994$ h.

and it follows $\bar{w} = \bar{w}''$ and

$$\frac{\bar{u}''\bar{w}''}{\bar{u}_0^2} = \frac{\bar{u}''}{\bar{u}_0} \frac{\bar{w}}{\bar{u}_0}. \quad (4.25)$$

Table 4.11 summarizes the estimation of $\langle \bar{u}''\bar{w}'' \rangle(z)$ for U1. A dispersive stress is existent and consistently negative. In the canopy space, it contributes strongest to the overall (weak) momentum exchange. Above z_h , the relative impact of $\langle \bar{u}''\bar{w}'' \rangle(z)$ decreases fast, as expressed by $\delta_{\bar{u}''\bar{w}''}$ in Tab. 4.11. The present estimation results in a positive $\partial \bar{u}''\bar{w}''/\partial z$ in the whole profile at U1, and hence, the dispersive stress divergence term in Eq. 4.13 is counter directed to $\partial \bar{u}'\bar{w}'/\partial z$. $\partial \bar{u}''\bar{w}''/\partial z$ is roughly constant with height and in the order of $2 \cdot 10^{-4} u_0^2 \text{ m s}^{-2}$. Figure 4.34 shows the average magnitude of all terms in Eq. 4.13 for neutral conditions. Terms are normalized by wind speed u_0 and z_h for dimensional consistency.

As a consequence of the above estimation, the dispersive stress divergence term may be regarded negligible for the description of the overall momentum transfer, and — at least above z_d — we can approx-

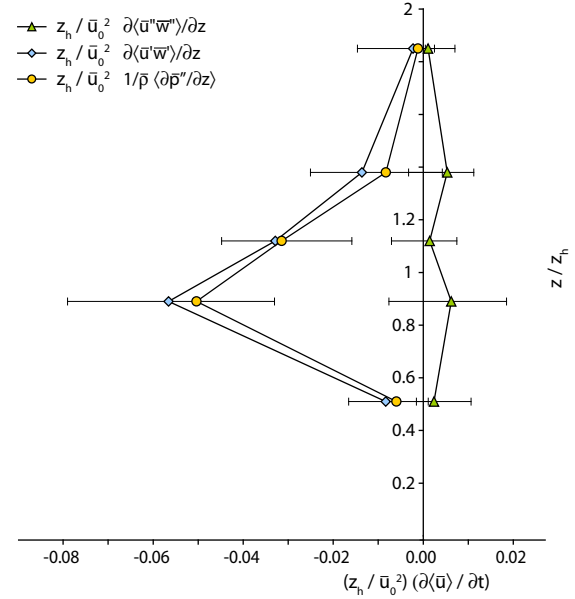


Figure 4.34: Scale analysis of the different terms in Eq. 4.13 normalized by z_h/u_0^2 . The residuum is interpreted as form drag. Viscous drag is neglected. Error bars denote the 25 and 75% percentile from all 16 wind direction classes. Data source similar to Fig. 4.33.

Table 4.11: Estimation of the dispersive stress at U1 for neutral conditions. $\delta_{\bar{u}''\bar{w}''} = \langle \bar{u}''\bar{w}'' \rangle / (\langle \bar{u}'\bar{w}' \rangle + \langle \bar{u}''\bar{w}'' \rangle)$, $r_{\bar{u}''\bar{w}''}$ according Eq. 4.26. Data source similar to Fig. 4.33.

	$\langle \bar{u}''\bar{w}'' \rangle / \bar{u}_0^2$	$\langle \bar{u}'\bar{w}' \rangle / \bar{u}_0^2$	$\delta_{\bar{u}''\bar{w}''}$	$r_{\bar{u}''\bar{w}''}$
1.53	-0.0007	-0.0298	2%	-0.26
1.23	-0.0024	-0.0255	8%	-0.48
1.01	-0.0027	-0.0182	13%	-0.51
0.77	-0.0042	-0.0048	46%	-0.57
0.25	-0.0054	-0.0004	93%	-0.81

imate Eq. 4.13 by

$$\frac{\partial \langle \bar{u}'\bar{w}' \rangle}{\partial z} \approx -\frac{1}{\bar{\rho}} \left\langle \frac{\partial \bar{p}''}{\partial x} \right\rangle. \quad (4.26)$$

In analogy to quadrant analysis, which investigates time series and classifies instantaneous values into outward interactions, ejections, sweeps, inward interactions, the method of quadrant analysis can be also applied to dispersive terms (Christen and Vogt, 2004a). Instead of $\hat{u}(t)$ and $\hat{w}(t)$, we draw $\bar{u}''/\bar{u}_0(k)$ against $\bar{w}''/\bar{u}_0(k)$ where k is a given wind direction sector (Fig. 4.33). This results in ascending accelerated realizations (Q1), ascending decelerated realizations (Q2), descending decelerated realizations (Q3) and descending accelerated realizations (Q4). By calculating the dispersive correlation coefficient

$$r_{\bar{u}''\bar{w}''} = \frac{\langle \bar{u}''\bar{w}'' \rangle}{\langle \bar{u}''^2 \rangle^{0.5} \langle \bar{w}''^2 \rangle^{0.5}} \quad (4.27)$$

Table 4.12: Summary of measured and calculated characteristics affecting momentum exchange at the urban towers, separately for the canyon layer (CAL), the roof layer (ROL), and the above-roof layer (ARL) which is a gradual transition towards the inertial sublayer.

Parameter	$z < z_d$	$z_d < z < z_f$	$z_f < z$
	CAL	ROL	ARL
$\partial\langle u'w' \rangle / \partial z$	≈ 0	< 0	≈ 0
Sk_u	≥ 0	$\gg 0$	≥ 0
Sk_w	≈ 0	< 0	≥ 0
ΔS_0	≈ 0	> 0	< 0
Ex	≈ -1	≈ -0.4	≈ -0.4
$\langle \bar{u}''\bar{w}'' \rangle$	< 0	< 0	≈ 0
$\delta_{\bar{u}''\bar{w}''}$	50-90%	10%	0%

we retain a measure for the importance of descending accelerated realizations and ascending decelerated realizations, and hence, information on the efficiency of $\langle \bar{u}''\bar{w}'' \rangle$. With increasing depth in the canopy, $r_{\bar{u}''\bar{w}''}$ increases (Tab. 4.11).

4.2.6 Summary

- Reynolds stress in the roughness sublayer is not constant with height. At the two urban canyons, the profile is characterized by a maximum at z_f and by a strong reduction with height below. z_f corresponds to the height of highest obstacles of the urban surface. Above z_f , Reynolds stress is roughly constant with height. The empirical parameterization according to Rotach (2001) fits well the observed vertical profile of $u_*(z)$ at all sites.
- Momentum transfer in the roughness sublayer can be conceptually separated into three regions. The lower canopy layer (CAL, $z < z_d$), the roof layer (ROL, $z_d < z < z_f$) and the above-roof layer (ARL, $z > z_f$) which forms a gradual transition towards the inertial sublayer. Table 4.12 summarizes characteristics of each layer based on observations in the present study.
- At z_f , flow perpendicular to the street canyon is characterized by an enhanced efficiency of Reynolds stress and a stronger drag coefficient compared to along-canyon flow. Cross-canyon flow shows analogies to a plane mixing layer.
- Momentum exchange is sweep dominated in

the roof layer and ejection dominated in the above-roof-layer. The height of the crossover from sweep to ejection dominated turbulence increases with increasing stability. It is found at z_f under the dominant unstable conditions. At z_f , turbulent exchange is small scale and locally determined whereas below, large far field sweeps transport momentum and penetrate into the roof region and upper street canyon. Small scale ejections dominate the exchange above z_f .

- Hence, for an adequate description of turbulent exchange processes in the urban roughness sublayer, at least third order moments are required. Higher order moments (≥ 4) are only of importance in the roof layer.
- The dispersive stress $\langle \bar{u}''\bar{w}'' \rangle$ is negligible above z_h . In the street canyon, dispersive stress can be in the same order as Reynolds stress. The dispersive stress divergence $\langle \bar{u}''\bar{w}'' \rangle / \partial z$ is negligible compared to Reynolds stress divergence and hence, is not an explanation for the increasing $u_*(z)$ with height. In the roof layer and above, the dispersive term in the horizontally equation of motion can be neglected.

4.3 Turbulent kinetic energy

Any accurate prediction of dispersion within and close to urban canopies is inherently coupled with an appropriate knowledge on the magnitude of turbulent fluctuations and the underlying physical processes that create, relocate and destroy turbulent kinetic energy (TKE). First, the analysis of time and length scales of TKE in Section 4.3.1 is the basis for the development of an appropriate scaling length in the urban roughness sublayer. In Section 4.3.2, we evaluate the magnitude of the different terms of the TKE-budget. The TKE-budget is used to further discuss velocity variances in Section 4.3.3. Finally, an alternate approach to velocity variances is tested which is based on the eigenvalues of the velocity correlation tensor (Section 4.3.4).

4.3.1 Length and time scales

In surface layer scaling, the dominant length scale is the distance above ground z or the height above zeroplane displacement $z - z_d$. This scaling fails in the lower roughness sublayer, and would result in absurd negative scaling lengths below z_d . The scaling of spectra by local wind velocity $\bar{u}(z)$ and $z - z_d$ does not result in a coincidence of the spectral peaks at same normalized frequency. Within canopies, turbulence properties are mainly dependent on size and configuration of roughness elements and not on height above ground (Amiro, 1990). In plant canopies, turbulence is expected to be mainly controlled by coherent structures of the scale of the whole canopy height z_h (Raupach, 1989). This is explained by the dominating structures shed at canopy top. Velocity fluctuations within vegetation canopies may be scaled with z_h and $\bar{u}(z_h)$ rather than $z - z_d$ and $\bar{u}(z)$ (Raupach et al., 1996; Finnigan, 2000).

Figure 4.35a shows spectral length scales deduced from peak frequency of neutral TKE-spectra. Length scales were determined according Eq. 4.10 and 4.11. Length scales within the street canyon do not vary significantly with height. The length scales of longitudinal fluctuations even increase with depth, and to some extent, the same can be found for lateral fluctuations (Fig. 4.35c). Nevertheless, scaling by a constant length scale over the whole canopy layer is appropriate compared to a height dependent

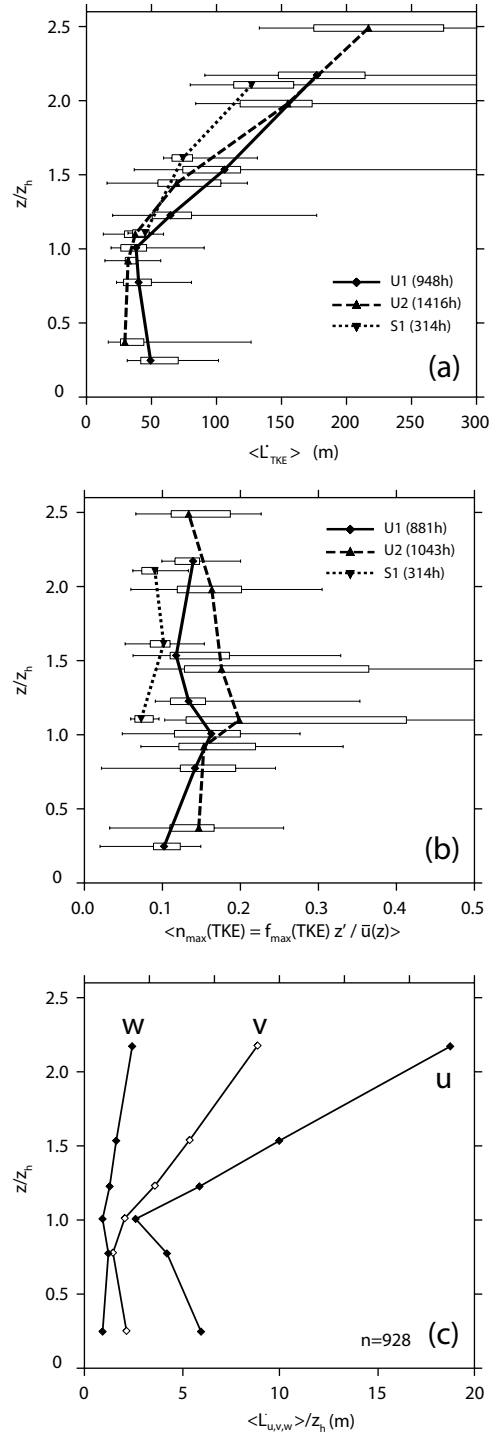


Figure 4.35: (a) Length scale $L_{TKE}(z)$ deduced from peak frequency of TKE-spectra ($L_{TKE} = \bar{u}/n_{max}$), (b) normalized peak frequency of TKE-spectra at U1, U2 and S1, and (c) Individual length scales $L_{u_i}(z)$ scaled with z_h for neutral runs at U1. Data source: Sonics, all levels, hourly spectra, full operation period, neutral stability. Error bars in this and the subsequent plots are similar to Fig. 4.8.

length scale. Above roofs, the height-dependence is restored, and length scales increase nearly linearly with height.

Scaling length — To account for this, the scaling parameter z' is introduced. It incorporates the street canyon scaling and surface layer scaling simultaneously:

$$z' = \begin{cases} z - z_d & \text{for } z > (x_s + z_d) \\ x_s & \text{for } z < (x_s + z_d) \end{cases} \quad (4.28)$$

Here, x_s is the distance between the instrument and the nearest canyon wall or floor. x_s corresponds to the largest eddies that fit into the street canyon at given instrument location. If we use our simplified urban geometry with infinitely long canyons, the horizontally averaged $\langle x_s \rangle$ can be related to the characteristic street canyon width x_c by $\langle x_s \rangle \approx x_c/4$. In the street canyon, $\langle x_s \rangle$ is the spatial average distance to the nearest wall.

This scaling is applied to normalize neutral peak frequencies n_{\max} of TKE spectra in Fig. 4.35b. The normalized peak frequencies of the individual components are summarized in Tab. 4.13. The scaling length z' allows a successful normalization of the TKE spectra and an adequate normalization of u -spectra and v spectra. Therefore, z' is further used to substitute $z - z_d$. The different normalized w -spectra do not overlap well with z' as scaling length in the roof layer and in the street canyon. Here, a scaling in the order twice z' or $z_h/2$ would result in an overlap of spectra of the different heights. This failure may be attributed to the contamination of w by longitudinal components, which are rotated into the canyon by the vortex-like flow situations. Indeed, under cross-canyon flow, when a vortex is present, normalized frequencies in w are lower than for along-canyon flow suggesting that fluctuations in w reflect previously u -components above the roof level, which have been rotated by the solid body rotation into the upper canyon.

4.3.2 Turbulent kinetic energy budget

TKE budgets of the flow within and above plant canopies have been addressed in a number of field experiments (e.g. Leclerc et al., 1990; Meyers and Baldocchi, 1991; Frenzen and Vogel, 2001).

Table 4.13: Neutral limits of normalized maximum peak frequency $n_{\max} = f_{\max} z' / \bar{u}$. SL denotes the surface layer values. Data source: hourly spectra, neutral stability (at given height).

Site	z' (m)	$n_{\max}(u)$	$n_{\max}(v)$	$n_{\max}(w)$
U1	2.17	0.08	0.21	0.59
	1.53	0.09	0.17	0.52
	1.23	0.09	0.17	0.39
	1.01	0.07	0.15	0.26
	0.77	0.05	0.19	0.21
	0.25	0.04	0.12	0.25
U2	2.49	0.08	0.27	0.61
	1.98	0.11	0.34	0.81
	1.44	0.20	0.37	0.59
	1.10	0.13	0.34	0.21
	0.92	0.10	0.24	0.11
	0.37	0.09	0.25	0.15
S1	2.11	0.07	0.16	0.44
	1.61	0.06	0.14	0.39
	1.11	0.07	0.16	0.36
R1		0.05	0.12	0.46
SL		0.08	0.22	0.55

The characteristic density, the non-permeability and stiffness of buildings that form an urban canopy compared to the flexible and highly fractal structures that are present in plant canopies do not imply a direct applicability of these results from plant canopies to urban environments. Up to now, no study measured the terms of the TKE budget within and above an urban canopy. Nevertheless, there are several physical scale studies addressing the TKE budget (Raupach et al., 1986; Poggi et al., 2004a), and also a number of numerical studies (e.g. Wilson and Shaw, 1977; Dwyer et al., 1997), but all focus on plant canopies.

By first applying temporal and then spatial averaging, the total kinetic energy of a unit mass is split up into a temporally and spatially resolved-scale turbulent kinetic energy (MKE) and two terms in the unresolved scale. The two unresolved parts are the dispersive (DKE) and the turbulent kinetic energy (TKE) (Raupach and Shaw, 1982):

$$\frac{1}{2} \langle u_i u_i \rangle = \frac{1}{2} \left(\langle \bar{u}_i \rangle \langle \bar{u}_i \rangle + \langle \bar{u}_i'' \bar{u}_i'' \rangle + \langle \bar{u}_i' \bar{u}_i' \rangle \right). \quad (4.29)$$

In the subsequent analysis, we focus on the budget of TKE only. For horizontal homogeneous conditions, the general three dimensional TKE budget equation

(Eq. 2.55) is rewritten according to Finnigan (2000):

$$\begin{aligned}
\frac{\partial \langle u'_i u'_i \rangle / 2}{\partial t} &= - \underbrace{\langle u' w' \rangle \frac{\partial \langle \bar{u} \rangle}{\partial z}}_{Ps} - \underbrace{\langle u' w'' \frac{\partial \bar{u}''}{\partial z} \rangle}_{Pd} \\
+ \frac{g}{T} \underbrace{\langle w' \theta' \rangle}_{Pb} + Pt &- \underbrace{\frac{\partial \langle u'_i u'_i w' \rangle / 2}{\partial z}}_{Tt} - \underbrace{\frac{\partial \langle \bar{w}'' u'_i u'_i \rangle / 2}{\partial z}}_{Td} \\
- \underbrace{\frac{\partial \langle p' w' \rangle}{\partial z}}_{Tp} &+ \underbrace{v \frac{\partial^2 \langle u'_i u'_i \rangle / 2}{\partial x_j \partial x_j}}_{Tv} - \epsilon. \quad (4.30)
\end{aligned}$$

Compared to Eq. 2.55, new terms arise from the horizontal averaging, namely the dispersive shear production term (Pd) and the dispersive turbulent transport term (Td). Pt is an extra term, which accounts for turbulence created by moving vehicles in the street canyon (Di Sabatino et al., 2003). In summary, turbulence is locally produced by turbulent shear production (Ps), dispersive shear production (Pd), buoyancy production (Pb) and traffic (Pt). The locally produced turbulent kinetic energy can be vertically relocated by turbulent (Tt), dispersive (Td), pressure (Tp), and viscous transport (Tv). Finally, dissipation of turbulent kinetic energy (ϵ) is always a sink.

In the stationary inertial sublayer, individual terms of the TKE budget are typically normalized by $k(z - z_d)/u_*^3(\text{IS})$. This results in the well known ϕ -functions (Frenzen and Vogel, 1992)

$$\phi_m + \phi_b + \phi_t + \phi_p = \phi_\epsilon \quad (4.31)$$

where ϕ_m is the normalized shear production, ϕ_b the normalized buoyancy production ($\phi_b \equiv (z - z_d)/L$), ϕ_t and ϕ_p are the normalized turbulent and pressure transport terms, and ϕ_ϵ is the normalized dissipation rate. The ϕ -functions are interrelated and are assumed to depend only upon $(z - z_d)/L$. Under neutral conditions, $\phi_m = \phi_\epsilon = 1$, and ϕ_t, ϕ_p are close to zero. These simplifications are not adequate in the roughness sublayer.

Turbulent shear production — The vertical gradient of wind velocity $\partial \bar{u} / \partial z$ has been approximated by the local derivative of a parametric cubic spline interpolation with the lower boundary set to zero at $z/z_h = 0$ and a relaxed upper boundary at

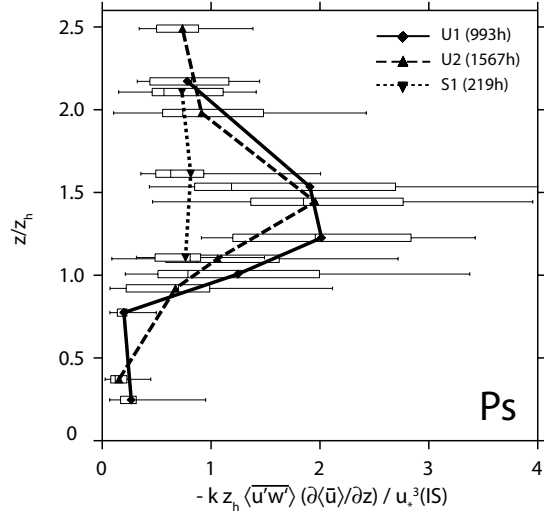


Figure 4.36: Vertical profiles of the shear production term at U1, U2 and S1. Data source: all sonics, hourly averages, full operation periods, neutral stability.

the topmost measurement level by minimizing tension.

Figure 4.36 shows the turbulent shear production term Ps for neutral conditions at U1, U2 and S1. Values are normalized by $kz_h/u_*^3(\text{IS})$, where the topmost measurement of $u_*(z)$ is taken as $u_*(\text{IS})$. This global normalization allows us to compare situations with varying mechanical forcing. On average, shear production is strongest at roof layer in the range $1.2 < z/z_h < 1.5$. Here, shear production is by far the most important source in the budget of TKE (see also the upcoming Fig. 4.43). Shear production decreases rapidly within the street canyon, both in absolute and relative numbers. At S1, the profile of Ps is nearly constant with height, and only half the magnitude compared to the dense urban surfaces. At S1, the mean wind profile is characterized by smaller gradients, and z_d is located significantly deeper in the canopy (cf. Section 4.1.2).

The height of strongest shear production as well as its magnitude depend on wind direction of the approaching flow, which is illustrated for U1 in Fig. 4.37. Wind over the flat roofs from NW result in a maximum between 1 and $1.2z_h$. Flow over the pitched roofs from SE shows a strong elevated shear layer at $1.5z_h$, associated with values that are more than twice the magnitude observed with wind over the flat roof. This can be mainly attributed to the vertical wind profile (cf. Section 4.1.2). If air flows first over the pitched roof row, this results in strong gra-

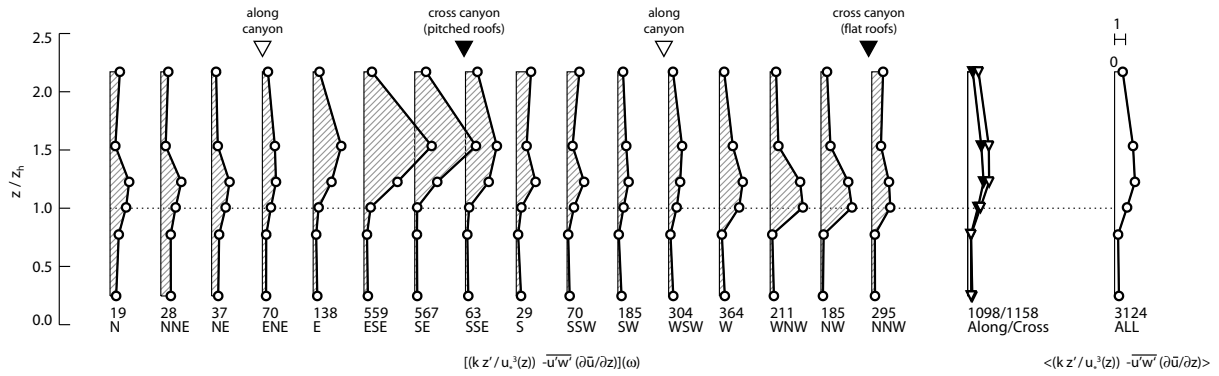


Figure 4.37: Profiles of the scaled shear production term $(kz'/u_*^3(z))\overline{u'w'}(\partial\bar{u}/\partial z)$ at U1 for different ambient wind directions. Data source: Sonics A to F, hourly values, November 1, 2001 to July 15, 2002, all stabilities.

dients and low winds in the street canyon. Weaker gradients are found with flow first over the flat roofs (where the vortex was observed). Along-canyon flow is characterized by slightly smaller shear production rates on average.

Dispersive shear production — The dispersive term Pd was not directly measured. It is approximated with a procedure analogous to the estimation of the dispersive stress described in Section 4.2.5, namely

$$\frac{\overline{u'w''}(z)}{u_*^2(\text{IS})} \approx \frac{\overline{u'w'}(z)}{u_*^2(\text{IS})} - \left\langle \frac{\overline{u'w'}}{u_*^2(\text{IS})} \right\rangle(z). \quad (4.32)$$

The dispersive gradient was approximated by

$$\frac{1}{u_*^2(\text{IS})} \frac{\partial \bar{u}''}{\partial z} \approx \frac{\partial(\bar{u}(z)/u_*^2(\text{IS}) - \langle \bar{u}/u_*^2(\text{IS}) \rangle(z))}{\partial z}. \quad (4.33)$$

The horizontally averaged dispersive shear production term was found 10^{-5} to 10^{-7} times smaller than turbulent shear production at all levels at U1 (not shown) and is therefore neglected in the subsequent analysis.

Buoyancy production / destruction — Over a compact and densely built-up urban surface, mainly roof areas contribute to buoyant production (see also the upcoming Section 4.4.1). In absolute numbers, buoyant production of TKE is small within the street canyon. Above the roofs, buoyancy production is typically five to ten times less important than shear production (Fig. 4.43). The lower importance of

Table 4.14: Characteristics of the buoyant production term at U1. Data source: Sonics A to F, hourly average, November 1, 2001 to July 15, 2002, all stabilities and flow situations, $n=3709\text{h}$.

z/z_h	Median $ Pb/Ps $	Cases $ Pb > Ps $	Cases $Pb < 0$
2.17	0.28	26.9%	9.8%
1.53	0.13	16.8%	6.4%
1.23	0.12	8.8%	6.6%
1.01	0.27	25.3%	6.7%
0.77	0.71	41.5%	9.2%
0.25	0.30	22.2%	14.6%

the buoyant production term results in a dominating neutral and slightly unstable stratification of the urban roughness sublayer. The ratio shear production to buoyancy production changes with height, and this results in a variable stability with height (Tab. 4.14).

It is not surprising that strongest buoyant production rates are found during summer days when sensible heat flux densities are large and typically in the order of $300 - 400 \text{ W m}^{-2}$. Figure 4.38 illustrates vertical profiles of Pb for convective runs with a stability at tower top in the range $-10 < z'/L < -0.5$. At the two dense urban sites, there is an increasing buoyancy production from street canyon floor up to approximately $z/z_h = 1.2$ and a nearly constant production with height above.

Dissipation of TKE — The very small eddies involved in viscous dissipation of TKE can not be measured directly with ultrasonic anemometers. Instead, dissipation was deduced from the inertial sub-

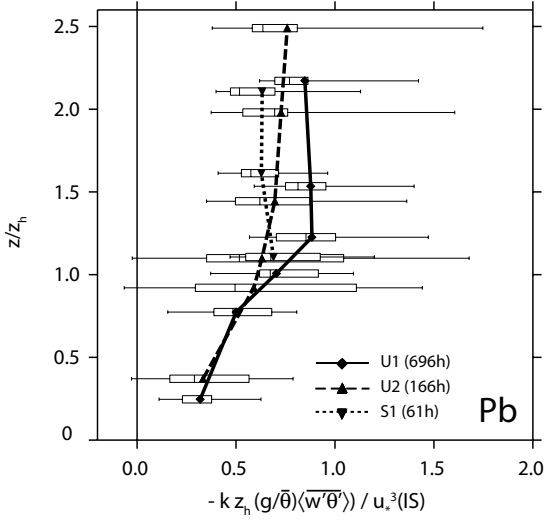


Figure 4.38: Vertical profiles of buoyancy production for convective runs at U1, U2 and S1. Data source: all sonics, hourly averages, full operation periods, convective runs only.

Table 4.15: Average properties of the inertial subrange (ISR) of longitudinal velocity spectra relevant for the calculation of ϵ . For definitions see text. Data Source: Sonics A to F at U1, hourly spectra, all stabilities. *SL* refers to the theoretical surface layer values.

z/z_h	I_u	ISR Slope	S_u/S_w	Err.
2.17	0.45	-1.63	1.14	12.8%
1.53	0.52	-1.64	1.07	13.6%
1.23	0.51	-1.62	1.03	14.0%
1.01	0.48	-1.60	1.15	15.2%
0.77	0.40	-1.59	1.05	15.3%
0.25	0.40	-1.52	1.05	19.5%
SL		-5/3	4/3	0%

range (ISR) of longitudinal velocity spectra using Kolmogorov's similarity approach and Taylor's hypothesis. Solving Eq. 2.48 for ϵ returns

$$\epsilon = \frac{2\pi n}{\bar{u}} \left(\frac{n S_u(n)}{\alpha_u} \right)^{3/2}. \quad (4.34)$$

A correct estimation of ϵ is only achieved if (i) an undisturbed ISR with local isotropy exists and (ii) the Taylor hypothesis is applicable (Section 2.2.7). From studies in plant canopies, it is known that effects like 'spectral shortcut' — a direct bypass of large scale turbulent kinetic energy to small scales by small canopy elements (leafs, branches) — may significantly alter spectra in high frequency bands. In the non-vegetated urban canopy at U1, such effects are supposed to be less relevant, since the highest spectral densities in the size of roughness elements (10^{-2} to 10^{-1} m^{-1}) are larger than the

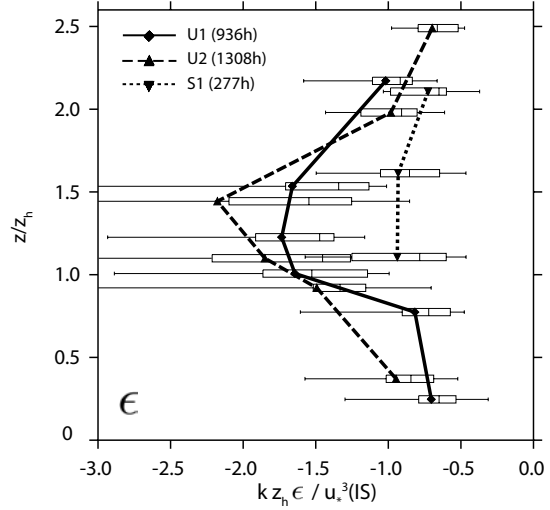


Figure 4.39: Vertical profiles of dissipation rate ϵ of TKE at U1, U2 and S1. Data source: all sonics, hourly averages, full operation periods, neutral stability.

corresponding wave numbers in the ISR (10^{-1} to 10^0 m^{-1}). However, one can not exclude the possibility of an overlapping of these two scales. In this case, the range where ϵ is determined would be slightly contaminated by kinetic energy directly produced in this small scale overlap-region. Measurements in the vegetated canyon at U2 and in the backyard at S1 are more error-sensitive due to the small scale vegetation structures. Here, results have to be interpreted with caution.

Critical for the dissipation calculation in the urban canopy layer may be the applicability of the Taylor hypothesis. Errors are not unlikely since strong wind shear creates turbulence intensities $I_u = \sigma_u/\bar{u}$ that are typically around 0.5 (Tab. 4.15), a value usually given as the threshold above which Taylor's hypothesis becomes inapplicable (Willis and Deardorff, 1976). Additionally, a strong pressure transport term may result in different propagation velocities for different wave numbers.

Dissipation was calculated in bands between 0.1 and 1 s^{-1} , which were identified as the most appropriate since higher frequencies are contaminated by back-folding and limited by instrument path length. The ISR-slope was calculated as the average slope of the longitudinal spectra converted to wave numbers in the ISR (Tab. 4.15 for U1). At U1 at all measurement levels, the slope is slightly lower than the theoretical value of $-5/3$, which is interpreted as an indication that small production rates still ex-

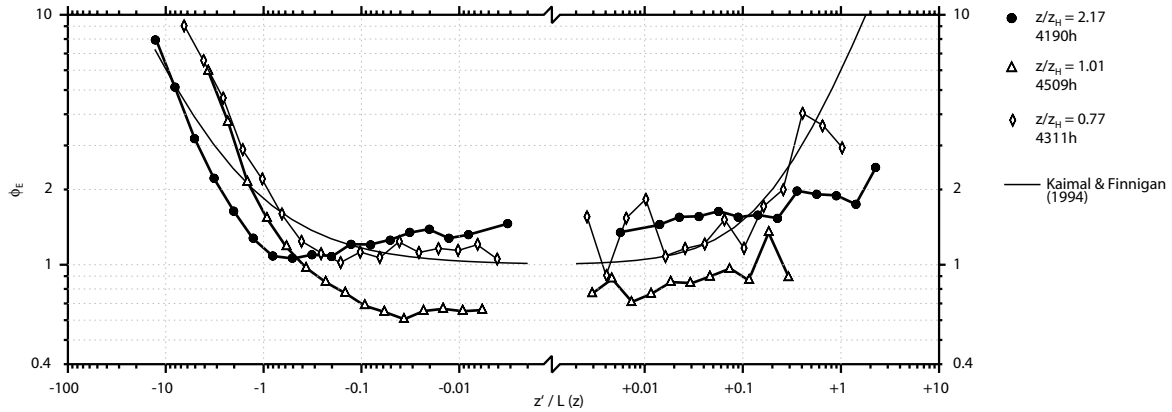


Figure 4.40: Locally scaled dissipation rate ($\phi_\epsilon = kz'\epsilon(z)/u_*^3(z)$, class median) against local stability determined by z'/L at U1. Data source: Sonics A, C and F, hourly values, November 1, 2001 to July 15, 2002, all stabilities.

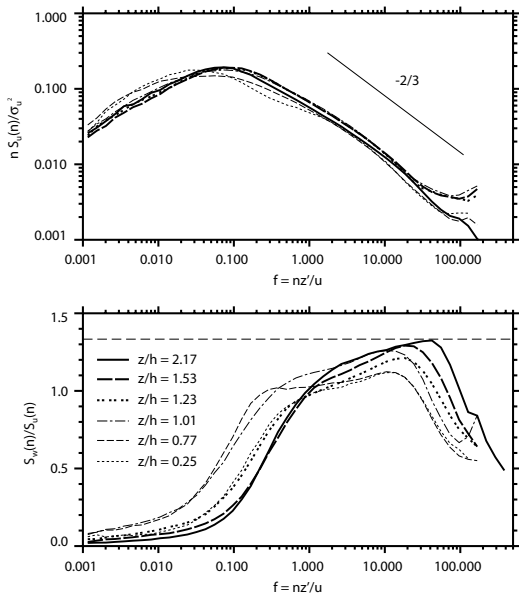


Figure 4.41: Top: Longitudinal velocity spectra with the inertial subrange slope indicated. Frequencies are normalized by local horizontal wind velocity u and z' according Eq.4.28. Bottom: Ratio S_w/S_u at U1. The dashed line indicates the ratio S_w/S_u in local isotropy (4/3). Data source: sonics A to F, hourly spectra, November 1, 2001 to July 15, 2002, neutral stability.

ist in this range. Moreover, the ratio S_w/S_u is below 4/3, the theoretical value for local isotropy (Fig. 4.41). Both values suggest an increase of ISR-contamination with decreasing height. However, the values show that the contamination levels are still small compared to the energy passed down in the cascade and therefore, dissipation is affected by small errors. However, a calculation is not impossible per se. The inertial subrange of spectra in the street canyons is — compared to spectra from plant canopies — not significantly different from the sur-

face layer prediction. The error in Tab. 4.15 can be interpreted as the average quality of estimating the $-5/3$ slope fit at given height. It is calculated as the RMS deviation of band individual ϵ_i relative to the average ϵ of all bands ($n = 13$). Dissipation rates have only been calculated for runs with an ISR-slope between -1.4 and -1.8 .

The resulting dissipation rates are highest between $z/z_h = 1.2$ and 1.5 and decrease in both directions (Fig. 4.39). The dissipation rate is significantly smaller at S1 where shear production creates less TKE compared to the dense urban surfaces at U1 and U2.

Figure 4.40 illustrates the locally scaled $\phi_\epsilon(z) = kz'\epsilon(z)/u_*^3(z)$. Local scaling explains dissipation as a function of only z' , (local) u_* , and (local) kinematic heat flux. Any transport terms are neglected. As a consequence, local dissipation is believed to depend only on production by shear and buoyancy. At tower top (filled circles), values are higher than predicted in neutral runs and lower than the empirical function in unstable runs. This is mainly because transport terms Tt and Pt are not zero. Close to roof top (triangles), ϕ_ϵ is systematically lower than predicted by the local scaling approach because large amounts of TKE are exported by Tt and Tp from this layer and are not longer available for dissipation as we will see in the subsequent analysis. On the other hand, in the upper street canyon, dissipation is higher than predicted in most cases because of the import of TKE. In order to better predict ϵ in the urban roughness sublayer, transport terms have to be analyzed more deeply.

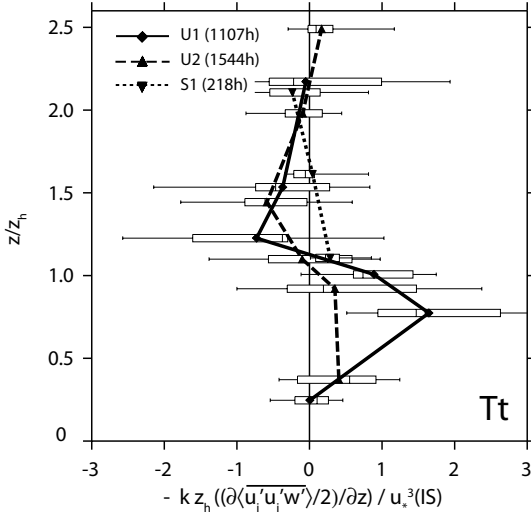


Figure 4.42: Vertical profiles of turbulent transport of TKE at U1, U2 and S1. Data source: all sonics, hourly averages, full operation periods, neutral stability.

Turbulent transport — Over the whole vertical profile, the TKE budget is not in local equilibrium, thus, locally produced turbulent kinetic energy does not equal local dissipation. TKE has to be vertically relocated by transport processes. Roth and Oke (1993a) suggested in their analysis of a suburban data set that large organized structures are involved in the relocation and transfer of turbulent kinetic energy. The only transport term that can be measured directly is the turbulent transport term (Tt). The gradient $\partial(u'_i u'_i w')/2/\partial z$ has been approximated by a cubic spline interpolation similar to the one described for the turbulent shear production term.

In neutral runs, on average all three third order moments of type $w' u_i'^2$ transport variances downwards, and strongest transport of TKE is measured around z_h (cf. Fig. 4.28c, f and i). Above $z/z_h = 2$, Tt is small in neutral runs (Fig. 4.43). With decreasing height, the transport term becomes important. The divergence results in a layer with a net export of TKE above the roofs and in a layer with a net import of TKE in the upper street canyon (Fig. 4.42). In other words, Tt transports excess TKE from the region above rooftop ($1.2 < z/z_h < 2$) down into the upper part of the street canyon. The crossover from export to import coincide roughly with the inflection point of the wind profile at U1 and U2 ($z/z_h \approx 1.2$). At S1, the crossover is higher (at $z/z_h \approx 1.6$), and the overall magnitude of the transport term is less pronounced, but note that all other terms of the TKE budget are also smaller. At U1, in the upper canopy,

Table 4.16: Turbulent transport (Tt) of TKE and estimation of the dispersive transport (Td) of TKE normalized by $kz_h/u_*^3(IS)$ for neutral conditions at U1. Data source: Sonics A to F, hourly values, November 1, 2001 to July 15, 2002, neutral stability at tower top $n = 1107h$.

z/z_h	Tt	Td	$ Td /(Tt + Td)$
2.17	-0.05	—	—
1.53	-0.37	-0.05	11%
1.23	-0.73	-0.09	11%
1.01	+0.89	-0.08	9%
0.77	+1.65	+0.06	4%
0.25	+0.01	+0.02	80%

Tt is the most important source of TKE and 10 times more important than local shear and buoyant production together (neutral and unstable, Fig. 4.43). Layers with a positive turbulent transport term in the upper street canyon correspond to the observed region of dominating large scale sweeps in the momentum JPDFs (Section 4.2.4). Down at street level, the magnitude of Tt is not relevant. This pattern fits well to the mixing layer analogy where turbulence is vertically relocated down into the canopy, the "low speed flow" (Brunet et al., 1994). The present results are in qualitative agreement with observations in forests (Leclerc et al., 1990; Meyers and Baldocchi, 1991) and simulations (Shen and Leclerc, 1997). Plant canopies show a slightly lower height of minimum Tt , which typically coincidences with z_h .

In the upper part of the profile, in the above-roof layer ($z > z_f$), the normalized Tt becomes stronger negative with increasing destabilization (Fig. 4.43), which is mainly an effect of the normalization by a (smaller) $u_*^3(IS)$.

Dispersive transport — The dispersive term $\overline{u'_i u_i''}$ in Td has been approximated by

$$\frac{\overline{u'_i u_i''}(z)}{u_*^2(IS)} \approx \frac{\overline{u'_i u_i}(z)}{u_*^2(IS)} - \langle \frac{\overline{u'_i u_i}}{u_*^2(IS)} \rangle(z) \quad (4.35)$$

and since $\langle \bar{w} \rangle = 0$, we again assume $\bar{w}''(z) = \bar{w}(z)$. The estimated dispersive transport term Td is summarized in Tab. 4.16. Except at roof top ($z/z_h = 1.01$), the dispersive transport has the same sign as the turbulent transport, but is typically 10 times less important. The small values of Td in the TKE budget allow to neglect Td .

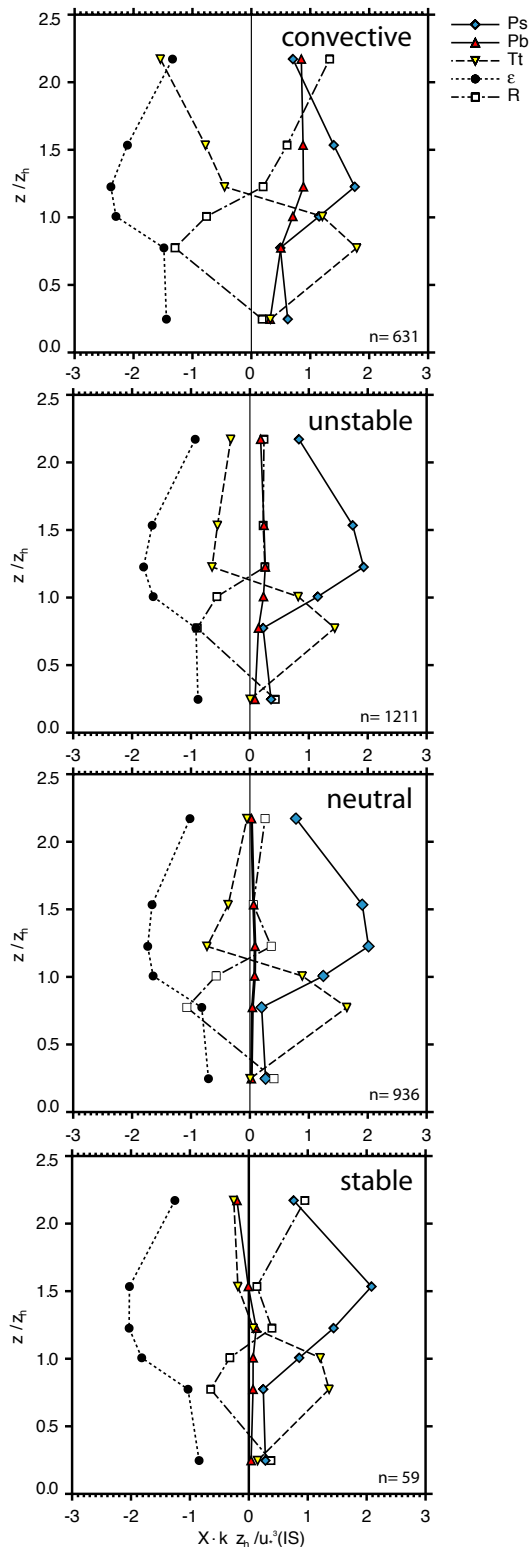


Figure 4.43: Normalized terms (X) of the TKE-budget for different stabilities (tower top) at U1. R denotes the residual term. Data source: Sonics A to F, hourly average values, November 1, 2001 to July 15, 2002, stability classification according Tab. 4.4.

Residual Term — Pressure transport is likely the most important non-measured term. Experimental results from pressure fluctuations are sparse (e.g. Elliott, 1972; Katul et al., 1996). Efforts to measure Tp directly by eddy-correlation are associated with instrumental problems (Wilczak et al., 1992). In the present setup, no attempts were made to measure the pressure transport directly. Here, the residual term is mainly interpreted as pressure transport. The results have to be interpreted with care since a residual term includes all errors of the measurements and all simplifications.

The analysis of the residual term suggests that pressure disturbances are primarily created in the region around roof top and in the upper street canyon (Fig. 4.43). Pressure transport relocates TKE from the roof layer and exports it up into higher layers and also down into the very bottom of the street canyon. In relative numbers, the pressure transport is an important source only in the lowest part of the street canyon. The observed pattern where pressure transport is a sink at roof top and a source in the lower street canyon is in qualitative agreement with the few indirect measurements of the pressure term in plant canopies (Maitani and Seo, 1985; Shaw et al., 1990) and with numerical model results (Shen and Leclerc, 1997; Dwyer et al., 1997).

The results from the LES study by Dwyer et al. (1997) suggest that thermal stability affects Tp by increasing it substantially under unstable stratifications. Stability mainly affects the higher above-roof layer ($z > z_f$) where pressure transport and turbulent transport are of opposite sign. This corresponds to observations in the surface layer (McBean and Elliott, 1975).

Turbulence produced by moving vehicles — In the bottom of the street canyon, the traffic produced turbulent kinetic energy Pt is part of the residual term. However, no correlation is found between the magnitude of the residual term and the traffic load at U1. Here, traffic load was counted over 4 weeks during the measurement campaign. The moderate traffic load (2000 vehicles per day) and the low speed limit (30 km/h) do not seem to strongly influence street canyon turbulence.

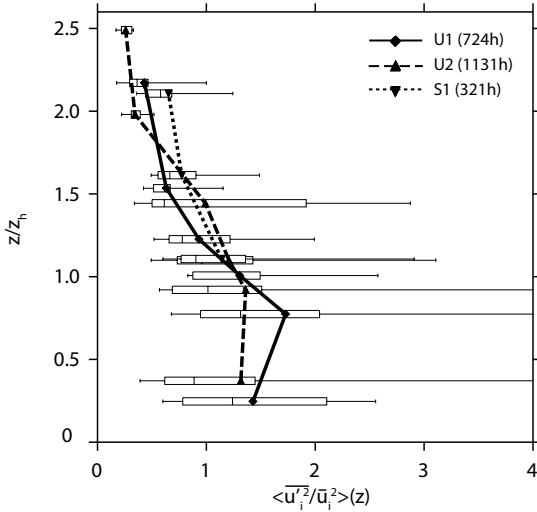


Figure 4.44: Ratio between turbulent kinetic energy (TKE) and mean kinetic energy (MKE) for neutral runs. Data source: all sonics, hourly averages, full operation periods, neutral stability.

4.3.3 Velocity variances

The ratio between turbulent kinetic energy and mean kinetic energy increases with decreasing height. The ratio shows a maximum between z_d and z_h and stays roughly constant in the lower street canyon (Fig. 4.44). Above z_f , slightly higher values are observed at S1 compared to U1 and U2. This reflects the effect of the higher roughness of the suburban surface with single buildings, expressed by the higher z_0/z_h value.

Local scaling — Many early urban studies demonstrated that velocity variances well above urban surfaces do only vary marginally from the prediction of Monin-Obukhov similarity theory (Brook, 1972; Högström et al., 1982; Steyn, 1982). Because in the roughness sublayer, velocity variances do not scale with a global $u_*(IS)$ as they do in the inertial sublayer, Högström et al. (1982) introduced a local scaling concept. In local scaling, the Obukhov length $L(z)$ is calculated with explicitly local values of $u_*(z)$ and $\overline{w'\theta'}(z)$. Local advection, turbulent transport and pressure transport of velocity variances are neglected.

Most previous studies address velocity variances with this local scaling approach, and report slightly different constants in the similarity relationships (e.g. Rotach, 1993b; Roth and Oke, 1993b; Feigenwinter, 2000). For a comparison with these exper-

iments, the local scaling approach has been applied to the present data set. To provide a comparable data set, the coordinate system has been rotated into local horizontal wind direction, hence addressing variances of u_l and v_l .

Frequency, intensity, and life span of turbulent structures all determine the integral variance of a time series. Local production of TKE (expressed in neutral conditions by $u_*(z)$ only) does indirectly describe the product of intensity and frequency of disturbances. A well behaved shape of velocity spectra links life span and intensity, i.e. strong excursions are related to large structures, which have a longer life span. Up to this point, the argumentation agrees with classical Monin-Obukhov similarity theory. But if transport of TKE is considered relevant, and transport processes export TKE before it can dissipate ad locum, this may reduce the ratio between TKE and local production and hence lower any $\sigma_{u_i}(z)/u_*(z)$.

In the previous section, we concluded that above z_f , Tp is counter-directed to Td , and that in neutral conditions, the transport terms are small compared to shear production. This supports the partial success of a local scaling, but also attributes the slight differences in the similarity constants to transport processes.

Neutral limits — Variances of u and v are typically contaminated by low frequency contributions from the outer layer. This results in larger scatter of u and v in the similarity functions than for w , as indicated by the error bars in Fig. 4.45 and 4.48.

Close to the inflection point of the wind profile, around z_e , the neutral limit of $\sigma_{ul}(z)/u_*(z)$ is lower compared to surface layer values (Fig. 4.45a, Tab. 4.17). On the other hand, in this roof layer, the neutral limit of $\sigma_{ul}(z)/u_*(z)$ is still higher than plane mixing layers values, which are typically 1.7 (Rau-pach et al., 1996). Individual values from selected flow sectors reach the plane mixing layer limit of 1.7. Figure 4.46 illustrates that there is a strong dependence of the neutral limit of $\sigma_{ul}(z)/u_*(z)$ on the ambient wind direction above roofs. For example, flow over the flat roofs at U1 has an average neutral $\sigma_{ul}(z)/u_*(z) = 1.69$ at z_h and flow over the pitched roof row shows average values around 1.73 at $z_h = 1.53$.

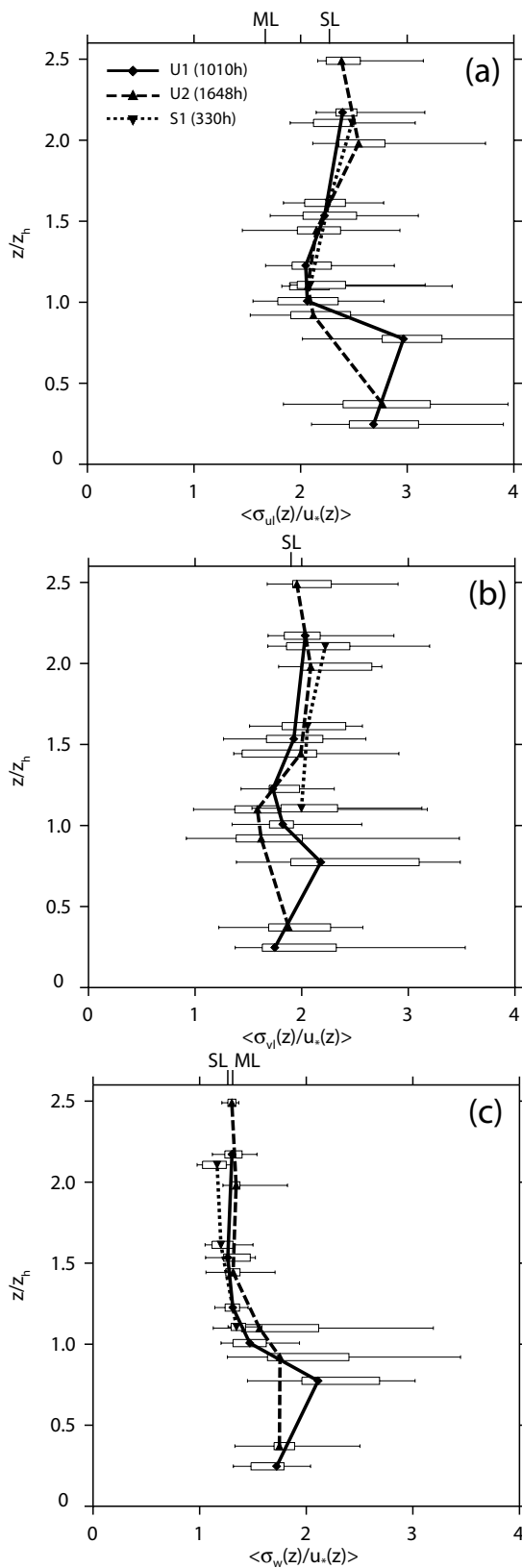


Figure 4.45: Profiles of the neutral limits of locally scaled velocity variances $\sigma_{ul}(z)/u_*(z)$ (a), $\sigma_{vl}(z)/u_*(z)$ (b) and $\sigma_w(z)/u_*(z)$ (c) at U1, U2 and S1. SL and ML denote the surface layer and the plane mixing layer limits. Data source: all sonics, hourly averages, full operation periods, neutral stability.

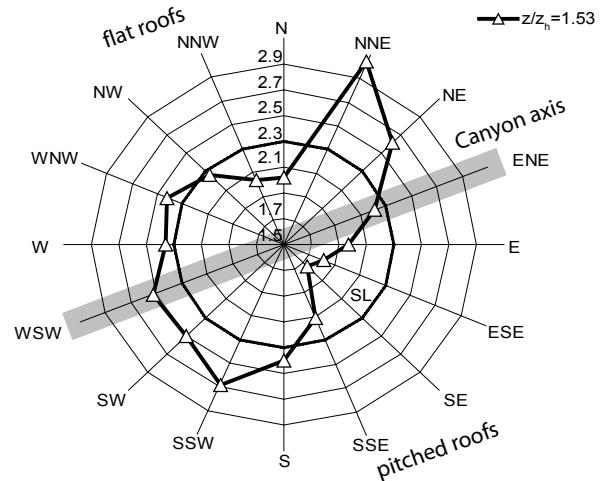


Figure 4.46: Locally scaled $\sigma_{ul}(z)/u_*(z)$ against ambient wind direction at U1, $z/z_h = 1.53$. Data source: Sonic E, hourly averages, November 1, 2001 to July 15, 2002, neutral stability, $n = 1010h$.

Variances created at roof level do not stay in this layer for a long time and are transported down in the street canyon before they are dissipated. These sweeps enhance $\sigma_{ul}(z)/u_*(z)$ in the whole street canyon, because here, local production by $u_*(z)$ is small.

The slightly higher values of $\sigma_{ul}(z)/u_*(z)$ at tower top may reflect either an enhanced contribution from inactive turbulence, or might be an effect of pressure transport. In the previous section, we stated that there is some evidence for pressure transport to relocate TKE from z_f into higher layers.

Generally, for locally scaled $\sigma_{vl}(z)/u_*(z)$, neutral limits fit adequately to surface layer predictions. Similarly to $\sigma_{ul}(z)/u_*(z)$, $\sigma_{vl}(z)/u_*(z)$ is also characterized by a slight reduction close to z_e . The channelling into the street canyon suppresses lateral deviations, and, in contrast to $\sigma_{ul}(z)/u_*(z)$, $\sigma_{vl}(z)/u_*(z)$ is not substantially enhanced in the street canyon.

For $\sigma_w(z)/u_*(z)$, profiles show good agreement to the surface layer values down to $1.2z_h$. No reduction is observed at z_f . In both street canyons, below $1.2z_h$, $\sigma_w(z)/u_*(z)$ increases significantly towards a maximum at $0.8z_h$. Here, in the upper street canyon, two processes enhance $\sigma_w(z)/u_*(z)$. First, the above turbulent downward transport of variance from the roof layer, and secondly, variances that were previously in the longitudinal may be rotated

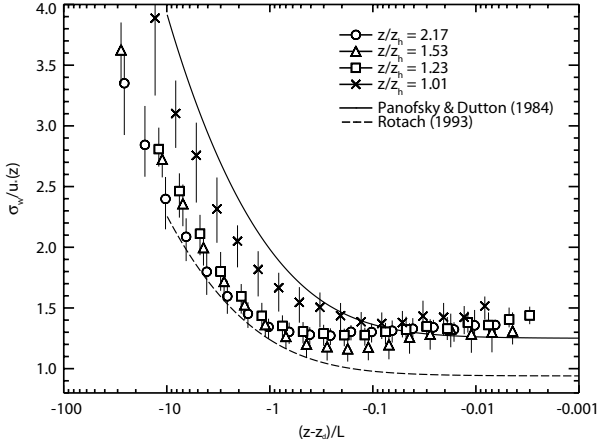


Figure 4.47: Locally scaled velocity variances $\sigma_w(z)/u_*(z)$ at the above roof levels against local stabilities at U1 for unstable runs. Data source: sonics C to F, hourly averages.

and deflected and hence channelled into a measured σ_w in the street canyon. At street level, $\sigma_w(z)/u_*(z)$ is again decreasing at both street canyon sites.

Stability dependence — The graphs in Fig. 4.48 illustrate the locally scaled similarity relationships for $\sigma_{u_i}(z)/u_*(z)$. Similar to other studies above urban surfaces (Rotach, 1993b; Feigenwinter et al., 1999), all three normalized standard deviations are below the classical SL-values in the unstable range. The differences between measured values and the SL-prediction increase with distance to the roofs. Revisiting the TKE-budget in Fig. 4.43, an increased magnitude of the normalized turbulent transport term is found (i) with increasing destabilization and (ii) with increasing height above roofs. Hence — always relative to u_* — variances are exported and local values are reduced.

Some studies report decreasing values for a_i with increasing z_0 . The review by Roth (2000) can not confirm such a trend. It is likely that with higher roughness, stronger mixing layers are formed. These mixing layers enhance turbulent and pressure transport, and hence remove variances in layers close to the roofs compared to local production.

4.3.4 Eigenvalue analysis

In this section, an alternative approach to velocity variances is tested. The above classification into σ_{ul} , σ_{vl} and σ_w is problematic within the street canyon.

Table 4.17: Neutral limits a_i (Eq. 2.79) for locally scaled $\sigma_{ul}/u_*(z)$, $\sigma_{vl}/u_*(z)$ and $\sigma_w/u_*(z)$. Values of a_i and b_i are determined with a numerical approximation in the unstable range $-10 < z'/L(z) < 0$ to minimize the RMS of the logarithm of A_i .

Site	z/z_h	a_u	a_v	a_w	n
U1	2.17	2.48	1.94	1.34	547
	1.53	2.30	1.87	1.28	1029
	1.23	2.13	1.94	1.36	1044
	1.01	2.20	1.79	1.46	1012
	0.77	3.00	2.03	2.00	611
	0.25	2.58	1.85	1.47	1059
U2	2.49	2.37	1.82	1.31	1250
	1.98	2.40	1.94	1.33	1258
	1.44	1.93	1.63	1.30	2919
	1.10	1.98	1.62	1.53	2056
	0.92	1.86	1.50	1.67	2052
	0.37	2.30	1.76	1.71	1995
S1	2.11	2.25	1.97	1.08	150
	1.61	2.26	1.96	1.17	163
	1.11	2.12	1.80	1.32	240
SL		2.2	1.9	1.25	
urban		1.88	1.52	1.15	

If approaching the three dimensional surface, the question of the local (scale dependent) direction of the surface becomes evident. For example close to a wall — in a local context — horizontal and vertical axis are swapped. Hence, what we see in σ_{vl} or σ_{ul} corresponds to σ_w over a flat surface, which is in that case the wall.

Eigenvalues are independent of the frame of reference. Their value is therefore not influenced by any arbitrary configuration of the coordinate system. We retain an independent information on (i) the orientation of the eigenvectors in space (principal axis) and (ii) the relative importance of all velocity variances in the direction of these three principal axis. The eigenvalues e and eigenvectors \mathbf{g} of the velocity correlation tensor \mathbf{M}_{ij} (cf. Eq. 2.10) are defined by

$$\mathbf{M}_{ij}\mathbf{g} = e\mathbf{g}. \quad (4.36)$$

The solutions of 4.36 are

$$\det\{\mathbf{M}_{ij} - e\mathbf{I}\}, \quad (4.37)$$

where \mathbf{I} is the identity matrix. There are exactly 3 eigenvalues and eigenvectors that fulfill 4.36. The three eigenvectors are all perpendicular. By definition, the eigenvalues are ordered by their magnitude,

$$e_1 \geq e_2 \geq e_3. \quad (4.38)$$

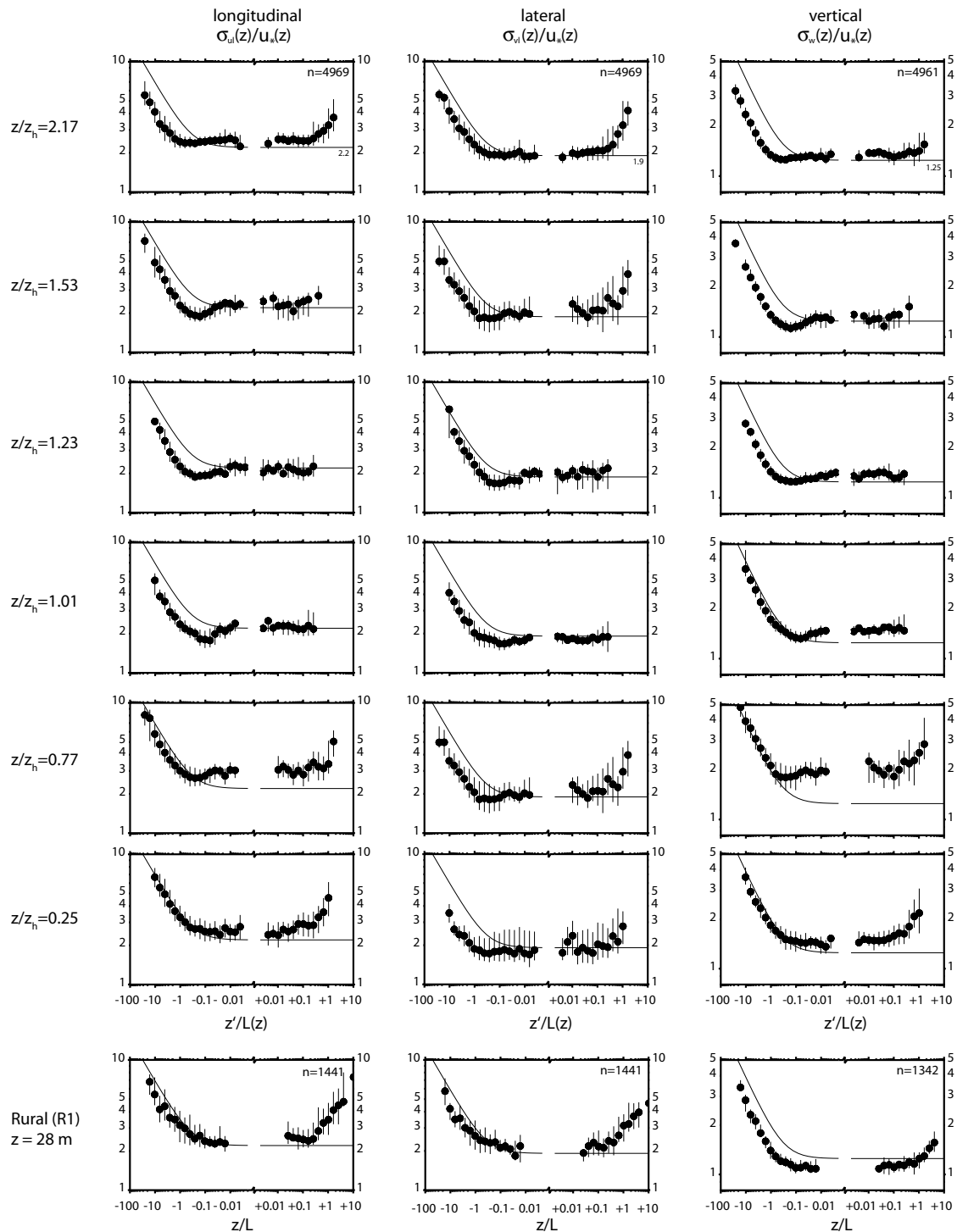


Figure 4.48: Locally scaled velocity variances $\sigma_{ul}(z)/u_*(z)$, $\sigma_{vl}(z)/u_*(z)$ and $\sigma_w(z)/u_*(z)$ against local stability at U1. The thin lines are relationships according to Eq. 2.81 with surface-layer coefficients from Tab. 2.1. Data source: sonics A to F, hourly averages, November 1, 2001 to July 15, 2002, all stabilities.

Table 4.18: Eigenvalues e_i of the velocity correlation tensor \mathbf{M}_{ij} at U1., normalized by twice the TKE. Data source: Sonics A to F, hourly values, November 1, 2002 to July 15, 2002, neutral stability only, $n = 1010h$.

z/z_h	$e_1/\overline{u_i'^2}$	$e_2/\overline{u_i'^2}$	$e_3/\overline{u_i'^2}$
2.17	0.61	0.31	0.12
1.53	0.56	0.31	0.12
1.23	0.52	0.32	0.13
1.01	0.55	0.32	0.17
0.77	0.57	0.25	0.19
0.25	0.58	0.25	0.14
R1	0.62	0.29	0.09
R2	0.60	0.34	0.06
SL	0.55	0.32	0.14

Their sum is equal twice the TKE, which is equal the trace of \mathbf{M}_{ij}

$$e_1 + e_2 + e_3 = \overline{u_i'^2}. \quad (4.39)$$

Eigenvectors — The polar plots in Fig. 4.49 illustrate the orientation of the eigenvectors at U1, and additionally for a rural measurement close to the surface (R2). The plots can be interpreted similar to a map of a globe, as seen from the North pole. The center point of the plot corresponds to the North pole and the outer border is the equatorial axis. The longitude corresponds to the horizontal direction of the eigenvector relative to the mean wind direction at given height (which flows from top to bottom, as indicated by the arrow in the top left). ξ denotes the latitude, which is the inclination of the principal axis to the horizontal plane. On this ‘map’, the piercing point between the eigenvector and our globe is indicated by a dot. Figure 4.49 shows piercing points from all data sampled at U1.

At the topmost level, the first eigenvector \mathbf{g}_1 roughly points in the direction of \mathbf{x} (at the equatorial plane top and bottom). \mathbf{g}_2 is the lateral component, and \mathbf{g}_3 points to the vertical (and is therefore close to the pole). With decreasing height, the orientation of the principal axis become more and more unordered, reflecting different realizations of the approaching flow.

Eigenvalues — In isotropic turbulence, $e_1 = e_2 = e_3$. If $e_1 \gg e_2 \geq e_3$ we encounter a cigar shaped distribution, with one axis contributing most to the

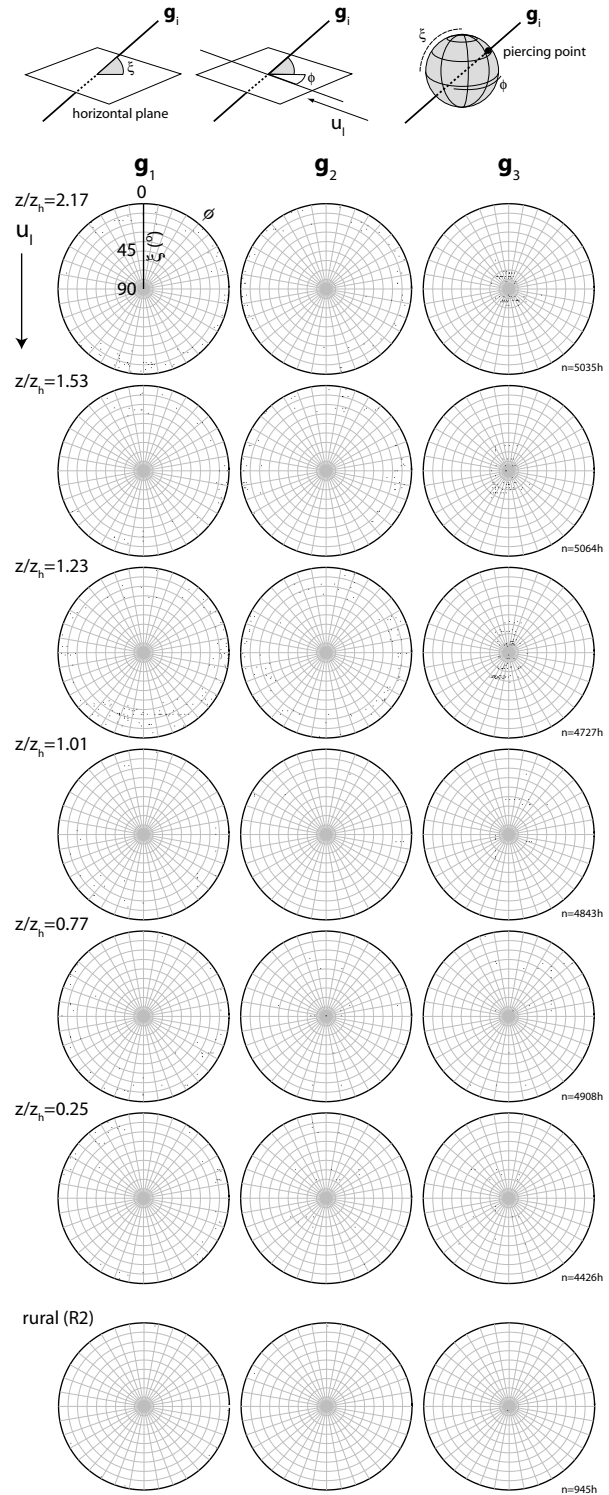


Figure 4.49: Orientation of the eigenvectors \mathbf{g}_i of the velocity correlation tensor \mathbf{M}_{ij} in the cartesian space. The plots illustrate the orientation relative to the mean wind direction u_i (azimuth) and the vertical inclination (radius) at U1 and R2. Data source: Sonics A to F (U1) and A (R2), hourly averages, full operation periods, all stabilities.

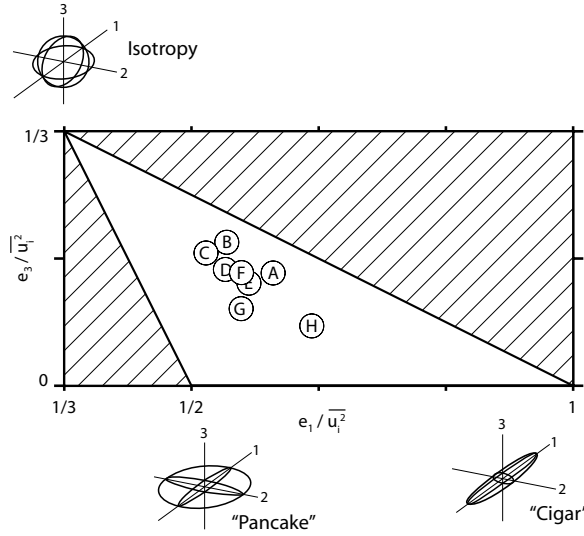


Figure 4.50: Average ratio of the eigenvalues $e_1 : e_2 : e_3$ at U1 drawn into the ‘eigenvalue triangle’, where $e_1/\overline{u_i'^2}$ is shown against $e_3/\overline{u_i'^2}$. The associated shapes of the velocity variance components are indicated by the sketches. Data source: sonics A to H, hourly averages, all stabilities.

total TKE. In the case $e_1 \approx e_2 \gg e_3$, we have a pancake shaped distribution. Figure 4.50 illustrates sketches of the associated distributions. The triangle draws $e_1/\overline{u_i'^2}$ against $e_3/\overline{u_i'^2}$. The hatched region is excluded due to the condition in Eq. 4.39. Under neutral conditions in the surface layer, $e_1/\overline{u_i'^2} = 0.55$, $e_2/\overline{u_i'^2} = 0.32$ and $e_3/\overline{u_i'^2} = 0.14$ (which corresponds to the ratio $a_u^2 : a_v^2 : a_w^2 = 2.5^2 : 1.9^2 : 1.25^2$, Tab. 4.18)

With decreasing height, there is a tendency of the flow to be more isotropic. While $e_1/\overline{u_i'^2}$ slightly decays, $e_2/\overline{u_i'^2}$ and especially $e_3/\overline{u_i'^2}$ become more important towards roof top (Fig. 4.51). Deeper in the street canyon, the opposite trend is observed. Due to channelling, the flow is mechanically forced into one principal direction, and excursions are suppressed by walls and the street floor. This results in a higher $e_1/\overline{u_i'^2}$. Here, the distribution resembles the ‘cigar’. A special case is found close to the wall (Sonic H) where we observe a ‘pancake’ distribution. The third eigenvalue e_3 is small compared to e_1 and e_2 and \mathbf{g}_3 is directed normal to the wall.

4.3.5 Summary

- Length scales of TKE within the street canyon do not vary significantly with height. The length scales of longitudinal fluctuations in-

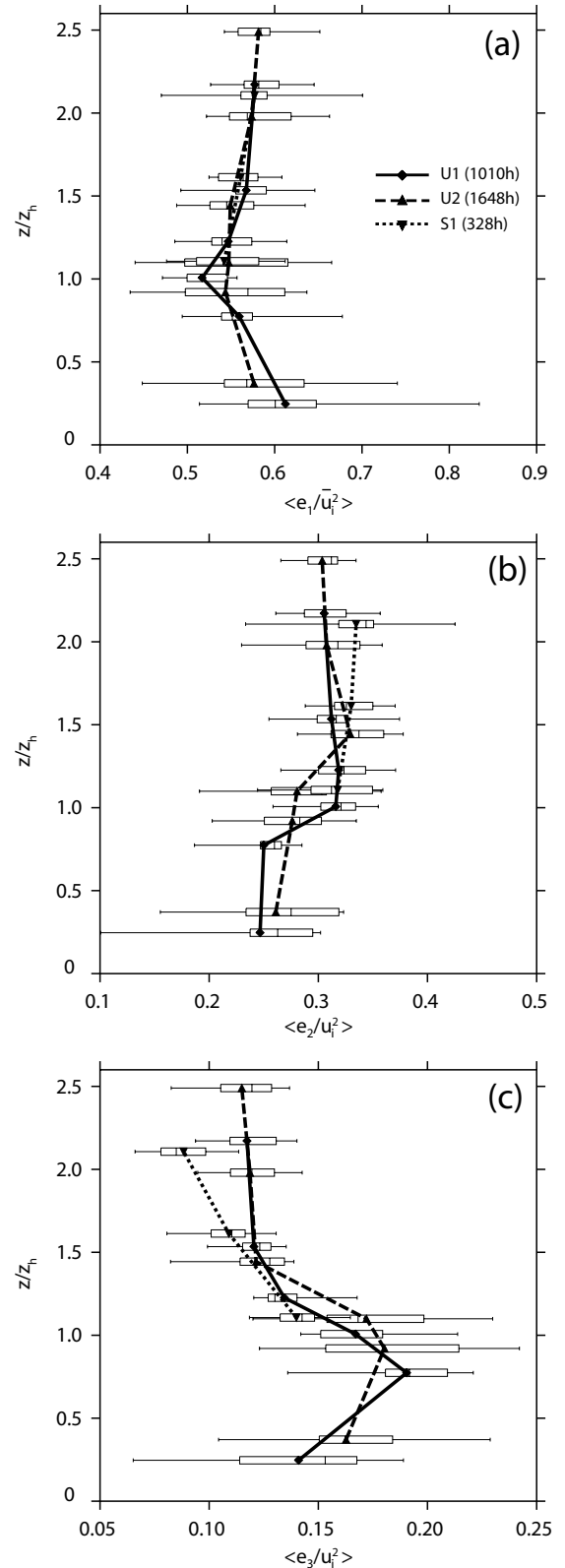


Figure 4.51: Vertical profiles of scaled eigenvalues $e_i/\overline{u_i'^2}$ of the velocity correlation tensor \mathbf{M}_{ij} at the three profile towers U1, U2 and S1. Data source: all sonics, hourly averages, full operation periods, neutral stability.

creases with depth. Above the roofs, length scales increase nearly linear with height. This is considered in a modified scaling length z' , which is equal $z - z_d$ above the roofs and constant in the street canyon (Eq. 4.28).

- Shear production of TKE peaks above roof top and is by far the most important source in the budget of TKE above the roofs. Shear production decreases rapidly within the street canyon. Dispersive shear production can be neglected. The overall production / destruction of TKE by buoyancy is small compared to shear production, resulting in a predominantly neutral stability of the roughness sublayer. In unstable runs, buoyancy production increases nearly linear with height in the canyon layer, stronger in the roof layer and is constant with height above $z/z_h = 2$.
- The inertial subrange of spectra in the street canyons is — compared to spectra from plant canopies — not significantly different from the surface layer prediction. This allows the calculation of ϵ by the inertial subrange method. The resulting ϵ are highest at z_h and decrease in both directions. In most height layers, ϵ does not counterbalance local production.
- Turbulent transport exports TKE from the region above rooftop down into the upper part of the street canyon. In the upper street canyon, turbulent transport is the most important source of TKE. Pressure transport relocates TKE from the roof layer and put it up into higher layers and also down into the very bottom of the street canyon. Dispersive transport can be neglected.
- Velocity variances are not completely different from surface layer values by applying a local scaling approach. Differences can be mainly attributed to transport processes. In the roof layer, standard deviations normalized by shear production are lowest, which is interpreted as an indication that structures shed at this shear layer transport TKE in lower regions of the urban canopy.
- The introduced eigenvalue analysis illustrates that close to roofs, TKE is more isotropically distributed. In the street canyon, due to channelling, TKE is mainly put into one component.

4.4 Exchange processes of heat and mass

In this chapter, we focus on turbulent exchange processes of heat (Section 4.4.1), water vapor (4.4.2) and CO₂ (4.4.3). First in each section, the vertical profiles of flux densities through the urban roughness sublayer are analyzed. Then, exchange processes are investigated using quadrant analysis and cospectra. The analysis focuses on processes rather than corresponding magnitudes of flux densities. The climatological variations of the two turbulent heat flux densities in terms of the surface energy balance are addressed in the subsequent Chapter 4.5.

4.4.1 Turbulent exchange of heat

The vertical profile of $\overline{w'\theta'}$ — Assuming horizontal homogeneous conditions on a larger scale, and a negligible molecular diffusion, we can simplify the conservation of virtual acoustic temperature from Eq. 2.52 to*

$$\frac{\partial \langle \bar{\theta} \rangle}{\partial t} = \langle S_{\theta} \rangle - \frac{\partial \langle \overline{w'\theta'} \rangle}{\partial z} - \frac{\partial \langle \bar{w}''\bar{\theta}'' \rangle}{\partial z}. \quad (4.40)$$

S_{θ} is the source or sink term, which is mainly driven by the surface energy balance at the building-air interfaces enclosed in the layer. It may further include net radiation divergence and evapotranspiration / condensation in the air volume (Eq. 2.53), but both effects are small compared to the impact of the building-air interfaces. In Eq. 4.40 we relate the measured turbulent flux density divergence to these sources (or sinks) in a given layer, to a temperature change in this layer or to a counter-directed dispersive flux density divergence. The dispersive flux density $\langle \bar{w}''\bar{\theta}'' \rangle$ may be responsible for additional heat transport in the street canyon. It could not be measured with the present setup and attempts to estimate its magnitude similar to the procedure applied for momentum fail due to the lack of an appropriate scaling of the temperature profile.

The good agreement between the three profile towers encountered in the analysis of momentum exchange is not found in the vertical profiles of $\overline{w'\theta'}$. At U2, the vertical profile differs significantly from

* For simplicity, we assume that $\bar{\theta}$ is constant at the air-building interface, which is not mandatorily true, especially when sun position is low and radiative heating systematically favors a particular wall-exposition.

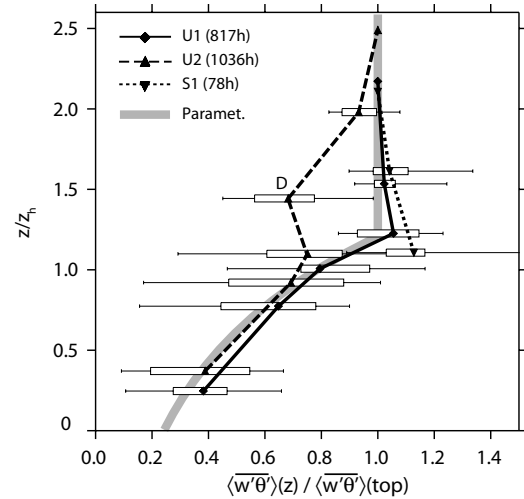


Figure 4.52: Horizontally averaged vertical profiles of $\overline{w'\theta'}$ normalized by its value at tower top at all three towers for convective situations. The thick gray line denotes the parametrization according to Eq. 4.41 with $z_e = 1.2z_h$ and $c_h = 1.4$. Data source: All sonics, hourly averages, median profiles, full operation periods, $z'/L < -0.5$. Error bars in this and the subsequent plots are similar to Fig. 4.8.

U1 and S1 (Fig. 4.52). Particularly, level D shows a reduced $\overline{w'\theta'}$ compared to corresponding heights at U1 and S1. The setup at U2 results in a number of situations in the afternoon, when the avenue canyon and the building-wall close to the sonics A to C are heated by direct solar irradiance. Simultaneously, the backyard to the East is shadowed (refer to the plan in Fig. 3.7). Due to the horizontal shift of the tower and the street canyon profile, level D measured exchange over the shadowed backyard during these conditions whereas sonics A to C probed the heated street canyon. The horizontal averaging procedure fails, because not only wind direction, but also sun-orientation affects the different realizations. The horizontally shifted profiles and the associated different source areas do not allow a calculation that can substitute a real horizontal average. Hence, we mainly focus on results of the thermally more ideal sites U1 and S1.

At U1 and S1, $\partial \langle \overline{w'\theta'} \rangle / \partial z$ is close to zero above most relevant building structures, namely in the layer $z/z_h > 1.2$ (Fig. 4.52). This suggests that S_{θ} and the local dispersive heat flux density divergence are negligible. The absence of building interfaces does not allow additional heat input in these layers.

Nevertheless, between $1.2 < z/z_h < 2.0$, a slight reduction of $\overline{w'\theta'}(z)$ with height is observed at U1 and S1. A decrease with height has been also re-

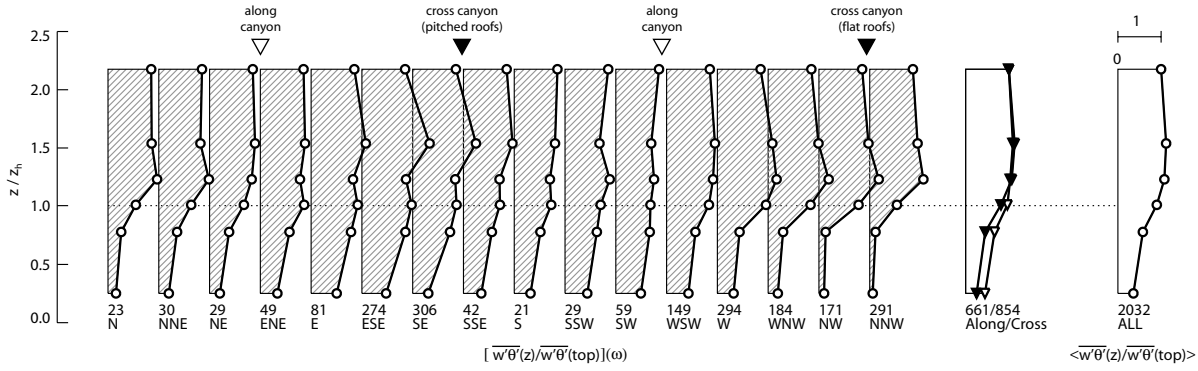


Figure 4.53: Vertical profiles of $\overline{w'\theta'}$ normalized by their value at tower top at U1 for different wind directions and all situations. Data source: Sonics A to F, hourly block averages, November 1, 2001 to July 15, 2002, all stabilities.

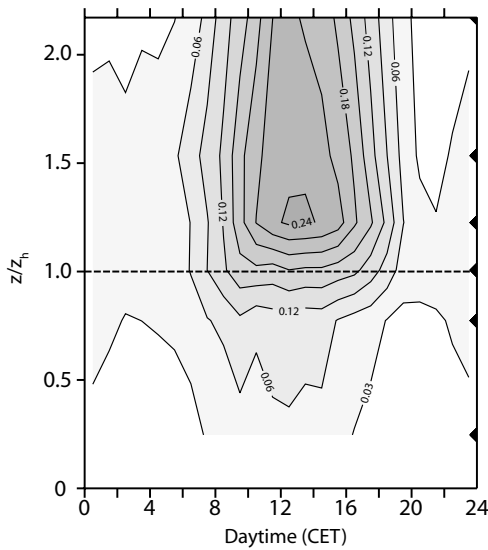


Figure 4.54: Average diurnal variation of $\overline{w'\theta'}$ within and above the street canyon at U1. Black triangles at the right axis indicate the six measurement heights. Data source: Sonics A to F, hourly block averages, June 12 to July 12, 2002, all situations.

ported from earlier urban studies (Rotach, 1991; Roth, 1991; Feigenwinter, 2000). The two latter studies argued that their decrease is an effect of different source areas*. The source areas of different levels do not incorporate mandatorily the same surface energy balance partitioning. In the present study, at least for U1, the slight reduction of $\overline{w'\theta'}$ with height is counterbalanced by an increasing $\overline{w'\rho'_v}$ (Section 4.4.3), suggesting that

* Rotach (1991) observed a more complex vertical profile of $\overline{w'\theta'}$ with first a decrease with height above z_h , and a continuous increase with height above $z_h = 1.5$. His observations show similarity to the profile at U2, but the theoretical frame given in Eq. 4.52 does not support an increase in the highest layers, if dispersive fluxes are small, temperature change and radiation divergence in the column is negligible and no building structures may act as heating surfaces anymore.

moisture availability is not homogeneously distributed. The overall impact of this heterogeneity at U1 is not crucial, and above $z/z_h = 1.2$, the horizontally averaged profile can be approximated by $\partial\langle\overline{w'\theta'}\rangle/\partial z = 0$. For nearly all wind directions, the measured divergence $\partial\overline{w'\theta'}/\partial z$ reaches values close to zero above $z/z_h = 1.5$ (Fig. 4.53), an indication that roughly the blending height z_* for the sensible heat flux is reached.

The profiles of $\overline{w'\theta'}$ suggest that strongest gradients are found around roof top (Fig. 4.54). This is indirectly supported by model calculations for the short-wave radiation divergence (cf. upcoming Fig. 4.68): the dense urban surface with its narrow street canyons absorbs mainly short-wave radiation in the roof layer and in the upper canopy. At U1, only about 15% of K_\downarrow gets directly through to the ground level in the yearly average. As a consequence, sources S_θ are strongest in the roof layer. These sources explain the strong vertical gradient $\overline{w'\theta'}/\partial z$ in the range $0.8 < z/z_h < 1.5$. Below, gradients slightly decrease, and the rate of the decrease depends on the flow configuration. Hence, the roofs and the upper street canyon can be regarded the *active surface*, even though a notable part of $\langle\overline{w'\theta'}\rangle$ origins from the deeper canyon.

From the present observations, a simple empirical parametrization of $\langle\overline{w'\theta'}\rangle$ is suggested, namely

$$\langle\overline{w'\theta'}\rangle(z) = \begin{cases} \overline{w'\theta'}(\text{IS}) & \text{for } z \geq z_e \\ \overline{w'\theta'}(\text{IS})e^{-k} & \text{for } z < z_e \end{cases} \quad (4.41)$$

with

$$k = c_h \frac{(z_e - z)}{z_e} \quad (4.42)$$

This parametrization is drawn in Fig. 4.52. $\langle w'\theta' \rangle(\text{IS})$ is the heat flux in the inertial sublayer above. z_e is the effective building height (previously encountered as the height of the inflection point of the mean wind profile). In the case of a hypothetical surface with uniform buildings, it would be expected that $z_e \approx z_h$. For the present urban surface with non-uniform building height, $z_e = 1.2z_h$ leads to best results. c_h is an empirical constant, which was determined for each run at U1 and U2 separately by minimizing the RMS error of the levels below z_e (only runs with $\overline{w'\theta'}(\text{IS}) > 0.05 \text{ K m s}^{-1}$ have been considered). $\langle w'\theta' \rangle(\text{IS})$ was approximated by the measurement at tower top. On the horizontal average, c_h is around 1.4 at both urban sites. The values of c_h might depend on morphometric configuration, especially on the vertical distribution of surfaces contributing to a sensible heat flux.

Gradients of $\partial \langle w'\theta' \rangle / \partial z$ are less pronounced during along-canyon flow compared to cross-canyon flow (Fig. 4.53). This can be seen as an indication that street canyon air masses are better coupled with the air aloft under along-canyon-flow, or that dispersive flux densities are larger for cross-canyon flow with a vortex, if assuming an exchange of similar magnitude. As a consequence, c_h for along-canyon flow is smaller ($c_h \approx 1$) compared to cross-canyon flow ($c_h \approx 2.5$) at U1. A further separation can be observed for cross-canyon flow. If the profile measures at the leeward wall, significantly stronger gradients of $\langle w'\theta' \rangle$ and a higher c_h are observed at both urban sites.

Implications for stability — The vertical flux density divergence of $\overline{w'\theta'}(z)$ and the vertical divergence of $u_*(z)$ (Section 4.2.2) together with the height-dependent scaling length $z'(z)$, result in a local Obukhov-Length $L(z)$, which is not constant with height.

During the day, in the roof layer, the air typically shows a tendency towards more neutral stabilities, which is a consequence of the strong shear production (Fig. 4.55). With increasing height above roofs, $\zeta(z)$ tends towards more unstable classes. A similar destabilization with height is observed at U2 and S1 (not shown).

During the night, $\overline{w'\theta'}$ transports energy away from the surface in the majority of runs. This phenom-

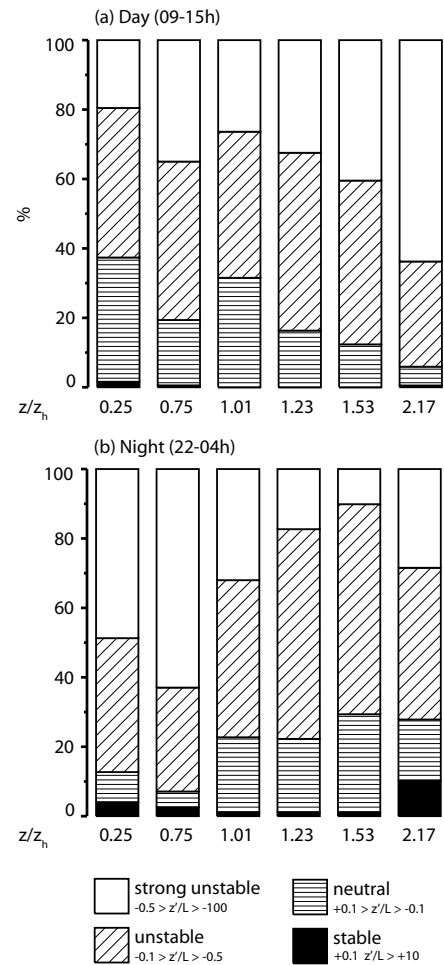


Figure 4.55: Histogram of locally scaled stability classes at different heights at U1, separately calculated for (a) daytime and (b) nocturnal situations. Data source: Sonics A to F, hourly block averages, November 1, 2001 to July 15, 2002, $n = 3620\text{h}$.

ena is mainly driven by high storage release and is discussed more deeply in Section 4.5.7. As a consequence, the nocturnal atmosphere close to the surface remains unstable. Below z_h , convective classes are most pronounced due to low shear production in the street canyon. In the roof layer, stable situations rarely occur ($< 3\%$). At tower top, only 10% stable cases are recorded.

Temperature variance — Variance of virtual acoustic temperature σ_θ is roughly constant with height (Fig. 4.56a). This suggests that σ_θ is equally distributed over the whole roughness sublayer, mainly because of efficient mixing and transport processes. From the vertical profile at U1 and S1, there is some evidence for a slight increase of σ_θ around roof level. At U1, a decrease of σ_θ down into

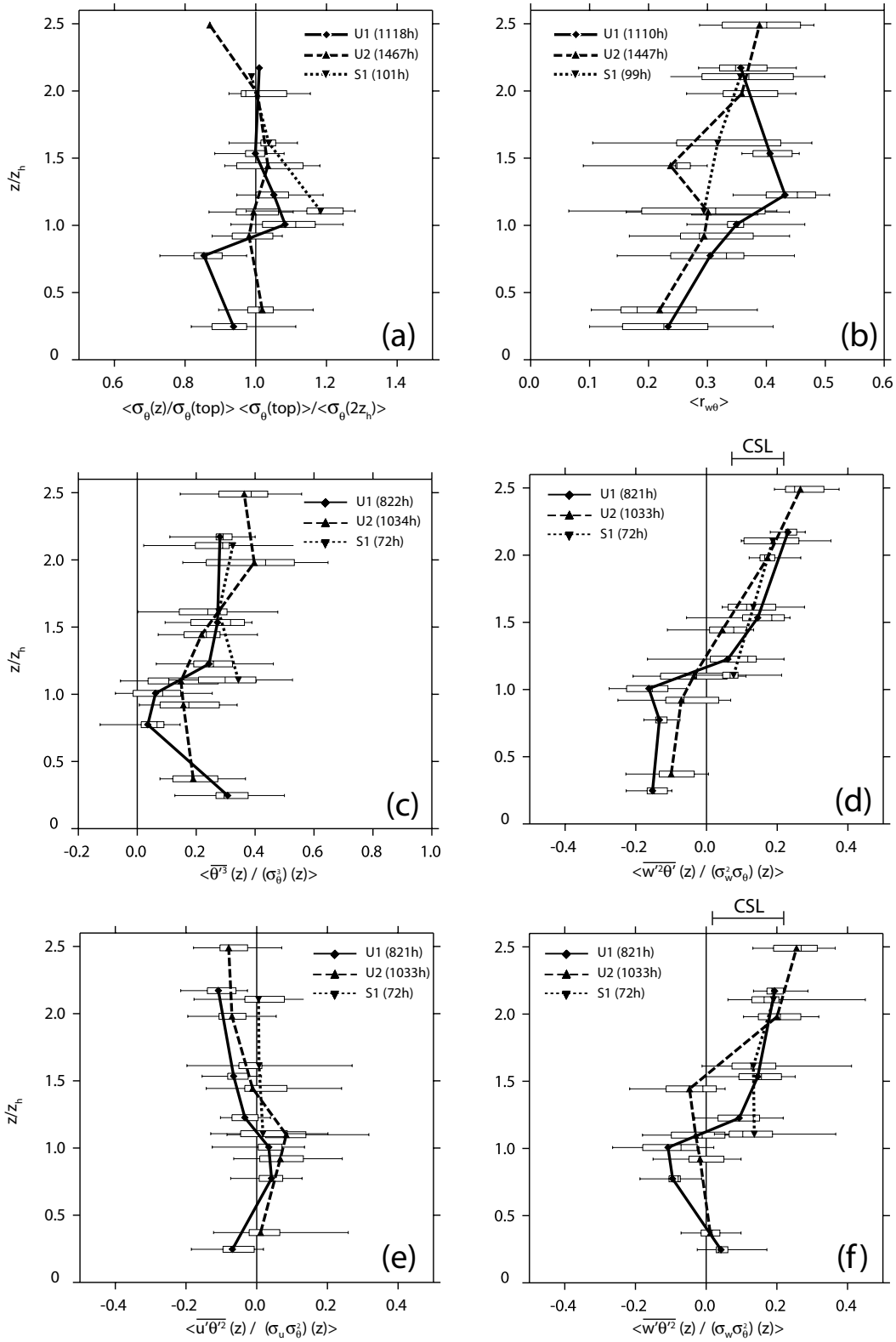


Figure 4.56: Vertical profiles of (a) $\langle \sigma_\theta(z) / \sigma_\theta(\text{top}) \rangle$, (b) $\langle r_{w\theta} \rangle(z)$, (c) skewness $\langle \overline{\theta'^3} / \sigma_\theta^3 \rangle(z)$, (d) $\langle \overline{w'^2 \theta'} / (\sigma_w^2 \sigma_\theta) \rangle(z)$, (e) $\langle \overline{u'^2 \theta^2} / (\sigma_u \sigma_\theta^2) \rangle(z)$ and (f) $\langle \overline{w'^2 \theta^2} / (\sigma_w \sigma_\theta^2) \rangle(z)$ at all three profile towers. CSL denotes the convective surface layer values for the same stability range. Error bars in this and subsequent figures are defined in Fig. 4.8. Data source: All sonics, hourly block averages, full operation periods, convective stability only.

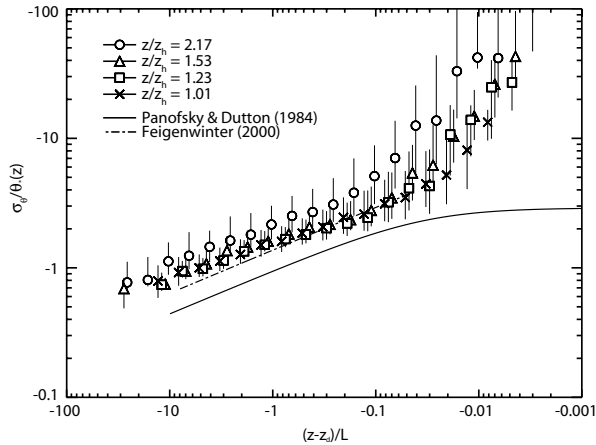


Figure 4.57: Local scaled temperature variances $\sigma_\theta(z)/\theta_*(z)$ at the above roof levels against local stability at U1 for unstable runs. Data source: sonics C to F, hourly averages.

the street canyon can be seen. The profile at U2 does not support much vertical variation.

Figure 4.57 illustrates locally scaled standard deviation of virtual acoustic temperature $\sigma_\theta(z)/\theta_*(z)$. The figure displays values from the four above-roof levels at U1 against stability. At all levels, the locally scaled $\sigma_\theta(z)/\theta_*(z)$ is stronger than predicted by the surface layer scaling (solid line). Also, previous urban studies reported higher values for $-\sigma_\theta(z)/\theta_*(z)$ (Oikawa and Meng, 1995; Feigenwinter, 2000). Modified parameters in the semi empirical relationship suggested by Feigenwinter (2000) better fit the values (dash-dotted line). Close to neutral stability, values take off, which is mainly an effect of the small θ_* , whereas simultaneously σ_θ is still higher than zero due to a contamination by large scale (inactive) temperature variance.

Interestingly, local scaling close to the roofs shows better agreement to the surface layer prediction than at the topmost tower level (Fig. 4.57). A similar pattern was observed by Feigenwinter (2000), who interpreted the higher $\sigma_\theta(z)/\theta_*(z)$ as an indication that thermal homogeneity is not given at his topmost measurement level.

The mixed moment $\overline{w'\theta'^2}$ describes the turbulent vertical transport of temperature variance. If its divergence $\partial\langle\overline{w'\theta'^2}\rangle/\partial z$ is non-zero, temperature variance is exported or imported from other layers. Figure 4.56f illustrates the vertical profile of $\overline{w'\theta'^2}$ for all three towers. In surface layer scaling, the normalized third-order moments $\overline{w'^2\theta'}/(\sigma_w^2\sigma_\theta)$ and $\overline{w'\theta'^2}/(\sigma_w\sigma_\theta^2)$ can be expressed as empirical func-

tions of ζ only (see Appendix in Katul et al., 1997). In the unstable and neutral surface layer, $\overline{w'\theta'^2}$ is greater than zero, hence indicating that temperature variance is transported upward (Wyngaard and Cote, 1971). The expected ranges for the normalized third-order moments in the convective situation are labelled ‘CSL’ in Fig. 4.56d and f.

$\overline{w'\theta'^2}$ is close to zero or negative in the street canyon (sweeps), small around roof level (equilibrium between sweeps and ejections), but large at tower top (ejections). Hence, there is a strong upward directed vertical flux of temperature variance at tower top and a downward directed one in the street canyon, at least at U1. As a consequence, around roof-top σ_θ is exported, and in the upper canopy, as well as above tower top, σ_θ is imported. This may explain the failure of the temperature variance method at tower top, and the fact that it delivers better results close to the roofs, where $\overline{w'\theta'^2}/(\sigma_w\sigma_\theta^2)$ is smaller (Section 4.1.3). Note that the measured variance σ_θ is further enhanced by inactive turbulence at all levels. The integral σ_θ may be regarded a superposition of (i) locally produced temperature variance described by $\overline{w'\theta'\partial(\hat{\theta}/\partial z)}$, (ii) vertical import or export of variance as described by $\partial\overline{w'\theta'^2}/\partial z$, and (iii) inactive contributions from larger scales.

Organized structures — To identify the relevant structures contributing to the turbulent heat exchange, joint probability density functions (JPDFs) $P(\hat{w}, \hat{\theta})$ were calculated similar to the procedure described for momentum flux (Section 4.2.4). In the case of a positive $\overline{w'\theta'}$, ejections denote warm upward motions (quadrant 2*) and sweeps are cool downward events (quadrant 4).

Figure 4.59 illustrates the vertical profile of JPDFs at U1 for unstable runs. In the right column, the corresponding non-Gaussian flux fractions (NGF) are drawn. NGFs are the counterpart of the non-Gaussian stress fractions (NGS) introduced in Section 4.2.4. NGFs show the difference between the actual JPDF and a Gaussian distribution $G(\hat{w}, \hat{\theta})$ with same $r_{w\theta}$.

Well above roofs, the exchange of $\overline{w'\theta'}$ is clearly dominated by ejections, and ΔS_0 is negative (Fig. 4.58a). At U1, ejections dominate down to 1.2 z_h .

* Note that quadrant numbering for momentum and scalars differ, see Fig. 2.2.5 for definitions.

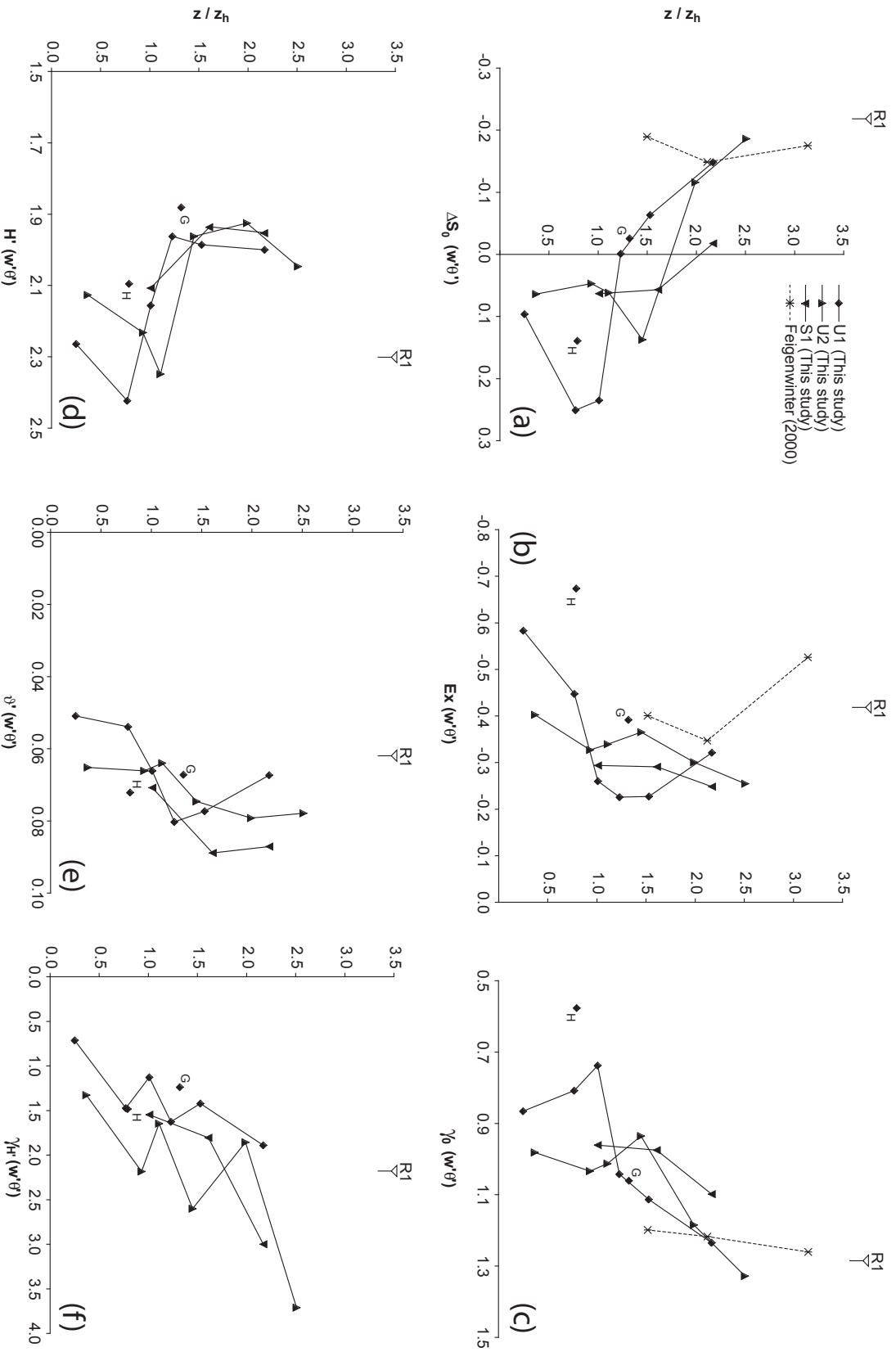


Figure 4.58: Vertical (median) profiles of quadrant measures at U1, U2 and S1 in comparison to results reported from the study of Feigenwinter (2000). G and H refer to the additional sonics at roof top and at the street canyon wall at U1. Data source: All sonics, temporal median profiles. from hourly JPPDFs, full operation periods, unstable stratification only.

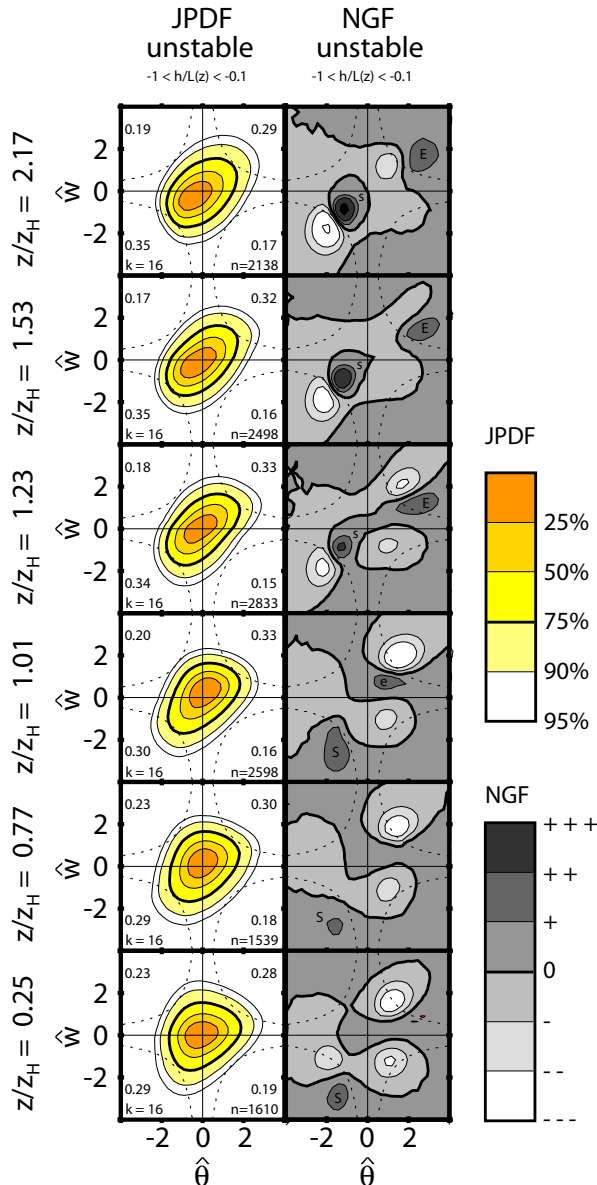


Figure 4.59: Left column: Normalized JPDFs of $\overline{w'\theta'}$ for unstable conditions at U1. The numbers in the individual quadrants denote the average time fractions. n is the number of hourly runs included in the average, k is the number of the 16 wind direction classes included in the horizontal average. **Right column:** Non-Gaussian flux fractions $NGF(\hat{w}, \hat{\theta})$ in the normalized joint probability density functions. ‘E’ and ‘e’ denote non-Gaussian large and small-scale ejections, respectively. ‘S’ and ‘s’ are non-Gaussian large and small-scale sweeps. Data source: sonics A to F (U1), horizontally averaged JPDFs, hourly values, November 1, 2001 to July 15.

Hence, an ejection-dominated regime is found in a layer where momentum exchange is already clearly dominated by sweeps (see Section 4.2.4). A dissimilarity between heat and momentum exchange is also reported from forests, for example in the experiment of Bergström and Högrström (1989), where ejection contribution was also stronger for heat than for momentum.

At roughly z_e , ejections and sweeps contribute equal to the turbulent heat exchange and ΔS_0 crosses zero (Fig. 4.58a). The skewness of temperature is smaller compared to the layers above and also compared to the deep street canyon (Fig. 4.56c). A similar pattern is reported from a wind tunnel study, where flux fractions of sweeps and ejections are equal around z_h (Coppin et al., 1986). This layer was therefore referred to as *equilibrium layer*. The wind tunnel study indicated for large hole-sizes that sweeps were dominant. The NGF at $z/z_h = 1.01$ support this observation. In the NGFs at $z/z_h = 1.01$, simultaneously large scale sweeps (S) and small scale ejections (e) characterize the exchange. At U1, the exchange is most efficient in this layer, as values of the exuberance Ex (Fig. 4.58b) and an increased correlation coefficient (Fig. 4.56b) suggest. An increased efficiency is not found at U2 and S1.

Below z_h , cool air structures (sweeps) exchange heat by penetrating into the street canyon. At U1, strongest $\Delta S_0(w'\theta')$ is found in the upper street canyon, which is similar to momentum exchange. In the NGFs, there are no indications for non-Gaussian ejections in the two lower levels.

Intermittency — In the street canyon, hole sizes H' are largest (Fig. 4.58d). The corresponding time fractions ϑ' (Fig. 4.58e) illustrate that the exchange of heat takes place in sporadic events. In the roof layer, close to the inflection point of the mean wind profile, exchange is dominated by smaller (small H') and more frequent structures (large ϑ'). With increasing height above roofs, the hole size H' slightly increases, and simultaneously, the time fraction ϑ' decreases, indicating that exchange tends again towards higher intermittency.

Stability influence — The magnitude of ΔS_0 clearly increases with destabilization (Fig. 4.60a). In

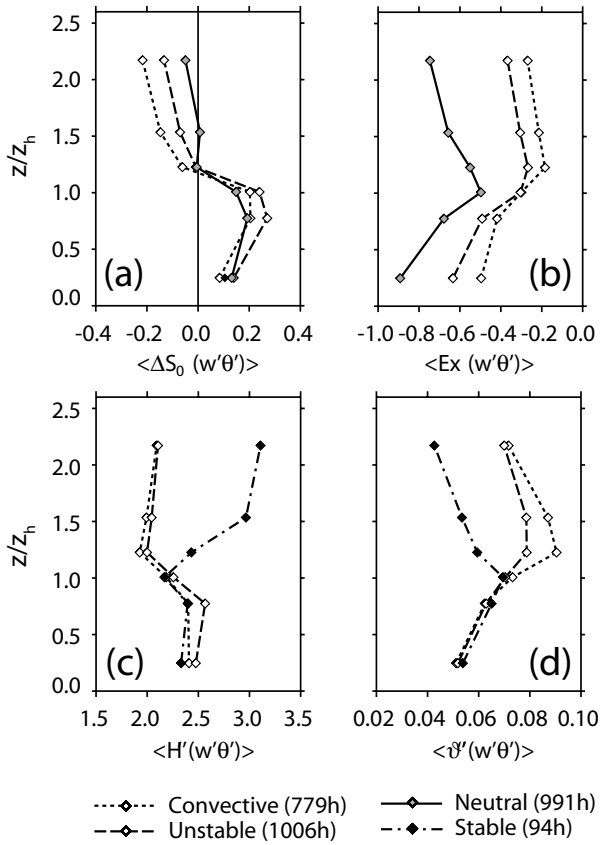


Figure 4.60: Stability dependence of quadrant measures (a) ΔS_0 , (b) Ex , (c) H' and (d) ϑ' for $\overline{w'\theta'}$ at U1. For ΔS_0 and Ex , the stable situation is not shown. For H' and ϑ' , neutral profiles are omitted, because fluxes are very small. Data source: Sonics A to F, hourly values, November 1, 2001 to July 15, 2002, median profiles. Stability determined at tower top.

contrast to momentum exchange, the height of the crossover from sweep-dominated exchange in the street canyon to ejection-dominated exchange above the roofs is not affected by destabilization. For all stability classes $z'/L < 0$, the crossover is found at z_e at U1. It is no surprise that the efficiency of the exchange is enhanced with destabilization, as illustrated by the exuberance (Fig. 4.60b).

Above roofs, unstable runs show that the hole size H' is smaller during unstable than during stable runs (Fig. 4.60c). The corresponding stable time fractions ϑ' illustrate that exchange in these infrequent cases is strongly intermittent (Fig. 4.60d).

4.4.2 Turbulent exchange of water vapor

Water vapor fluctuations (ρ'_v) were measured only once per site, except at U1, where two H_2O/CO_2

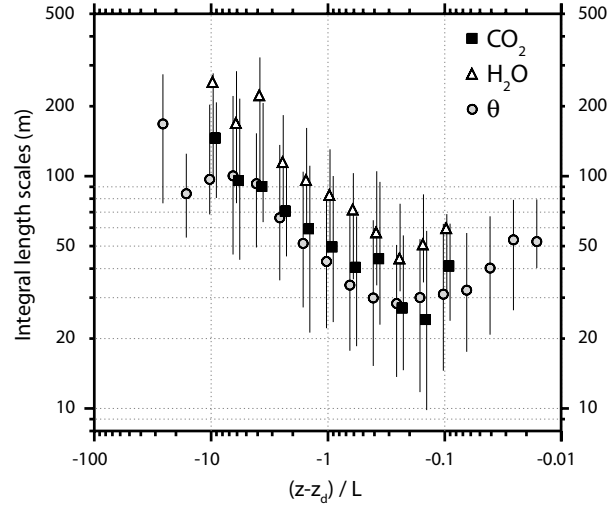


Figure 4.61: One-point integral length scales of heat, water vapor and CO_2 under unstable conditions from tower top at U1. Data source: Sonic and Licor 7500 at level F, hourly values, linearly detrended, June 15 to July 15, 2002.

gas-analyzers were operated simultaneously at two levels for a limited period from June 24 to July 13, 2002.

The vertical profile of $\overline{w'\rho'_v}$ — The lower gas-analyzer at U1 ($z/z_h = 1.01$) probed the top of the completely vegetation-free street canyon. Here, flux densities $\overline{w'\rho'_v}$ are extremely small ($2 \cdot 10^{-3} \text{ g m}^{-2} \text{ s}^{-1}$ on average). In one third of all cases, $\overline{w'\rho'_v}$ is slightly downward directed. The downward directed flux densities indicate that small amounts of humid air are put into the warmer and drier street canyon. These situations are most frequent during midday. The average daytime Bowen ratio β at this height shows typical values around 6.

At tower top where the measurement responds to the whole neighborhood, fluxes are still small (see also Section 4.5.6), but on average they are four times more important than at canyon top ($8 \cdot 10^{-3} \text{ g m}^{-2} \text{ s}^{-1}$). The average β at tower top is 2.6. Here, air masses are more mixed and the source areas include vegetation in backyards and open soil patches. The positive $\partial \overline{w'\rho'_v} / \partial z$ between canyon top and tower top may be an explanation for the small negative $\partial \overline{w'\theta'} / \partial z$ in this layer as discussed in the previous Section 4.4.1. Over an inhomogeneous surface, a patchy moisture availability influences the vertical profiles of both turbulent flux densities, even if available energy is equally distributed.

Table 4.19: Peak frequency $f_{\max} = (n_{\max} z')/\bar{u}(z)$ of cospectra determined from the peak of the median normalized spectra over all runs with given stability. Data source: Sonics: F (U1), F (U2), C (S1) and A (R1), hourly values, linear detrended, June 10 to July 10, 2002.

	z/z_h	$\overline{u'w'}^a$	$\overline{w'\theta'}^b$	$\overline{w'\rho'_v}^b$	$\overline{w'c'}^c$
U1	2.17	0.05	0.11	0.11	0.13
U2	2.49	0.08	0.10	0.11	
S1	2.11	0.11	0.11	0.15	
R1	28 m	0.08	0.09	0.05	
SL		0.07	0.09		

a Neutral runs, $-0.1 < z'/L < +0.1$

b Unstable runs, $-0.5 < z'/L < -0.1$

c All runs $z'/L < 0$

Length scales and cospectra — Figure 4.61 presents one point integral length scales for temperature, water vapor and CO₂. Values are determined from autocorrelation functions. The three variables were simultaneously measured at tower top (U1) during the IOP. Integral length scales of CO₂ and temperature have more similarity and are smaller than length scales of water vapor. This reflects the fact that the urban surface is more homogeneous for heat and CO₂ than for water vapor. CO₂-fluctuations and temperature are driven by surface emissions and heating. Vertical fluxes of water vapor are small compared to the distinct and dominantly upward directed flux densities of heat and CO₂.

The cospectra of the corresponding vertical fluxes of heat, water vapor and CO₂ do not reveal a pronounced difference. At tower top, all three cospectra show a pronounced peak and a marked roll-off in the low frequency end. The normalized peak frequencies $f_{\max} = (n_{\max} z')/\bar{u}(z)$ are summarized in Tab. 4.19. f_{\max} match well to corresponding values in the surface layer and also to previous urban studies (Roth, 1991; Feigenwinter, 2000). In particular, the cospectra do not imply a contribution of large scale fluctuations to the flux density in low frequency bands.

Organized structures — Roth (1991) points out that there are two modes in water vapor exchange. In the classical textbook case of the moistening boundary layer, w and ρ_v are well correlated and the flux is mainly driven by moist updrafts. Here, the latent heat flux from the surface is the main source of moisture fluctuations. θ and ρ_v are highly similar

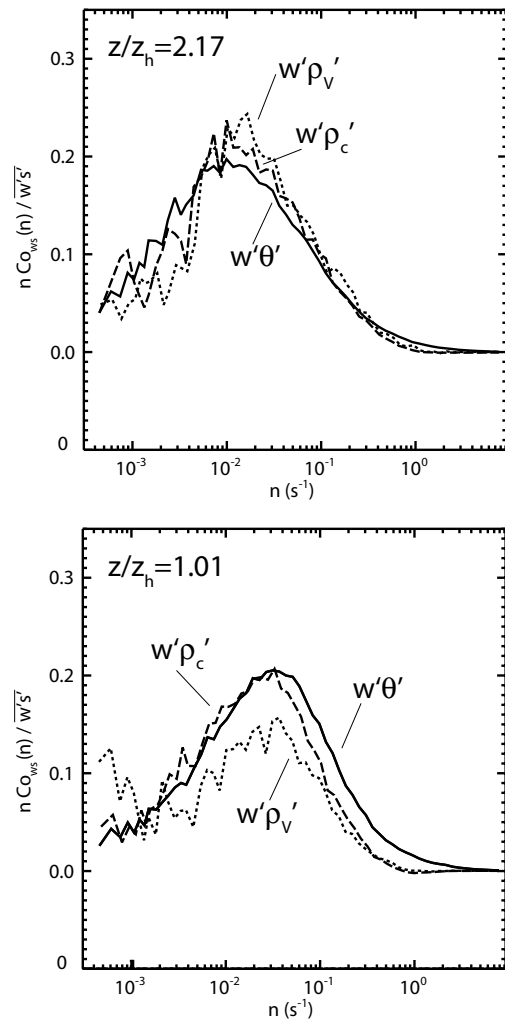


Figure 4.62: Band median values of all cospectra of $\overline{w'\theta'}$ (solid line), $\overline{w'\rho'_v}$ (dotted line) and $\overline{w'\rho'_c}$ (dashed line) from tower top and canyon top at U1. Data source: Sonics and Licor 7500 at level C and F, hourly spectra, 64 logarithmic bands, June 15 to July 15, 2002, all situations.

and hence $r_{\theta\rho_v}$ is close to 1. This mode is predominantly found at rural sites, which are characterized by a strong evapotranspiration. At R1 for example, ejections dominate, and $\Delta S_0(w'\rho'_v)$ is negative most of the time (Tab. 4.20). $r_{w\rho_v}$ shows midday values around 0.35 and $r_{\theta\rho_v}$ is above 0.5 (Fig. 4.63). These indicators imply an efficient water vapor exchange and high similarity between the flux density of water vapor and heat. The surface layer at R1 has a consistent positive $\overline{w'\rho_v'^2}/(\sigma_w\sigma_{\rho_v}^2)$, which further underlines that water vapor variance is transported upwards, and active surface processes (ejections[†]) dominate. The water vapor fluctuations at the suburban site S1 also are driven in this mode.

[†] For $\overline{w'\rho'_v}$ directed away from the surface, "ejections" denote humid air correlated with upward motions (quadrant 2) and "sweeps" are dry air directed downward (quadrant 4).

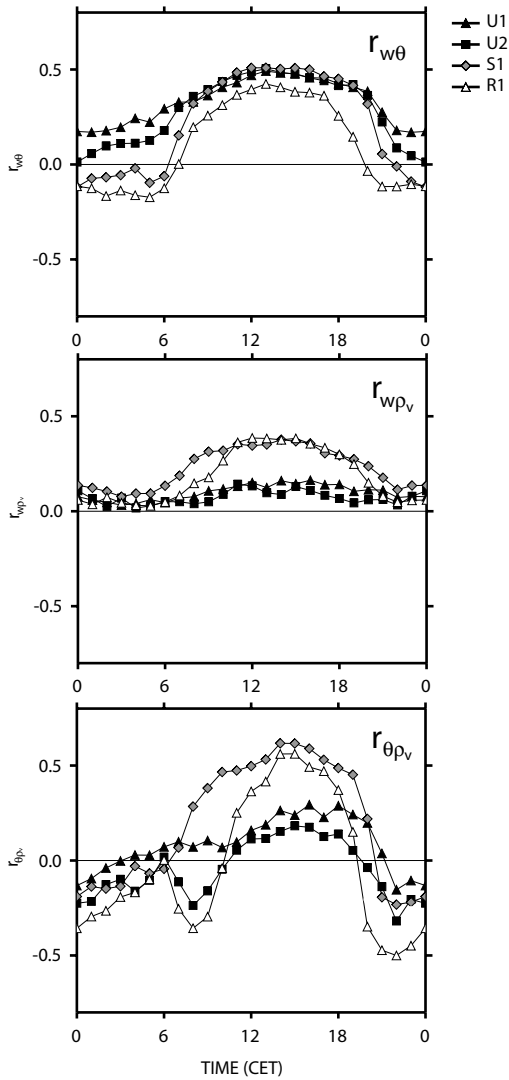


Figure 4.63: Average diurnal course of $r_{w\theta}$, $r_{w\rho_v}$ and $r_{\theta\rho_v}$ at U1, U2, S1 and R1 during the summertime IOP. Data source: Sonics F (U1), F (U2), C (S1), A (R1), hourly block averages, June 10 to July 10, 2002, all situations.

Table 4.20: Horizontally averaged median of quadrant analysis measures for turbulent fluxes of momentum, heat, water vapor and carbon dioxide at two levels at U1, in comparison to surface layer values from R1. Data source: Soncis C and F (U1), A (R1), median values from hourly JPDFs, full operation periods, all stabilities.

	z/z_h	$\overline{u'w'}$	$\overline{w'\theta'}$	$\overline{w'\rho'_v}$	$\overline{w'c'}$
ΔS_0	R1	-0.01	-0.08	-0.08	
	2.17	-0.03	-0.13	+0.01	-0.01
	1.01	+0.33	+0.20	+0.04	+0.14
γ_0	R1	1.15	1.18	1.14	
	2.17	1.04	1.25	0.96	1.54
	1.01	0.69	0.78	0.94	2.05
Ex	R1	-0.62	-0.89	-0.62	
	2.17	-0.39	-0.59	-0.67	-0.50
	1.01	-0.47	-0.50	-0.93	-0.59
H'	R1	1.94	2.07	1.88	
	2.17	2.07	2.05	1.92	1.81
	1.01	2.31	2.09	2.03	1.88
ϑ'	R1	0.077	0.068	0.081	
	2.17	0.066	0.065	0.063	0.063
	1.01	0.054	0.068	0.074	0.056

In the second mode described by Roth (1991), water vapor fluctuations are mainly driven by large scale entrainment processes in the whole atmospheric boundary layer, and not by surface evapotranspiration. In this second mode, dry downdrafts dominate the water vapor regime. There are several indications that water vapor fluctuations at U1 and U2 are mainly driven by the second mode. Both, the magnitude of the latent heat flux and the correlation coefficients $r_{w\rho_v}$ are small (Fig. 4.63). At the dense urban sites, $r_{w\rho_v}$ shows no stability-dependence and stays constant between 0 and 0.1. The normalized vertical flux density of water vapor variance, $\overline{w'\rho'_v{}^2}/(\sigma_w\sigma_{\rho_v}^2)$, is negative most of the day (Fig. 4.65). This implies that water vapor variance is transported downwards at tower top and at canyon top. Further, water vapor exchange at U1 is slightly sweep dominated over the whole profile (Tab. 4.20 and Fig. 4.64). The exuberance suggests a much less efficient exchange compared to heat and CO₂. This pattern fits to results from Roth and Oke (1993b), who found that efficiency of $\overline{w'\rho'_v}$ is least efficient over urban surfaces.

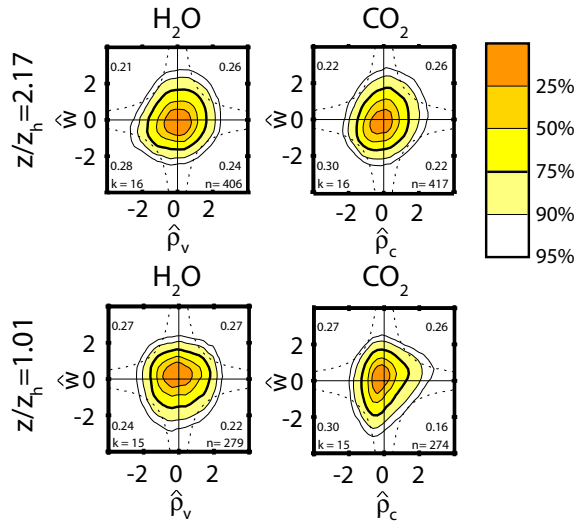


Figure 4.64: Normalized JPDFs of the vertical flux of H₂O and CO₂ for neutral, unstable and convective conditions at U1. The numbers labelling the individual quadrants denotes the average time fractions. Data source: sonics C and F (U1), horizontally averaged JPDFs, hourly values, June 15 to July 15, 2002.

4.4.3 Turbulent exchange of CO₂

The dominant sources for CO₂ in this neighborhood are the motor vehicles, which emit deep in the street canyon. Minor sources are fixed roof level emissions, and also the respiration of the sparse urban vegetation during night. A daytime CO₂-uptake by the vegetation is included in the flux at tower top, but is likely absent at top of the vegetation free street canyon.

The vertical profile of $\overline{w'\rho'_c}$ — During the summertime IOP, the daily averaged (WPL-corrected) CO₂-flux is $12.3 \mu\text{mol m}^{-2} \text{s}^{-1}$ at canyon top and $10.5 \mu\text{mol m}^{-2} \text{s}^{-1}$ at tower top (Fig.4.66a). The intensity of the flux density, especially at canyon top, is related to the traffic load in the street canyon (Fig.4.66b). As we intuitively expect, the street canyon at U1 can be regarded a local spot of higher CO₂-emissions compared to the area average of the urban surface. The measurement at tower top integrates over larger areas and is more representative for an area average at neighborhood scale. It incorporates vegetated backyards as well as other street canyons with different traffic frequency.

During the night, the pattern changes. The low traffic load in the Sperrstrasse results in an almost zero flux of CO₂ at canyon top. The sparse vegetation in the backyards and roof level emissions release small

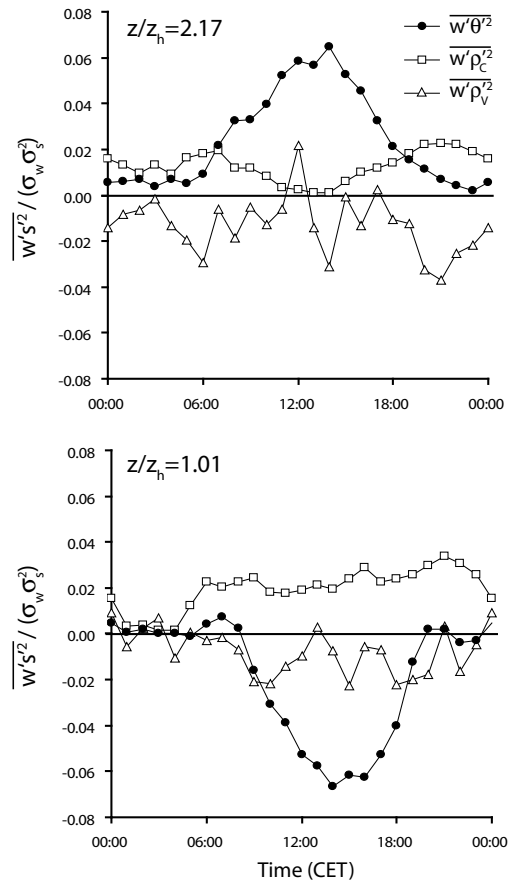


Figure 4.65: Diurnal courses of third order moments $\overline{w'\theta'^2}/(\sigma_w\sigma_\theta^2)$, $\overline{w'\rho_v'^2}/(\sigma_w\sigma_{\rho_v}^2)$, and $\overline{w'\rho_c'^2}/(\sigma_w\sigma_{\rho_c}^2)$ at tower top and canyon top (U1). Data source: Sonics and Licor 7500 at levels C and F, hourly block averages, June 24 to July 12, 2002, all stabilities.

amounts of CO₂. This results in a positive nocturnal flux at tower top. The (local) nocturnal flux density divergence above roof level is slightly positive. The interactions between the urban biosphere, roof level emissions, and the inhomogeneous traffic load of the different streets in this neighborhood do not allow to derive general profiles from only those two measurement heights, which have completely different source areas. Vogt et al. (2005) discuss variations in fluxes and the vertical concentration profile of CO₂ at U1, and relate the pattern to traffic load, urban vegetation and mixed layer height.

CO₂ variance — Not only temperature and water vapor variances, but also the scaled standard deviations of CO₂ are distinctly higher than predicted by surface layer scaling (Fig. 4.67). The vertical flux of CO₂-variance $\overline{w'\rho_c'^2}/(\sigma_w\sigma_{\rho_c}^2)$ is upward directed at both levels (Fig. 4.65). All over the day, variances

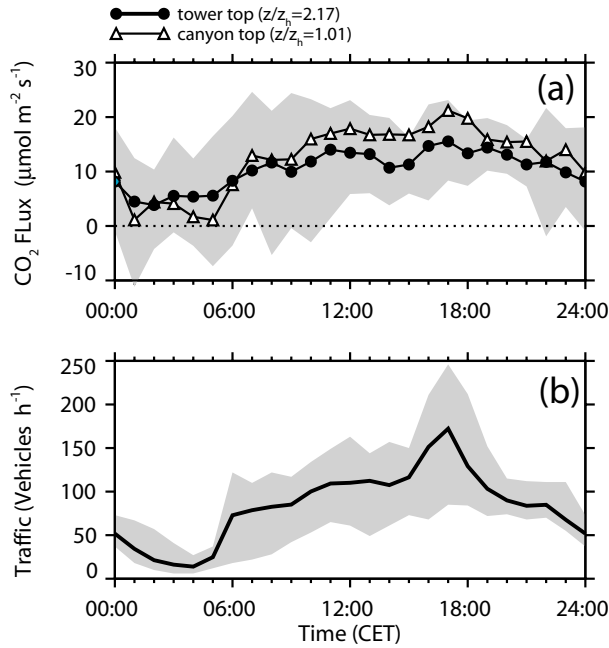


Figure 4.66: Average diurnal courses of (a) CO₂-flux densities and (b) traffic load at U1. Gray shaded areas include 50% of all data measured (a: top level only). Data source: Sonics and Licor 7500, levels C and F, traffic counter, hourly averages, June 15 to July 12, 2002, all situations. Modified from Vogt et al. (2005).

of CO₂ are transported out of the street canyon. This underlines that the active surface for CO₂ is found deep in the canyons, where concentration variances are produced by motor vehicles. The exception is the very early morning, when overall flux densities $\overline{w' \rho'_c}$ are close to zero at canyon top. At tower top, $\overline{w' \rho'_c} / (\sigma_w \sigma_{\rho_c}^2)$ is reduced during midday.

Similar to heat variance transport, the negative $\partial \overline{w' \rho'_c} / \partial z$ between the two layers may explain (part of) the enhanced CO₂ variance measured at tower top. Again, the scaled standard deviations of σ_{ρ_c} / c_* is closer to the surface layer prediction at $z/z_h = 1.01$, compared to the measurement at tower top (not shown).

Organized structures — The JPFDs of turbulent CO₂-flux densities reveal fundamental differences between the exchange at canyon top and at tower top (Fig. 4.64). At tower top, the CO₂-flux density is nearly in equilibrium between sweeps and ejections. At street canyon top, the flux is strongly skewed towards the 4th quadrant, suggesting that the dominant structures are sweeps which transport ‘clean air’ into the street canyon.

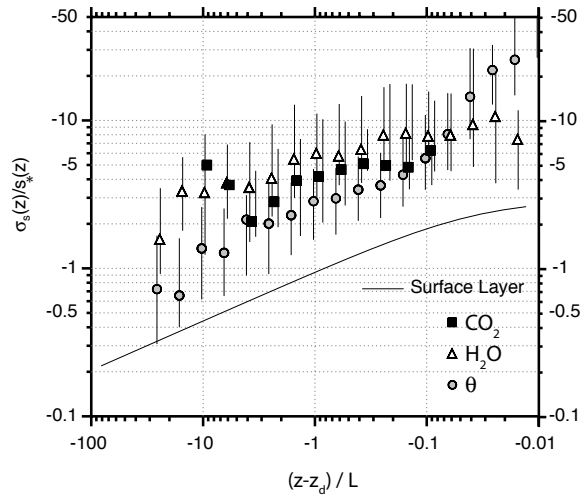


Figure 4.67: Locally scaled standard deviations $\sigma_s(z)/s_*(z)$ of heat, water vapor and CO₂ during unstable conditions from tower top at U1. Data source: Sonic F, Licor 7500, hourly averages, June 15 to July 15, 2002, unstable conditions.

CO₂-exchange is more effective than water vapor exchange. At both levels, $r_{w\rho_c}$ slightly decreases with destabilization (not shown). The correlation is likely affected by the diurnal course of the buoyancy flux. Usually, strong unstable situations are encountered during afternoon, when simultaneously traffic load is small and uptake by vegetation is strong. As a consequence, emissions of CO₂ are reduced, and variations in CO₂ are more dominated by inactive processes on larger scales, which reduces $r_{w\rho_c}$.

The cospectra of CO₂ at tower top coincide with those of the two other scalars (Fig.4.62). They agree well with those from measurements in the homogeneous surface layer (Ohtaki, 1985). However, at canyon top, a dissimilarity between heat and CO₂ is found: heat is transported by smaller structures than CO₂. CO₂ is exchanged by large sweeps, which mix-up the whole street canyon, while temperature may also be exchanged by weaker and smaller sweeps that only affect the upper part of the street canyon. Here, the exchange of CO₂ is more intermittent compared to heat (Tab. 4.20). This again supports the different heights of the active surfaces of the two scalars (heat: roof region and upper street canyon, CO₂: street level).

4.4.4 Summary

- The vertical profiles of the turbulent heat flux $\overline{w' \theta'}$ suggest a nearly continuous increase

Table 4.21: Summary of characteristics affecting heat and mass exchange at the three urban towers, separately for the canyon layer (CAL), the roof layer (ROL), and the above-roof layer (ARL) for convective situations.

Parameter	$z < z_d$	$z_d < z < z_f$	$z_f < z$
	CAL	ROL	ARL
Heat			
$\partial \langle w'\theta' \rangle / \partial z$	> 0	$\gg 0$	≈ 0
$\Delta S_0(w'\theta')$	> 0	≈ 0	< 0
$\overline{w'^2\theta'} / (\sigma_w^2\sigma_\theta)$	< 0	Crossover ^a	> 0
$\overline{w'\theta'^2} / (\sigma_w\sigma_\theta^2)$	≈ 0	Crossover ^a	> 0
$r_{w\theta}$ ^b	≈ 0.2	≈ 0.5	≈ 0.35
Water vapor^c			
$\Delta S_0(w'\rho'_v)$		< 0	< 0
$\overline{w'\rho_v'^2} / (\sigma_w\sigma_{\rho_v}^2)$		< 0	≤ 0
$r_{w\rho_v}$		≈ 0	≈ 0.1
CO₂^c			
$\Delta S_0(w'\rho'_c)$		> 0	< 0
$\overline{w'\rho_c'^2} / (\sigma_w\sigma_{\rho_c}^2)$		> 0	≥ 0
$r_{w\rho_c}$		≈ 0.2	≈ 0.15

^a Change of sign associated with strong gradients.

^b Convective conditions at U1 only. U2 and S1 differ.

^c Observations from U1 only.

up to z_e ($\approx 1.2z_h$, inflection point of the mean wind profile) and a constant value above. Gradients of $\overline{w'\theta'}(z)$ are slightly stronger around z_h compared to the lower street canyon, leading to the exponential parametrization suggested in Eq. 4.41.

- Information on the vertical profiles of turbulent water and CO₂ flux densities are limited in the present data set, since the resolution with only two levels of direct flux measurements at U1 is low. The larger source areas at tower top result in both cases in more representative measurements. At the top of the vegetation-free street canyon, $\overline{w'\rho'_c}(z)$ is stronger than at tower top, and $\overline{w'\rho'_v}(z)$ is smaller.
- The normalized standard deviations of virtual acoustic temperature, water vapor and CO₂ are all distinctly higher than predicted by surface layer scaling. For temperature and CO₂, differences to the surface layer prediction even increase with height above roof level. The enhanced variances are explained by (i) far-field contributions from large scale inactive turbulence and by (ii) a near-field vertical divergence of turbulent variance transport. The analysis in-

dicates that water vapor fluctuations are mostly driven by inactive turbulence while standard deviations of virtual acoustic temperature, and CO₂ are more characterized by active fluctuations created by the surface exchange.

- The heat flux is characterized by ejections above the height z_e and by sweeps below. In the region $1.2 < z/z_h < 1.6$, a dissimilarity between the turbulent heat flux and Reynolds stress is observed. While Reynolds stress is dominated by sweeps, heat flux is mainly driven by ejections in this layer. Deep in the street canyon and well above roofs, processes qualitatively coincide.
- The different scalars do not have the same active surfaces, and as a consequence, exchange processes between heat, water vapor, and CO₂ are different (Tab. 4.21). Sources for $\overline{w'\theta'}$ are mainly found at roof level and in the upper street canyon. In contrast, there is evidence for water vapor and especially CO₂ that their active surfaces are deeper, since the majority of sources (vegetation, vehicles) are found in lower layers of the urban canopy.
- At tower top, cospectra of $\overline{w'\theta'}$, $\overline{w'\rho'_v}$ and $\overline{w'\rho'_c}$ show high agreement, and peak frequencies are similar to the ones observed in the surface layer. The cospectra suggest that roughly the same scales dominate turbulent exchange. At roof level, the scales of the exchange are different, which is explained by the different heights of the active surfaces.

4.5 Surface energy balance[†]

In this last chapter, we shift the focus from physical exchange processes to a more ‘climatological’ approach, and address the urban surface energy balance modification. The energy balance network operated during the IOP allows the simultaneous comparison of urban, suburban, and rural energy balance partitioning during one month of summertime measurements. The partitioning is analyzed together with long-term data to evaluate the magnitude of the urban flux density modification, and to document characteristic values in their diurnal and yearly course. After introductory definitions (4.5.1), the first three sections address the radiative processes, namely the short-wave components (Section 4.5.3), the long-wave components (4.5.4) and implications on net-radiation (4.5.5). Then, latent heat flux densities (4.5.6), sensible heat flux densities (4.5.7) and the storage term (4.5.8) are analyzed. Finally, the estimation of the anthropogenic heat input (4.5.9), and the calculation of the overall energy balance modification (4.5.10) summarize the topic.

4.5.1 Definitions and concepts

The general approach to estimate the urban energy balance is not to measure close to ground level, but to observe the turbulent fluxes high above the mean building height z_h in order to avoid local effects of single roughness elements, i.e. the measurement height z_m has to be above the roughness sublayer height (Rotach, 2002). Therefore, calculations of the surface energy budget have been done with the highest available measurements at each tower, which then refer to the upper margin z_m of an imaginary box enclosing all buildings and vegetation of the urban surface from ground up to this measurement height.

The measured turbulent flux densities at height z_m are an area-averaged response of the surface, where the flux source areas depend on wind direction and stability (Schmid and Oke, 1990). The instruments at any urban site measure an integrated flux from an array of buildings, streets, backyards, and vegetation, which is representative of the neighborhood scale (Section 2.1.2).

[†] Part of this chapter has been published in Christen and Vogt (2004b)

The ‘box view’ of the urban surface simplifies the storage by enclosing all surface elements (ground, buildings, and vegetation), but it also incorporates the air volume between the ground and the measurement level, within which a small amount of energy, ΔQ_T , can be stored (removed) by warming (cooling) the air. This energy change is not part of the ground storage heat flux density ΔQ_S and not a component of the *surface* energy balance. It is a consequence of our concept of an elevated surface when measuring flux densities at z_m and not at ground level. In the present work, it is assumed that Q_T is mainly driven by sensible heat flux density divergence $\partial Q_H/\partial z$ from ground up to z_m . Therefore, in order to reduce the surface down to a theoretically flat ground level, ΔQ_T is incorporated into Q_H . Most of the time, ΔQ_T is below 10% of ΔQ_S and its magnitude is always less than 20 W m^{-2} . Moreover, ΔQ_T nearly vanishes when calculating daily totals and therefore does not affect the long-term energy partitioning.

The source areas of the down-looking radiation instruments and the variable source areas of the eddy correlation instrumentation usually do not refer to the same area. Therefore, such a setup has to assume horizontal homogeneity of the surface properties and flux densities at ground level.

4.5.2 Schedule of observations

In summary, data from three observations periods are presented in this chapter. First, the *summertime IOP* (June 10 to July 10, 2002) allows for the detailed comparison of the diurnal variation of urban-rural differences during a period of high energy availability. During this period, the mean solar radiation was $23 \text{ MJ d}^{-1} \text{ m}^{-2}$, mean air temperature 20°C and precipitation 65 mm (mostly from thunderstorms). The IOP includes 10 clear-sky days and is significantly warmer and slightly dryer than the 30 year average (16.8°C and 89 mm , respectively). Winds 10 m above z_h were in average 2.0 m s^{-1} , and due to a thermal circulation in the Rhine Valley mainly from the sectors W to N (51%, day) and E to S (36%, night). Second, measurements taken during the *full year period* (Sep 2001 – Aug 2002) are presented. Data are available for U1, U2 and R3. This period is characterized by an annual mean temperature of 10.7°C and 826 mm of precipitation

(30-year average: 9.0°C and 791 mm). Winds 10 m above z_h were 2.1 m s⁻¹ in average and sectors SW to NW (44%) and E to SE (34%) dominated. Finally, at U2 and R3, several parameters like radiation and temperature / humidity profiles are available since 1994. This urban *long-term data-set* 1994–2002 is used to compare the findings from the IOP and year long data with climatological values.

4.5.3 Short-wave flux densities

Table 4.23 summarizes the daily total of all radiation flux densities at the seven energy balance sites for the summertime IOP period. The solar irradiance K_{\downarrow} during this period is nearly of similar magnitude at all urban and rural sites. This is in contrast to earlier urban climate studies, which concluded that K_{\downarrow} is significantly attenuated in the city due to higher aerosol concentrations (Landsberg, 1981). This effect is not found in the mid-size town of Basel. It may be masked by instrument resolution and the fact that all rural reference sites are located close to the urban core.

At the built-up sites, K_{\downarrow} is not equally distributed within individual layers of the urban canopy. Shading and exposition of the building structures highly influence its vertical distribution and therefore, a vertical divergence of the short-wave radiation flux density $\partial K_{\downarrow} / \partial z > 0$ is observed. The three dimensional morphometric structure of the urban surface is important when determining where radiation interacts with buildings and vegetation. This identifies layers where net-radiation can be converted into storages, or put into latent or sensible heat flux densities. Figure 4.68 illustrates $\partial K_{\downarrow} / \partial z$ within the urban canopy based on calculations with a 1 m digital building model of the urban canopy around U1. The curves show the short-wave irradiance reaching different layers of the canopy under different sun elevation angles relative to the irradiance reaching a horizontal plane under the same sun elevation angle. The calculation neglects reflections and diffuse radiation. Under realistic sun elevations around 30°, only about 15% of the incoming solar radiation reaches the ground unmodified as direct K_{\downarrow} . 50% is absorbed and reflected by building parts above z_h . With increasing sun elevation, more radiance penetrates directly to the ground level, e.g. 30% at 60°. $\partial K_{\downarrow} / \partial z$ determines the locations where energy is

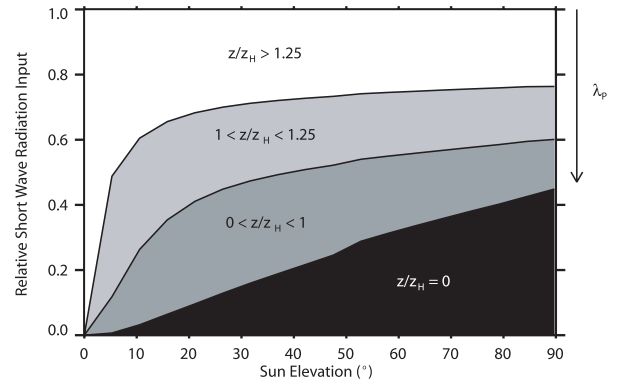


Figure 4.68: Relative amount of the short-wave input radiation into different height layers of the urban canopy at U1 as a function of sun elevation. Values are normalized to the short-wave input on a horizontal plane assuming similar sun elevation. The partitioning was calculated from the 3d model with 1 m resolution and for a box of 500 by 500 m around the tower location.

available and exchanged within the urban canopy, and therefore the magnitude and the partitioning of the urban energy flux densities in the urban canopy layer (see also Section 4.4.1).

Table 4.22: Yearly totals of the radiation balance components for the full-year period (September 2001 – August 2002).

	Urban (U1,U2)	Rural (R3)	Difference (U1,U2) - (R3)	
	GJ yr ⁻¹	GJ yr ⁻¹	GJ yr ⁻¹	Wm ⁻²
	m ⁻²	m ⁻²	m ⁻²	
K_{\downarrow}	+4.17	+4.17	+0.00	+0.1
K_{\uparrow}	-0.47	-0.91	+0.44	+14.0
K^*	+3.70	+3.25	+0.44	+14.1
L_{\downarrow}	+10.05	+10.16	-0.12	-3.7
L_{\uparrow}	-11.94	-11.61	-0.33	-10.5
L^*	-1.89	-1.44	-0.45	-14.2
Q^*	+1.81	+1.81	-0.00	-0.1

Most urban surfaces have a significantly lower magnitude of K_{\uparrow} compared to the rural sites and therefore a higher short-wave input K^* . The observed mean albedo $\alpha = K_{\uparrow} / K_{\downarrow}$ in the city center (U1, U2) are around 10%, rural values are all around 20% (Tab. 4.23). The parking lot (U3) is an exception. As aerial photos and satellite images show, the very high value of 32% is not representative of large urban areas because the spatial extent of this concrete surface is limited. The field of view of the down facing sensor at U3 includes only a concrete surface, while the other urban measurements integrate over larger areas (Tab. 4.23). At U1, U2 and S1, the large field of view includes different surface

Table 4.23: Average daily totals of all radiation fluxes in $\text{MJ m}^{-2} \text{d}^{-1}$ for the summertime IOP period (June 10 to July 10, 2002).

Site		U1	U2	U3 ^a	S1	R1	R2	R3
FOV ^b		100 m	100 m	5 m	50 m	5 m	5 m	5 m
Short-wave	K_{\downarrow} ($\text{MJ m}^{-2} \text{d}^{-1}$)	+22.8	+22.7	+22.7	+22.6	+22.9	+22.8	+22.9
	K_{\uparrow} ($\text{MJ m}^{-2} \text{d}^{-1}$)	-2.4	-2.6	-7.1	-3.0	-4.8	-4.5	-4.5
	K^* ($\text{MJ m}^{-2} \text{d}^{-1}$)	+20.4	+20.1	+15.6	+19.6	+18.1	+18.4	+18.4
Long-wave	L_{\downarrow} ($\text{MJ m}^{-2} \text{d}^{-1}$)	+30.7	+30.6	+30.7	+30.5	+30.6	+30.8	+30.9
	L_{\uparrow} ($\text{MJ m}^{-2} \text{d}^{-1}$)	-38.4	-37.7	-39.8	-37.9	-37.9	-36.8	-36.7
	L^* ($\text{MJ m}^{-2} \text{d}^{-1}$)	-7.7	-7.1	-9.1	-7.4	-7.3	-6.0	-5.8
Net Radiation	Q^* ($\text{MJ m}^{-2} \text{d}^{-1}$)	+12.6	+13.0	+6.4	+12.3	+10.8	+12.3	+12.6
Albedo ^c	α %	10.4	10.9	31.7	13.1	21.9	20.2	19.5

^a only June 24 to July 10 2002.

^b approximate radii of the field of view of the downlooking sensors.

^c median albedo for $K_{\downarrow} > 50 \text{ W m}^{-2}$

materials and the complex morphometric configuration (orientations, density, height) results in multiple reflections and shading, which all lower the reflectivity of the surface. The measured albedo in the city center is significantly lower compared to values applied in numerical models, which are typically in the order of 15 to 20% for residential neighborhoods (Sailor and Fan, 2001), suggesting that dense European city centers are better absorbers of K_{\downarrow} than most North American city surfaces. Comparably low values of $\sim 8\%$ were recently reported from a dense urban canopy in Lodz, Poland (Offerle et al., 2003a) and from the city center of Marseilles, France (Lemonsu et al., 2004). In the long-term mean, the lower albedo of the city leads to a surplus in K_{\uparrow} in the order of $0.44 \text{ GJ yr}^{-1} \text{ m}^{-2}$ compared to rural surfaces. K_{\uparrow} is the most strongly modified term of all four radiation components (Tab. 4.22).

The present study suggests that the albedo decreases with increasing height and density of buildings. The mean summertime albedo is highest at the suburban site (13.1%), lower at U2 (10.9%) and again slightly lower at the most compact urban canopy U1 (10.4%) (Tab. 4.23).

Daily variations — Similar to most natural surfaces, the urban albedo also shows a dependence on sun elevation. Figure 4.69 illustrates this angular dependency for the city center (U1), suburban (S1) and one of the rural (R1) surfaces. For the urban and suburban surfaces, angular dependency becomes important when sun elevation is below 20° , due to highly directional reflectance of horizontal surfaces. In

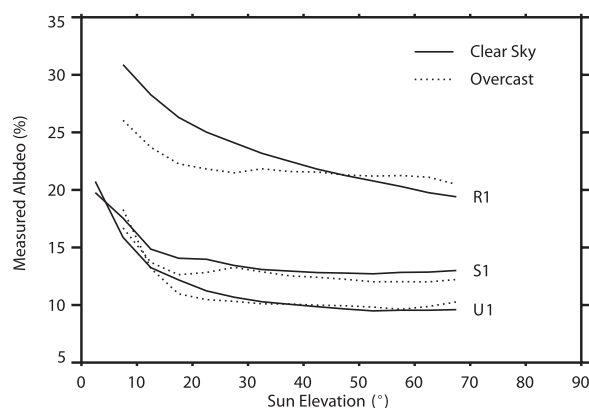


Figure 4.69: Angular variation of the average measured albedo for an urban (U1), the suburban (S1) and a rural surface (R1, grassland).

contrast to physical models (Li et al., 1995) and observations over vegetated surfaces (R1), the albedo of both urban and suburban surfaces is fairly constant between 20° and 65° sun elevation under both, clear-sky and overcast conditions. No difference between clear and overcast conditions is observed for the urban surfaces (Fig. 4.69) in contrast to plant canopies, where clear-sky situations in general increase albedo (e.g. R3 at low sun elevation angles).

Yearly variations — The long-term measurements at U2 (1996–2002) show little monthly variation of urban albedo values during snow-free conditions. In the long-term average, the albedo at U2 is 10.7% (snow excluded). All monthly averages lie within 2%. The urban albedo increases slightly throughout the summer from an average value of 10.2% in March to 11.8% in October (not shown).

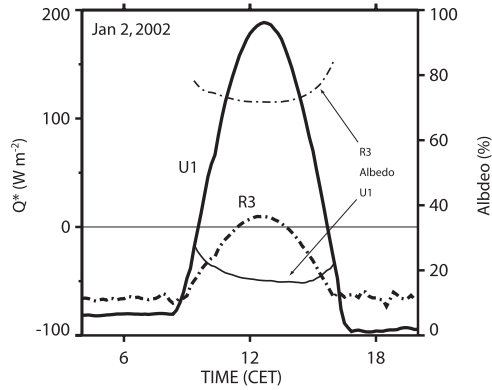


Figure 4.70: Net radiation Q^* (thick lines) and albedo (thin lines) during a clear winter day with a 20 cm snow cover. Solid lines are measurements over the urban surface (U1), dashed-dotted lines are simultaneously measured rural values (R3).

This small increase can be mainly attributed to urban trees, since similar increases — but higher in magnitude — are observed over forests (Lehn, 1991). In general, changes in the urban albedo due to different sun elevation angles are more important compared to monthly variations due to phenological influences. The most dramatic urban-rural difference $\Delta K_{\uparrow U-R}$ is observed in winter during periods with snow cover. Figure 4.70 shows data from one clear day with a 20 cm snow cover in the rural area. The mid-day albedo values in the city center are around 17% (U1) and 15% (U2, not shown). These values are surprisingly low compared to the simultaneously measured rural value of 70% (R3). The snow-free vertical walls, shading, faster snow melt, and removal (road maintenance) all work to reduce the impact of snow on urban albedo.

4.5.4 Long-wave flux densities

Most of the time, urban L_{\uparrow} values are higher in magnitude than L_{\uparrow} measured over rural surfaces (Tab. 4.23). This implies a higher urban radiation surface temperature T_s and/or a different emissivity ϵ . Moreover, the radiation trapping in street canyons affects L_{\uparrow} significantly.

Urban L_{\downarrow} values are slightly lower than rural values (except R1) all around the day (Tab. 4.23). Air masses close to the sensor at the urban sites are dryer than the air masses measured over the rural surfaces, resulting in a reduction of L_{\downarrow} . However, L_{\downarrow} is also affected by aerosol content and ABL temperatures, which are both supposed to enhance L_{\downarrow} in urban ar-

reas. Note that L_{\downarrow} differs also between rural sites and the observed urban-rural differences are in the order of the instrumental errors. Measurements of L_{\downarrow} are surely affected by larger uncertainties compared to the short-wave irradiance.

Daily variations — In the diurnal course, urban-rural differences $\Delta L_{\uparrow U-R}$ are strongest in the evening when the city emits much more long-wave radiation than the rural surrounding and $\Delta L_{\uparrow U-R}$ reaches values of about 20 W m^{-2} (Fig. 4.71c). $\Delta L_{\uparrow U-R}$ decreases during night to about 10 W m^{-2} in the early morning, primarily an effect of the different cooling rates due to radiation trapping in street canyons. The intensity of the nocturnal heat island displayed as air temperature (Fig. 4.72) shows a close relationship with L_{\uparrow} , i.e. the highest urban heat island intensity ($\sim +3 \text{ K}$) is observed just after sunset, with continuously decreasing values during night. The lower daytime urban-rural differences in air temperature again correspond well to the observed daytime $\Delta L_{\uparrow U-R}$, which reaches its smallest values with only -5 W m^{-2} around noon (Fig. 4.71c). Note that the measurement height of urban temperatures significantly influences urban-rural temperature differences. At street-level, the heat island is found all over the day, but at roof level during midday, slightly cooler air temperatures are measured compared to the rural surroundings (Fig. 4.72). This (roof level) urban cool island is especially prominent during summer (-0.5 K) and also reported from other studies (Unwin, 1980; Jauregui et al., 1992).

The summertime absolute humidity content in the city center (U1, U2) is around 0.6 g m^{-3} less compared to the humidity at the rural sites (R1, R2, R3). This urban dry island is most pronounced in the evening and almost disappears in the early morning (Fig. 4.72). The influence of the dryer urban atmosphere on L_{\downarrow} is not negligible. This humidity difference corresponds to a reduction of the total water vapor content by about 10%. The urban dry-island is also shown in the long-term 1994–2003 data, where the average daytime humidity difference U1 - R3 is -0.5 g m^{-3} (-6% of the total water content).

Annual variations — In the yearly total, the city center at U1 and U2 loses $0.33 \text{ GJ yr}^{-1} \text{ m}^{-2}$ more

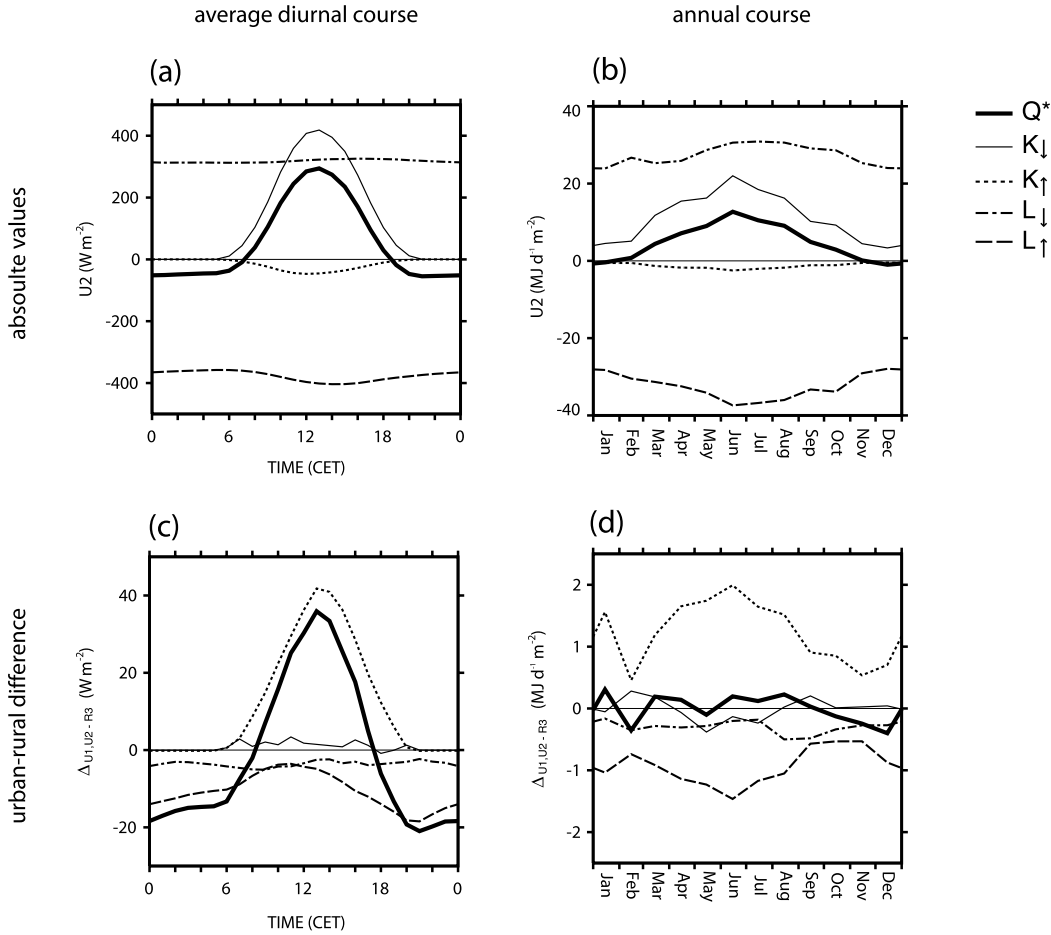


Figure 4.71: upper row: Daily variation (a) and annual variation (b) of the radiation balance components for the period Sep. 2001 to Aug 2002 at U2. Lower row: Differences of radiation components between the dense urban surfaces (U1,U2) and one rural reference site (R3) in the daily variation (c) and annual variation (d) for the same period. Negative values indicate components with a relative energy loss of the city, positive terms are components where the city can achieve an energy surplus compared to the rural reference.

energy through L_{\uparrow} than the rural reference R3. The energy loss through L_{\uparrow} is slightly higher in summer (Fig. 4.71d). The observed urban reduction of L_{\downarrow} is in the order of $0.12 \text{ GJ yr}^{-1} \text{ m}^{-2}$ (Tab. 4.22).

4.5.5 Net radiation

The larger short-wave energy input K^* of the urban surfaces due to the lower albedo is mostly offset by larger L^* loss. This results in a more or less equal daily total of the net all-wave radiation Q^* over the urban, suburban and rural surfaces, except at the parking lot U3 (Tab. 4.23). In the yearly average (day and night), ΔQ_{U-R}^* even vanishes (Tab. 4.22).

Daily variations — During daytime, ΔQ_{U-R}^* is greater and positive (Fig. 4.71c), i.e. the city cen-

ter gains more energy compared to the rural sites, an effect mainly controlled by the low urban albedo (Section 4.5.3). The mid-day ΔQ_{U-R}^* is typically around $+40 \text{ W m}^{-2}$. Throughout the night on the other hand, the city loses more energy through Q^* than any of the rural sites ($\Delta Q_{U-R}^* \approx 15 \text{ W m}^{-2}$). During nighttime, the higher long-wave emission and the partly dryer atmosphere in the city enhance the loss (Section 4.5.4).

Annual variations — The yearly variations show little difference between urban and rural sites. Daily totals of Q^* lie in average between $\pm 0.5 \text{ MJ d}^{-1} \text{ m}^{-2}$ (Fig. 4.71). Neglecting snow conditions, wintertime daily Q^* totals are slightly more negative than rural ones, i.e. the long nights cause the city to lose more radiation than it can gain due to its lower albedo during the shorter daylight pe-

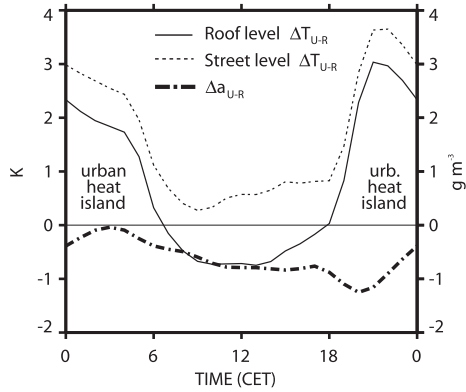


Figure 4.72: Urban-rural differences in air temperature ΔT_{U-R} and absolute humidity Δa_{U-R} . Temperature and humidity values are an average of U1 and U2 (urban) and R1, R2 and R3 (rural) over the summertime IOP period from June 10 to July 10 2002. Roof level temperatures are measured 5m above z_h , street level are from instruments operated inside street canyons at U1 and U2 (2–3 m above ground).

riod. The highest daytime differences ΔQ_{U-R}^* are observed in winter when the contrasting albedo of snow-covered rural surfaces and the darker urban surfaces are dramatically increasing $\Delta K_{\uparrow U-R}$, and hence, ΔQ_{U-R}^* up to 200 W m^{-2} can be measured (Fig. 4.70). The sample day with snow cover illustrates that Q^* at the urban site is positive most of the day, compared to the values of the snow covered rural surface that is either negative or around zero. The enhanced Q^* accelerates urban snow-melt (Todhunter et al., 1992; Semadeni-Davies et al., 2001).

4.5.6 Latent heat flux densities

Mid-latitude cities with negligible irrigation show less evapotranspiration than their rural surroundings since Q_E is mainly driven by vegetation and in cities, vegetation covers only a small fraction of the surface. Additionally, a faster run-off at the built-up areas lowers the water availability. Therefore, it is not surprising that the city center (U1, U2) with its low vegetation aspect ratio λ_V , its large impervious surfaces, and its negligible irrigation shows small Q_E values (Table 4.24).

Daily variations — Figure 4.75 shows the average diurnal course of all energy balance components for each site measured during the summertime IOP. All weather conditions from clear to completely overcast and rainy days are included. The

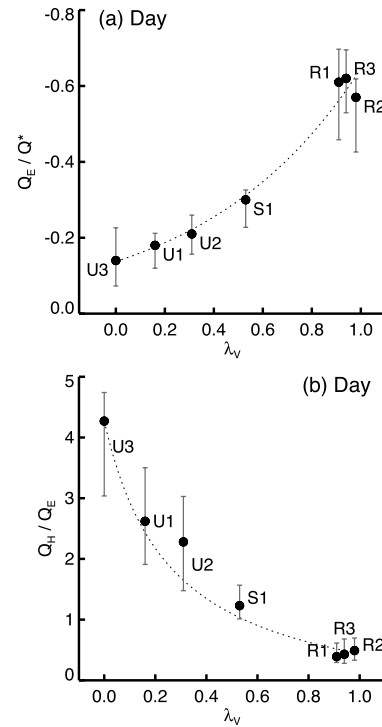


Figure 4.73: **a:** Relationship between daytime Q_E/Q^* ratio and vegetation aspect ratio λ_V . **b:** Daytime Bowen ratio β as a function of the vegetation aspect ratio λ_V . Points represent the average values from the summertime IOP between June 10 and July 10 2002. Error bars enclose 50% of all hourly data; their ends indicate the 25% and 75% quartile.

average daytime partitioning during the IOP is illustrated in Fig. 4.74. The triangle shows the partitioning of Q^* into Q_H , Q_E and ΔQ_S . The ratios Q_H/Q^* , Q_E/Q^* , and $\Delta Q_S/Q^*$ are useful parameters for the detection of diurnal trends in the partitioning of Q^* and for comparing situations with different magnitudes of Q^* forcing.

During summer days, the magnitude of Q_E in the city center is around 20% of Q^* . With increasing green space, Q_E becomes more important. The magnitude of the simultaneously measured Q_E at the suburban site is 30% of Q^* and about 60% of Q^* at the rural sites (Tab. 4.24). The relationship between daytime Q_E/Q^* and the vegetation aspect ratio λ_V is illustrated in Fig. 4.73a. It is not surprising that vegetation in the urban environment significantly enhances daytime Q_E and reduces Q_H , a result also supported by other studies where simultaneous measurements were carried out in neighborhoods with different λ_V (Grimmond et al., 1996). λ_V can be easily retrieved from aerial photos and satellite pictures and is therefore a useful surface parameter to estimate the daytime Q_E .

Table 4.24: Average energy balance components of the daytime and nocturnal hours during the IOP. Daytime values are averaged from 1100–1500 CET, nocturnal values from 2200–0400 CET. Sites are sorted according to increasing plan aspect ratio of buildings λ_P . Positive (negative) fluxes are directed towards (away) from the surface. At the sites where all components of the energy balance are measured directly, any missing energy — i.e. the gap to close the balance — was used to increase the two turbulent flux densities slightly, and force the closure without changing β .

	Q^* W m^{-2}	Q_H W m^{-2}	Q_E W m^{-2}	ΔQ_S W m^{-2}	Q_F W m^{-2}	Q_H/Q^*	Q_E/Q^*	$\Delta Q_S/Q^*$	β
<i>Daytime</i>									
R1	+423	-101	-260	-62		-0.24	-0.61	-0.15	+0.39
R2	+443	-123	-251	-69		-0.28	-0.57	-0.15	+0.49
R3	+455	-122 ^a	-282 ^a	-51		-0.27	-0.62	-0.11	+0.43
S1	+453	-168	-134	-153 ^b	+5 ^c	-0.37	-0.30	-0.34	+1.23
U2	+481	-228	-100	-163 ^b	+10 ^d	-0.47	-0.21	-0.34	+2.28
U1	+482	-230	-88	-184 ^b	+20 ^d	-0.48	-0.18	-0.38	+2.62
U3 ^e	+322	-193	-45	-104	+20 ^c	-0.60	-0.14	-0.32	+4.27
<i>Night</i>									
R1	-57	+18	+13	+26		-0.31	-0.23	-0.46	+1.35
R2	-45	+4	+9	+32		-0.09	-0.20	-0.71	+0.45
R3	-41	+12 ^a	+8 ^a	+21		-0.29	-0.20	-0.50	+0.43
S1	-56	+7	-9	+53 ^b	+5 ^c	-0.13	+0.16	-0.95	-0.78
U2	-62	-8	-4	+64 ^b	+10 ^d	+0.13	+0.06	-1.03	+1.94
U1	-65	-23	-13	+80 ^b	+20 ^d	+0.35	+0.19	-1.23	+2.62
U3 ^e	-81	-10	-5	+76	+20 ^c	+0.13	+0.06	-0.94	+2.08

a values determined by profile method.

b values determined as residual term of the energy balance equation.

c constant anthropogenic heat flux Q_F estimated.

d constant anthropogenic heat flux Q_F determined according to Section 4.5.9

e site only operated from June 24 to July 10 2002.

Figure 4.73b illustrates the average daytime Bowen ratio $\beta = Q_H/Q_E$ during the summertime IOP as a function of the vegetation aspect ratio λ_V . Typical daytime values of β are around 2.5 at urban sites and 0.5 over the rural surfaces. The measurement values suggest that the daytime Bowen ratio can be parameterized as a function of λ_V . This has been formulated in relationship 4.43. The relationship is shown in Fig 4.73b (dashed curve). It simplifies the response of a patchy urban surface to a linear superposition of the rural Bowen ratio β_{rural} weighted by the fraction of vegetated surfaces λ_V and a hypothetical Bowen ratio for a completely impervious surface β_{imp} weighted by the fraction of impervious surfaces ($1 - \lambda_V = \lambda_I + \lambda_P$):

$$\beta(\lambda_V) = \frac{1}{\lambda_V - \lambda_V k + k} + \beta_{rural} - 1 \quad (4.43)$$

with

$$k = \frac{1}{\beta_{imp} - \beta_{rural} + 1} \quad (4.44)$$

and the condition

$$\beta_{imp} > \beta_{rural}. \quad (4.45)$$

$\beta(\lambda_V)$ is the average daytime Bowen ratio for a given vegetation aspect ratio λ_V , i.e. for a particular urban or suburban neighborhood. β_{rural} is the (known) Bowen ratio over grassland in the rural surroundings of the city ($\lambda_V = 1$). Because β_{imp} is usually not available, the global parameter k between 0 and 1 is introduced, which is valid for the whole rural-urban region. k may depend on various factors like climatic setting of the city, precipitation, phenology and the difference between rural and urban discharge coefficients. This empirical relationship works well for Basel where the long-term value of k is surprisingly constant around 0.2 (see below). It would certainly cause problems in cities with extensive irrigation.

Site U2 is dryer than the vegetation aspect ratio suggests (Fig. 4.73b). This is because the relationship does not accurately represent the forcing or because

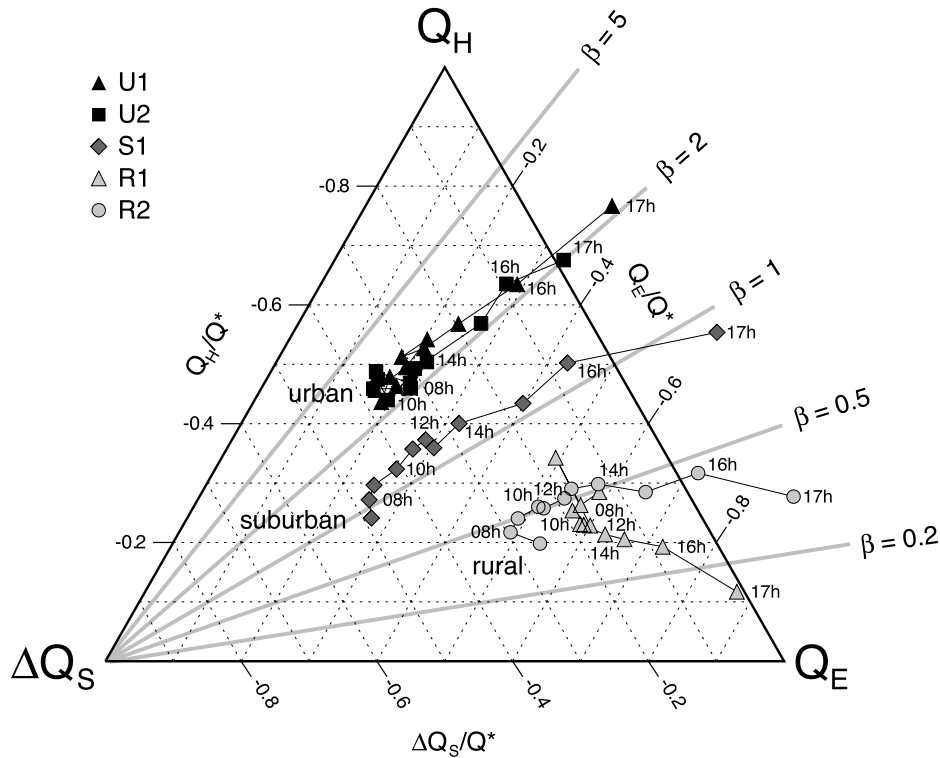


Figure 4.74: Ensemble daytime variation of the energy balance partitioning at the different sites for the IOP (June 10 to July 10, 2002). The symbols show how Q^* is partitioned into Q_H , Q_E and ΔQ_S for all sites. Any point fulfils $Q_H + Q_E + \Delta Q_S = 0$. The trajectories in the triangle show the temporal evolution of the partitioning throughout the day, as indicated by the time labels.

either β or λ_V are erroneous. Indeed, a large city park can be found 150 m to the S and SW of the tower and increases λ_V of that particular neighborhood by nearly 10%. This wind direction is rarely observed ($< 7\%$) and therefore does not affect the overall moisture availability. If the flow is from that particular wind direction, a β of 1.5 is measured compared to the average value $\beta = 2.3$ when taking all wind directions into account.

The rural surfaces show increasing evapotranspiration towards the evening and therefore a decreasing β throughout afternoon. In the early morning, rural values start around $\beta \approx 0.5$. β is continuously decreasing throughout the day to $\beta \approx 0.2$ at 1700 (Fig. 4.74). This decrease of β is most pronounced in summer (March to October). An increasing vapor pressure deficit which is caused by the diurnal course of temperature and the growth of the mixed layer and the associated entrainment of dryer air from the free troposphere enhances Q_E . At the built-up sites, there is also a small decrease of β , but the overall partitioning is less affected. In the city center, β stays close to 2 all the day (see also 4.5.7).

Nocturnal values of Q_E in the city center are gener-

ally low. Q_E is directed upward most of the time (Fig. 4.76c). Exceptions are early morning hours when Q_E can be directed downward.

Annual variations — Figure 4.78b illustrates the monthly averages over six years of daytime (1100–1500) urban and rural β . Here, β is calculated from vertical gradients of potential temperature, $\partial\theta/\partial z$, and specific humidity, $\partial q/\partial z$. The temperature and humidity gradients were continuously measured at an urban (U2) and a rural (R3) site. Both sites show a nearly similar yearly course, but with distinctly different magnitudes. The higher precipitation during summer, together with an increased transpiration activity, lowers the summertime β of both urban and rural surfaces. On the other hand, when vegetation activity is low in winter and spring, values are generally higher at both sites. Highest values are measured in March, when available energy is large ($6 \text{ MJ d}^{-1} \text{ m}^{-2}$) but precipitation is moderate and vegetation activity still low. A similar annual course of β has been recently reported from long-term measurements in the city center of Lodz, Poland (Offerle et al., 2003b). Relationship 4.43 to estimate β as a

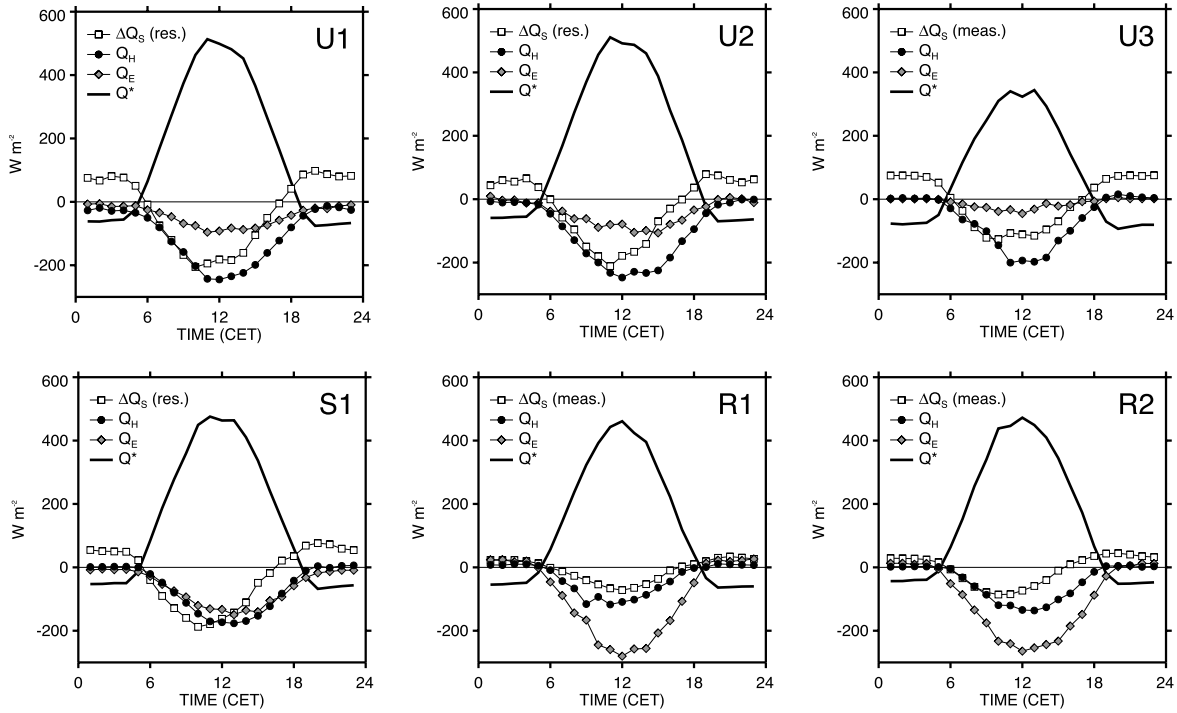


Figure 4.75: Ensemble diurnal course of energy balance at 3 urban (U1-U3), 1 suburban (S) and 2 rural (R1,R2) sites during the IOP (June 10 to July 10, 2002). U3 has been only operated for part of the IOP (July 24 to June 12, 2002).

function of λ_V is capable of modelling the annual variation of the urban β in the present dataset, if the variation of rural is known from e.g. measurements, climatology, or models. The factor k (Eq. 4.44) is retrieved for each month and is included in Fig. 4.78a. For most of the year, k is constant at around 0.2. However, between January and March when transpiration is low but additional human water vapor input by combustion is artificially increasing Q_E , the performance of a constant $k=0.2$ is poor. The year-long eddy-correlation measurements carried out between September 2001 and August 2002 show a similar annual variation in β (see also Tab. 4.25). The eddy correlation measurements suggest a slightly higher yearly average of the daytime β of around 2.5 compared to the average urban value retrieved from the 1997–2002 profile data, where the average urban value is $\beta = 1.8$. There is evidence that the overestimation of β is due to a more patchy distribution of water vapor sources in the urban neighborhoods, and hence mainly attributed to an inappropriate flux-gradient relationship of water vapor.

During winter nights, both the absolute magnitude and the nocturnal ratio Q_E/Q^* at the urban sites indicate a higher energy loss through Q_E than in summer nights. The wintertime nocturnal β in the city

center is surprisingly low ($\beta \approx 0.5$) compared to summertime nocturnal values where Q_H is typically twice as large as Q_E and β is nearly identical with its daytime value ($\beta \approx 2$). The low β indicates that the energy input by combustion through Q_F affects Q_E during winter nights.

Figure 4.77 summarizes typical daily totals of all energy balance components in the city center for each month of the year. Positive values indicate an energy surplus of the city, negative values an energy loss of the city. The yearly total of Q^* is $+1.9 \text{ GJ yr}^{-1} \text{ m}^{-2}$. Its yearly course has already been discussed in Section 4.5.5. Neglecting the fact that Q_E contains marginal amounts of dewfall, the yearly total of Q_E corresponds to an urban evapotranspiration of approximately 300 mm yr^{-1} . This is a reasonable value compared to the value over grassland of 700 mm yr^{-1} obtained from long-term lysimeter measurements close to Basel (precipitation 800 mm yr^{-1}). The urban evapotranspiration includes human water vapor input.

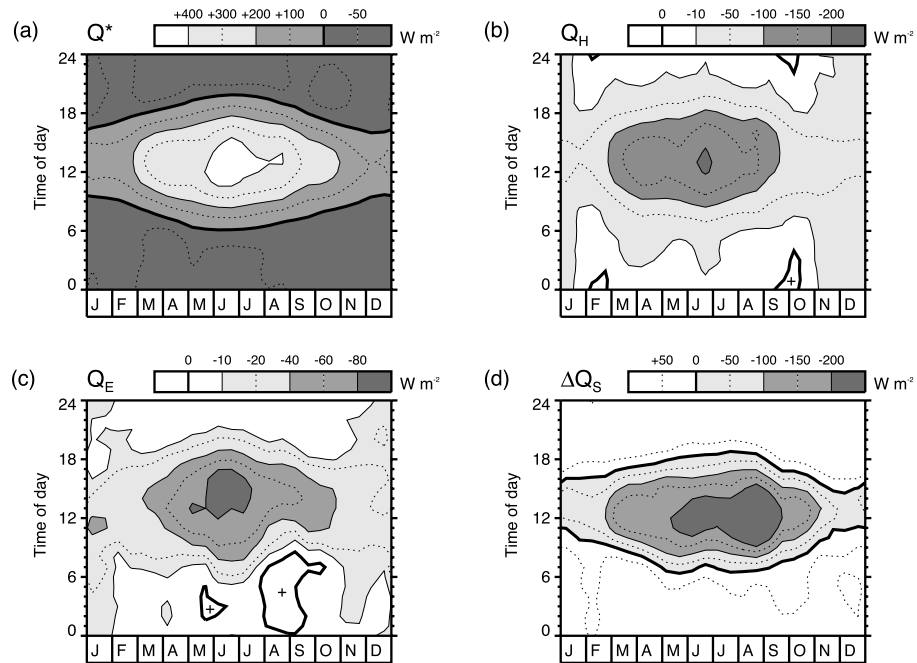


Figure 4.76: Isofluxdiagrams of annual (x -axis) and daily (y -axis) variation of (a) Q^* , (b) Q_H , (c) Q_E and (d) the residual ΔQ_S in the city center measured at U2 for the period September 2001 to August 2002. Plots are smoothed (boxcar-type filter of ± 15 days and $1h$, respectively) in order to remove noise and generalize results. Missing data are interpolated. Note that the contour lines are not equidistant.

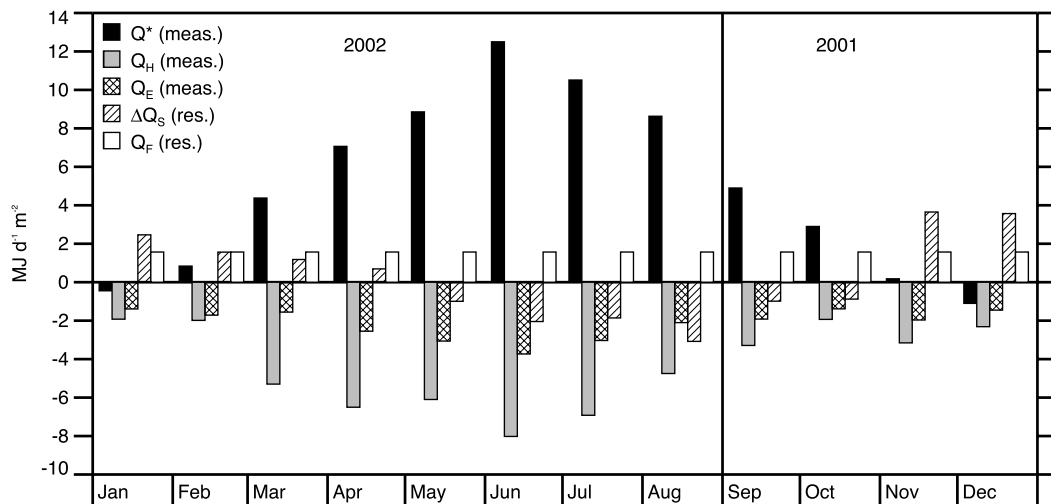


Figure 4.77: Average daily totals of the energy balance components in the city center for each month. Data are an average of U1 and U2 (Dec–Jul) and U2 (Aug–Nov). Flux densities directed towards the surface are positive (energy gain) and away from the surface negative (energy loss).

Table 4.25: Average daytime partitioning (1100–1500 CET) of the energy balance for the full year period Sep 2001 – Aug 2002. The chosen periods are: Fall: Sep - Nov 2001, Winter: Dec 2001 – Feb 2002, Spring: Mar – May 2002, Summer: Jun – Aug 2002.

Q_H/Q^*	U1	U2	R3 ^a
Fall		-0.66	-0.34
Winter	-0.56	-0.56	-0.41
Spring	-0.56	-0.50	-0.27
Summer	-0.49	-0.46	-0.23
Year	-0.54 ^b	-0.55	-0.31

Q_E/Q^*	U1	U2	R3 ^a
Fall		-0.27	-0.59
Winter	-0.28	-0.29	-0.51
Spring	-0.19	-0.18	-0.59
Summer	-0.20	-0.20	-0.66
Year	-0.22 ^b	-0.24	-0.59

$\Delta Q_S/Q^*$	U1 ^c	U2 ^c	R3 ^a
Fall		-0.17	-0.08
Winter	-0.34	-0.36	-0.08
Spring	-0.31	-0.37	-0.14
Summer	-0.36	-0.37	-0.11
Year	-0.34 ^b	-0.37	-0.10

β	U1	U2	R3 ^a
Fall		2.46	0.58
Winter	2.01	1.98	0.81
Spring	3.13	3.18	0.45
Summer	2.50	2.27	0.35
Year	2.55 ^b	2.47	0.55

^a values determined by profile method. All other turbulent fluxes are directly determined by eddy covariance.

^b yearly values of U1 are calculated with fall values of U2.

^c values determined as residual term.

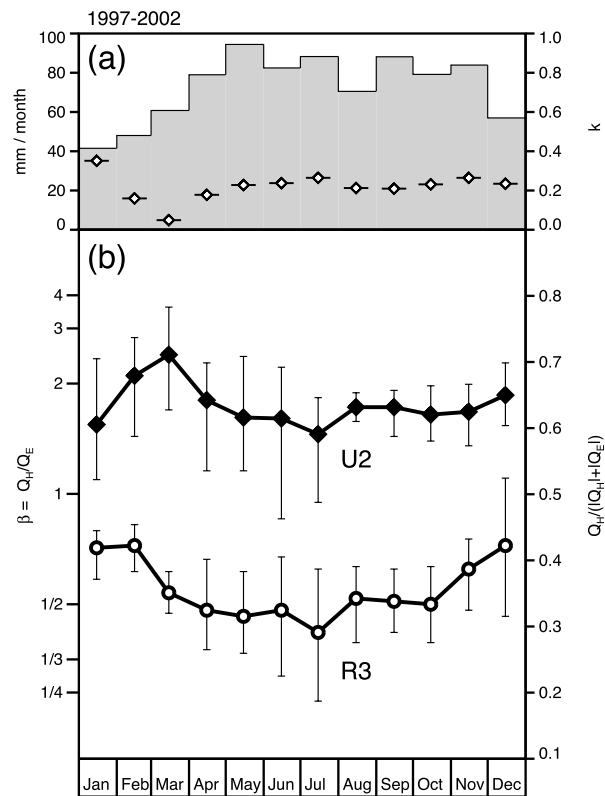


Figure 4.78: a: Annual variation of precipitation (grey shaded area) and k -factor (diamonds) for the period 1997–2002. b: Annual variation of daytime Bowen ratio β over a rural (R3) and an urban surface (U2). β is retrieved from continuous profile measurements of $\partial\theta/\partial z$ and $\partial q/\partial z$. The error bars indicate the maxima and minima of the six years 1997–2002. At the urban sites temperature and humidity profiles were calculated from measurements sufficiently far above roof top to reduce effects of the roughness sublayer, i.e. between $1.8 < z/z_h < 2.5$. Rural profiles are retrieved from differences between 2 and 10 m.

4.5.7 Sensible heat flux densities

The reduced Q_E at the urban sites is counterbalanced by increased magnitudes of Q_H and ΔQ_S . Q_H is the most significant energy loss of all built-up sites. The yearly total of measured Q_H ($-1.6 \text{ GJ yr}^{-1} \text{ m}^{-2}$) is twice the magnitude of measured Q_E ($-0.8 \text{ GJ yr}^{-1} \text{ m}^{-2}$) (Fig. 4.77).

Daily variations — Daytime Q_H values are typically twice as large in the city compared to the rural surroundings. During the IOP, the magnitude of Q_H is characteristically around 50% of Q^* in the city center, 40% of Q^* at the suburban site, and below 30% of Q^* over rural surfaces. Because Q_H is large when λ_V is low, meaning impervious surfaces and

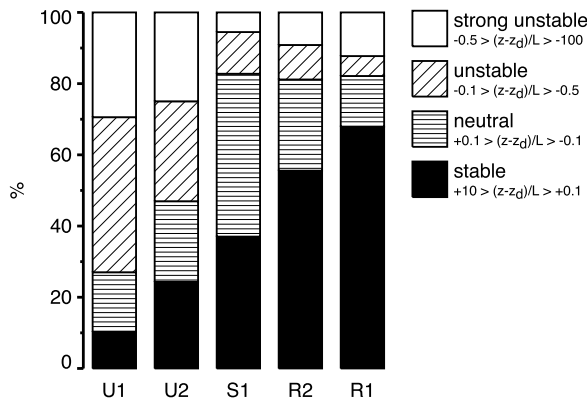


Figure 4.79: Near surface stability histogram for nighttime (22–04h) during the summertime IOP. Stability was calculated from sonic-measurements at $z/z_h > 2$ at the built up sites.

buildings are occupying larger area fractions, there are relationships between all these land-use parameters and the daytime Q_H .

In contrast to rural surfaces where Q_H is directed towards the surface all night (up to $+20 \text{ W m}^{-2}$), both turbulent flux densities remain negative in the city on average, i.e. energy is transported away from the surface. The nocturnal urban atmosphere close to the surface remains unstable, an effect mainly driven by the large storage release (see Section 4.5.8). In contrast to the city stations, the nocturnal Q_H at the suburban site is positive (Tab. 4.24). Here, the surplus energy from the storage release is channelled into an upward directed Q_E flux due to higher water availability. The intensity of the nocturnal upward directed Q_H is linearly related to the complete aspect ratio λ_C (Fig. 4.81b). During the IOP, highest nocturnal Q_H are measured at the dense urban site U1 with -23 W m^{-2} in average. Note that even if the average Q_H is negative in the city center, there are periods with positive Q_H . The first 3 hours after sunset are characterized by the highest frequency of positive Q_H (U1: 20%, U2: 39% of all cases during IOP). Throughout night, the frequency of periods with positive Q_H decreases (not shown).

The sign of Q_H determines the stability of the near surface air layers. Figure 4.79 shows the near surface stability histogram for night-time situations during the summertime IOP. At the built up sites, stability was calculated from measurements at $z/z_h > 2$. The number of nighttime stable situations is dramatically decreasing with increasing building density and unstable situations are more commonly

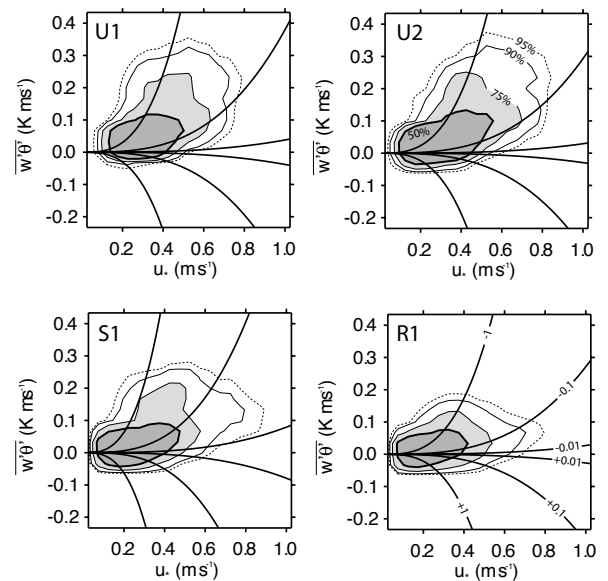


Figure 4.80: Joint probability density function between u_* and $w'\theta'$ simultaneously measured at the topmost measurements at U1, U2, S1 and R1. Black lines denote values of the stability parameter $\zeta = (z - z_d)/L$ according to the labels in the lower right plot. Data source: Sonics F (U1), F (U2), C (S1) and A (R1), 30 min values, June 10 to July 10, 2002, $n=1346h$.

measured in the city center. However, remote sensing instruments and tethered balloon measurements during BUBBLE show that this nocturnal unstable layer is only found very close to the urban surface. An elevated inversion layer is observed over the city, often at heights between 50 – 250 m.

Over the whole 24 hours, at the urban sites, the majority of cases are neutral to slightly unstable stratified, not because of a low $w'\theta'(z)$, but as the effect of an enhanced $u_*(z)$. Figure 4.80 illustrates this pattern with simultaneously measured data from four sites. The plots draw $u_*(z)$ against $w'\theta'(z)$. Corresponding contours indicate the joint probability density for a given $u_*(z)$ and a given $w'\theta'(z)$ according to the labels in the upper right plot. The black lines denote the corresponding stability parameters determined as $(z - z_d)/L$. The dominant difference between urban and rural sites is an enhanced u_* , and simultaneously a strong $w'\theta'$, which compensate the effect on stability.

The upward directed turbulent flux densities and a modified turbulent exchange finally result in a nocturnal urban heat island, with ΔT_{U-R} between $+2$ to $+3\text{K}$ in the city of Basel (Section 4.5.4, Fig. 4.72). The combination of reduced urban moisture availability, nocturnal heat island, and unstable near surface layer explains the often observed reduction of

dewfall (Richards and Oke, 2002; Richards, 2004) and reduction of radiation fog within cities (Sachweh and Koepke, 1995).

Annual variations — Daytime Q_H/Q^* is higher in fall and winter and lower in summer (Tab. 4.25), an effect mainly driven by water availability as already discussed in Section 4.5.6. The average nocturnal Q_H is fairly constant between -5 and -10 W m^{-2} throughout the year (Fig. 4.76b). Slightly higher magnitudes of Q_H are recorded in winter, possibly because of higher anthropogenic heat input Q_F .

4.5.8 Storage heat flux densities

A problem arises from the determination of the urban storage heat flux density into the ground and buildings, ΔQ_S . In contrast to rural surfaces, ΔQ_S of an urban surface can not be measured easily. The large number of surface materials, orientations and their interaction makes direct measurements very laborious and nearly impossible. Therefore, ΔQ_S is usually modelled or determined as the residual term of the energy balance equation, assuming complete closure of the energy balance.

A typical feature of the urban energy balance is an increased magnitude of the storage heat flux density ΔQ_S (Grimmond and Oke, 1995, 1999b). Thermal properties like heat capacity and thermal conductivity of the urban fabrics are different from soils and vegetated surfaces (Oke, 1987). Moreover, the three dimensional surface-area in the city center is nearly doubled compared to a plane surface. This surface enlargement — described by the complete aspect ratio λ_C — adds additional surface, where other flux densities can be converted into storage and increases the volume of shallow depth layers where energy can be temporary stored.

Daily variations — Values of ΔQ_S are two to three times higher in the city center compared to rural sites. During the IOP, ΔQ_S ranges between -30% and -40% of Q^* at the built-up sites. An average $\Delta Q_S / Q^*$ of -0.32 is measured with the heat flux plates at the parking lot (U3, Tab. 4.24). Previous experiments with a direct measurement of ΔQ_S

Table 4.26: Coefficients of the objective hysteresis model (OHM) for the summertime IOP period. Correlation coefficients r^2 and RMS are calculated between the hourly measured or residual ΔQ_S and the modelled ΔQ_S of all individual hourly blocks of the IOP.

	a_1	a_2	a_3	r^2	RMS
		h	W m^{-2}		W m^{-2}
R1	-0.17	-0.05	14	0.89	12
R2	-0.22	-0.34	26	0.83	22
R3	-0.14	0.02	9	0.80	9
S1	-0.41	-0.45	32	0.88	36
U2	-0.44	-0.12	26	0.82	43
U1	-0.40	-0.17	38	0.81	41
U3	-0.41	-0.10	50	0.94	21

report a similar range around -0.3 (Nunez and Oke, 1977). Rural sites show smaller ΔQ_S values that lie between -10% and -15% of Q^* (Tab. 4.24). ΔQ_S -values that are derived as residual terms have to be interpreted carefully and are an estimation of the upper limit, since any underestimation of the turbulent flux densities (closure gap) would consequently lower ΔQ_S .

ΔQ_S shows a pronounced temporal hysteresis at all sites (Fig. 4.75 and 4.74). The daily peak values are reached 1 to 2 hours before the maximum intensity of Q^* is recorded. At all sites, $\Delta Q_S / Q^*$ decreases during afternoon hours. In order to keep the balance, the two turbulent flux densities increase their relative magnitudes towards the evening. The surface starts to release stored energy one to three hours before Q^* changes sign. The hysteresis effect is more pronounced at the urban sites because of the higher magnitude of ΔQ_S (Fig. 4.74). When estimating ΔQ_S in its diurnal course, it is important taking into account the hysteresis effects. Grimmond and Oke (1991, 1999b) suggested the objective hysteresis model (OHM) for urban storage heat flux parametrization, namely

$$\Delta Q_S = a_1 Q^* + a_2 \frac{\partial Q^*}{\partial t} + a_3. \quad (4.46)$$

The parameters a_1 , a_2 and a_3 were determined at all sites and are summarized in Tab. 4.26. They were retrieved by a multiple linear regression between the diurnal course of ΔQ_S in relation with Q^* and $\partial Q^* / \partial t$ during the summertime IOP. Sites where ΔQ_S is determined as residual term, the model results in higher hourly errors, i.e. enhance the root mean square error (RMS), compared to sites where

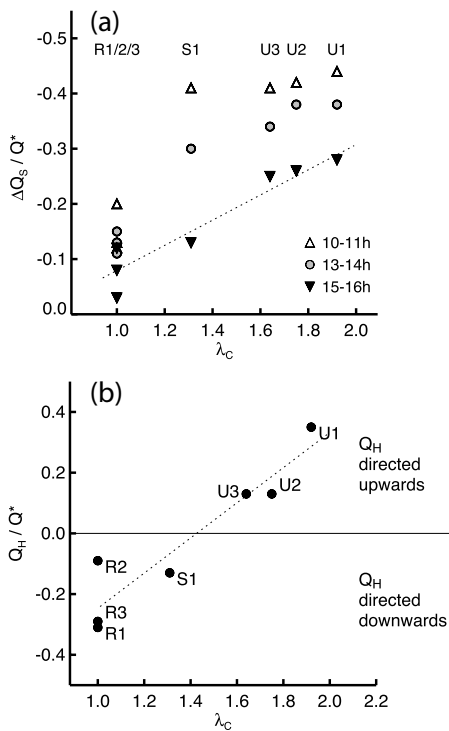


Figure 4.81: a: Relationship between storage heat flux $\Delta Q_S/Q^*$ and complete aspect ratio λ_C for different times of the day. ΔQ_S at the rural sites and U3 are measured directly. At U1, U2 and S1, ΔQ_S was determined as a residual. b: Average nocturnal sensible heat flux Q_H/Q^* in function of complete aspect ratio λ_C . In both figures, points represent the average of hourly block values from the summertime IOP between June 10 and July 10 2002.

ΔQ_S was directly measured (R1-3, U3). This can be seen as an indication that errors from other flux densities are accumulated in the residual ΔQ_S .

a_1 describes the overall strength of ΔQ_S relatively to Q^* . This parameter is closely related with the daytime $\Delta Q_S/Q^*$. It is strong over built-up surfaces (≈ -0.4) and smaller in magnitude at the rural sites (≈ -0.2). a_1 shows a significant relationship with λ_P and λ_V . a_2 determines the strength of the phase shift between Q^* and ΔQ_S . The present data set indicates no clear relationship between any land use parameter or moisture availability and a_2 , a fact already concluded in Grimmond and Oke (1999b). Highest values of a_2 were retrieved at the suburban and the "bare-soil" site (R2). The sites in the city center (U1-3) show values around -0.15 . The offset a_3 corrects the fact that the absolute values of the daytime $\Delta Q_S/Q^*$ and the nocturnal $\Delta Q_S/Q^*$ are not identical. a_3 is stronger at the built-up sites in the city center (30 to 50 W m^{-2}) than over rural surfaces (9 – 25 W m^{-2}).

In the morning, ΔQ_S is of nearly similar magnitude in the city center (Fig. 4.81a). It seems to be primarily the different materials and the sunlit area that determine ΔQ_S and not the complete aspect ratio during this part of the day. During morning, most of Q^* is available at roof level in the city center and the majority of energy exchange processes take place in this layer. The radiative benefit of the roofs relative to walls and ground surfaces is especially prominent when sun elevation is low and shading effects constrict the storage to upper parts of the canopy (see also Section 4.5.3). Measurements of the roof surface temperatures at U1 show typical heating rates between 5 and 10 K h^{-1} in the early morning. The heating and cooling rates at roof level are much stronger (diurnal amplitude ≈ 30 K) compared to inside the street canyon (amplitude ≈ 15 K). Further, the heating rate is much higher in the first morning hours compared to the rest of the day. Roofs are thin and designed to thermally insulate. They have a higher thermal conductivity than vegetated plant surfaces. This results in large urban storage heat fluxes in the morning but also fast saturation effects. Early in the morning, strongest ΔQ_S -values are determined at the suburban site (Fig. 4.74). In the suburban neighborhood, a significant part of the wall and ground surfaces have also direct K_{\downarrow} due to the lower building density (single houses). It is interesting that differences are also observed between the different rural surfaces in the morning. The agricultural surface with bare soil (R2) has morning peak values of $\Delta Q_S/Q^* = 0.24$ at 0900, compared to the simultaneously measured values at the sites with a thick grass cover, R1 and R3 ($\Delta Q_S/Q^* = 0.10$). These inter-rural differences are vanishing throughout the day.

At midday, roofs achieve quicker equilibrium between storage and radiative loss compared to vegetated and bare soil surfaces. But throughout the day, the three-dimensional urban surface can progressively store additional energy into newly illuminated surfaces due to a changing relative position of the sun. Previously shaded surfaces can be made accessible for efficient storage in the afternoon when horizontal surfaces (rural sites) are already in equilibrium. Also redistribution of the energy within the urban canopy by radiative or turbulent transport processes can enhance the storage into lower layers of the UCL. In the evening, a pronounced relationship between $\Delta Q_S/Q^*$ and λ_C is found. At this time

of the day, λ_C seems to be a suitable parameter to explain differences in ΔQ_S between sites (Fig. 4.81a).

The huge daytime ΔQ_S into buildings is counter-balanced by an extremely high nocturnal release of ΔQ_S at U1, U2, and S1. The nocturnal ΔQ_S in the city center can be even higher in magnitude than the radiative loss. In summer nights, ΔQ_S ranges between +50 and +80 W m^{-2} at the built-up sites (Tab. 4.24). The strong nocturnal ΔQ_S is mainly channelled into L_{\uparrow} (Section 4.5.4), and a small part is put into upward directed Q_E and Q_H . The release of stored heat reaches its maximum 1-2 hours after sunset and then slightly decays throughout the night to a value around 80% of its maximum. In general, nocturnal ratios of $\Delta Q_S/Q^*$ in the city center are between 0.9 and 1.3, a range already reported in previous studies (Grimmond and Oke, 1999b).

Annual variations — Typical daytime peak values of ΔQ_S are -50 W m^{-2} in winter and above -200 W m^{-2} in summer (Fig. 4.76d). The monthly totals of ΔQ_S in Fig. 4.77 reflect the energy stored (lost) in the urban fabrics by warming (cooling) from day to day and month to month. The directions of the daily totals shown in Fig. 4.77 are plausible. However, most months show magnitudes of ΔQ_S that are too large (especially Nov – Jan and Jun – Aug). The measured daily totals of ΔQ_S during summertime months are typically $2 \text{ MJ d}^{-1} \text{ m}^{-2}$. This energy would increase the temperatures of the urban materials by 0.1 to 0.5 K d^{-1} , depending on thermal and morphometric properties of the surface. Because the heating rates are far from realistic assumptions, it must be assumed that errors of the other flux densities are accumulated in ΔQ_S . All daily totals of ΔQ_S are affected with large errors because ΔQ_S changes sign in its diurnal course. The daily totals of ΔQ_S (and also Q_F , see Section 4.5.9) are therefore very sensitive to small errors in the other flux densities. The overestimation of ΔQ_S may be an indication that the two turbulent flux densities are slightly — but systematically — underestimated because of theoretical, methodical or instrumental errors. Any underestimation of Q_E and Q_H would lead to an overestimation of ΔQ_S . Further, the large errors in winter are an indication that winter-time values of Q_F are possibly larger than assumed (Section 4.5.9). But a larger wintertime Q_F would conversely increase the summertime daily to-

Table 4.27: Estimated urban energy balance modification for the summertime IOP period. Positive (negative) values indicate an energy surplus (loss) of the city by the particular term relative to the rural surroundings. Urban values are an average of sites U1 and U2. Rural values are an average of R1, R2 and R3.

	Daily total Δ_{U-R} $\text{GJ yr}^{-1} \text{ m}^{-2}$	Daytime Δ_{U-R} W m^{-2}	Night Δ_{U-R} W m^{-2}
K_{\downarrow}	- 0.1	-5	0
K_{\uparrow}	+ 1.9	+51	0
L^*	- 1.0	- 10	- 15
Q_H	- 5.0	- 106	- 26
Q_E	+ 6.1	+ 168	-18
ΔQ_S	- 1.5	- 122	+ 46
Q_F^a	+ 1.3	+ 15	+ 15

a Based on the estimation for the full year total (Section 4.5.9)

tals of ΔQ_S , which are already overestimated.

4.5.9 Anthropogenic heat flux densities

At both city center sites, the residual term of the energy balance equation ($Q^* + Q_H + Q_E$) shows a small surplus in the yearly total. This suggests a missing energy source in the order of $-0.5 \text{ GJ yr}^{-1} \text{ m}^{-2}$ at U1 and $-0.3 \text{ GJ yr}^{-1} \text{ m}^{-2}$ at U2. This missing source is only attributed to the anthropogenic heat flux density Q_F , because the yearly total of ΔQ_S has to be zero by definition, i.e. the city can not be expected to cool down or heat up. We can only determine the yearly total of Q_F , but not its time-dependent values. Inventory data and/or models (Taha, 1999a) would be needed to simulate annual and daily variations. Here, simply a constant Q_F throughout the year has been assumed. The determined ‘constant’ anthropogenic emission implies a Q_F of approximately $+20 \text{ W m}^{-2}$ at U1 and $+10 \text{ W m}^{-2}$ at U2 in the annual average. These are realistic values compared to calculations and studies in literature (Taha, 1999b; Oke, 1987). Especially during winter, Q_F is surely enlarged due to firing, as inventory methods in other European cities show (Klysisik, 1996).

4.5.10 Urban energy balance modification

Table 4.27 summarizes the estimated urban energy balance modification for the summertime IOP pe-

riod. During daytime, the city has a higher energy input due its lower albedo ($+51 \text{ W m}^{-2}$) and due to the significantly reduced evapotranspiration ($+168 \text{ W m}^{-2}$). In absolute numbers, the reduced Q_E is the most severe modification in the city center. Its local magnitude is highly dependent on the total vegetation cover of the neighborhood. On the other hand, the surface enlargement and the thermal properties of the urban surface allow additional storage into buildings, an effect that typically increases ΔQ_S by a factor of two to three compared to rural values. The increased urban ΔQ_S drains an additional -122 W m^{-2} . The remaining surplus of -106 W m^{-2} is put into the increase of Q_H . Its magnitude is doubled compared to the rural measurements. Modification of long-wave radiation components and the effects of Q_F are small. Urban modifications of Q_E , ΔQ_S and Q_H were in similar direction, but slightly lower in magnitude in a study reported from Vancouver, which addressed rural-suburban differences (Cleugh and Oke, 1986).

The nocturnal release of heat storage ΔQ_S in the city center is typically twice the value over rural surfaces ($+46 \text{ W m}^{-2}$). ΔQ_S is the most significant modification in the nocturnal energy balance. In the city center, the available energy through ΔQ_S is often higher in magnitude than the radiative loss through Q^* . Therefore, both turbulent flux densities have to transport this excess energy away from the surface, i.e. they are directed upward. The sign and intensity of the nocturnal Q_H is roughly related to the building density.

The magnitude of the residual term, ΔQ_S , calculated for the full year is not well defined. Further investigation of the temporal variation of Q_F and a deeper analysis of ΔQ_S would be needed to enhance the significance of the estimation.

4.5.11 Summary

- The simultaneous operation of seven energy balance sites in different urban and rural environments allowed a detailed and successful investigation of the urban energy balance modification.
- K_{\uparrow} is strongly reduced in urban environments. The three dimensional configuration of buildings, the associated shading, and dark surface

materials result in a low albedo. The average albedo are in the order of 10% over the dense urban surfaces, and 13% over the suburban surface.

- In the radiation budget, the lower K_{\uparrow} and a stronger L_{\uparrow} counterbalance. As a consequence, net radiation measured over the investigated urban surfaces is not significantly different from the one measured in the rural environment. During day, net radiation is slightly higher at the urban sites. During night, long-wave loss is enhanced in the urban environment.
- The Bowen ratio β is clearly related to the vegetation fraction λ_v of the different urban neighborhoods. The proposed relationship in Eq. 4.43 reproduces adequately urban-rural differences most of the year.
- Urban surfaces are characterized by a strong storage term in the energy balance. Typically, at the urban sites, ΔQ_S is increased by a factor of two to three compared to rural values.
- During night, turbulent flux densities Q_H and Q_E are directed upwards in dense urban environments. This is a consequence of a strong nocturnal release of stored heat, which is typically twice as strong as over rural surfaces. As a consequence, the urban inertial sublayer and the roughness sublayer are unstable most of the time.

5 Conclusions

The turbulence measurements at the three full-scale profile towers provided valuable insights into mean flow, turbulent kinetic energy, and exchange processes of momentum, energy and mass within the urban roughness sublayer, namely the region from street level up to 2.5 times the mean building height. Further, the network of spatially distributed energy balance measurements not only yielded information on exchange processes, but also allowed a study of the surface energy partitioning simultaneously measured over different land use (urban, sub-urban, rural).

5.1 Methodology

Individual profiles — With the term ‘roughness sublayer’, we inherently associate the fact that individual values of any property strongly depend on location and specific flow configuration. Indeed, individual profiles measured at the towers show a strong dependence on the direction of the ambient flow relative to the local street canyons and building structures. Close to the roofs and in the street canyon, a large variability is measured, which further camouflage any other driving processes known from surface layer scaling, in particular thermal stratification.

Horizontally averaged profiles — In order to reduce complexity, ‘horizontally averaged’ profiles have been introduced by averaging over different wind directions (equally weighted). These ensemble profiles of turbulence parameters agree in nearly all cases, i.e. most profiles (with the exception of heat flux densities) show a similar shape at the three different towers. This underlines that the averaging procedure described in Section 3.3.3, together with the large number of realizations measured, can be successfully regarded as a surrogate for a real horizontal average. In other words, the real horizontal average, deduced from simultaneous measurements at different locations under a particular ambient flow may converge with this ensemble average of many

realizations measured at one location with varying ambient flow. Horizontal averaging does not only provide the advantage of representing a generalized flow field at neighborhood scale, it additionally allows many simplifications. For example, measured $\langle \overline{v'w'} \rangle$ nullifies, even if particular situations are characterized by a consistent nonzero $\overline{v'w'}$, due to a rotation of the wind direction with height as an effect of flow channelling into the street canyon.

Urban family portrait — The three vertical profiles of selected mean flow and turbulence characteristics can be summarized in a generalized ‘urban family portrait’ (Fig. 5.1). The family portrait is an approach known from plant canopy studies, as compiled by (Raupach et al., 1996) and (Finnigan, 2000), and summarizes vertical profiles from a variety of wind tunnel and full-scale experiments. Many features found in our small urban family consisting of ‘only’ three towers reflect processes that are characteristic for flow over rough surfaces, and resemble flow properties measured within and above plant canopies.

5.2 Synthesis

5.2.1 Vertical structure of the urban roughness sublayer

In previous work, the roughness sublayer is typically separated into an urban canopy layer (UCL) confined by buildings, and a layer above (Oke, 1987). The present results from a surface with non-uniform building height suggest a further conceptual division into three layers, namely the deep *canyon layer* (CAL, $z < z_d$), the *roof layer* (ROL, $z_d < z < z_f$), and the *above-roof layer* (ARL, $z > z_f$), where z_f is the height of maximum Reynolds stress. As a practical approximation, we can write $z_f = z_e + \sigma_h$, where z_e is the height of the principal inflection point in the mean wind profile, referred to as *effective building height*. In the present results, $z_e \approx 1.2z_h$. However,

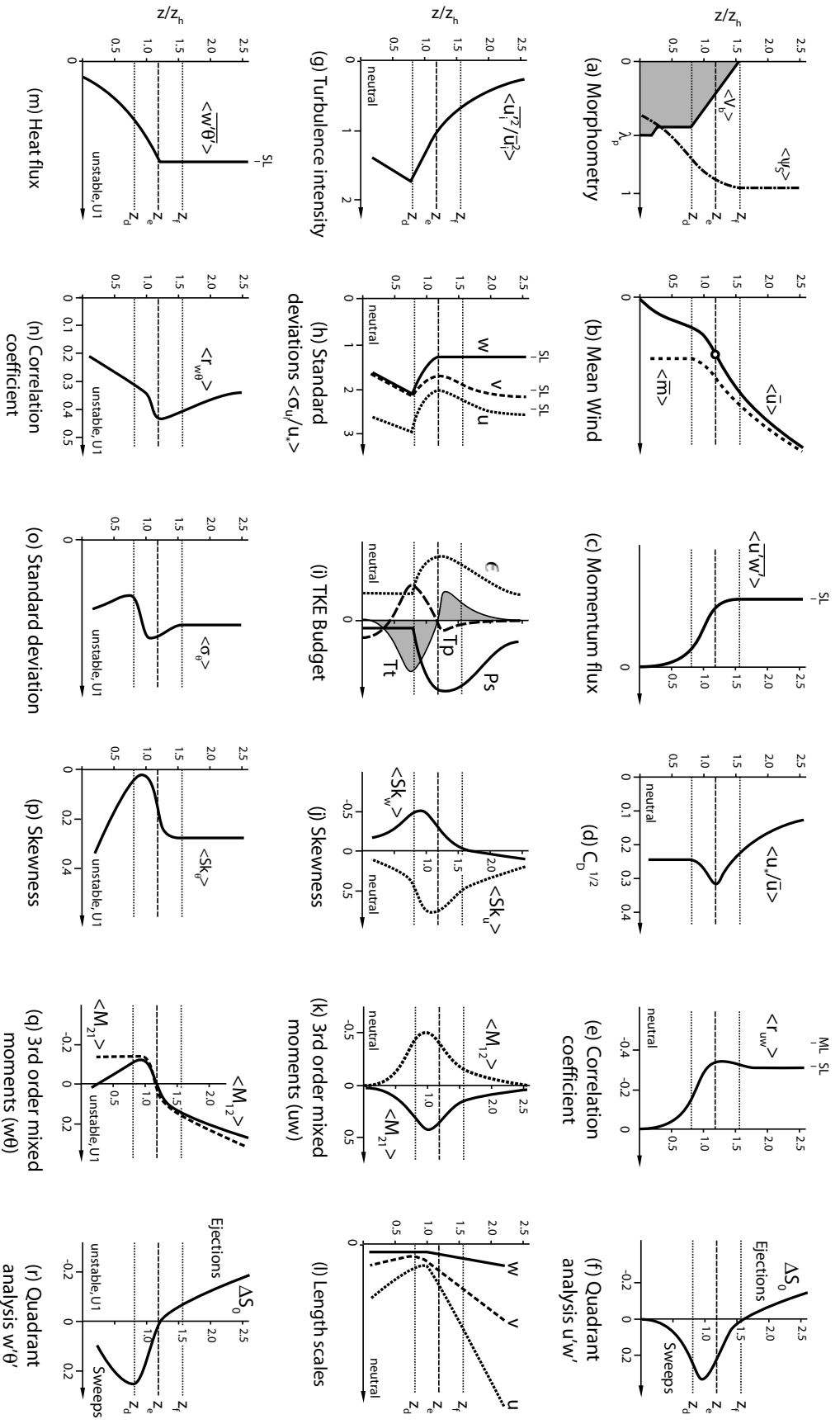


Figure 5.1: Concept of generalized and horizontally averaged profiles through the roughness sublayer derived from the present study. The three reference heights are zeroplane displacement z_d , the effective building height (height of the wind profile inflection point) z_e , and the height of maximal Reynolds stress z_f . (a) Building volume density (V_b) in $m^3 m^{-3}$ in a given layer and sky view factor (ψ_s), (b) global longitudinal wind velocity ($\langle u \rangle$) and horizontal scalar wind speed ($\langle \overline{m} \rangle$), (c) turbulent momentum flux ($\langle u'w' \rangle$), (d) square root of the neutral drag coefficient ($\langle u_* / \overline{u} \rangle$), (e) correlation coefficient of turbulent momentum flux ($\langle r_{uw} \rangle$), (f) the quadrant measure $\Delta S_0(u'w')$ indicating if sweeps or ejections are dominant in the turbulent momentum flux, (g) local turbulence intensity expressed as the local ratio between TKE and MKE under neutral conditions ($\langle \sigma_{u_i} / u_* \rangle$), (h) the relevant terms of the neutral TKE-budget (PS : shear production, Tr : turbulent transport, Tp : pressure transport, ϵ : dissipation rate), (i) skewness of horizontal ($\langle Sk_u \rangle$) and vertical wind component ($\langle Sk_w \rangle$), (k) third order mixed moments of u and w (M_{12} : $\langle u'w'^2 / (\sigma_u^2 \sigma_w) \rangle$, M_{21} : $\langle u'u'^2 / (\sigma_u^2 \sigma_w) \rangle$), (l) Integral length scales derived from peak frequency of power spectra, (m) turbulent heat flux ($\langle \overline{w'\theta'} \rangle$), (n) correlation coefficient of turbulent heat flux ($\langle r_{w\theta} \rangle$), (o) Standard deviation of temperature σ_θ , (p) skewness of temperature ($\langle Sk_\theta \rangle$), (q) third order mixed moments of w and θ (M_{21} : $\langle w'^2 \theta' / (\sigma_w^2 \sigma_\theta) \rangle$, M_{12} : $\langle w'\theta'^2 / (\sigma_w \sigma_\theta^2) \rangle$), (r) the quadrant measure $\Delta S_0(w'\theta')$ for turbulent heat flux. 'ML' and 'SL' denote surface layer and plane mixing layer limits, respectively.

if we would omit the one storey backyard buildings in the calculation of z_h because these flat and enclosed structures are aerodynamically not important, we could even simplify $z_e \approx z_h^*$.

Canyon layer (CAL) — At least in its upper part, the horizontally averaged wind profile can be well approximated by an exponential decay law, which supports the findings of Macdonald (2000). Large differences between the (global) longitudinal wind velocity $\langle \bar{u} \rangle$ and horizontal mean wind speed $\langle \bar{m} \rangle$ are found. Roof shape was determined as an important factor affecting exchange in the street canyon. Flow over flat roofs results in a clear primary vortex and is characterized by higher wind speed at street level compared to flow over pitched roofs, which shows no clear vortex. This supports findings from wind tunnel studies (Kastner-Klein et al., 2004).

Reynolds stress and turbulent heat flux both are of minor importance in the CAL.

Turbulence in the canopy layer is very intermittent, and the well known street canyon vortex is only found on average and only for selected configurations. The major part of TKE is imported by sweeps from the ROL. This is expressed by strongly negative Sk_w and M_{12} . Fluctuations of velocity components and scalars are rather uncorrelated. Further, there is evidence from the present data set that TKE could be transported down in the very bottom of the street canyon by pressure fluctuations.

In the canopy layer, one point length scales slightly increase with depth. However, the most appropriate scaling length was determined as the average distance to the nearest obstacles, which in the canyon may be approximated by $z' \approx \langle x_c \rangle / 4$, where $\langle x_c \rangle$ is the characteristic street canyon width.

Roof layer (ROL) — Around roof top, the profiles in the ‘urban family portrait’ are characterized by strongest gradients. Generally, cross-canyon flow results in stronger gradients and more efficient exchange, whereas along-canyon flow is characterized by a nearly linear wind profile with height and a less efficient exchange around roof top.

* Note that for an appropriate calculation of σ_h , it should also be calculated with the exclusion of the one-storey backyard buildings (see Tab. 3.3).

In the ROL, shear production is a strong source of TKE. The inflectional mean wind profile creates instabilities, which export a notable amount of TKE and temperature variance by sweeps into the upper street canyon and by ejections into the surface layer above. Around z_e , temperature is less skewed. With increasing height — but also down into the street canyon — skewness is enhanced. Further, there is evidence that pressure fluctuations may transport TKE from the ROL and the upper street canyon down into the deep street canyon. Hence, the ROL can be seen as an export region. As a consequence, dissipation is lower than locally produced turbulence, and neutral limits of horizontal velocity variances are slightly smaller than predicted by local scaling.

Length scales are smallest in the ROL. Further, correlation coefficients are often higher, exchange is more efficient, and takes place in larger time fractions.

All these results fit well with features of flow over plant canopies. This suggests that — at least for cross-canyon flow — the plane mixing layer analogy of Raupach et al. (1996) is valid. There are many indicators that for along-canyon flow, the analogy is less appropriate. Therefore, many values lie between surface and mixing layer values on average, and effects are blurred in the horizontal average. However, the consequences of the inflected velocity profiles still dominate the ‘family portrait’. Note that the height of the inflection point z_e of the urban canopies is slightly higher than the calculated mean building height z_h , as discussed above.

Above-roof layer (ARL) — Above highest roofs, the wind profile approximates the well-known logarithmic form of the inertial sublayer. Here, all flow characteristics approach surface layer values. The lower boundary of the ARL is defined as z_f , the height of the maximum Reynolds stress. Most flow situations show a minor decrease of Reynolds stress with height above z_f . In particular, flow over pitched roofs results in more pronounced peaks of Reynolds stress and decay stronger above, whereas flow over flat roofs shows a nearly constant Reynolds stress profile with height in the ARL. Kastner-Klein and Rotach (2004) argue that peaks in Reynolds stress are reported mainly from smooth-

rough transitions where the flow is not readjusted. Over horizontally homogeneous surfaces, peaks are less pronounced or vanish. In a generalized view, Reynolds stress and turbulent heat flux can be regarded constant with height in the ARL.

The scaling length in the ARL is clearly the height above zeroplane displacement. While shear production is the main source in the ROL, both buoyancy and shear production of turbulence are important in the ARL. In the temporal mean, local stability is shifted from neutral towards more unstable / stable with increasing height, and many parameters show a clear stability dependence.

Turbulent transport processes of momentum and heat are dominated by ejections. These ejections relocate temperature variance from the ROL and export it into higher layers where they enhance temperature variance. Local scaling neglects this turbulent transport divergence. Simultaneously, inactive turbulence, which originates from larger scales and is not related to surface exchange, enhances corresponding values. This explains why the normalized standard deviations of temperature, water vapor, and CO₂ are all distinctly higher in the ARL than predicted by the classical semi-empirical functions developed for the surface layer.

The question of the upper boundary of the roughness sublayer is more difficult to answer, since the transition to the inertial sublayer is rather gradual. Any exact height depends on the definition of the blending height z_* , originally defined as the height where the flow is ‘blended’, i.e. where for any parameter a , we may write $\langle \bar{a} \rangle \approx \bar{a}$ at any horizontal location. In reality, we have to define an arbitrary threshold value for the horizontal variation, which is highly sensitive for the resulting z_* , and different for different parameters.

In terms of scaling, indeed, there are many indicators that would allow a surface layer scaling with modified constants already in the ARL. Or can the ARL even be interpreted as the inertial sublayer, i.e. may we write $z_* = z_f$? In order to prevent confusion, the author suggests using z_f as the lower limit in which surface layer scaling is valid in the horizontal average, i.e. above which $\partial \langle \overline{u'w'} \rangle / \partial z \approx 0$. z_* should be reserved for the ‘blending’ definition, which is typically encountered higher up.

5.2.2 Exchange processes

The present dense urban surfaces are characterized by surprisingly low albedo values in the order of 10%. The low K_{\uparrow} however is counterbalanced by a stronger L_{\uparrow} , resulting in a nearly equivalent net radiation measured over urban surfaces and rural environments on average. During the day, net radiation is slightly higher at urban locations whereas during night, long-wave loss is enhanced at the urban sites.

The daytime urban energy balance is characterized by a strong storage term, a strong upward directed sensible heat flux, and a weak evapotranspiration. The situation at night is different from that in rural environments: on average, both turbulent flux densities remain upward directed in dense urban environments. This is a consequence of a strong nocturnal release of stored heat, which is typically twice as strong as over rural surfaces. As a consequence, the urban inertial sublayer and the roughness sublayer are thermally unstable most of the time. Close to the roofs, the high shear production shifts local stability towards neutral values.

In the ARL, cospectra of vertical flux densities of temperature, water vapor and CO₂ show high agreement, and peak frequencies are similar to the ones observed in the surface layer. This suggests that roughly the same scales dominate turbulent exchange. At roof level, the scales of exchange are different, which is explained by different heights of the active surfaces.

The efficiency of the exchange over the urban surfaces is lowest for water vapor and stronger for heat and CO₂. Water vapor fluctuations are mostly driven by inactive turbulence, while variances of virtual acoustic temperature and CO₂ are more characterized by active fluctuations created at the local surface-atmosphere interface.

5.3 Implications

Implications for models — These presented results are of particular importance for air pollution and near-field dispersion modelling. The roughness sublayer hosts the majority of pollutant sources, but also most human activities take place in this layer.

As already underlined by Rotach (1991) and Rotach (1999), it is therefore essential to appropriately resolve the roughness sublayer in these applications.

If the inertial sublayer values of u_* (IS) and $\overline{w'\theta'}$ (IS) are known, their average vertical profiles below z_f can be parameterized with the empirical formula suggested for $\langle u_* \rangle(z)$ by Rotach (2001) (Eq. 4.18) and by the suggested exponential decay below z_e of $\langle w'\theta' \rangle$ in Eq. 4.41.

However, the local scaling approach propagated by many urban studies (Roth, 2000) does only work partially. Velocity variances follow rather well the surface layer scaling in the higher ARL. As with decreasing height, turbulent transport processes become increasingly important and even dominate in the street canyon. Therefore, in these layers turbulence is inappropriately described by local production. It is again notable that locally scaled variances of temperature and CO₂ better match the surface layer predictions close to z_e than above and below, where they underestimate measured values due to variance import by turbulent transport.

When exchange is modelled in the roughness sublayer, either in a large eddy simulation or in a mesoscale model, moments of at least order three have to be considered. Hence, many classical local turbulence closure schemes like the K -theory or the mixing length are only applicable well above z_f and fail below. For most applications, considering a third order closure scheme seems to be appropriate, and influences of higher order moments (≥ 4) are only important in the upper street canyon (tested for momentum exchange only). If third order moments are not solved, they have to be appropriately parameterized. Further, non-local closures could promise enhanced performance.

If the roughness sublayer is not explicitly simulated in a model, the urban surface may be described by modified surface properties. The following properties have been evaluated to be characteristic for the investigated ‘European urban’ surfaces: zeroplane displacement $z_d = 0.8 - 0.9z_h$, roughness length $z_0 = 0.1z_h$, albedo $\alpha = 10\%$, vegetation fraction $\lambda_V = 0.2$, and sky view factor at ground level $\psi_{S0} = 0.4$. For the ‘European suburban’ surface, $z_d = 0.6z_h$, $z_0 = 0.3z_h$, $\alpha = 13\%$, $\lambda_V = 0.5$, and $\psi_{S0} = 0.6$. The measured Bowen ratio β can be related to the vegetation fraction λ_v (Eq. 4.43), mak-

ing vegetation fraction a suitable input parameter for the estimation of the partitioning in simple models if irrigation is low and the partitioning at a rural reference is known. Vegetation fraction can be easily derived from maps, aerial photos, or from NDVI deduced from satellite images.

Implications for measurements — In many applications, standardized urban wind observations are requested. Currently, reference heights are in discussion (Oke, 2004). From the present data set it follows that if ever possible, wind speed measurements should be performed above z_f to avoid not only spatial inhomogeneity but also the strong gradients and high turbulence intensities in the ROL. This height is a good compromise between a feasible setup and reasonably representative results.

Currently undertaken attempts to start long-term flux monitoring sites for CO₂ and other trace gases in urban environments (Grimmond et al., 2004) call for appropriate estimations of their upwind influence regions (footprints) in order to assess the representativeness of monitoring sites. Because most emissions of interest are released at street level, backward Lagrangian dispersion models should cope with probability density functions incorporating the mixing layer analogy.

Flux-gradient approaches fail in the roughness sublayer, and corresponding ϕ -functions are altered in the ARL. The Bowen-ratio method is roughly applicable in the ARL, even if there is evidence that it overestimates β due to a more patchy distribution of water vapor sources in the urban neighborhoods. The strong asymmetric exchange (skewed PDFs) and associated turbulent transport further questions any parameterized flux measurement technique, for example the relaxed eddy accumulation method (Businger and Oncley, 1990).

The inertial subrange method, which derives dissipation rate ϵ from velocity spectra, worked reasonably in the urban roughness sublayer, in particular because there are no indications for relevant small scale turbulence production rates, which is an advantage compared to highly fractal plant canopies. In order to find more support, the applicability of Taylor’s hypothesis calls for further research (see below).

5.4 Outlook and future research

The present results incorporate large potential to test model improvements and turbulence closure schemes. They already allowed to validate urban surface parameterizations in mesoscale meteorological models (Roulet, 2004; Hamdi and Schayes, 2004) and dispersion models, in particular combined with the near-field tracer experiment data (Rotach et al., 2004; Gryning et al., 2005).

Possible exploration of the present data set —

Most approaches in the present thesis integrate a large number of cases, but do not focus on single events. There is still much potential in the present data set to analyze and visualize the fluid mechanical structures explaining the exchange in the urban roughness sublayer, as for example recently demonstrated by Feigenwinter and Vogt (2005) for the upper urban roughness sublayer. Since data were sampled at each tower in a quasi-synchronized mode, the BUBBLE data would allow the investigation of spatial vertical cross-correlations as well as conditional sampling of time-height cross sections through coherent structures (micro-fronts). For carefully selected cases, turbulent air movements could be visualized, and ensembles of these events would provide further insights and understanding of exchange structures above rough surfaces.

Wavelet analysis allows detecting the number, magnitude, and periodicity of structures in a turbulent time series. This is of major interest at the height of the inflection point, in order to further support the applicability of the mixing layer analogy, together with the length scale L_s suggested by Raupach et al. (1996).

Future experimental areas — Shaw et al. (1995) demonstrated that for plant canopies one-point length scales in the canopy are not equal to two point length scales and hence, the convection velocity u_c is larger than the Eulerian velocity. The magnitude of this dissimilarity is important for the application of Taylor's hypothesis. This field could be experimentally addressed for urban areas in wind tunnel experiments or with simultaneously operated arrays of instruments at a given height layer.

Eddy correlation measurements of pressure fluctuations are still an instrumental challenge. The residual term in the TKE budget gives evidence that pressure fluctuations are important in the lower street canyon, but up to now, neither direct nor indirect measurements support this observation in urban environments.

Further, the transfer from Eulerian to Lagrangian statistics is rather neglected in experimental studies. 'Lagrangian micro-sensors' are currently in early stages of development (e.g. Manobianco et al., 2004) but promise new insights and new approaches to dispersion characteristics.

Concluding remarks — There are still many details and steps to be done for a successful implementation and transfer of these results into applications, mainly numerical models. These models will hopefully provide a sound basis for actions to increase health and safety by forecasting dispersion and meteorological processes in tomorrow's urban environments. Both, an adequate short-term response to releases of chemical and biological agents, and the long-term impacts of pollutants from routine sources will be of increasing relevance in urban areas with ongoing urbanization.

Bibliography

- Allwine, J. K., Leach, M. J., Stockham, L. W., Shinn, J. S., Hosker, R. P., Bowers, J. F. and Pace, J. C. (2004), Overview of Joint Urban 2003. An atmospheric dispersion study in Oklahoma City, in 'Symposium on Planning, Nowcasting, and Forecasting in the Urban Zone, Seattle WA. January 10 to 12, 2004', Am. Met. Soc.
- Allwine, J. K., Shinn, J. H., Streit, G. E., Clawson, K. L. and Brown, M. (2002), 'Overview of URBAN 2000', *Bull. Amer. Meteorol. Soc.* **83**, 521–536.
- Amiro, B. D. (1990), 'Drag coefficients and turbulence spectra within three boreal forest canopies', *Boundary-Layer Meteorol.* **52**, 227–246.
- Antonia, R. A. (1981), 'Conditional sampling in turbulence measurements', *Annu. Rev. Fluid Mech.* **13**, 131–156.
- Arnfield, A. J. (2003), 'Two decades of urban climate research: A review of turbulence, exchanges of energy and water, and the urban heat island', *Int. J. Climatol.* **23**, 1–26.
- Arnold, S. J., ApSimon, H., Barlow, J., Belcher, S., Bell, M., Boddy, J. W., Britter, R., Cheng, H., Clark, R., Colville, R. N., Dimitroulopoulou, S., Dobre, A., Grealley, B., Kaur, S., Knights, A., Lawton, T., Makepace, A., Martin, D., Neophytou, M., Neville, S., Nieuwenhuijsen, M., Nickless, G., Price, C., Robins, A., Simmonds, D. S. P., Smalley, R. J., Tate, J., Tomlin, A. S., Wang, H. and Walsh, P. (2004), 'Introduction to the DAPPLE air pollution project', *Science of the Total Environment* **332**, 139–153.
- Baik, J. J. and Kim, J. J. (1999), 'A numerical study of flow and pollutant dispersion characteristics in urban street canyons', *J. Appl. Meteorol.* **39**, 1576–1589.
- Baik, J. J. and Kim, J. J. (2004), 'A numerical study of the effects of ambient wind direction on flow and dispersion in urban street canyons using the RNG k-epsilon turbulence model', *Atmos. Environ.* **38**, 3039–3048.
- Baik, J. J., Park, R. S., Chun, H. Y. and Kim, J. J. (2000), 'A laboratory model of urban street canyon flows', *J. Appl. Meteorol.* **39**, 1592–1600.
- Bergström, H. and Högström, U. (1989), 'Turbulent exchange above a pine forest. II. Organized structures', *Boundary-Layer Meteorol.* **49**, 231–263.
- Böhm, M., Finnigan, J. J. and Raupach, M. R. (2000), Dispersive fluxes and canopy flows: just how important are they?, in '24th Conf. Agr. For-Meteorol., 14-18 August 2000, Davis, CA', Am. Met. Soc.
- Britter, R. E. and Hanna, S. E. (2003), 'Flow and dispersion in urban areas', *Annu. Rev. Fluid Mech.* **35**, 469–496.
- Brook, R. R. (1972), 'The measurement of turbulence in a city environment', *J. Appl. Meteorol.* **11**, 443–450.
- Brown, R. A. (1991), *Fluid mechanics of the atmosphere*, Academic Press Inc., San Diego.
- Brunet, Y., Finnigan, J. J. and Raupach, M. R. (1994), 'Wind-tunnel study of air-flow in waving wheat - single-point velocity statistics', *Boundary-Layer Meteorol.* **70**, 95–132.
- Brunet, Y. and Irvine, M. R. (2002), 'The control of coherent eddies in vegetation canopies: Streamwise structure spacing, canopy shear scale and atmospheric stability', *Boundary-Layer Meteorol.* **94**, 139–163.
- Busch, N. E. and Kristensen, L. (1976), 'Cup anemometer overspeeding', *J. Appl. Meteorol.* **15**, 1328–1332.
- Businger, J. A. and Oncley, S. P. (1990), 'Flux measurement with conditional sampling', *J. Atmos. Oc. Tech.* **7**, 349–352.
- Caton, F., Britter, R. E. and Dalziel, S. (2003), 'Dispersion mechanisms in a street canyon', *Atmos. Environ.* **37**, 693–702.
- Cebeci, T. (2004), *Turbulence models and their application*, Springer, Long Beach.

- Chang, J. C. and Hanna, S. R. (2004), 'Air quality model performance evaluation', *Meteorol. Atm. Phys.* **87**, 167–196.
- Cheng, H. and Castro, I. P. (2002), 'Near wall flow over urban-like roughness', *Boundary-Layer Meteorol.* **104**, 229–259.
- Christen, A. (2003), Impact of the LICOR 7500 lag correction on field data sampled 2000–2003 at the University of Basel, Technical report, Institute of Meteorology, Climatology and Remote Sensing, University of Basel.
- Christen, A. and Rotach, M. W. (2004), Estimating wind speed at an urban reference height, in 'Fifth AMS Symposium on the Urban Environment 23–27 August', Am. Met. Soc.
- Christen, A., van Gorsel, E., Andretta, M., Calanca, P., Rotach, M. W. and Vogt, R. (2000), Inter-comparison of ultrasonic anemometers during the MAP-Riviera project, in 'Proc. 9th Conf. Mount. Met., Aspen CO, USA', Am. Met. Soc., pp. 130–131.
- Christen, A., van Gorsel, E., Vogt, R., Andretta, M. and Rotach, M. W. (2001), 'Ultrasonic anemometer instrumentation at steep slopes : Wind tunnel study - field intercomparison - measurements', *MAP Newsletter* **15**, 164–167.
- Christen, A. and Vogt, R. (2004a), Direct measurement of dispersive fluxes within a cork oak plantation, in '26th AMS Conf. Agr. For. Meteorol. 23–27 August, Vancouver, BC, Canada.', Am. Met. Soc.
- Christen, A. and Vogt, R. (2004b), 'Energy and radiation balance of a Central European city', *Int. J. Clim.* **24**, 1395–1421.
- Christen, A. and Vogt, R. (2005), *Quality control and corrections of the radiation measurements at the BUBBLE-surface sites*, Stratus Technical Report / Arbeitsbericht 003, ISSN 1661-3228.
- Cionco, R. M. (1965), 'A mathematical model for air flow in a vegetative canopy', *J. Appl. Meteorol.* **4**, 517–522.
- Clarke, C. F., Ching, J. and Godowich, J. M. (1982), A study of turbulence in an urban environment, Technical report, EPA.
- Cleugh, H. A. and Oke, T. R. (1986), 'Suburban-rural energy balance comparisons in summer for Vancouver, B.C.', *Boundary-Layer Meteorol.* **36**, 351–369.
- Coppin, P., Raupach, M. R. and Legg, B. J. (1986), 'Experiments on scalar dispersion within a model-plant canopy. II. An elevated plane source', *Boundary-Layer Meteorol.* **35**, 167–191.
- Corrsin, S. (1974), 'Limitations of gradient transport models in random walks and in turbulence', *Adv. Geophys.* **18A**, 25–71.
- Counihan, J. (1971), 'Wind tunnel determination of the roughness length as a function of fetch and density of three-dimensional roughness elements', *Atmos. Environ.* **5**, 273–292.
- Craig, K. J. and Bornstein, R. D. (2002), *Urbanization of Numerical mesoscale models*, Workshop on Urban Boundary Layer Parameterisations, European Commission EUR 20355, pp. 17–30.
- CSI (1995), *KH2O Krypton Hygrometer User Guide*, Campbell Scientific Ltd.
- de Bruin, H. A. R., Kohsiek, W. and Hurk, B. J. V. D. (1993), 'A verification of some methods to determine the fluxes of momentum, sensible heat, and water vapour using standard deviation and structure parameter of scalar meteorological quantities.', *Boundary-Layer Meteorol.* **63**, 231–257.
- de Haan, P., Rotach, M. W. and Werfeli, M. (2001), 'Modification of an operational dispersion model for urban applications', *J. Appl. Meteorol.* **40**, 864–879.
- Di Sabatino, S., Kastner-Klein, P., Berkowicz, R., Britter, R. E. and Fedorovich, E. (2003), 'The modelling of turbulence from traffic in urban dispersion models. I. Theoretical considerations', *Env. Fluid. Mech.* **3**, 129–143.
- Dwyer, M. J., Patton, E. G. and Shaw, R. H. (1997), 'Turbulent kinetic energy budgets from a large-eddy simulation of airflow above and within a forest canopy', *Bound.-Layer Meteorol.* **84**, 23–43.
- Ellefsen, R. (1991), 'Mapping and measuring buildings in the canopy boundary layer in ten U.S. cities', *Energ. Buildings.* **15-16**, 1025–1049.

- Elliott, J. A. (1972), 'Microscale pressure fluctuations measured within the lower atmospheric boundary layer', *J. Fluid Mech.* **53**.
- Fedderson, B., Leitl, B. and Schatzmann, M. (2004), Wind tunnel modelling of urban turbulence and dispersion over the city of Basel (Switzerland) within the BUBBLE project, in 'Fifth AMS Symposium on the Urban Environment 23-27 August', Am. Met. Soc.
- Feigenwinter, C. (2000), The vertical structure of turbulence above an urban canopy, PhD thesis, University of Basel, Institute of Meteorology, Climatology and Remote Sensing.
- Feigenwinter, C. and Vogt, R. (2005), 'Detection and analysis of coherent structures in urban turbulence', *Theor. Appl. Climatol.* **In press**, DOI: 10.1007/s00704-004-0111-2.
- Feigenwinter, C., Vogt, R. and Parlow, E. (1999), 'Vertical structure of selected turbulence characteristics above an urban canopy', *Theor. Appl. Clim.* **62**, 51-63.
- Finnigan, J. J. (1979), 'Turbulence in waving wheat II: Structure of momentum transfer', *Boundary-Layer Meteorol.* **16**, 213-236.
- Finnigan, J. J. (2000), 'Turbulence in plant canopies', *Annu. Rev. Fluid Mech.* **22**, 519-557.
- Fisher, B. E. A., Joffre, S., Kukkonen, J., Piringer, M., Rotach, M. W. and Schatzmann, M. (2005), *Meteorology applied to Urban Air Pollution Problems. Final Report COST 715*, European Commission. Directorate General for Research, Brussels.
- Fisher, B. E. A., Kukkonen, J. and Schatzmann, M. (2002), 'Meteorology applied to urban air pollution problems cost 715', *Int. J. Env. Pollution* **16**, 560-569.
- Foken, T. (2003), *Angewandte Meteorologie - Mikrometeorologische Methoden*, Springer, Berlin.
- Frenzen, P. and Vogel, C. A. (1992), 'The turbulent kinetic-energy budget in the atmospheric surface-layer - a review and an experimental reexamination in the field', *Boundary-Layer Meteorol.* **60**, 49-76.
- Frenzen, P. and Vogel, C. A. (2001), 'Further studies of atmospheric turbulence in layers near the surface: Scaling the tke budget above the roughness sublayer', *Boundary-Layer Meteorol.* **99**, 173-206.
- Garratt, J. R. (1993), *The atmospheric boundary layer*, Cambridge University Press, Cambridge.
- Gempeler, M. (1995), 'Analyse der Strömungsbedingungen an der BASTA-Station im Hinblick auf die messtechnischen Aspekte bei der Bestimmung turbulenter Flüsse.'
- Gill Instruments (1992), *3-Axis Research Ultrasonic Anemometer User Manual*, 4.1 edn, Gill Instruments Limited.
- Grant, A. L. M. and Watkins, R. D. (1989), 'Errors in turbulence measurements with a sonic anemometer', *Boundary-Layer Meteorol.* **46**, 181-194.
- Grelle, A. and Lindroth, A. (1994), 'Flow distortion by a solent sonic anemometer: wind tunnel calibration and its assessment for flux measurements over forest and field', *J. Atmos. Oc. Tech.* **11**, 1529-1542.
- Grimmond, C. S. B., Dragoni, D., Anderson, D. E., Beringer, J., Christen, A., Coutts, A., Crawford, B., Fowler, D., Hu, F., Hom, J., Kanda, M., King, T. S., Kuttler, W., Masson, V., Mayer, H., McFadden, J., Miglietta, F., Moriwaki, R., Nemitz, E., Offerle, B., Oke, T. R., Scherer, D., Soegaard, H., Tapper, N., Walsh, C. J. and Vogt, R. (2004), Urban fluxnet: CO₂-flux measurements, in 'Fluxnet International Workshop, Firenze, Italy, December 13-15 2004'.
- Grimmond, C. S. B., King, T. S., Cropley, F. D., Nowak, D. J. and Souch, C. (2002), 'Local-scale fluxes of carbon dioxide in urban environments: methodological challenges and results from chicago', *Environ. Poll* **116**, S243-S254.
- Grimmond, C. S. B., King, T. S., Roth, M. and Oke, T. R. (1998), 'Aerodynamic roughness of urban areas derived from wind observations', *Boundary-Layer Meteorol.* **89**, 1-24.
- Grimmond, C. S. B. and Oke, T. R. (1991), 'An objective urban heat-storage model and its comparison with other schemes.', *Atmos. Environ. B-Urb.* **25**, 311-326.

- Grimmond, C. S. B. and Oke, T. R. (1995), 'Comparison of heat fluxes from summertime observations in the suburbs of four north American cities', *J. Appl. Meteor.* **34**, 873–889.
- Grimmond, C. S. B. and Oke, T. R. (1999a), 'Aerodynamic properties of urban areas derived from analysis of surface form', *J. Appl. Meteor.* **38**, 1262–1292.
- Grimmond, C. S. B. and Oke, T. R. (1999b), 'Heat storage in urban areas: Local-scale observations and evaluation of a simple model', *J. Appl. Meteor.* **38**, 922–940.
- Grimmond, C. S. B., Salmond, J. A., Oke, T. R., Offerle, B. and Lemonsu, A. (2004), 'Flux and turbulence measurements at a densely built-up site in Marseille: Heat, mass (water and carbon dioxide), and momentum', *J. Geophys. Res. - Atmospheres* **109**, D24101.
- Grimmond, C. S. B., Souch, C. and Hubble, M. D. (1996), 'Influence of tree cover on summertime surface energy balance fluxes, San Gabriel Valley, Los Angeles', *Climate Research* **6**, 45–57.
- Gryning, S.-E., Batchvarova, E., Rotach, M. W., Christen, A. and Vogt, R. (2005), 'Roof-level SF₆ tracer experiments in the city of Basel', *Zürcher Geographische Schriften. IAC-ETH in press*.
- Hamdi, R. and Schayes, G. (2004), 'Improving the martilli's urban boundary layer scheme: offline validation over different urban surfaces', *Internal draft*.
- Hanna, S. R., Chang, J. C. and Strimaitis, D. G. (1993), 'Hazardous gas-model evaluation with field observations', *Atmos. Environ. Part A* **23**, 2265–2285.
- Högström, U., Bergström, H. and Alexandersson, H. (1982), 'Turbulence characteristics in a near-neutrally stratified urban atmosphere', *Bound.-Layer Meteorol.* **23**, 449–472.
- Hoydysh, W. G. and Dabberdt, W. F. (1988), 'Kinematics and dispersion characteristics of flows in asymmetric street canyons', *Atmos. Environ.* **22**, 2677–2689.
- Hunter, L. J., Johnson, G. T. and Watson, I. D. (1992), 'An investigation of 3-dimensional characteristics of flow regimes within the urban canyon', *Atmos. Environ. B-Urb.* **26**, 425–432.
- Jackson, P. S. (1981), 'On the displacement height in the logarithmic velocity profile', *J. Fluid Mech.* **111**, 15–25.
- Jauregui, E., Godinez, L. and Cruz, F. (1992), 'Aspects of heat-island development in Guadalajara, Mexico', *Atmos. Environ. B-Urb.* **26**, 391–396.
- Kaimal, J. C. and Finnigan, J. J. (1994), *Atmospheric boundary layer flows - their structure and measurement*, Oxford University Press, New York.
- Kanda, M., Moriwaki, R. and Kasamatsu, F. (2004), 'Large-eddy simulation of turbulent organized structures within and above explicitly resolved cube arrays', *Bound.-Layer Meteorol.* **112**, 343–368.
- Kastner-Klein, P., Berkowicz, R. and Britter, R. (2004), 'The influence of street architecture on flow and dispersion in street canyons', *Meteorol. Atmos. Phys.* **87**, 121–131.
- Kastner-Klein, P., Fedorovich, E. and Rotach, M. W. (2001), 'A wind-tunnel study of organised turbulent motions in urban street canyons', *Journal of Wind Engineering and Industrial Aerodynamics* **89**, 849–861.
- Kastner-Klein, P. and Plate, E. J. (1999), 'Wind-tunnel study of concentration fields in street canyons', *Atmos. Environ.* **33**, 3973–3979.
- Kastner-Klein, P. and Rotach, M. W. (2004), 'Mean flow and turbulence characteristics in an urban roughness sublayer', *Boundary-Layer Meteorol.* **111**, 55–84.
- Katul, G. G., Albertson, J. D., Hsieh, C. I., Conklin, P. S., Sigmon, J. T., Parlange, M. B. and Knoerr, K. R. (1996), 'The 'inactive' eddy motion and the large-scale turbulent pressure fluctuations in the dynamic sublayer', *J. Atmos. Sci.* **53**, 2512–2524.
- Katul, G. G., Geron, C. D. and Hsieh, C. I. (1998), 'Active turbulence and scalar transport near the forest-atmosphere interface', *J. Appl. Meteorol.* **37**, 1533–1546.
- Katul, G. G., Hsieh, C. I., Kuhn, G., Ellsworth, D. and Nie, D. (1997), 'Turbulent eddy motion at the forest-atmosphere interface', *J. Geophys. Res.* **102**, 13409–13421.

- Katul, G. G., Kuhn, G., Schieldge, J. and Hsieh, C. I. (1997), 'The ejection-sweep character of scalar fluxes in the unstable surface layer', *Boundary-Layer Meteorol.* **83**, 1–26.
- Klysik, K. (1996), 'Spatial and seasonal distribution of anthropogenic heat emissions in Lodz, Poland.', *Atmos. Environ.* **30**, 3397–3404.
- Kolmogorov, A. N. (1941), 'The local structure of turbulence in incompressible viscous fluid for very large Reynolds numbers', *Doklady ANSSSR* **30**, 301–304.
- Kovar-Panskus, A., Louka, P., J.-F.Sini, E.Savory, Czech, M., Abdelqari, A., P.G.Mestayer and Toy, N. (2002), 'Influence of geometry on the mean flow within urban street canyons : a comparison of wind tunnel experiments and numerical simulations', *Water, Air, and Soil Pollution Focus* **2**, 365–380.
- Kruijt, B., Malhi, Y., Lloyd, J., Norbre, A. D., Miranda, A. C., Pereira, M. G. P., Culf, A. and Grace, J. (2000), 'Turbulence statistics above and within two Amazon rain forest canopies', *Boundary-Layer Meteorol.* **94**, 297–331.
- Kutzbach, J. (1961), Investigations of the modifications of wind profiles by artificially controlled surface roughness, Master's thesis, Department of Meteorology, University of Wisconsin, Madison.
- Landsberg, H. E. (1981), *The urban climate*, Vol. 28 of *International geophysics series*, Academic Press, New York.
- Laubach, J. and Teichmann, U. (1996), 'Measuring energy budget components by eddy correlation: data corrections and application over low vegetation', *Contr. Atmos. Phys.* **69**, 307–320.
- Leclerc, M. Y., Beissner, K. C., Shaw, R. H., den Hartog G, G. and Neumann, H. H. (1990), 'The influence of atmospheric stability on the budgets of the Reynolds stress and turbulent kinetic energy within and above a deciduous forest.', *J. Appl. Climatol.* **29**, 916–933.
- Lemonsu, A., Grimmond, C. S. B. and Masson, V. (2004), 'Modeling the surface energy balance of the core of an old Mediterranean city: Marseille', *J. Appl. Meteor.* **43**, 312–327.
- Li, X. W., Strahler, A. H. and Woodcock, C. E. (1995), 'A hybrid geometric optical-radiative transfer approach for modeling albedo and directional reflectance of discontinuous canopies.', *IEEE Trans. Geosc. Remote Sensing* **33**, 466–480.
- Licor (2003), 'Customer letter on timing error of 7500 open-path analyzer'.
- Longley, I. D., Gallagher, M. W., Dorsey, J. R., Flynn, M. and Barlow, J. F. (2004), 'Short-term measurements of airflow and turbulence in two street canyons in Manchester', *Atmos. Environ.* **38**, 69–79.
- Louka, P., Belcher, S. E. and Harrison, R. G. (2000), 'Coupling between air flow in streets and the well-developed boundary layer aloft', *Atmos. Environ.* **34**, 2613–2621.
- Lu, S. S. and Wilmarth, W. W. (1973), 'Measurements of the structure of the Reynolds stress in a turbulent boundary layer', *J. Fluid. Mech.* **60**, 481–571.
- Macdonald, R. W. (2000), 'Modelling the mean velocity profile within the urban canopy layer', *Boundary-Layer Meteorol.* **97**, 25–45.
- Macdonald, R. W., Griffiths, R. F. and Hall, D. J. (1998), 'An improved method for estimation of surface roughness of obstacle arrays', *Atmos. Environ.* **32**, 1857–1864.
- Maitani, T. and Seo, T. (1985), 'Estimates of velocity-pressure and velocity pressure gradient interactions in the surface layer above plant canopies', *Bound.-Layer Meteorol.* **33**, 51–60.
- Manobianco, J., L. Case, J., Evans, R. J., Short, D. A. and Pister, K. S. J. (2004), Global environmental MEMS sensors (GEMS): A revolutionary observing system for the 21st century, in '7th Symposium on Integrated observing systems: February 8 - 13, 2003, Long Beach, CA', Am. Met. Soc.
- Martilli, A., Clappier, A. and Rotach, M. W. (2002), 'An urban surface exchange parameterisation for mesoscale models', *Boundary-Layer Meteorol.* **104**, 261–304.
- Martucci, G., Mitev, V., Matthey, R. and Srivastava, M. K. (2004), Remote-controlled automatic

- backscatter lidar for PBL and troposphere measurements: description and first results, in 'Remote Sensing of Clouds and the Atmosphere VIII. Edited by Schaefer, Klaus; Comeron, Adolfo; Carleer, Michel R.; Picard, Richard H. Proceedings of the SPIE, Volume 5235, pp. 661-672', pp. 661-672.
- Masson, V. (2000), 'A physically-based scheme for the urban energy budget in atmospheric models', *Boundary-Layer Meteorol.* **94**, 357-397.
- McBean, G. A. and Elliott, J. A. (1975), 'Vertical transports of kinetic-energy by turbulence and pressure in boundary-layer', *J. Atmos. Sci.* **32**, 753-766.
- McMillen, R. T. (1988), 'An eddy correlation technique with extended applicability to non-simple terrain', *Boundary-Layer Meteorol.* **43**, 231-245.
- McNaughton, K. G. and Brunet, Y. (2002), 'Townsend's hypothesis, coherent structures and monin-obukhov similarity', *Boundary-Layer Meteorol.* **102**, 161-175.
- Mestayer, R. G., Durand, P., Augustin, P., Bastin, S., Bonnefond, J. M., Benech, B., Campistron, B., Coppalle, A., Delbarre, H., Dousset, B., Drobiniski, P., Druilhet, A., Frejafon, E., Grimmond, C. S. B., Groleau, D., Irvine, M., Kergomard, C., Kermadi, S., Lagouarde, J. P., Lemonsu, A., Lohou, F., Long, N., Masson, V., Moppert, C., Noilhan, J., Offerle, B., Oke, T. R., Pigeon, G., Puygrenier, V., Roberts, S., Rosant, J. M., Said, F., Salmond, J., Talbaut, M. and Voogt, J. (2005), 'The urban boundary-layer field campaign in Marseille (UBL/CLU-ESCOMPTE): Set-up and first results', *Boundary-Layer Meteorol.* **114**, 315-365.
- Meyers, T. P. and Baldocchi, D. D. (1991), 'The budgets of turbulent kinetic energy and Reynolds stress within and above a deciduous forest', *Agric. Forest Meteorol.* **53**, 207-222.
- Miguel, A. F., van de Braak, N. J., Silva, A. M. and Bot, G. P. A. (2001), 'Wind-induced airflow through permeable materials Part I: The motion equation', *Journal of Wind Engineering and Industrial Aerodynamics* **89**, 45-57.
- Monin, A. S. and Obukhov, A. M. (1958), *Fundamentale Gesetzmässigkeit der turbulenten Vermischung in der bodennahen Schicht der Atmosphäre*, Statistische Theorie der Turbulenz, Akademie Verlag, Berlin, pp. 199-226.
- Moore, C. J. (1986), 'Frequency response corrections for eddy correlation systems', *Boundary-Layer Meteorol.* **37**, 17-35.
- Moriwaki, R. and Kanda, M. (2004), 'Seasonal and diurnal fluxes of radiation, heat, water vapor, and carbon dioxide over a suburban area', *J. Appl. Clim.* **43**, 1700-1710.
- Nakagawa, H. and Nezu, I. (1977), 'Prediction of the contributions to the Reynolds stress from bursting events in open channel flow', *J. Fluid Mech.* **80**, 99-128.
- Nielsen, M. (2000), 'Turbulent ventilation of a street canyon', *Environ. Monitoring and Assessment* **65**, 389-396.
- Nunez, M. and Oke, T. R. (1977), 'The energy balance of an urban canyon', *J. Appl. Meteor.* **16**, 11-19.
- Offerle, B., Grimmond, C. S. B., Fortuniak, K., Oke, T. R. and Klyzik, K. (2003), 'Temporal variability in heat fluxes over a northern European downtown', *Proc. 5th Int. Conf. Urb. Clim., September 1-5 2003, Lodz, Poland*.
- Offerle, B., Grimmond, C. S. B. and Oke, T. R. (2003), 'Parameterization of net all-wave radiation for urban areas', *J. Appl. Meteor.* **42**, 1157-1173.
- Ohtaki, E. (1985), 'On the similarity in atmospheric fluctuations of carbon dioxide, water vapour and temperature over vegetated fields', *Boundary-Layer Meteorol.* **32**, 25-37.
- Oikawa, S. and Meng, Y. (1995), 'Turbulence characteristics and organized motion in a suburban roughness sublayer', *Boundary-Layer Meteorol.* **74**, 289-312.
- Oke, T. R. (1981), 'Canyon geometry and the nocturnal heat island: comparison of scale model and field observations', *J. Climatol.* **1**, 1-16.
- Oke, T. R. (1987), *Boundary layer climates*, Routledge, London.
- Oke, T. R. (1988), 'Street design and urban canopy layer climate', *Energ. Bldg.* **11**, 103-113.

- Oke, T. R. (2004), 'Initial guidance to obtain representative meteorological observations at urban sites', *IOM Report, World Meteorological Organization Geneva, 2004*.
- Oke, T. R., Spronken-Smith, R. A., E, E. J. and Grimmond, C. S. B. (1999), 'The energy balance of central Mexico City during the dry season', *Atmos. Environ.* **33**, 3919–3930.
- Orlanski, I. (1975), 'A rational subdivision of scales for atmospheric processes', *Bull. Amer. Meteor. Soc.* **56**, 529–530.
- Otte, T. L., Lacser, A., Dupont, S. and Ching, J. K. S. (2004), 'Implementation of an urban canopy parameterization in a mesoscale meteorological model', *J. Appl. Meteorol.* **43**, 1648–1665.
- Panofsky, H. A. and Dutton, J. A. (1984), *Atmospheric turbulence*, John Wiley and Sons, New York.
- Panofsky, H. A., Tennekes, H., Lenschow, D. H. and Wyngaard, J. C. (1977), 'The characteristics of turbulent velocity components in the surface layer under convective conditions', *Boundary-Layer Meteorol.* **11**, 355–361.
- Parlow, E. (1996), 'The regional climate project REKLIP - An overview', *Theor. Appl. Clim.* **53**, 355–361.
- Philipona, R., Fröhlich, C. and Betz, C. (1995), 'Characterization of pyrgeometers and the accuracy of atmospheric long-wave radiation measurements', *Appl. Opt.* **34**, 1598–1605.
- Poggi, D., Katul, G. G. and Albertson, J. D. (2004a), 'Momentum transfer and turbulent kinetic energy budgets within a dense model canopy', *Bound.-Layer Meteorol.* **111**, 589–614.
- Poggi, D., Katul, G. G. and Albertson, J. D. (2004b), 'A note on the contribution of dispersive fluxes to momentum transfer within canopies', *Bound.-Layer Meteorol.* **111**, 615–621.
- Pope, S. B. (2000), *Turbulent flows*, Cambridge University Press, Cambridge.
- Prölss, G. W. (2001), *Physik des erdnahen Weltraums*, Springer, Berlin.
- Rambert, A., Elcalfsi, A. and Gougat, P. (2000), 'Optical flow velocimetry inside an entrained cavity, in '10th Int. Sym. Appl. Laser Tech. Fluid Mech.'.
- Raupach, M. R. (1981), 'Conditional statistics of Reynolds stress in rough wall and smooth-wall turbulent boundary layers', *J. Fluid Mech.* **108**, 363–382.
- Raupach, M. R. (1989), 'Applying lagrangian fluid-mechanics to infer scalar source distributions from concentration profiles in plant canopies', *Agric. For. Meteorol.* **47**, 85–108.
- Raupach, M. R. (1994), 'Simplified expressions for vegetation roughness length and zero-plane displacement as functions of canopy height and area index', *Boundary-Layer Meteorol.* **71**, 211–216.
- Raupach, M. R., Antonia, R. A. and Rajagopalan, S. (1991), 'Roughwall turbulent boundary layers', *Applied Mechanics Reviews* **44**, 1–25.
- Raupach, M. R., Coppin, P. A. and Legg, B. J. (1986), 'Experiments on scalar dispersion within a model-plant canopy. I. The turbulence structure', *Boundary-Layer Meteorol.* **35**, 21–52.
- Raupach, M. R., Finnigan, J. J. and Brunet, Y. (1989), 'Coherent eddies in vegetation canopies', *4th Proc. Australasian Conf. Heat Mass Transfer, May 9-12 1989, Christchurch, New Zealand* pp. 75–90.
- Raupach, M. R., Finnigan, J. J. and Brunet, Y. (1996), 'Coherent eddies and turbulence in vegetation canopies: the mixing-layer analogy', *Boundary-Layer Meteorol.* **78**, 351–382.
- Raupach, M. R. and Shaw, R. H. (1982), 'Averaging procedures for flow within vegetation canopies', *Bound.-Layer Meteorol.* **22**, 79–90.
- Raupach, M. R. and Thom, A. S. (1981), 'Turbulence in and above plant canopies', *Annu. Rev. Fluid Mech.* **13**, 97–129.
- Richards, K. (2004), 'Observation and simulation of dew in rural and urban environments.', *Prog. Phys. Geogr.* **28**, 76–94.
- Richards, K. and Oke, T. R. (2002), 'Validation and results of a scale model of dew deposition in urban environments.', *Int. J. Climatol.* **22**, 1915–1933.

- Rotach, M. W. (1991), 'Turbulence within and above an urban canopy', *Zürcher Geographische Schriften. PhD Thesis*. **45**, 245.
- Rotach, M. W. (1993a), 'Turbulence close to a rough urban surface. I. Reynolds stress', *Boundary-Layer Meteorol.* **65**, 1–28.
- Rotach, M. W. (1993b), 'Turbulence close to a rough urban surface. II. Variances and gradients', *Boundary-Layer Meteorol.* **66**, 75–92.
- Rotach, M. W. (1994), 'Determination of the zero plane displacement in an urban-environment', *Boundary-Layer Meteorol.* **67**, 187–193.
- Rotach, M. W. (1995), 'Profiles of turbulence statistics in and above an urban street canyon', *Atmos. Environ.* **13**, 1473–1486.
- Rotach, M. W. (1999), 'On the influence of the urban roughness sublayer on turbulence and dispersion', *Atmos. Environ.* **33**, 401–408.
- Rotach, M. W. (2001), 'Simulation of urban-scale dispersion using a lagrangian stochastic dispersion model', *Boundary-Layer Meteorol.* **99**, 379–410.
- Rotach, M. W. (2002), *The siting, choice, and operation of surface instrumentation in urban areas*, Surface energy balance in urban areas, European Commission EUR 19447, Antwerp, Belgium.
- Rotach, M. W. (2005), *Modification of flow and turbulence structure over urban areas*, Meteorology applied to Urban Air Pollution Problems. Final Report COST 715, European Commission. Directorate General for Research, Brussels.
- Rotach, M. W. and Christen, A. (2005), *Preparation of meteorological input data for urban air pollution models. Part I*, Meteorology applied to Urban Air Pollution Problems. Final Report COST 715, European Commission. Directorate General for Research, Brussels.
- Rotach, M. W., Gryning, S. E., Batchvarova, E., Christen, A. and Vogt, R. (2004), 'Pollutant dispersion close to an urban surface - the BUBBLE tracer experiment', *Theor. Appl. Clim.* **87**, 39–56.
- Rotach, M. W., Vogt, R., Bernhofer, C., Batchvarova, E., Christen, A., Clappier, A., Feddersen, B., Gryning, S. E., Martucci, G., Mayer, H., Mitev, V., Oke, T. R., Parlow, E., Richner, H., Roth, M., Roulet, Y. A., Ruffieux, D., Salmond, J., Schatzmann, M. and Voogt, J. (2005), 'BUBBLE - an urban boundary layer meteorology project', *Theor. Appl. Climatol.* **In press**, DOI: 10.1007/s00704-004-0117-9.
- Roth, M. (1991), Turbulent transfer characteristics over a suburban surface, PhD thesis, University of British Columbia, Departement of Geography.
- Roth, M. (2000), 'Review of atmospheric turbulence over cities', *Q. J. R. Meteorol. Soc.* **126**, 941–990.
- Roth, M. (2004), Application of scintillometry in the urban atmosphere, in 'Proc. 5th Conf. Urban Environment, Vancouver BC, Canada, August 22-27, 2004', Am. Met. Soc.
- Roth, M. and Oke, T. R. (1993a), 'Turbulent transfer relationships over an urban surface. I. Spectral characteristics', *Q. J. R. Meteorol. Soc.* **119**, 1071–1104.
- Roth, M. and Oke, T. R. (1993b), 'Turbulent transfer relationships over an urban surface. II. Integral statistics', *Q. J. R. Meteorol. Soc.* **119**, 1105–1120.
- Rotta, C. (1972), *Turbulente Strömungen, Leitfäden der angewandten Mathematik und Mechanik*, B. G. Teubner, Stuttgart.
- Roulet, Y.-A. (2004), Validation and application of an urban turbulence parameterisation scheme for mesoscale atmospheric models, PhD thesis, Ecole Polytechnique Fedrale de Lausanne, Faculte environnement naturel, architectural et construit.
- Ruffieux, D., Tharin, N. and Berger, H. (2002), Use of a low tropospheric wind profiler within an urban environment, in 'Instruments and Observing Methods TECO-2002 23-25 September, 2002', Bratislava (SL). WMO Report 25, WMO/TD-No 1123', WMO.
- Sachweh, M. and Koepke, P. (1995), 'Radiation fog and urban climate.', *Geophys. Res. Lett.* **22**, 1073–1076.
- Sailor, D. J. and Fan, H. (2001), 'Modeling the diurnal variability of effective albedo for cities', *Atmos. Environ.* **36**, 713–725.

- Salmond, J. A., Roth, M., Oke, T. R., Satyanarayana, A. N. V., Vogt, R. and Christen, A. (2004), Comparison of turbulent fluxes from roof top versus street canyon locations using scintillometers and eddy covariance techniques, in 'Proc. 5th Int. Conf. Urb. Clim., September 1-5 2003, Lodz, Poland', ICUC.
- Schmid, H. P. and Oke, T. R. (1990), 'A model to estimate the source area contribution to turbulent exchange in the surface layer over patchy terrain', *Q. J. R. Meteorol. Soc.* **116**, 965–998.
- Schönwiese, C. D. (1992), *Praktische Statistik für Meteorologen und Geowissenschaftler*, Gebr. Borntraeger, Berlin.
- Schotanus, P., Nieuwstadt, F. T. N. and De Bruin, H. A. R. (1983), 'Temperature-measurement with a sonic anemometer and its application to heat and moisture fluxes', *Boundary-Layer Meteorol.* **26**, 81–93.
- Semadeni-Davies, A., Lundberg, A. and Bengtsson, L. (2001), 'Radiation balance of urban snow: a water management perspective', *Cold Region Sci. and Tech.* **33**, 59–76.
- Shaw, R. H., Brunet, Y., Finnigan, J. J. and Raupach, M. R. (1995), 'A wind tunnel study of air flow in waving wheat: Two-point velocity statistics', *Boundary-Layer Meteorol.* **76**, 349–376.
- Shaw, R. H., Paw U, K. T., Zhang, X. J., Gao, W., den Hartog, G. and Neumann, H. H. (1990), 'Retrieval of turbulent pressure fluctuations at the ground surface beneath a forest', *Bound.-Layer Meteorol.* **50**, 319–338.
- Shaw, R. H., Tavangar, J. and Ward, D. P. (1983), 'Structure of Reynolds stress in a canopy', *J. Clim. Appl. Meteorol.* **22**, 1922–1931.
- Shen, S. H. and Leclerc, M. Y. (1997), 'Modelling the turbulence structure in the canopy layer', *Agr. For. Meteorol.* **87**, 3–25.
- Sini, J. F., Anquetin, S. and Mestayer, P. G. (1996), 'Pollutant dispersion and thermal effects in urban street canyons', *Atmos. Environ.* **30**, 2659–2677.
- Sorbjan, Z. (1989), *Structure of the Atmospheric Boundary Layer*, Prentice Hall, Englewood Cliffs.
- Steyn, D. G. (1982), 'Turbulence in an unstable surface layer over suburban terrain', *Boundary-Layer Meteorol.* **22**, 183–191.
- Stull, R. B. (1984), 'Transilient turbulence theory. I. The concept of eddy mixing across finite distances', *J. Atmos. Sci.* **41**, 3351–3367.
- Stull, R. B. (1988), *An introduction to boundary layer meteorology*, Atmospheric Sciences Library; 13, Kluwer Academic Publ., Dordrecht.
- Taha, H. (1999a), 'Modifying a mesoscale meteorological model to better incorporate urban heat storage: A bulk-parameterization approach', *J. Appl. Meteor.* **38**, 466–473.
- Taha, H. (1999b), 'Urban climates and heat islands: albedo, evapotranspiration, and anthropogenic heat', *Energ. Buildings.* **25**, 99–103.
- Tanner, B. D. and Greene, J. P. (1989), Measurement of sensible heat and water vapour fluxes using eddy correlation methods. Prepared for U.S. Army Dugway Proving Ground, Utah, Technical report, Campbell Scientific Inc.
- Tanner, B. D., Swiatek, E. and Greene, J. P. (1993), Density fluctuations and use of the Krypton hygrometer in surface flux measurements, in 'Proc. Management of Irrigation and Drainage Systems, Park City, Utah'.
- Tanner, C. B. and Thurtell, G. W. (1969), Anemometer measurements of Reynolds stress and heat transport in the atmospheric surface layer, Technical report, Department of Soil Science, University of Wisconsin, Madison, WI, Research and Development Technical Report ECOM 66-G22-F to the US Army Electronics Command.
- Todhunter, P. E., Xu, F. and Buttle, J. M. (1992), 'A model of net-radiation over suburban snowpacks', *Atmos. Environ. B - Urb.* **26**, 17–27.
- Townsend, A. A. (1961), 'Equilibrium layers and wall turbulence', *J. Fluid Mech.* **11**, 97–120.
- Unwin, D. J. (1980), 'The synoptic climatology of Birmingham's urban heat island, 1965-1974', *Weather* **35**, 43–50.
- Vaisala (1991), *Instructions manual for wind measurement system anemometer WAA15A, WAA15A-T0560-1.1 edn*, Vaisala Met Systems.

- van Gorsel, E. (2005), Ground based remote sensing measurements during BUBBLE, Technical report, Institute for Atmospheric and Climate Science, ETHZ.
- van Gorsel, E., Christen, A., Feigenwinter, C., Parlow, E. and Vogt, R. (2003), 'Daytime turbulence statistics above a steep forested slope', *Boundary-Layer Meteorol.* **109**, 311–329.
- Vardoulakis, S., Fisher, B. E. A., Pericleous, K. and Gonzalez-Flesca, N. (2003), 'Modelling air quality in street canyons: a review', *Atmos. Environ.* **37**, 155–182.
- Versteeg, H. K. and Malalasekera, W. (1995), *An introduction to computational fluid dynamics: the finite volume method*, Longman Scientific and Technical, Harlow.
- Villani, M. G., Schmid, H. P., Su, H.-B., Hutton, J. L. and Vogel, C. S. (2003), 'Turbulence statistics measurements in a northern hardwood forest', *Boundary-Layer Meteorol.* **108**, 343–364.
- Vogt, R. (1995), Theorie, Technik und Analyse der experimentellen Flussbestimmung am Beispiel des Hartheimer Kiefernwaldes, PhD thesis, University of Basel, Geographical Institute.
- Vogt, R., Christen, A., Rotach, M. W., Roth, M. and Satyanarayana, A. N. V. (2005), 'Temporal dynamics of CO₂ fluxes and profiles over a Central European city', *Theor. Appl. Climatology* **In press**.
- Vogt, R. and Feigenwinter, C. (2004), Sonic anemometers tested in a wind tunnel, in 'Proc. 26th Conf. Ag. For. Met., Vancouver BC, Canada, August 22-27, 2004', Am. Met. Soc.
- Vogt, R., Feigenwinter, C., Paw U, K. T. and Pitacco, A. (1997), Intercomparison of ultrasonic anemometers, in 'Preprints of the 12th Symposium of Boundary Layers and Turbulence, Vancouver, Canada.', Am. Met. Soc., pp. 354–355.
- Vogt, R. and Reber, S. (1992), 'Das REKLIP-Energiebilanzmessnetz', *Regio Basiliensis - Basler Zeitschrift für Geographie* **108**, 81–92.
- Wallace, J. M., Brodkey, R. S. and Eckelman, H. (1972), 'Wall region in turbulent shear-flow', *J. Fluid Mech.* **54**, 39–48.
- Warner, S., Platt, N. and Heagy, J. F. (2004), 'Comparisons of transport and dispersion model predictions of the URBAN 2000 field experiment', *J. Appl. Meteorol.* **43**, 829–846.
- Webb, E., Pearman, G. and Leuning, R. (1980), 'Correction of flux measurements for density effects due to heat and water vapour transfer', *Q. J. R. Met. Soc.* **106**, 85–100.
- Wilczak, J. M., Oncley, S. P. and Bedard, A. J. (1992), Turbulent pressure fluctuations in the atmospheric surface layer, in 'Proc. 10th Symp. Turb. and Diffusion, Portland, OR,', Am. Met. Soc., p. 167170.
- Wilczak, J. M., Oncley, S. P. and Stage, S. A. (2001), 'Sonic anemometer tilt correction algorithms', *Boundary-Layer Meteorol.* **99**, 127–150.
- Willis, G. E. and Deardorff, J. W. (1976), 'On the use of Taylor's hypothesis for diffusion in the mixed layer', *Quart. J. Roy. Meteor. Soc.* **102**, 817–822.
- Wilson, N. R. and Shaw, R. H. (1977), 'Higher-order closure model for canopy flow', *J. Appl. Clim.* **16**, 1197–1205.
- Wyngaard, J. C. (1988), 'Flow-distortion effects on scalar flux measurements in the surface layer: implications for sensor design', *Boundary-Layer Meteorol.* **42**, 19–26.
- Wyngaard, J. C. and Clifford, S. F. (1977), 'Taylor's hypothesis and high frequency turbulence spectra', *J. Atmos. Sci.* **34**, 922–929.
- Wyngaard, J. C. and Cote, O. R. (1971), 'The budgets of turbulent kinetic energy and temperature variance in the atmospheric surface layer', *J. Atmos. Sci.* **28**, 190–201.
- Wyngaard, J. C., Cote, O. R. and Izumi, Y. (1971), 'Local free convection, similarity and the budgets of shear stress and heat flux', *J. Atmos. Sci.* **28**, 1171–1182.
- Xu, L. K., Matista, A. A. and Hsiao, T. C. (1999), 'A technique for measuring CO₂ and water vapor profiles within and above plant canopies over short periods.', *Agric. For. Met.* **94**, 1–12.

Curriculum Vitae

Dipl. Geogr. Andreas Christen
Born: April 28, 1975, Binnigen, Switzerland
Languages: German, English, French

Current affiliation:

Technical University of Berlin
Institute of Ecology Climatology Section
Rothenburgstrasse 12 AB3-1/2
12165 Berlin
Germany
Phone: ++49-30-314-71330
andreas.christen@tu-berlin.de
<http://www.klima.tu-berlin.de/english/team/christen/>

Education

Apr 2005: PhD in Meteorology at the University of Basel (Switzerland) on ‘Atmospheric turbulence and surface energy exchange in urban environments’ (6.0 of 6.0, summa cum laude).

Nov 2000: Diploma in Geography at the University of Basel (6.0 of 6.0). Minors: Meteorology (8 Sem.), Chemistry (4. Sem.) and Earth Sciences (4 Sem.). Diploma thesis in Meteorology on ‘Turbulence structure of the nocturnal boundary layer at a steep alpine slope’.

Dec 1994: Swiss Matura (Type C, Mathematics and Natural Sciences, Kanton Basel-Land) at Gymnasium Oberwil (5.3 of 6.0).

Positions

Since Apr 2005: Post-doc and lecturer position at the Institute of Ecology, Climatology Section, Technical University of Berlin, Germany (Prof. Dr. D. Scherer).

Jan 2001 – Dec 2003 and Apr 2004 – Mar 2005: Assistant position at the Institute of Atmospheric

and Climate Science of the Federal Institute of Technology (ETH) Zurich, Switzerland (PD Dr. M. Rotach). Working place: University of Basel, Department of Geosciences, Institute of Meteorology, Climatology and Remote Sensing.

Jan 2004 – Mar 2004: Research Assistant position at the Institute of Meteorology, Climatology and Remote Sensing at the University of Basel, Switzerland (Prof. Dr. E. Parlow).

Oct 1998 – Dec 2000: Undergraduate assistant position at the Institute of Meteorology, Climatology and Remote Sensing, University of Basel, Switzerland (Dr. R. Vogt).

Research Activities

2003 – 2004: Scientific contributions to the final report of COST-715. Working groups ‘Urban wind field’ (Dr. M. Rotach) and ‘surface energy balance and mixed layer height’ (Dr. M. Piringer).

Sep 2003: Short experimental study at the Bulgarian Meteorological and Hydrological Service in Sofia (Dr. E. Batchvarova) through an Institute Partnership of the Swiss National Science Foundation.

2001 – 2002: Field work in the framework of the PhD thesis within the international Basel Urban Boundary Layer Experiment (BUBBLE). Operation of micrometeorological towers, tracer release experiments and analysis of turbulence data.

2001 – 2003: Participation in three field campaigns of the European project WATERUSE: Eddy covariance flux measurements and high resolved vertical profiles of turbulence parameters, CO₂ and water vapour over plantations in Italy and Portugal.

2001: Participation in the MORE I experiment (VERTIKO) on vertical advection of CO₂ within a forest (TU Dresden).

2000: Two-month research scholarship of the Swiss

Academy of Science to participate in the international Energy Balance Experiment (EBEX) hosted by NCAR/ATD near Fresno, CA, USA.

1999: Three months field work in the Southern Alps (Boundary Layer Group of the Mesoscale Alpine Project, MAP).

Work Experience

1995 – 1998: Programmer in a software development company for medical image analysis (Triangle Micro Research AG, Liestal, Switzerland).

1998: Four-month internship at the environmental authorities of the City Bad Säkingen (Germany): Analysis of chemical indicators in a eutrophic lake and contributions to a limnological expert report (in collaboration with Prof. Dr. H. Leser, Physical Geography, University of Basel).

Awards

2002: ‘Best student presentation’ at AMS 4th Symposium on the Urban Environment 2002, Norfolk, VA, USA.

2003: ICUC award ‘Exceptional Presentation’ at the 5th International Conference on Urban Climate, Lodz, Poland.

2004: Best student presentation and ‘Outstanding contribution to the conference’, 5th Symposium on the urban environment, Vancouver B.C., Canada, 2004.